SOME ASPECTS OF STRAIN LOCALIZATION MODELING IN LARGE DEFORMATION FINITE-ELEMENT ANALYSES

by

© Jin Chen

A Thesis is submitted to the

School of Graduate Studies

in partial fulfilment of the requirements for the degree of

Doctor of Philosophy

Faculty of Engineering and Applied Science

Memorial University of Newfoundland

May 2022

St. John's Newfoundland and Labrador Canada

ABSTRACT

Shear strength of soils might decrease with an increase of shear strain, which is called "strain-softening." The degradation of strength occurs in different types of soils (e.g., loose sand and sensitive clay) and under different loading conditions (e.g., drained or undrained). Strain-softening plays a major role in a wide range of geotechnical problems, including catastrophic failures (e.g., large-scale landslides) and laboratory tests (e.g., biaxial tests). While physical modeling and laboratory testing provide an overall or macro-scale response, numerical analysis could contribute insights into the mechanisms for a wide range of conditions. Unfortunately, numerical simulation of problems involving strain-softening materials is equally challenging, and the challenges include strain localizations, mesh sensitivity and large deformation. Several methods have been proposed and implemented in traditional Lagrangian-based finite element (FE) programs to overcome mesh sensitivity and localization issues. However, the suitability of these methods for large deformation problems has been verified in limited studies. While the soil types and loading conditions might be different, the geotechnical problems involved in softening could be analyzed developing a common framework. Therefore, the aim of the present study is to develop large-deformation FE modeling techniques for minimizing mesh sensitivity and simulating large-scale landslides.

Nonlocal regularization methods were previously proposed to solve the mesh dependency issues in modeling strain localization. These methods relate the strength reduction of the local element to the strains of neighbouring elements by using weight functions. However, their applications for a large-deformation FE are limited. In the present study, several numerical

algorithms are developed, successfully implemented in a Eulerian-based FE program, and validated against previous numerical studies with three nonlocal regularization methods. Simplification and optimization are applied to reduce the computational costs. The performance of the three nonlocal methods is evaluated by simulating a biaxial test, and one of them is found to be relatively more effective and thus used for further in-depth study of strain regularization.

Shear bands in local and nonlocal models are usually much thicker than in real soil, and their thickness increases with an increase in shear displacement. Softening scaling is effective to model the macroscopic force–displacement behaviour without modeling the thin shear band that develops in real soil. Softening scaling in a local model can also function as a regularization tool, which is usually called "element size scaling." The element size scaling method and the nonlocal method show comparable effects in strain regularization in a biaxial compression test simulation and a slope failure analysis with Eulerian-based FE program. However, a significantly larger computational time is required for a nonlocal analysis and some interaction between two neighbouring shear bands might occur. Therefore, the element size scaling method is chosen in the analysis of a large-scale slope failure.

Finally, the large-scale flow slide failure of the Lower San Fernando Dam is modeled using the techniques developed in a Eulerian-based FE program. Simplified constitutive models are developed to simulate the strain-softening behaviour of different soil layers. The seepage is modeled by developing a new technique based on the thermal–fluid analogy, which is incorporated in the in-situ stress calculations. Eulerian-based FE simulations show a similar failure pattern observed in post-slide investigations and also explain potential failure processes.

ACKNOWLEDGEMENTS

First of all, I would like to express my sincerest gratitude to my supervisor, Dr. Bipul Hawlader, Professor and Research Chair in Seafloor Mechanics at Memorial University of Newfoundland and Labrador, who encouraged me to overcome research challenges and taught me the art of geotechnical engineering. I have been so greatly benefited from his knowledge, patience, innovative ideas, skillful supervision, and most importantly, his attitude towards research work.

I am tremendously fortunate to have my co-supervisors, Dr. Kenton Pike, Senior Geotechnical Engineer, TechnipFMC, and Dr. Kshama Roy, Lead-Special Projects/Pipeline Integrity, Northern Crescent. They have always been supportive of my research and career development. It has been a privilege working under their guidance.

I am thankful for the support from the Natural Sciences and Engineering Research Council of Canada (NSERC), InnovateNL, formerly Research and Development Corporation of Newfoundland and Labrador (RDC), the School of Graduate Studies, and Memorial University.

It has been enjoyable to work in such an amazing research group. Many thanks go to Dr. Rajib Dey, Dr. Sujan Dutta, Dr. Chen Wang, Dr. Mahmud Al Tarhouni, Dr. Rajith Dayarathne, Dr. Ripon Karmaker, Mr. Rabindra Subedi, Mr. Diponkar Saha, Mr. Anan Morshed, Mr. Piash Saha and other group members for their encouragement, suggestions and support.

Special thanks to my parents and parents-in-law who continuously supported my crazy ideas and encouraged me to pursue my dreams. Finally, I want to express my sincere appreciation to my wife and daughter for your companionship and patience.

TABLE OF CONTENTS

ABSTRACT ii

ACKNOWLEDGEMENTS iv

LIST OF FIGURES ix

LIST OF TABLES xiii

LIST OF SYMBOLS xiv

CHAPTER 1 15

Introduction 15

1.1 Background and motivation 15

1.2 Focus of the research 18

1.3 Objectives 21

1.4 Outline of thesis 22

CHAPTER 2 25

Literature Review 25

2.1 Introduction 25

2.2 Numerical modeling in geotechnical engineering 26

2.3 Ill-posed boundary value problem 27

2.4 Regularization techniques 29

2.5 Nonlocal methods and their applications 34

2.6 Seepage modeling 46

2.7 The failure of the Lower San Fernando Dam 47

2.8 Summary 57

CHAPTER 3 59

A novel nonlocal Eulerian-based finite-element approach for strain-softening materials 59

3.1 Abstract 59

3.2 Introduction 60

3.3 Eulerian-based finite-element method 63

3.4 Nonlocal strain regularization 64

3.5 Implementation of nonlocal methods in Eulerian FE code 70

3.6 Numerical simulation 81

3.7 Results 85

3.8 Discussions 90

3.9 Conclusions 97

CHAPTER 4 106

Effectiveness of softening-scaling rules of local and nonlocal methods in Eulerian-based large deformation finite element modeling 106

4.1 Abstract 106

4.2 Introduction 107

4.3 Eulerian-based finite-element method 111

4.4 Nonlocal methods 111

4.5 Softening-scaling rule 115

4.6 Numerical simulations 116
4.7 Discussions 137
4.8 Practical implications 152
4.9 Conclusions 153
CHAPTER 5 162
Large Deformation Finite-Element Modeling of the Lower San Fernando Dam Failure in 1971 162
5.1 Abstract 162
5.2 Introduction 163
5.3 FE Modeling 170
5.4 Modeling of soil 176
5.5 Results 186
5.6 Parametric studies 192
5.7 Conclusions 200
CHAPTER 6 209
Conclusions and Recommendations for Future Research 209
6.1 Conclusions 209
6.2 Recommendations for future research 211
REFERENCES 213
APPENDIX-I 222
Comparison of Two Mesh Regularization Approaches for Large Deformation Finite Element

Analysis 222

APPENDIX-II 234

Modeling of Seepage Using a Eulerian-based Finite Element Method 234

LIST OF FIGURES

Figure 1.1 Shear band formation: (a) a plane strain test (Marello 2004); and (b) the Lower San Fernando Dam failure (Castro et al. 1992) 16

Figure 2.1 Load–displacement diagram for a one-dimensional tensile bar composed of a strain-softening elastoplastic material with an imperfection in the centre. An element-free Galerkin method was used without regularization (Pamin et al. 2003) 28

Figure 2.2 Load vs. displacement results for undrained analyses (Summersgill et al. 2017a) 36

Figure 2.3 Comparison between a Gaussian-type and the G&S weight function 37

Figure 2.4 Schematic distributions of local and nonlocal strains: (a) after initiation of softening; (b) at later stage (Galavi and Schweiger 2010) 39

Figure 2.5 The effect of α on nonlocal strain 42

Figure 2.6 The cross section of the failed dam (a) condition after the earthquake-induced failure; (b) schematic drawing of the reconstructed cross section (Castro et al. 1992) 47

Figure 2.7 The slip surface and factor of safety from an LE analysis: (a) primary slip surface; (b) primary and secondary slip surface (Seed 1979) 49

Figure 2.8 The deformed mesh 40 s after the start of earthquake (Ming and Li 2003) 49

Figure 2.9 Comparison between the field observation and MPM modeling result of the Lower San Fernando Dam failure (a) cross-section in the field; (b) deformation pattern with material zonation; (c) deviatoric strain (Huang et al. 2020) 50

Figure 2.10 Large-deformation modeling of landslide in Eulerian-based FE (Dey et al. 2015) ... 51

Figure 2.11 Schematic undrained response of a saturated, contractive sandy soil 52

Figure 2.12 Idealized undrained behaviour of sands under monotonic load: 53

Figure 2.13 Idealized undrained behaviour of sands under cyclic load: 54

Figure 2.14 Qualitative driving and resisting forces at initiation of slide (Castro et al. (1989)) ... 55

Figure 2.15 Simplified undrained model for liquefiable soils (Gu et al. 1993) 57

Figure 3.1 The operator splitting for Eulerian-based finite-element method 64

Figure 3.2 (a) Reference integration points for nonlocal calculation; (b) the variation of weighting function 67

Figure 3.3 Comparison of the three nonlocal weight functions 69

Figure 3.4 The return method for the von Mises softening model 71

Figure 3.5 Implementation of nonlocal von Mises model in Eulerian-based FE 76

Figure 3.6 The nonlocal searching algorithm for Eulerian-based FE 77

Figure 3.7 (a) Geometry and boundary conditions of Case I; (b) geometry and boundary conditions of Case II; (c) stress-strain curve for the soil 83

Figure 3.8 Local equivalent plastic shear strain distribution with different mesh sizes after 50 mm vertical displacement 87

Figure 3.9 Load–displacement curves: (a) local model; (b) original nonlocal; (c) G&S nonlocal; (d) over-nonlocal ($\alpha = 1.5$); (e) over-nonlocal ($\alpha = 2.0$) 88

Figure 3.10 Simulation results for case II: (a) comparison of axial stress–strain curves for nonlocal CEL and nonlocal MPM; (b, c, d) plastic shear strains for 0.125-m, 0.0625-m, and 0.03125-m meshes 89

Figure 3.11 Schematic distribution of weight functions and their approximation in Eulerian-based FE 93

Figure 3.12 Stress–displacement curves of Case I with and without optimization 95

Figure 3.13 Computational cost of Case I with local and over-nonlocal ($\alpha = 1.5$) methods 96

Figure 4.1 The over-nonlocal method in Eulerian-based FE: (a) schematic plot of the weight function; (b) the influencing area 114

Figure 4.2 (a) Geometry and boundary conditions of case 1; (b) geometry and boundary conditions of case 2; (c) stress–strain curve of soil 118

Figure 4.3 Local deviatoric plastic strain contours from three methods with different mesh sizes (case 1) 124

Figure 4.4 Load–displacement curves with three mesh sizes (case 1) 126

Figure 4.5 Local deviatoric plastic strain contours for nonlocal models (t_{FE} = 0.0625 m) 128

Figure 4.6 Load–displacement for nonlocal models with softening scaling (t_{FE} = 0.0625 m) 129

Figure 4.7 Load–displacement curves of local and over-nonlocal models without scaling 130

Figure 4.8 Local deviatoric plastic strain contours of three methods with different mesh sizes . 132

Figure 4.9 Load–displacement curves 133

Figure 4.10 Local deviatoric plastic strain contours of over-nonlocal models with softening scaling 134

Figure 4.11 Load–displacement curves of over-nonlocal models with softening scaling 135

Figure 4.12 Shear band formation and propagation in local and nonlocal models 136

Figure 4.13 Shear band formation and propagation 137

Figure 4.14 Normalized shear band thickness (t_{sFE}/l) vs. α 139

Figure 4.15 Schematic view of (a) external work increment; (b) dissipated plastic energy per cubic meter 142

Figure 4.16 Variation of shear band thickness 146

Figure 4.17 Normalized shear band thickness vs normalized vertical displacement 148

Figure 4.18 Computational costs of the biaxial test with local (element size scaling) and over-nonlocal methods.....150

Figure 4.19 Modeling of comparable shear band thickness in local and nonlocal models.....150

Figure 5.1 Cross-Section through the Lower San Fernando Dam: (a) after 1971 earthquake; (b) reconstruction of failed cross-section (Seed et al. 1973) 164

Figure 5.2 Eulerian-based FE model of the Lower San Fernando Dam 171

Figure 5.3 Schematic diagram of the phases of the failure of the Lower San Fernando Dam (adapted from Castro et al. 1989).....176

Figure 5.4 Schematic behaviour of the sandy hydraulic fill 180

Figure 5.5 Total head distribution 1 day after reservoir filling.....187

Figure 5.6 Total head distribution at the steady state.....187

Figure 5.7 Total head variation with time at point A in Fig. 5.2.....187

Figure 5.8 Deviatoric stress in Eulerian-based FE and SIGMA/W 188

Figure 5.9 Deviatoric plastic strain contours of the representative case.....190

Figure 5.10 Deviatoric plastic strain contours for different apparent cohesions 195

Figure 5.11 Deviatoric plastic strain of Case E.....196

Figure 5.12 Deviatoric plastic strain contours for different strength degradation rates.....198

Figure 5.13 Deviatoric plastic strain contours for different pseudostatic loads:.....199

LIST OF TABLES

Table 2.1 Overview of regularization methods 31

Table 2.2 Implementations of regularization methods in geotechnical engineering with large-deformation numerical techniques 33

Table 2.3 A summary of applications of nonlocal methods in geotechnical engineering 44

Table 3.1 Parameters used in CEL analyses 85

Table 4.1 Parameters used in FE simulations 121

Table 4.2 Input data for the study of softening scaling for the over-nonlocal method 122

Table 5.1 Numerical modeling techniques for the Lower San Fernando Dam 167

Table 5.2 Soil parameters used in FE analysis 177

Table 5.3 Soil parameters used in seepage analysis 185

LIST OF SYMBOLS

As the thesis is written in manuscript format, symbols used in this study are listed at the end of each chapter (Chapters 3–5). The symbols used in Chapters 1, 2 and 6 are listed below:

α	amplification factor
$\varepsilon^{p}_{eq(NL)}$	nonlocal equivalent plastic shear strain
ε^{p}_{eq}	equivalent plastic shear strain
$\omega_g()$	G&S weight function
$\omega_o()$	Gaussian-type weight function
d_{50}	mean particle size
t_s	thickness of the shear band
V_w	reference volume
$\mathbf{x}$	position vector

CHAPTER 1

Introduction

1.1 Background and motivation

Shear bands are localized regions that undergo large plastic shear strains, and the phenomenon is known as strain localization. Strain localization can be observed in both a laboratory-scale test (e.g., a plane strain test on an overconsolidated clayey material (Fig. 1.1(a))) and a large-scale failure (e.g., a landslide, like the famous failure of the Lower San Fernando Dam in 1971 (Fig. 1.1(b))). The consequences of such a failure can be catastrophic. The deaths caused by landslides per year have been more than one thousand on average, and the annual economic losses have been estimated to be tens of billions dollars worldwide (Brabb 1991). During the failure of the Lower San Fernando Dam, a large portion of the dam crest slid into the reservoir, and the reservoir water almost overtopped the remaining crest (Fig. 1.1(b)), which nearly induced a dam breach. About 80, 000 people living downstream had to be evacuated until the reservoir water was drawn down to a safe level (Seed et al. 1973).

Strain localization can occur in strain-softening soils. Various types of soils show strain-softening behaviour under different loading conditions (e.g., drained and undrained) (Hsu and Liao 1988; Chu and Wanatowski 2009; Gylland et al. 2014; Mesri et al. 2021). For example, the failure of the Lower San Fernando Dam occurred about 30 seconds after a major earthquake in 1971 (Seed et al. 1973). Given that the initiation of failure and the post-failure process occurred over a short period, the submerged loose sandy layer is considered undrained with strain-softening behaviour. However, the dense sandy soil well above the phreatic line showed a drained

strain-softening behaviour. Multiple shear bands were observed in the failure of the Lower San Fernando Dam, and the shear displacement was extremely large (e.g., more than 30 m at the upstream toe area, Fig. 1.1(b)).

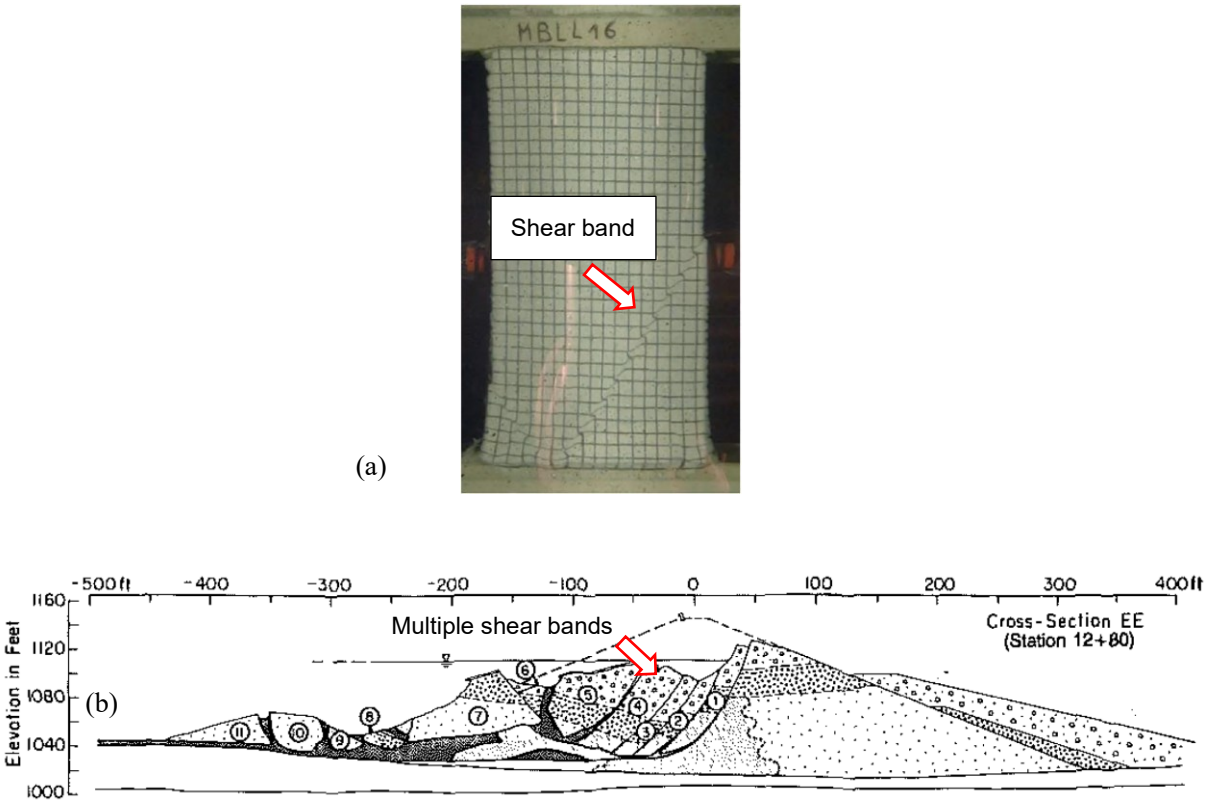

Figure 1.1 Shear band formation: (a) a plane strain test (Marello 2004); and (b) the Lower San Fernando Dam failure (Castro et al. 1992)

Seepage can significantly influence the stress distribution and therefore the strain localization in soils. Seepage forces on the soil skeleton affect the effective stresses and driving forces for a landslide. In other words, seepage forces can influence both the shear stress and shear resistance in the soil, which can potentially affect the development of shear bands. Li and Ming (2004) conducted finite element analyses of the Lower San Fernando Dam with and without

seepage forces. Although the shear bands were not directly shown from their analyses, different deformation was observed in the absence of seepage forces, and the difference increased with time. However, the analyses only showed the results until t = 40 s, when the horizontal velocity of the upstream toe was still high, (0.66 m/s without seepage forces and 0.38 m/s with seepage forces).

The shear band thickness (t_s) is extremely small in real soils and is usually related to the mean particle size of granular materials, d_{50}, as summarized by Guo (2012). The typical range of t_s is 10 to 20 d_{50} for different types of sand, based on the data collected by Marcher (2003), though a slightly wider range was shown by Maier (2003) and Finno et al. (1997). In other words, the t_s in sand can be millimeters to centimeters. However, the shear band thickness was reported to be 2 to 4 millimeters for sensitive clay, based on a set of biaxial plane strain tests (Thakur 2007). The shear band thickness is not a constant in the loading process. The shear band thickness observed by Thakur (2007) increases with the increase of shear strain. Similarly, Sadrekarimi and Olson (2010) showed that the shear band thickness in sand also increased with the shear loading in ring shear tests.

Numerical modeling is an important tool to analyze soil failures and provide guidance for geotechnical engineering design. Without special treatments, mesh dependency (i.e., the solution depends on the mesh size) occurs in a numerical model (de Borst et al. 1993). The shear band thickness in a numerical model is dependent on the mesh size (Pietruszczak and Mroz 1981; Galavi and Schweiger 2010). This shear band thickness is usually significantly larger than that of the real soil, because an extremely fine mesh is required to model the real one, which is computationally very expensive. Furthermore, when modeling large strains of shear bands, a traditional FE program

can encounter numerical issues (Griffiths and Lane 1999).

1.2 Focus of the research

Large-deformation analyses are pivotal to understand the post-failure mechanism and potential consequences of many soil failure problems, e.g., landslides. Though numerous studies have been done previously to numerically model these problems, many of them used the traditional Lagrangian-based finite-element (FE) method which encounters excessive mesh distortion under large deformation (e.g., Griffiths and Lane 1999). The Coupled Eulerian–Lagrangian (CEL) method that is mesh distortion-free (Benson 1992) has been proved effective in modeling large-deformation geotechnical engineering problems (e.g., Qiu et al. 2011; Dey et al. 2015; Hamann et al. 2015) and is therefore selected for this study. When the analyses do not involve interaction with Lagrangian bodies, and the soil is modeled with Eulerian elements, the CEL is referred to herein as Eulerian-based FE.

Multiple challenges are encountered when modeling shear bands for large deformation instead of small deformation problems. The following areas are the focus of the present study:

- Various types of soil can present strain-softening behaviour under certain loading conditions (e.g., drained and undrained). While many constitutive models have been applied to model strain-softening behaviour in Lagrangian-based FE, the implementation was typically limited to a relatively small range of deformation (e.g., Gu et al. 1993; Griffiths and Lane 1999). Appropriate constitutive models for strain-softening soils are necessary to address the strain localization in a large deformation failure (e.g., the failure

of the Lower San Fernando Dam).

- Mesh dependency issues arise when modeling strain-softening soils (de Borst et al. 1993). To overcome the mesh dependency effect, several strain regularization techniques have been developed previously, such as element size scaling (Pietruszczak and Mroz 1981) and the nonlocal method (Eringen 1981; Bažant and Lin 1988). However, the implementation of strain regularization techniques in a numerical modeling framework that can accommodate large soil deformation without mesh distortion issues is limited (e.g., Burghardt et al. 2012; Zhang et al. 2017; Monforte et al. 2019), and most of these implementations used an in-house solver. Existing regularization methods need to be applied and compared to establish best practices in a more attainable large-deformation analysis code, e.g., Eulerian-based FE that is commercially available.
- An extremely fine mesh is required to capture the thin shear bands existing in the soil, increasing the computational costs dramatically for a large-scale problem, e.g., landslides. To model a thicker shear band with the same macroscopic behaviour, the "softening scaling" technique has been used in local and nonlocal methods (e.g., Pietruszczak and Mroz 1981; Brinkgreve 1994). Soil strength decreases with local strains in the former while it varies with nonlocal strains (e.g., weighted average deviatoric plastic strain) in the latter methods. The effectiveness of softening scaling for both methods needs to be evaluated to provide guidance to the modeling practice.
- The shear band thickness increases with the increase of shear displacement in real soils (Thakur 2007; Sadrekarimi and Olson 2010), and Mallikarachchi and Soga (2020) showed

a similar trend using a nonlocal model in FE. However, the shear band thickness remains constant in the shear loading process, based on the equation proposed by Brinkgreve (1994) and the results of many other FE modeling studies (e.g., Maier 2003; Galavi and Schweiger 2010). Considering that all these FE analyses were limited to a relatively small deformation, the potential variation of shear band thickness under a larger deformation can be investigated in a Eulerian-based FE program.

- Seepage needs to be incorporated in large-deformation FE models, due to its remarkable influence on effective stresses and driving forces. However, the available elements in Eulerian-based FE are only single-phase, and cannot be used to model the seepage directly. An innovative approach is therefore needed so that the seepage can be modeled, and its induced seepage forces can be applied to the submerged Eulerian elements. The in-situ stresses under seepage can then be established.
- The famous failure of the Lower San Fernando Dam in 1971 was triggered by an earthquake of 6.6 magnitude (Seed et al. 1973). The failed soil in the upstream slope moved more than 30 meters. Most of previous numerical studies focused on the triggering mechanism of the failure and were restricted to relatively small deformation (e.g., Ming and Li 2003; Khoei et al. 2004; Blázquez and López-Querol 2007). A large-deformation analysis is required to understand the post-failure mechanisms.

1.3 Objectives

To include the post-failure deformation in a numerical model, a large-deformation analysis is required. This poses new challenges for numerical modeling techniques. The main purpose of this study is to address these challenges and provide guidance to the modeling practice. The findings are implemented in simulating the Lower San Fernando Dam failure, where various strain-softening soil layers were present. New algorithms are developed for soil constitutive modeling, strain regularization, and the consideration of seepage forces in Eulerian-based FE. The main objectives of this research are listed below:

- Develop simplified constitutive models that can capture the large-deformation behaviour of various types of strain-softening soils.
- Develop algorithms and write user-subroutines to implement three nonlocal regularization methods in Eulerian-based FE program. Simplify and optimize the algorithms to reduce the computational costs. Calibrate the algorithms with the results of biaxial tests from two other nonlocal FE programs.
- Evaluate the effectiveness of the three nonlocal methods in addressing the mesh dependency in Eulerian-based FE. Identify the most effective nonlocal method and explain the findings from a theoretical view.
- Evaluate the performance of softening scaling with local and nonlocal methods in modeling shear bands in Eulerian-based FE. Discuss the mutual influence between two shear bands for both methods. Note that the softening scaling in a local model is also a strain regularization tool, i.e., the element size scaling. Its efficacy in addressing mesh

dependency is compared with the nonlocal method.

- Implement an energy theory to explain the variation of shear band thickness in the loading process when using local and nonlocal methods in Eulerian-based FE. Discuss the limitations of a previous analytical solution for the shear band thickness.
- Develop a technique to model seepage in Eulerian-based FE using the thermal-fluid analogy. Calculate seepage forces and establish initial effective stresses based on the result of the seepage analysis. Calibrate the results with a widely used FE solver.
- Conduct a large-deformation analysis of the Lower San Fernando Dam failure in 1971 in Eulerian-based FE. Model the seepage and simulate the strain-softening behaviour of multiple soil layers. Compare the numerical results with the field observation for calibration and perform a parametric study to understand the relative influence of several important factors.

1.4 Outline of thesis

This thesis is prepared in manuscript format. The outcome of this study is presented in six chapters and two appendices.

- The first chapter provides the background information, research focus, objectives, and contributions of this study.
- Chapter 2 presents a short literature review. However, the problem-specific literature reviews are considered in Chapter 3–5 and Appendices I–II, as this thesis is in a manuscript format.

- Chapter 3 presents the algorithms to implement three nonlocal methods and the validation process into Eulerian-based FE. Simplification and optimization of the algorithms are performed to reduce the computational cost. The effectiveness of the three nonlocal methods is evaluated and compared in biaxial compression tests. This chapter will be submitted to a journal as a technical paper for review.
- Chapter 4 presents the effectiveness of the softening scaling in local and nonlocal methods in Eulerian-based FE, in terms of mesh dependency, macroscopic modeling, mutual influence between two shear bands, shear band thickness, and computational cost. In addition, the variation of shear band thickness under shearing is discussed based on an energy theory. This chapter will be submitted to a journal as a technical paper for review. A part of this study has been published on the 4th International Symposium on Frontiers in Offshore Geotechnics, ISFOG 2020. (Appendix-I).
- Chapter 5 presents the large-deformation analysis of the famous failure of the Lower San Fernando Dam in 1971. A technique is developed to model the seepage and establish the in-situ stresses under the steady-state seepage. Simplified soil models are developed for the strain-softening behaviour of different soil layers. Furthermore, the results are compared with the field, and a parametric study is conducted. This chapter will be submitted to a journal as a technical paper for review. A part of this study has been published for the 72nd Canadian Geotechnical Conference, Geo St. John's 2019 (Appendix-II). The author of this thesis also co-authored another journal paper that adopted the seepage modeling technique presented in this chapter (Wang et al. 2021). For that paper, the author of this thesis is the

principal contributor for the development of the seepage modeling technique in Eulerian-based FE based on the thermal-fluid analogy.

- Chapter 6 presents the general conclusions and recommendations for future research. The problem-specific conclusions are presented at the end of Chapter 3–5 and Appendices I–II. The references cited in Chapters 1 and 2 are listed in the References section at the end of the thesis.

CHAPTER 2

Literature Review

2.1 Introduction

A large-deformation analysis is pivotal to provide a deeper insight into the failure mechanisms and potential risks of catastrophic damages of soil failure problems (e.g., landslides). However, the numerical simulation of strain localization for large-deformation analyses present significant challenges. An effective numerical tool should be robust for modeling large-deformation behaviour. Furthermore, mesh dependency, macroscopic modeling, shear band thickness, influences of multiple shear bands, as well as soil constitutive models and seepage modeling, are among the most important topics that should be addressed for a large-deformation analysis.

As the thesis is written in manuscript format, a problem specific literature review is presented in Chapters 3–5 and Appendices A–B. The main purpose of this chapter is to provide additional critical review of previous research work relevant to the present study. This literature review chapter is organized as follows:

- A brief introduction to numerical modeling techniques comprises Section 2.2. The reasons for selecting Eulerian-based FE are presented in this section.
- The cause of the mesh dependency problem and the necessity to address it are discussed in Section 2.3.
- Existing regularization tools to reduce mesh dependence are introduced, and the selections of regularization tools for this study are then justified in Section 2.4.

- In Section 2.5, a more specific literature review on various nonlocal regularization methods is presented. Multiple technical gaps are identified. At the end of this section, a brief literature review of the softening scaling law is also presented, considering that it was commonly implemented in both nonlocal and local models.
- The necessity and technical gap in seepage modeling in Eulerian-based FE are discussed in Section 2.6.
- Finally, previous studies on the famous failure of the Lower San Fernando Dam are discussed in Section 2.7. Technical gaps are identified from the discussions.

2.2 Numerical modeling in geotechnical engineering

A variety of numerical modeling techniques has been used for geotechnical engineering analyses. Those under the scope of continuum mechanics can be divided into two main categories: (a) mesh-based and (b) mesh-free techniques (Soga et al. 2016). Mesh-based approaches include traditional Lagrangian-based FE (e.g., Griffiths and Lane 1999), finite-difference method (FDM) (e.g., Chowdhury et al. 2019), arbitrary Lagrangian Eulerian method (ALE) (including the Remeshing and interpolation technique with small strain, RITSS) (e.g., Wang et al. 2013), and the coupled Eulerian–Lagrangian method (CEL) (e.g., Qiu et al. 2011). Note that CEL becomes a Eulerian-based FE when no Lagrangian element is present. The mesh-free category contains the material point method (MPM) (e.g., Soga et al. 2016), smooth particle hydrodynamics (SPH) (e.g., Bui and Nguyen 2017), particle finite-element method (PFEM) (e.g., Zhang et al. 2017), finite-element method with Lagrangian integration points (FEMLIP) (e.g., Cuomo et al. 2013), and

the element-free Galerkin (EFG) method (e.g., Kumar and Dodagoudar 2009).

The traditional Lagrangian-based FE cannot handle large-deformation problems, due to excessive mesh distortion (Griffiths and Lane 1999). A large-deformation analysis is usually conducted using RITSS, CEL (including Eulerian-based FE), and mesh-free techniques. Among them, CEL, along with Eulerian-based FE, are commercially available, while most of the other large-deformation techniques are in-house programs. Furthermore, Eulerian-based FE has been successfully implemented to simulate various types of landslides in sensitive clays (Dey et al. 2015; Wang et al. 2020). Therefore, Eulerian-based FE is selected for the present study.

2.3 Ill-posed boundary value problem

Strain localization refers to the occurrence of narrow bands in a strain-softening material where any additional deformation concentrates, with the remaining areas loading and unloading in a near-rigid manner. This destructive phenomenon can induce large-scale failures, for example, a landslide.

Numerous studies have modeled shear bands and other strain localization problems. However, in those early attempts, the results were highly influenced by the fineness and direction of the discretization, due to a dramatic change of characters of the governing equations at the emergence of shear bands (de Borst 2001). The governing equations lose ellipticity in a static or quasi-static model. Additionally, in a dynamic problem, the initial boundary value problem loses hyperbolicity (Sluys 1992). For both static and dynamic problems, the boundary value problem becomes ill-posed (de Borst 2001). Therefore, a unique stress–strain response and shear band

thickness cannot be obtained from models with different discretization of the domain.

As aforementioned, the discretization sensitivity is caused by the change of characters of the governing equations, which is essentially a mathematical problem instead of a numerical issue for a numerical modeling tool (de Borst and Verhoosel 2017). Therefore, the discretization sensitivity can occur in both mesh-based and mesh-free methods, and it can be called "mesh dependency" for a mesh-based method. An example is shown in Fig. 2.1, which presents the load–displacement curves of a one-dimensional tensile bar for different discretization with the element-free Galerkin (EFG) method. The post-peak force is significantly dependent on the number of nodes in the EFG model.

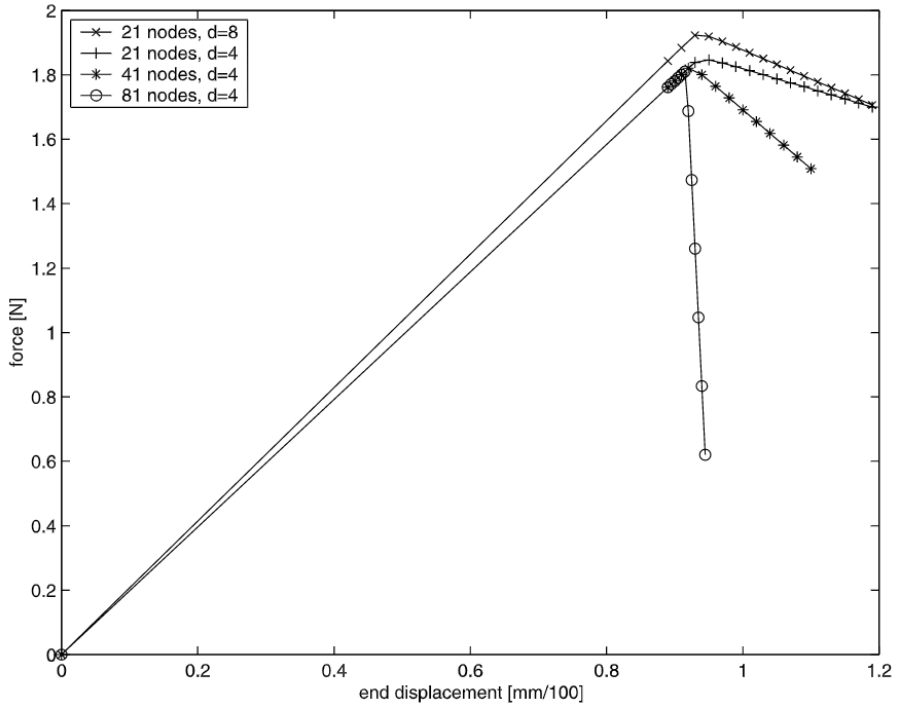

Figure 2.1 Load–displacement diagram for a one-dimensional tensile bar composed of a strain-softening elastoplastic material with an imperfection in the centre. An element-free Galerkin method was used without regularization (Pamin et al. 2003)

2.4 Regularization techniques

In order to address the mesh dependency (or discretization sensitivity), multiple regularization techniques have been developed previously; for example, element size scaling (Pietruszczak and Mroz 1981), nonlocal method (Eringen 1981; Bažant and Lin 1988), gradient-dependent method (de Borst et al. 1993; de Borst and Mühlhaus 1992; Toupin 1962), rate-dependent or viscoplastic modeling (Perzyna 1963; Needleman 1988; Loret and Prevost 1990; Prevost and Loret 1990), and the Cosserat method (Cosserat and Cosserat 1909; Muhihaus and Vardoulakis 1987; de Borst and Mühlhaus 1992). The concepts and features of these methods are summarized in Table 2.1.

Regularization methods have been implemented in both small-deformation numerical techniques (e.g., traditional Lagrangian-based FE, Summersgill et al. 2017a), and large-deformation numerical techniques (e.g., MPM, Burghardt et al. 2012; Goodarzi and Rouainia 2017,)). Due to a shorter history of the large-deformation techniques, more applications of regularization methods have been seen in small-deformation numerical programs, especially in a variety of traditional Lagrangian-based FE codes.

In recent years, several regularization methods have been implemented in a limited number of large-deformation techniques, as summarized in Table 2.2. Among these regularization methods, the element size scaling and nonlocal methods are the most popular, because each of them has been implemented in at least three different large-deformation techniques, as presented in Table 2.2. However, the nonlocal methods have not been used in Eulerian-based FE, and no comparison has been made between two regularization methods in a large-deformation code. More research can be

done to provide guidance to the implementation and selection of regularization methods in large-deformation techniques.

In the present study, algorithms are developed to implement nonlocal methods in Eulerian-based FE. In addition, the effects of the element size scaling and nonlocal methods are discussed and compared based on modeling results.

Table 2.1 Overview of regularization methods

Regularization methods	Concepts	Remarks	References
Element size scaling modeling	This method assumes that the post-peak softening modulus is proportional to the element size. It is also called as the "crack band model" or "fracture energy trick."	A mesh-independent load–displacement response can be obtained, while the shear band thickness is still dependent on the mesh size.	Pietruszczak and Mroz 1981; Moore and Rowe 1988; Bažant and Jirásek 2002; Jirásek and Bauer 2012; Dey et al. 2015
Nonlocal modeling	The strain (or another internal state variable in a constitutive model) at one integration point is determined by the weighted average of its neighbouring points. The covering area of neighbouring points is calculated by introducing an internal length.	This approach has been successfully implemented in many mesh-based and mesh-free techniques. Various nonlocal weight functions are available, and detailed comparison of them was only available for very few numerical techniques.	Bažant and Lin 1988; Brinkgreve 1994; Bažant and Jirásek 2002; Galavi and Schweiger 2010; Summersgill et al. 2017a
Gradient dependent modeling	The gradients (or spatial derivatives) of internal state variables, rather than the internal state variables themselves, are used in the constitutive description. Usually, strain gradients are adopted.	Gradient-dependent models also fall into the nonlocal category, as the gradients are used to reflect the nonlocal effects at the microscopic level. An internal length can be introduced implicitly by each gradient term. However, the computational complexity increases by performing extra numerical derivation. It is challenging to handle the gradients at the boundary.	Toupin 1962; de Borst and Mühlhaus 1992; de Borst et al. 1993; Jirásek and Rolshoven 2009

Regularization methods	Concepts	Remarks	References
Rate dependent (or viscoplastic) modeling	The material behaviour is time dependent in a rate-dependent or viscoplastic model. The time-dependency can be modeled with a rate-independent yield function by taking the "overstress" effect into account. Another type of rate-dependent model utilizes a rate-dependent yield function to make the shear strength degradation rate dependent on the strain rate.	This category of methods also implicitly introduces an internal length. Mesh independent results were reported from previous research, while the mesh sensitivity can be affected by the value of viscosity.	Heeres et al. 2002; Loret and Prevost 1990; Needleman 1988; Perzyna 1963; Prevost and Loret 1990
Cosserat continuum modeling	Rotational degrees-of-freedom are added to the traditional translational degrees-of-freedom in a Cosserat continuum model. The independent rotations, curvatures, together with coupled stresses, are implemented in the constitutive descriptions.	The use of this approach is relatively straightforward. However, it is indicated that the rotational degrees-of-freedom, along with the micro-curvatures and coupled stresses, are activated only under shearing, rather than pure tension.	de Borst and Mühlhaus 1992; Cosserat and Cosserat 1909; Muhihaus and Vardoulakis 1987

Table 2.2 Implementations of regularization methods in geotechnical engineering with large-deformation numerical techniques

References	Modeled problems	Numerical methods	Regularization methods
Dey et al. 2015; Islam et al. 2019	Large-scale landslides	CEL/Eulerian-based FE	Element size scaling
Burghardt et al. 2012	Biaxial tests; slope failures	Material point method (MPM)	Nonlocal method
Tran and Sołowski 2019	Large-scale landslides	Material point method (MPM)	Element size scaling
Zhang et al. 2019	Retrogressive landslides	Remeshing and interpolation technique with small strain (RITSS)	Element size scaling
Singh et al. 2021	Biaxial tests; buried pipe uplift; cyclic T-bar penetration	Remeshing and interpolation technique with small strain (RITSS)	Nonlocal method
Monforte et al. 2019	Biaxial tests; Indentation of rigid strip footing	Particle finite element method (PFEM)	Nonlocal method
Zhang et al. 2017	Collapse of soil column; retrogressive landslides	Particle finite element method (PFEM)	Viscoplastic model

2.5 Nonlocal methods and their applications

2.5.1 The nonlocal model

Shear band propagation is not only determined by the stress and strain in the elements of the highest strain but is also influenced by its energy dissipation to and from neighbouring elements. A nonlocal method provides a means of regulating strain calculations to avoid excessive softening and relates strain-softening to the surrounding area. Therefore, energy dissipation can also occur in the neighbouring elements. This reduces the mesh dependency and potential numerical convergence issues associated with strain-softening analyses. A nonlocal model calculates the strain (or another internal state variable in a constitutive model) at each local integration point by conducting a weighted average of its neighbouring points in the area defined by an internal length (Bažant and Jirásek 2002).

A fully nonlocal model will treat both stress and strain as nonlocal components (Eringen 1981). However, as a regularization tool, usually only the softening component is chosen for nonlocal calculation (Galavi and Schweiger 2010). The nonlocal strain is calculated as a softening parameter to evaluate the strength degradation, or material softening, at the local integration point. This makes it relatively convenient to be implemented in an existing FE code. Three commonly used nonlocal methods, the original nonlocal, the G&S nonlocal, and the over-nonlocal methods, are introduced below.

2.5.1.1 Original nonlocal method

The formulation for a three-dimensional nonlocal strain model was presented by Eringen (1981), for a strain-hardening problem. A nonlocal strain-softening model was proposed by Bažant et al. (1984). Equations (2.1) and (2.2) were used to calculate the nonlocal strain.

$$d\varepsilon^{\mathrm{p}}_{\mathrm{eq(NL)}}(\mathbf{x}_{\mathrm{n}}) = \frac{1}{V_{\mathrm{w}}}\iiint \left[\omega_{\mathrm{o}}(\mathbf{x}'_{\mathrm{n}})d\varepsilon^{\mathrm{p}}_{\mathrm{eq}}(\mathbf{x}'_{\mathrm{n}})\right]dx'dy'dz' \tag{2.1}$$

$$V_{\mathrm{w}} = \iiint \omega_{\mathrm{o}}(\mathbf{x}'_{\mathrm{n}})dx'dy'dz' \tag{2.2}$$

where $d\varepsilon^{\mathrm{p}}_{\mathrm{eq(NL)}}(\mathbf{x}_{\mathrm{n}})$ is the nonlocal equivalent plastic shear strain increment of the integration point at location $\mathbf{x}_{\mathrm{n}}$, and the subscript n denotes the dimension of the model; $d\varepsilon^{\mathrm{p}}_{\mathrm{eq}}(\mathbf{x}'_{\mathrm{n}})$ is the equivalent plastic shear strain increment at location $\mathbf{x}'_{\mathrm{n}}$ which refers to all the reference integration points for the location $\mathbf{x}_{\mathrm{n}}$; $\omega_{\mathrm{o}}(\mathbf{x}'_{\mathrm{n}})$ is a Gaussian-type weight function that is centered at the point $\mathbf{x}_{\mathrm{n}}$, and defines the weight of all the reference points $\mathbf{x}'_{\mathrm{n}}$ in the calculation of $d\varepsilon^{\mathrm{p}}_{\mathrm{eq(NL)}}(\mathbf{x}_{\mathrm{n}})$; and V_{w} is the reference volume, where x', y' and z' are the three dimensions.

In the "original nonlocal method" by Summersgill et al. (2017a), a Gaussian type of distribution, Eq. (2.3), is adopted as the weight function $\omega_{\mathrm{o}}(\mathbf{x}'_{\mathrm{n}})$.

$$\omega_{\mathrm{o}}(\mathbf{x}'_{\mathrm{n}}) = \frac{1}{l\sqrt{\pi}}\exp\left[-\frac{|\mathbf{x}'_{\mathrm{n}} - \mathbf{x}_{\mathrm{n}}|^2}{l^2}\right] \tag{2.3}$$

where l is an internal length parameter that is related to the shear band width.

Another Gaussian-type weight function, Eq. (2.4), was proposed by (Bažant and Lin 1988). In the presented study, both Eqs. (2.3) and (2.4) are considered as the "original nonlocal method".

$$\omega_{\mathrm{o}}(\mathbf{x}'_{\mathrm{n}}) = \exp\left[-\frac{k|\mathbf{x}'_{\mathrm{n}} - \mathbf{x}_{\mathrm{n}}|^2}{l^2}\right] \tag{2.4}$$

where $k = \sqrt{\pi}$ for 1D conditions; $k = 2$ for 2D conditions; $k = \left(6\sqrt{\pi}\right)^{1/3}$ for 3D conditions.

As shown in Fig. 2.2, the original method can significantly reduce mesh dependency in comparison to the local method (Summersgill et al. 2017a); however, a small gap can still be observed from the results using different mesh sizes (Fig. 2.2(b)). The main reason is that the local point still provides the greatest contribution to the nonlocal strain and the strength degradation, by using Eq. (2.3).

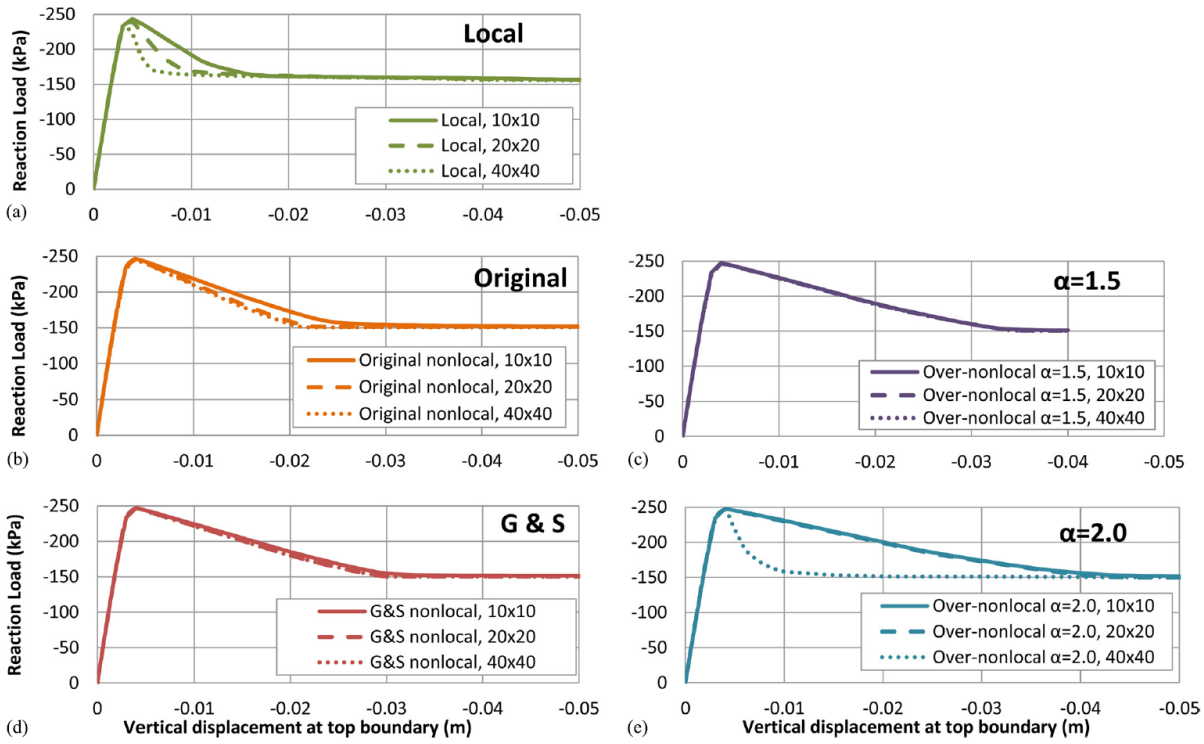

Figure 2.2 Load vs. displacement results for undrained analyses (Summersgill et al. 2017a)

2.5.1.2 G&S nonlocal method

To avoid the shortcoming shown in the original method, another weight function, $\omega_g(\mathbf{x}_n')$, as presented in Eq. (2.5), was developed by Galavi and Schweiger (2010). A nonlocal method that adopts this weight function can be called the G&S nonlocal method (Summersgill et al. 2017a).

$$\omega_g(\mathbf{x}'_n) = \frac{|\mathbf{x}'_n - \mathbf{x}_n|}{l^2} \exp\left[-\frac{|\mathbf{x}'_n - \mathbf{x}_n|^2}{l^2}\right] \tag{2.5}$$

This weight function recognized that the formation of the shear band is directly determined by the areas surrounding the strain localization and not influenced by the local strain. A comparison has been made between the Gaussian-type weight function and the G&S weight function by Galavi and Schweiger (2010), as presented in Fig. 2.3. The lowest contribution of strains is observed at the centre of the G&S weight function, while the highest is seen at the same location as the Gaussian-type distribution. This indicates that a larger portion of the concentrated local strain can be distributed to the neighbouring zone by using the G&S nonlocal method. From the research conducted by Summersgill et al. (2017a), the G&S method provided an improved mesh-independent result compared to the original nonlocal method (Fig. 2.2). Note that no new parameters need to be introduced in the G&S nonlocal method.

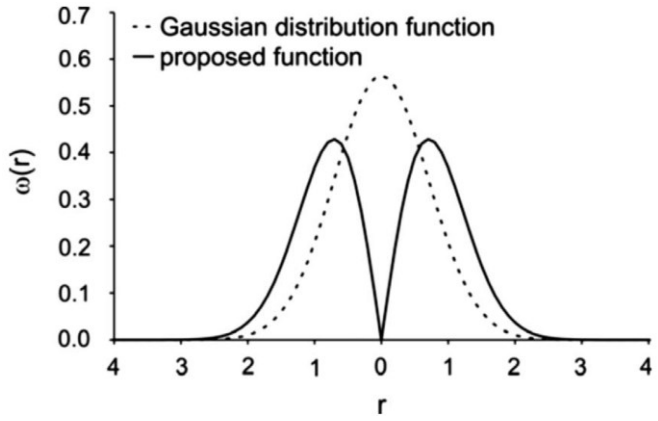

Figure 2.3 Comparison between a Gaussian-type and the G&S weight function (Galavi and Schweiger 2010)

2.5.1.3 Over-nonlocal method

The over-nonlocal method was proposed by Brinkgreve (1994). Similar to the G&S nonlocal method, the over-nonlocal strain weight function was designed to prevent the formation of a concentrated peak at the local integration point. A new parameter, α, was implemented to change the distribution of a Gaussian-type weight function. The nonlocal strain is calculated as shown in Eq. (2.6).

$$d\varepsilon^{\mathrm{p}}_{\mathrm{eq(NL)}}(\mathbf{x}_{\mathrm{n}}) = (1-\alpha)d\varepsilon^{\mathrm{p}}_{\mathrm{eq}}(\mathbf{x}_{\mathrm{n}}) + \frac{\alpha}{V_{\mathrm{w}}}\iiint \left[\omega_{\mathrm{o}}(\mathbf{x}'_{\mathrm{n}})d\varepsilon^{\mathrm{p}}_{\mathrm{eq}}(\mathbf{x}'_{\mathrm{n}})\right]dx'dy'dz' \qquad (2.6)$$

where $\omega_{\mathrm{o}}(\mathbf{x}'_{\mathrm{n}})$ is a Gaussian-type weight function (e.g., Eqs. (2.3) and (2.4)). Note that Eq. (2.3) was adopted by Brinkgreve (1994) and Summersgill et al. (2017a), while Eq. (2.4) was used by Burghardt et al. (2012).

An over-nonlocal model has to adopt $\alpha > 1$, as it becomes an original nonlocal method when $\alpha = 1$. A higher value of α leads to a lower strain contribution from the local integration point (Brinkgreve 1994). The over-nonlocal method is more capable of distributing strains to the neighbourhood than the original method (Fig. 2.4). Figure 2.4 shows that the strain at the centre is even smaller in the over-nonlocal model ($\alpha = 2$), in comparison to the G&S nonlocal model. In other words, the over-nonlocal model is theoretically more effective than the G&S nonlocal model to regulate the strains. However, the stability of the over-nonlocal method was challenged when a large value of α was adopted (Fig. 2.2) (Summersgill et al. 2017a), and the G&S nonlocal method was adopted for further study in a traditional Lagrangian-based FE (Summersgill et al. 2017b).

Based on the findings of these studies, several issues need to be investigated further:

- Does the over-nonlocal become unstable with a larger α due to the use of a traditional Lagrangian-based FE (Summersgill et al. 2017a)?
- If the instability issue can be resolved, will the over-nonlocal method provide the best performance?

To answer these questions, previous applications of nonlocal methods are reviewed in the next section.

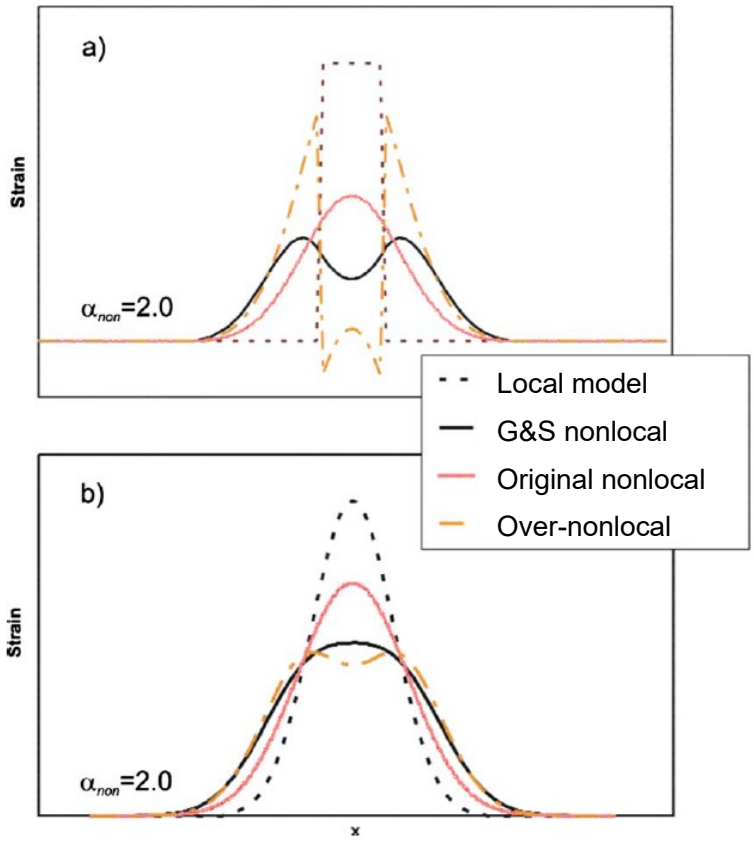

Figure 2.4 Schematic distributions of local and nonlocal strains: (a) after initiation of softening; (b) at later stage (Galavi and Schweiger 2010)

2.5.2 Previous applications of nonlocal methods

The nonlocal models have been implemented in various numerical modeling techniques as a strain regularization tool. In geotechnical engineering, the applications of various nonlocal methods (e.g., original, G&S, and over-nonlocal) have been implemented to model biaxial tests, strip footings, slope failures, etc. (e.g., Brinkgreve 1994; Maier 2003; Summersgill 2014; Summersgill et al. 2017a). A summary is presented in Table 2.3.

2.5.2.1 Choices of nonlocal methods (or weight functions)

The G&S nonlocal method was believed to be more effective than the original nonlocal and over-nonlocal methods for regularization, from the studies by Summersgill et al. (2017a). The over-nonlocal method was not recommended due to the numerical issue found when using a large α, as mentioned in Section 2.5.1.3. Following their conclusion, several studies adopted the G&S nonlocal method for various numerical techniques (Mánica et al. 2018; Monforte et al. 2019; Mallikarachchi and Soga 2020; Singh et al. 2021). However, numerical issues were not reported from other applications of the over-nonlocal method (Brinkgreve 1994; Burghardt et al. 2012; Lu et al. 2012; D'Ignazio et al. 2017), even when an extremely large α (= 6.763) was used (Brinkgreve 1994). Therefore, the effectiveness and robustness of the over-nonlocal method should be re-evaluated. When both the G&S nonlocal and over-nonlocal methods are robust in a numerical modeling technique, a comparison between them can be valuable.

Note that some researchers also used the original nonlocal method for geotechnical analyses (Maier 2003; Troncone 2005; Conte et al. 2010; Summersgill et al. 2017a), showing only a small

gap between the results from different mesh sizes (Maier 2003; Summersgill et al. 2017a). Therefore, the original nonlocal method is also discussed in this study.

2.5.2.2 Choices of α in the over-nonlocal method

By increasing the value of α, a lower nonlocal strain is obtained at the local integration points, while a higher nonlocal strain is present in the neighbouring integration points (Brinkgreve 1994). This was illustrated in Fig. 2.5 by Summersgill et al. (2017a). More energy can be dissipated in the neighbouring area using a larger α. As a result, with the increase of α, the shear band thickness also increases (Brinkgreve 1994).

A value of $\alpha = 2$ was adopted in several studies (Brinkgreve 1994; Lu et al. 2012; Burghardt et al. 2012; D'Ignazio et al. 2017) without providing a comparison with varying values of α. A comparison was conducted by Summersgill et al. (2017a) to explore the effect of α on mesh convergence. However, as aforementioned, the result became unstable for a fine mesh when using a relatively large α, e.g., $\alpha = 2.0$. This numerical issue needs to be addressed so that the effectiveness of larger α can be explored in the analysis.

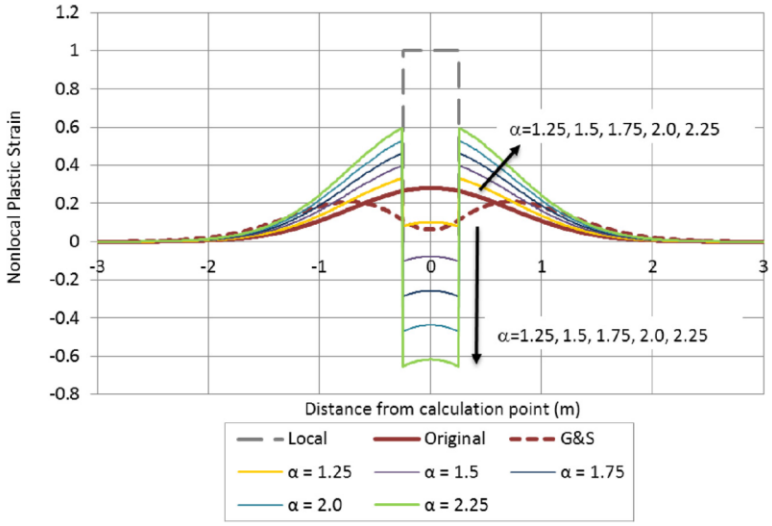

Figure 2.5 The effect of α on nonlocal strain

2.5.2.3 Applications of nonlocal methods in traditional Lagrangian-based FE

A traditional Lagrangian-based FE was adopted by most of the applications listed in Table 2.3. The strain range of these applications was relatively small. For example, only the early stage of a progressive failure, rather than the whole failure process that includes large movement of failure mass, has been modeled (Troncone 2005; Conte et al. 2010). Therefore, they could not determine whether the nonlocal methods are applicable at the large-deformation stage.

2.5.2.4 Applications of nonlocal methods in large-deformation analysis codes

Nonlocal methods have been applied in large-deformation analyses (Burghardt et al. 2012; Monforte et al. 2019; Singh et al. 2021); as mentioned in Section 2.5.2.1 and Table 2.3, only one type of nonlocal method was implemented in each of these studies. A comprehensive comparison of the three nonlocal methods in a large-deformation code is identified as a research gap. In addition,

none of the nonlocal methods were implemented in Eulerian-based FE. Hence, an investigation of the applicability of nonlocal methods in Eulerian-based FE is necessary.

2.5.2.5 Softening scaling

Due to the limited capacity of computing resources, the adopted element size in a numerical model is usually significantly larger than the real shear band thickness in soils. The shear band thickness in a nonlocal model has to be larger than the element size (Summersgill et al. 2017a). Therefore, it is difficult to model the real shear band thickness in a nonlocal model with conventional computational resources. Softening scaling has been implemented by many researchers to model a thick shear band while successfully displaying the macroscopic behaviour of soils (e.g., Brinkgreve 1994; Maier 2003; Galavi and Schweiger 2010). Soil strength decreases with local strains in a local model while it varies with nonlocal strains (e.g., weighted average deviatoric plastic strain) in a nonlocal model. In a local model, softening scaling is also referred to as the element size scaling technique, proposed by Pietruszczak and Mroz (1981). However, the internal length, instead of the element size, is used as the scaling parameter to determine the strength degradation rate for a nonlocal method. The effectiveness of the softening scaling for nonlocal methods in Eulerian-based FE needs to be investigated. Furthermore, a comparison between the nonlocal method and the element size scaling method is necessary to understand their effectiveness in addressing mesh dependency. Thereafter, the practical guidelines can be provided for strain regularization and softening scaling in large-deformation modeling.

Table 2.3 A summary of applications of nonlocal methods in geotechnical engineering

References	Modeled problems	Numerical methods	Types of nonlocal methods	Remarks
Brinkgreve 1994	1D tension bar; biaxial test; slope failure	Lagrangian-based FE	Over-nonlocal	α = 2.0, 5.0, 6.763, etc. No numerical issues were reported.
Maier 2003	Biaxial test; strip foundation	Lagrangian-based FE	Original nonlocal	The ill-posed boundary value problem was addressed as only a very small gap was observed from the load–displacement curves with different mesh sizes.
Troncone 2005	Slope failure	Lagrangian-based FE (TOCHNOG)	Original nonlocal	The early stage of a progressive failure was successfully modeled.
Galavi and Schweiger 2010	Biaxial test; tunnel excavation	Lagrangian-based FE	G&S nonlocal	The G&S nonlocal model was proposed by these authors. No numerical issues were reported.
Conte et al. 2010	Slope failure	FE with mesh refinements (TOCHNOG)	Original nonlocal	The early stage of a progressive failure was successfully modeled.
Burghardt et al. 2012	Biaxial test; slope failure	Material point method (MPM)	Over-nonlocal method	α = 2.0 was applied. A nonlocal iteration scheme is implemented in each time increment of an explicit MPM.
Lu et al. 2012	Biaxial test	Lagrangian-based FE	Over-nonlocal method	α = 2.0 was applied. No numerical issues were reported from the over-nonlocal model.

References	Modeled problems	Numerical methods	Types of nonlocal methods	Remarks
Summersgill 2014; Summersgill et al. 2017a; b	Biaxial test; slope failure	Lagrangian-based FE (Imperial College finite-element program, ICFEP)	Original nonlocal, G&S nonlocal, and over-nonlocal	G&S nonlocal method provided the best overall performance as the over-nonlocal was unstable using a larger α
D'Ignazio et al. 2017	Slope failure	Lagrangian-based FE (Plaxis 2D)	Over-nonlocal	α = 2.0 was applied. No numerical issues were reported.
Mánica et al. 2018	Biaxial test	Lagrangian-based FE (Plaxis)	G&S nonlocal	The G&S nonlocal method was selected based on the results from Summersgill et al. (2017a)
Monforte et al. 2019	Biaxial test; Indentation of rigid strip footing	Particle finite element method (PFEM)	G&S nonlocal method	The G&S nonlocal method was selected based on the results from Summersgill et al. (2017a) and Mánica et al. (2018).
Mallikarachchi and Soga 2020	Biaxial test	Lagrangian-based FE (Abaqus/Standard)	G&S nonlocal	The G&S nonlocal method was selected based on the results from Summersgill et al. (2017a). Numerical convergence issues were reported when adopting a small ratio of the internal length to the mesh size
Singh et al. 2021	Biaxial test; buried pipe uplift; cyclic T-bar penetration	Remeshing and interpolation technique with small strain (RITSS)	G&S nonlocal method	The G&S nonlocal method was selected based on the results from Summersgill et al. (2017a).

2.6 Seepage modeling

Seepage is an important factor in a geotechnical engineering analysis as it directly influences the effective stresses and driving forces and thus affects the strain localization. For example, the initial stress state of the Lower San Fernando Dam was significantly influenced by steady-state seepage forces (Li and Ming 2004). Different sliding displacements were observed with and without modeling the seepage forces (Li and Ming 2004). To establish the initial effective stresses in an FE code, the seepage forces and the buoyancy forces need to be applied to each submerged element. However, the Eulerian element (EC3D8R) available in Eulerian-based FE program in Abaqus/Explicit is designed to model single-phase materials. A seepage problem cannot be simulated with this element.

Hamann et al. (2015) proposed a technique to model the soil as a two-phase material using the thermally coupled Eulerian element (EC3D8RT) by implementing the thermal−fluid analogy theory, that is, to model the pore fluid flow as a heat transfer problem. The problem of pile jacking in fully saturated sand was investigated, and a hypoplastic sand model was implemented using a VUMAT user-subroutine in Abaqus. The dissipation of excess pore water pressure was successfully simulated (Hamann et al. 2015). However, this approach cannot be used directly to model seepage and establish in-situ stresses of a slope or embankment under seepage. Therefore, further developments are needed to simulate the seepage, and calculate and then incorporate seepage forces and buoyancy forces for in-situ stress modeling.

2.7 The failure of the Lower San Fernando Dam

A major flow slide occurred in the Lower San Fernando Dam in California due to the 1971 San Fernando earthquake (Seed et al. 1973). The cross section through the failed dam and its reconstruction are shown in Fig. 2.6. A large number of experimental, analytical and numerical studies were conducted to investigate this famous failure (e.g., Seed et al. 1973; Lee et al. 1975; Seed 1979; Castro et al. 1989; Gu et al. 1993; Olson and Stark 2001; Ming and Li 2003). They provided extensive data for the large-deformation analysis of the Lower San Fernando Dam. The Lower San Fernando Dam was subject to steady-stage seepage before the earthquake, thus being a good example to benchmark the proposed seepage and in-situ stress modeling technique. Note that the nonlocal regularization is not used for the large-deformation analysis of this dam in the current study, due to its limitation in modeling multiple soil layers and in computational efficiency.

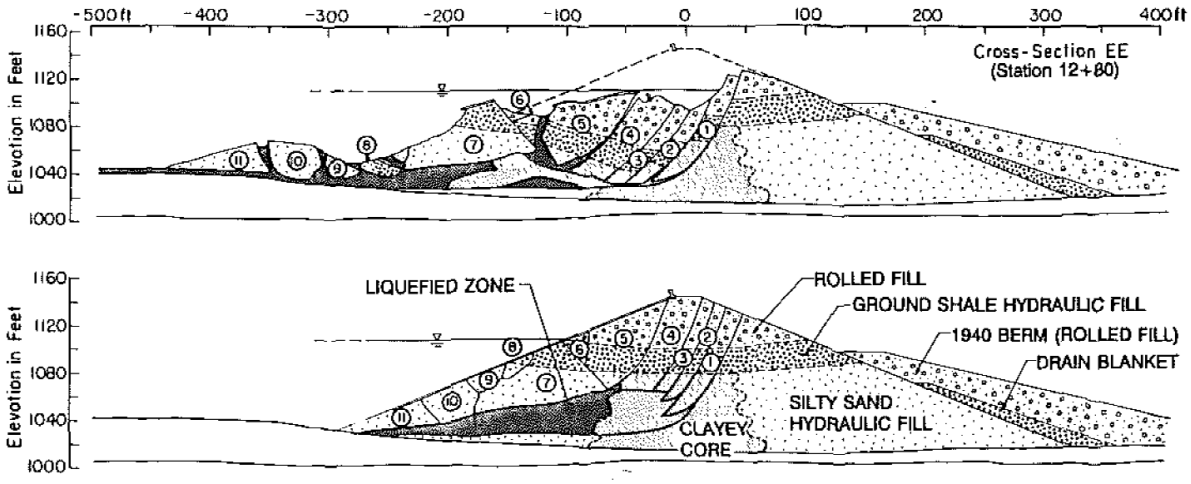

Figure 2.6 The cross section of the failed dam (a) condition after the earthquake-induced failure; (b) schematic drawing of the reconstructed cross section (Castro et al. 1992)

2.7.1 Numerical modeling techniques

The LE method has been widely used for the analysis of the Lower San Fernando Dam failure (e.g., Seed et al. 1973; Seed 1979; Castro et al. 1989; Olson and Stark 2001). This method has been mainly implemented to evaluate of the stability of slopes. The factor of safety can be calculated from an LE analysis (Fig. 2.7). Normally, only the initial slip surface can be determined from the LE method. A plausible attempt has been made to calculate the secondary slip surface of the Lower San Fernando Dam failure (Seed 1979), as shown in Fig. 2.7(b). Though this could explain the occurrence of multiple shear bands in the central area of the dam (Fig. 2.6), the whole post-failure process of the Lower San Fernando Dam cannot be handled by the LE method.

The FE method is a powerful tool to analyze a slope stability problem. A number of traditional Lagrangian-based FE analyses have been conducted to simulate the failure of the Lower San Fernando Dam (e.g., Gu et al. 1993; Jitno 1995; Ming and Li 2003). For example, this famous failure has been modeled using a two-dimensional Lagrangian-based FE procedure, SUMDES2D, as shown in Fig. 2.8 (Ming and Li 2003). Generally, the initiation of the dam failure can be successfully simulated using a traditional Lagrangian-based FE method; however, as aforementioned, mesh distortion can occur when the elements are subject to large deformation. This could cause inaccuracy and convergence issues (Mánica et al. 2018). Therefore, traditional Lagrangian-based FE analyses failed to disclose the whole post-failure process. To explore the full failure process, a numerical technique that is capable of modeling large-deformation behaviour is needed.

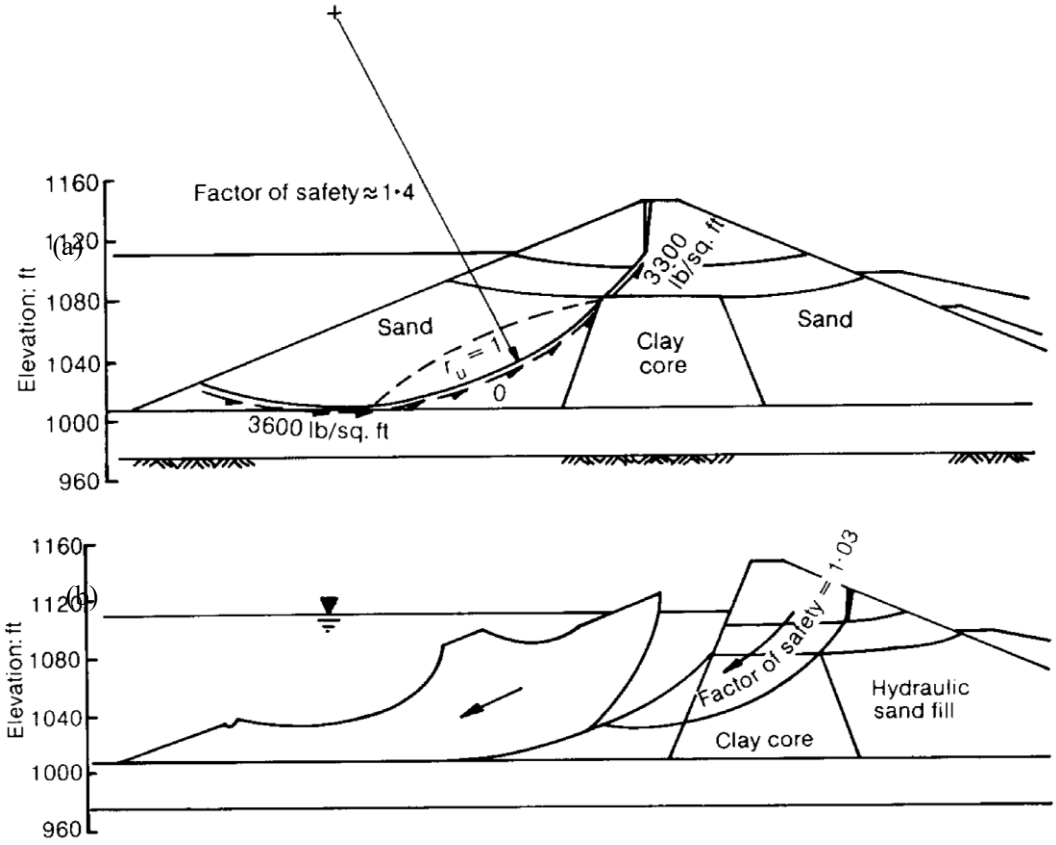

Figure 2.7 The slip surface and factor of safety from an LE analysis: (a) primary slip surface; (b) primary and secondary slip surface (Seed 1979)

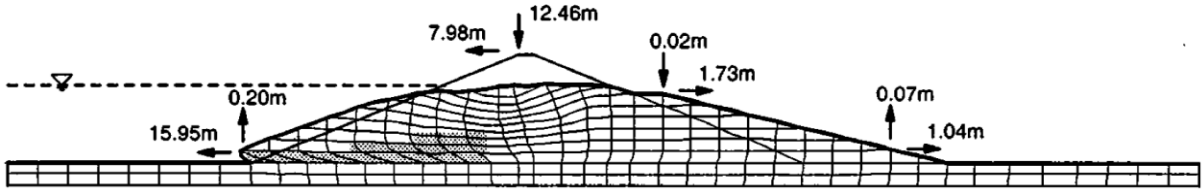

Figure 2.8 The deformed mesh 40 s after the start of earthquake (Ming and Li 2003)

The only large-deformation numerical technique used for modeling the Lower San Fernando Dam failure was the MPM (Huang et al. 2020; Feng et al. 2021). The nonlinear mechanism during the earthquake and the post-failure large deformation were modeled. Figure 2.9 shows the comparison between the field observation and the MPM modeling results. The final

deformation is similar to the fields, while the slip surfaces and failure blocks observed in the field were unclear in the MPM model. A more effective numerical technique is needed to clearly show the shear bands and failure blocks so that the post-quake failure mechanism can be appropriately explained.

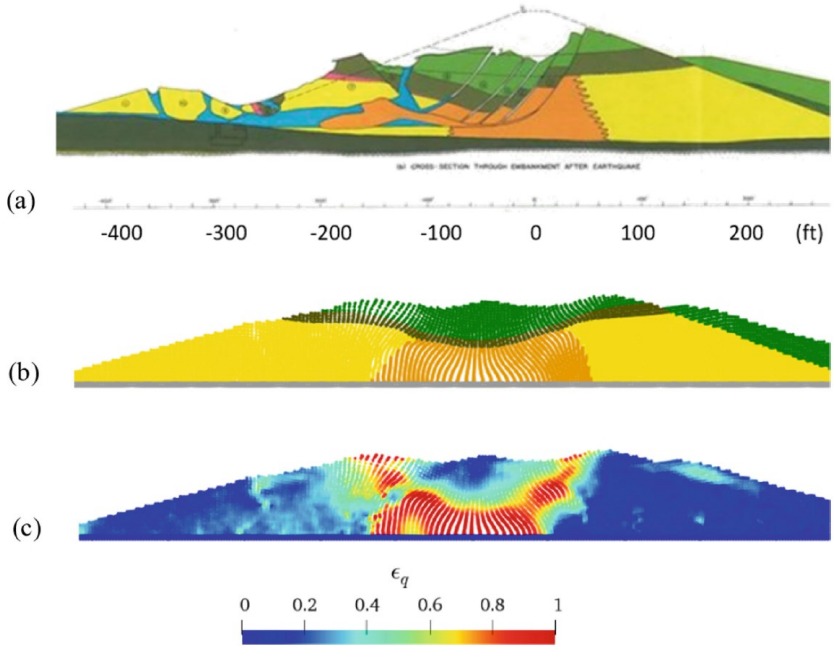

Figure 2.9 Comparison between the field observation and MPM modeling result of the Lower San Fernando Dam failure (a) cross-section in the field; (b) deformation pattern with material zonation; (c) deviatoric strain (Huang et al. 2020)

Eulerian-based FE method is capable of modeling large-deformation problems and has been used for large-scale landslide analyses (e.g., Dey et al. 2015; Islam et al. 2019). Slip surfaces and failure blocks can be clearly presented in a Eulerian-based FE analysis, as shown in Fig. 2.10. This makes Eulerian-based FE a competitive tool for the analysis of post-failure large deformation. The Lower San Fernando Dam was under a steady-state seepage before the earthquake. The seepage,

seepage forces and in-situ stresses can be computed in Eulerian-based FE with the new technique proposed in this study.

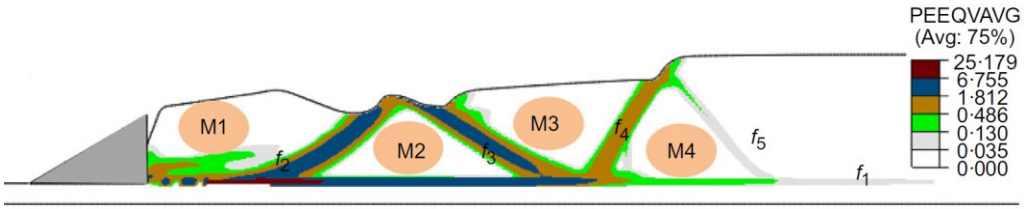

Figure 2.10 Large-deformation modeling of landslide in Eulerian-based FE (Dey et al. 2015)

2.7.2 Soil behaviour and constitutive models

As shown in Fig. 2.6, the Lower San Fernando Dam mainly consisted of silty sand hydraulic fill, clayey core, rolled fill, ground shale hydraulic fill, berm, and alluvium. For simplicity, the silty sand hydraulic fill is called the hydraulic fill, and the ground shale hydraulic fill is called the ground shale, in this study. In a large-deformation numerical analysis, an appropriate constitutive model that is still effective under large strain is required for each of the soil layers. As the large deformation occurred at the post-failure stage, the seismic behaviour of the soil is not our main focus at this stage.

2.7.2.1 Hydraulic fill

Based on the field investigation by Castro et al. (1989), the bottom layer of the hydraulic fill is loose, while the upper part is medium dense to dense. For loose sand, contractive behaviour commences when shearing. Under an undrained loading, this contractive tendency leads to the generation of excess pore water pressure, thus reducing the effective stress and inducing a

strain-softening behaviour. As shown by Olson (2001) (Fig. 2.11), an undrained strain-softening behaviour could be initiated under monotonic or cyclic loads. Gu et al. (1993) also showed the schematic strain-softening behaviour of undrained loose sand under monotonic and cyclic loads, respectively (Figs. 2.12(a) and 2.13(a)).

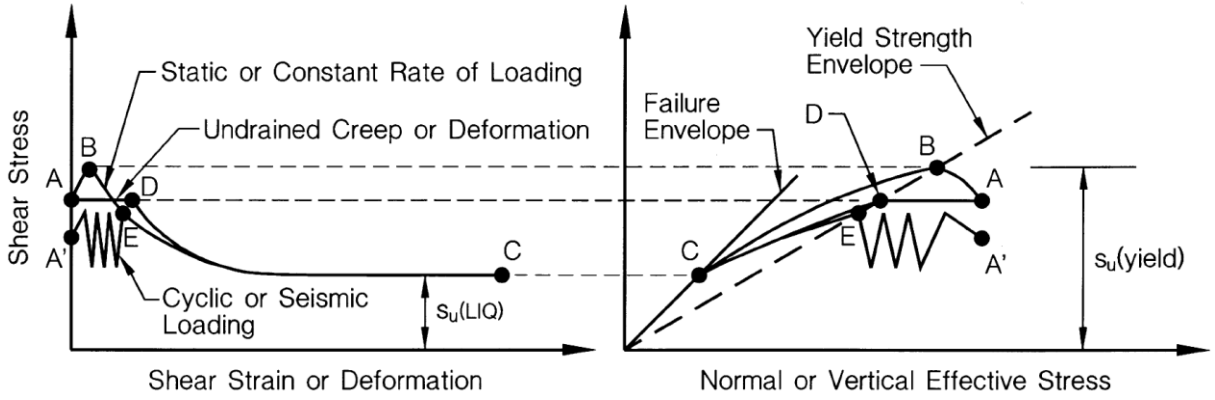

Figure 2.11 Schematic undrained response of a saturated, contractive sandy soil (cited from Olson (2001))

Medium dense to dense sand usually presents a dilative behaviour during shearing. This leads to the generation of negative excess pore water pressure under undrained loading and thus increases the effective stress and shear strength (Figs. 2.12(b) and 2.13(b)). In other words, a strain-hardening behaviour is present for the undrained medium dense to dense sand, and the undrained shear strength is significantly larger than the drained strength. However, drainage could occur. The strength can then gradually decrease to its drained value, which is similar to the behaviour of the dense sandy toe dike shown in Fig. 2.14 (Castro et al. 1989).

(a)

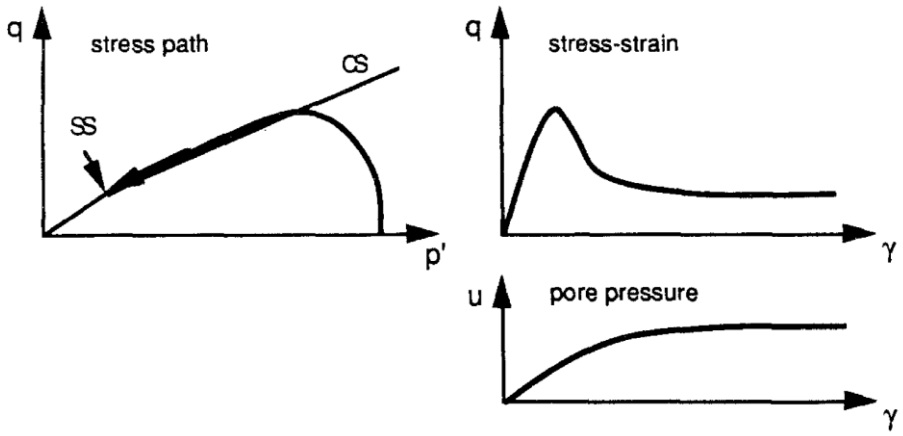

(b)

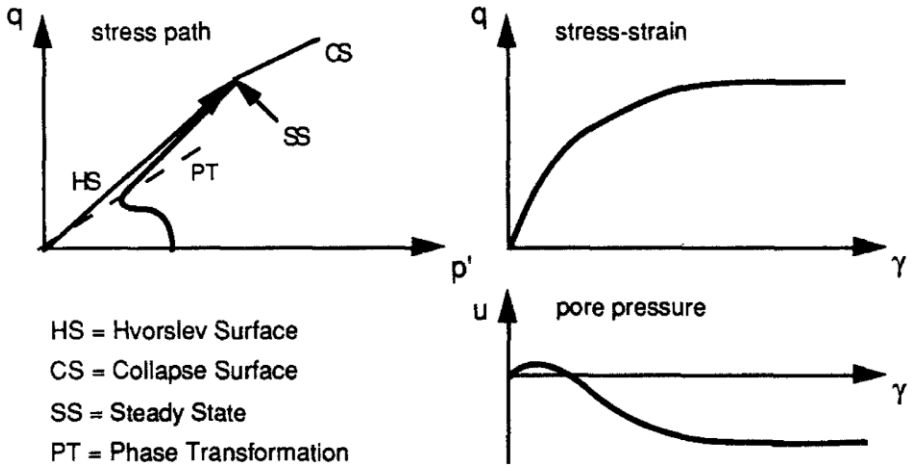

Figure 2.12 Idealized undrained behaviour of sands under monotonic load:

(a) contractive; (b) dilative (Gu et al. 1993)

(a)

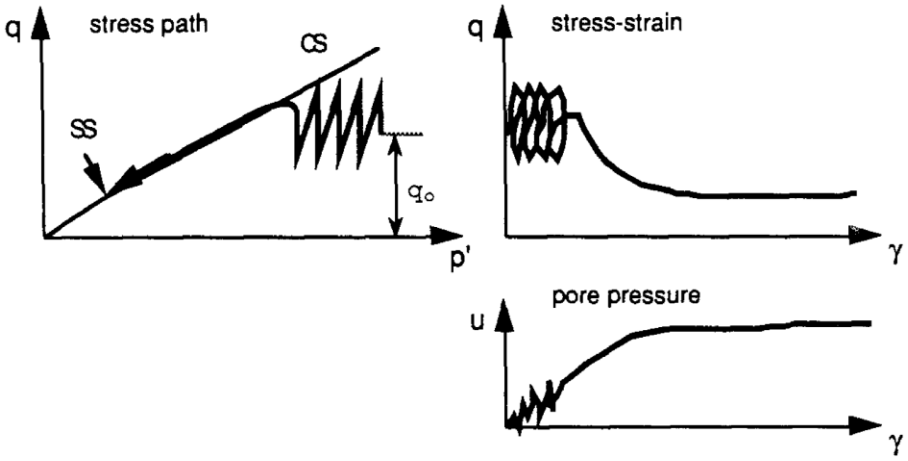

(b)

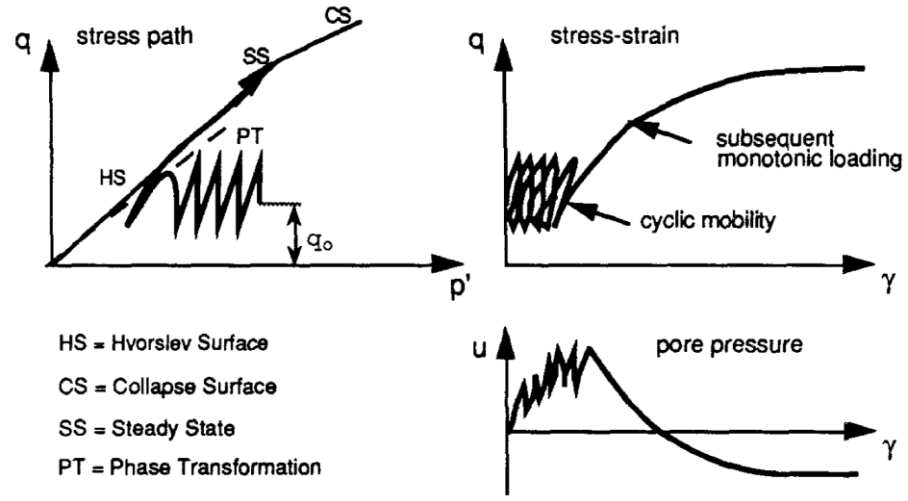

Figure 2.13 Idealized undrained behaviour of sands under cyclic load:

(a) contractive; (b) dilative (Gu et al. 1993)

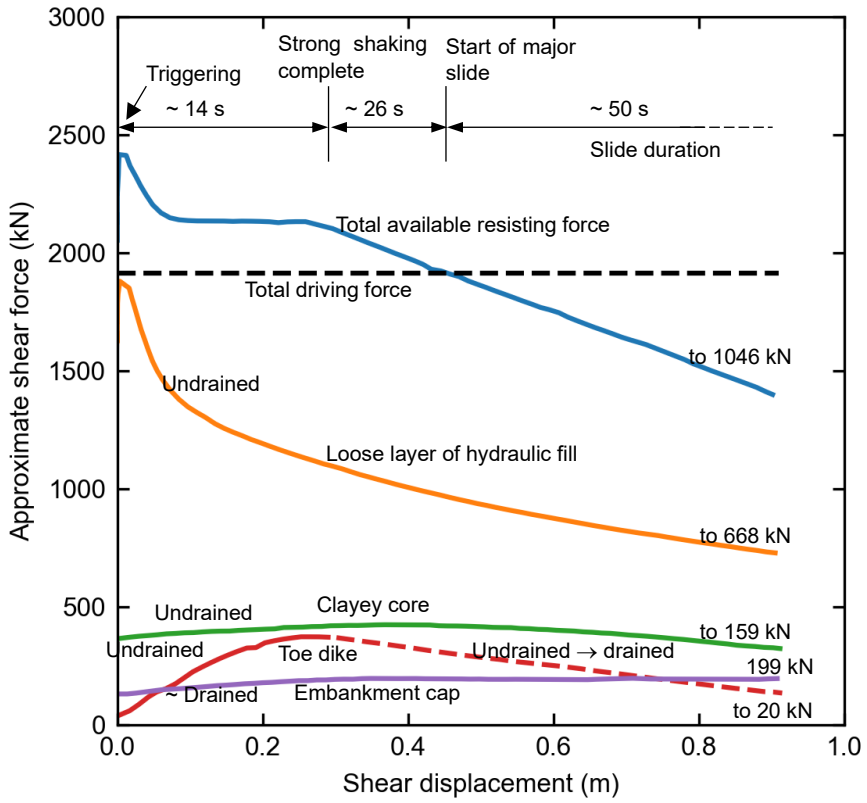

Figure 2.14 Qualitative driving and resisting forces at initiation of slide (Castro et al. (1989))

2.7.2.2 Clayey core

The clayey core mainly consisted of a silty clay with about 20% of sandy layers ranging from about 25.4 to 762 mm thick (Castro et al. 1989). The permeability of a sand-clay mixture layer is governed by the clayey fraction (Dafalla et al. 2020), which means the clayey core presents undrained behaviour under a quick loading, e.g., landslides. Based on Fig. 2.14, an undrained strain-softening behaviour was present in the clayey core during the Lower San Fernando Dam failure; however, the strength degradation rate was remarkably smaller than for the loose hydraulic sandy fill.

2.7.2.3 Other soils

Castro et al. (1989) showed that the ground shale layer was mainly composed of widely graded sand and silty sand. SPT test results indicate that this layer was in a dense condition (Castro et al. 1989). The rolled fill at the top was a mixture of heavy clay and gravel (Seed et al. 1973). Also, this layer was in a dense condition, based on SPT results (Castro et al. 1989). Its behaviour was assumed to be strain-softening, as clear shear bands were observed in the field. The berm also consisted of rolled fill. Furthermore, the alluvium consisted primarily of stiff clay with lenses of sand and gravel. However, slip surfaces were not observed in this layer.

2.7.2.4 Constitutive models

Several constitutive models have been implemented in the numerical analysis of the Lower San Fernando Dam failure (e.g., Gu et al. 1993; Huang and Zienkiewicz 1998; Ming and Li 2003; Khoei et al. 2004). Most of them have been developed to model the dynamic response of the soil so that the deformation and failure mechanism at the co-seismic stage can be analyzed. Gu et al. (1993) has adopted a simplified undrained model for the post-failure behaviour of liquefiable soils (Fig. 2.15). The strain-softening behaviour was modeled by using a hyperbolic stress–strain relationship. This model was implemented to show the post-failure deformation of the Lower San Fernando Dam failure by successfully modeling a stress redistribution process. However, the whole post-failure stage was not fully addressed. One possible reason could be that a traditional Lagrangian-based FE was used, and a convergence issue occurred under a certain level of deformation.

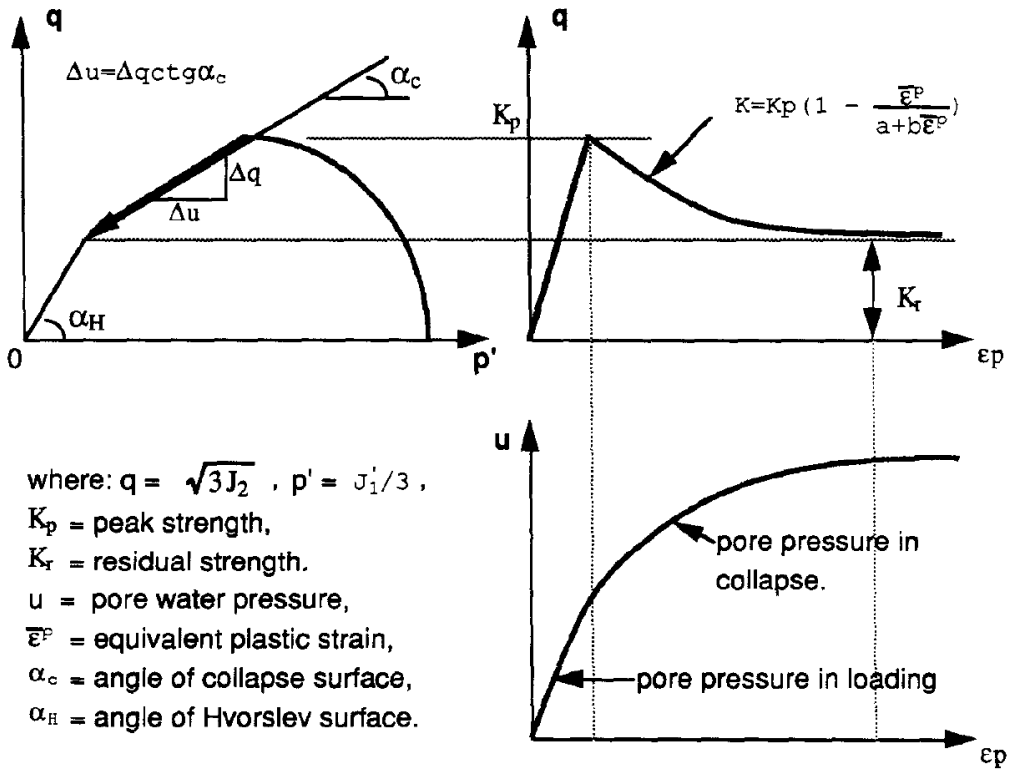

Figure 2.15 Simplified undrained model for liquefiable soils (Gu et al. 1993)

Besides the simulation by Gu et al. (1993), the deformation was mostly limited to a relatively small range in previous numerical studies of the Lower San Fernando Dam failure. Their constitutive models were not tailored for a large-deformation analysis. Therefore, appropriate constitutive models that are capable of large-deformation analysis need to be selected or proposed for this study.

2.8 Summary

The literature review presented in this chapter shows that the modeling of strain localization in a large-deformation FE program needs further research. Many geotechnical failures are of the progressive type, always accompanied by the strain-softening behaviour of soils. However, when

incorporating the strain-softening behaviour in a finite element code, mesh dependency issues occur, leading to an unreliable result. Researchers have proposed varieties of regularization techniques to address the mesh dependency issues, and element size scaling and the nonlocal method are among them. Nevertheless, very few publications discussed the capability of various regularization techniques for a large-deformation numerical technique. A comparison between different regularization techniques is needed to guide their implementations in large-deformation programs. Only the element size scaling technique has been implemented in Eulerian-based FE so far. Other regularization techniques need to be implemented to understand which is the best of practice for Eulerian-based FE. Softening scaling is a method to reduce the computational cost of shear band modeling. The effectiveness of softening scaling for local and nonlocal methods needs to be examined. Seepage modeling is another important topic for a large-deformation geotechnical engineering analysis. While the available Eulerian elements are single-phase, an innovative approach will be required to model the seepage and establish the in-situ stresses in Eulerian-based FE.

A large number of studies investigated the failure of the Lower San Fernando Dam in 1971. While the LE and FE methods can address the early stage of the failure, a large-deformation analysis is still needed to help us understand the post-failure mechanisms. Appropriate soil constitutive models capable of large-deformation modeling need to be implemented or developed to model the strain-softening behaviour of the multiple soil layers in this dam. This famous dam failure is also a great case for the calibration of the seepage modeling technique in Eulerian-based FE.

CHAPTER 3

A novel nonlocal Eulerian-based finite-element approach for strain-softening materials

Co-Authorship: This chapter will be submitted as a technical paper for publication in a journal as: Chen, J., Hawlader, B., Roy, K. and Pike, K., "A novel nonlocal Eulerian-based finite-element approach for strain-softening materials".

Most of the research work presented in this chapter was conducted by the first author. He also prepared the draft manuscript. The other authors supervised the research and reviewed the manuscript.

3.1 Abstract

The dependency of finite element (FE) results on mesh size is a major concern for the numerical analysis of strain-softening materials. The local methods of strain regularization rely on the shear strains of a solitary point. However, the nonlocal methods incorporate strain-softening, including the strain in surrounding soil elements which show less mesh dependency. Previously, nonlocal methods were mostly implemented in Lagrangian-based FE programs and simulated the response for small to moderate strain levels. However, many geotechnical problems, such as large-scale landslides in sensitive clays, involve extremely large deformation. This study presents the implementation of the original and two modified nonlocal methods in a Eulerian-based large deformation FE program using a relatively simplified approach where simple soil models such as von-Mises criteria for undrained behaviours can be used. Two biaxial compression tests are

simulated by using the nonlocal Eulerian-based FE program, and the results are compared with a nonlocal Lagrangian-based FE analysis and a nonlocal Material Point Method (MPM) of simulation, respectively. Among the three, the modified nonlocal methods, especially the over-nonlocal method, show a better performance in mesh convergence analysis. Several approaches have been proposed to minimize the computational costs, as nonlocal modeling is generally computationally expensive.

3.2 Introduction

Strain-softening of soil occurs on many occasions, depending upon soil type and loading conditions; for example, drained loading of dense sand, highly overconsolidated or structured clay, and undrained loading of loose sand and sensitive clays. The strain-softening would not be a major concern if the shear stress under the working load were below the peak shear strength. However, in many geotechnical problems (e.g., landslides in sensitive clay, flow slides in loose sand), the post-peak strength degradation governs the response. The failure planes in strain-softening materials generally develop by progressive formation of shear bands. Numerical modeling of such progressive failure is challenging because the solution might be significantly dependent on the finite-element (FE) mesh size.

Mesh convergence analysis is generally performed in FE analysis to identify the optimum global mesh size, below which the reduction of mesh size does not significantly change the simulation results. However, strain-softening soil behaviour could turn the governing differential equations from a hyperbolic (in non-softening materials) into an elliptical nature, which could lead

to an ill-posed initial boundary value problem for a dynamic case (Bažant and Belytschko 1985), while ellipticity of governing differential equations is lost for a static or quasi-static problem (de Borst and Verhoosel 2017). Therefore, despite the global mesh convergence analysis, the FE results can still significantly depend on the mesh size, especially for strain-softening materials.

To address the issues related to mesh dependency, various strain regularization approaches have been developed and implemented in numerical techniques, such as element size scaling (Anastasopoulos et al. 2007), nonlocal methods (Bažant and Lin 1988; Brinkgreve 1994; Conte et al. 2010; Galavi and Schweiger 2010; Summersgill 2014), viscoplastic models (Loret and Prevost 1990), strain gradient models (de Borst and Mühlhaus 1992), polar models or Cosserat continuum models (de Borst et al. 1993; Tejchman and Bauer 1996). Most of these studies were restricted to small strain FE analyses. However, convergence issues or excessive mesh distortions could occur in a conventional small-strain Lagrangian-based FE analysis. Therefore, a large-deformation problem, like landslides, could not be modeled using such programs.

Strain regularization has been discussed in several studies using large-deformation analysis techniques that do not experience convergence or mesh distortion issues. For example, the Smooth Particles Hydrodynamics (SPH) method is proven to be an inherently nonlocal method, though a certain value of smoothing length is required to address the spatial resolution dependency (Vignjevic et al. 2014). Chen and Qiu (2014) also showed that sensitivity to spatial resolution is still significant in a slope failure analysis using SPH without a regularization technique. A viscoplastic constitutive model was implemented in another large-deformation analysis technique, the Point Finite Element Method (PFEM), and a mesh independent solution was presented from a

1D extension test and a collapse test of a sensitive clay column (Zhang et al. 2017). However, Thakur (2007) recognized that unusually high viscosity values are needed for a mesh size independent solution. Nonlocal formulations were implemented in PFEM (Monforte et al. 2019), Remeshing and Interpolation Technique with Small Strain (RITSS) (Singh et al. 2021), and in MPM (Burghardt et al. 2012; Goodarzi and Rouainia 2017). In other words, limited applications of nonlocal methods for large-deformation problems are available in the literature, and most of them have used in-house computer codes. The implementation of different nonlocal methods in a commercial large-deformation FE program and comparison of their performance will be beneficial for future researchers and engineering practice. In the present study, three nonlocal methods are implemented in the commercial Eulerian-based FE solver of Abaqus, which is capable of modeling large-deformation geotechnical engineering problems (Dey et al. 2015; Qiu et al. 2011).

The chapter has been organized in the following way. First, some fundamental concepts of Eulerian-based FE analysis and different types of nonlocal methods are introduced. Second, the algorithms to implement the nonlocal Eulerian-based FE model in the software are presented. Third, the results of two biaxial loading cases in the nonlocal Eulerian-based FE are benchmarked with a nonlocal Lagrangian-based FE program and a nonlocal MPM program. Finally, the effectiveness of three nonlocal methods and the computational cost of both local and nonlocal models are discussed.

3.3 Eulerian-based finite-element method

In the conventional Lagrangian-based FE analyses, nodes move with the material, and mesh deforms as the material deforms. The Lagrangian-based FE elements are filled with a single material. Therefore, the material boundary coincides with the boundary of the mesh. Due to these features, excessive mesh distortion or convergence issues occur in the large deformation modelling. However, in a Eulerian-based FE analysis, the mesh is permanently fixed, and the deformation can be viewed as material flow through the fixed mesh. In other words, the mesh distortion can be avoided in a Eulerian-based FE analysis.

An operator splitting algorithm is used in Abaqus/Explicit for Eulerian-based FE formulations. Equation (3.1) shows the general form of the governing equations, which is divided into two steps, a Lagrangian step (Eq. (3.2)) followed by a Eulerian step (Eq. (3.3)) (Benson and Okazawa 2004). As shown in Fig. 3.1, the Lagrangian step is the same as in the conventional Lagrangian formulation except for the use of the spatial time derivative instead of the material time derivative (Benson and Okazawa 2004). In the Eulerian step, the solution variables, which are calculated from the Lagrangian step, are remapped on the permanently fixed mesh using a second-order advection algorithm proposed by Van Leer (1977). As a result of this operator splitting algorithm, Eulerian-based finite-element analysis does not suffer from any mesh distortion when dealing with a large deformation problem.

$$\frac{\partial \phi}{\partial t} + \nabla \cdot \mathbf{\Phi} = \mathbf{S} \tag{3.1}$$

$$\frac{\partial \phi}{\partial t} = \mathbf{S} \tag{3.2}$$

$$\frac{\partial \phi}{\partial t} + \nabla \cdot \mathbf{\Phi} = 0 \tag{3.3}$$

where ϕ is the arbitrary solution variable; $\partial\phi/\partial t$ is the spatial time derivative of ϕ; $\mathbf{\Phi}$ is the flux function, and $\mathbf{S}$ is the source term. An explicit central difference method is adopted to advance the solution in time as:

$$\mathbf{a}^{n} = \mathbf{M}^{-1}\left(\mathbf{F}^{ext} - \mathbf{F}^{int}\right) \tag{3.4}$$

$$\mathbf{v}^{n+1/2} = \mathbf{v}^{n-1/2} + \Delta t \mathbf{a}^{n} \tag{3.5}$$

$$\mathbf{x}^{n+1} = \mathbf{x}^{n} + \Delta t \mathbf{v}^{n+1/2} \tag{3.6}$$

where $\mathbf{a}$ is the spatial acceleration; $\mathbf{M}$ is the diagonal lumped mass matrix; $\mathbf{F}^{int}$ is the internal force vector; $\mathbf{F}^{ext}$ is the external force vector, and $\mathbf{x}$ is the position vector. The superscript n denotes the number of time increments, and n ± 1/2 represents the center of each time increment.

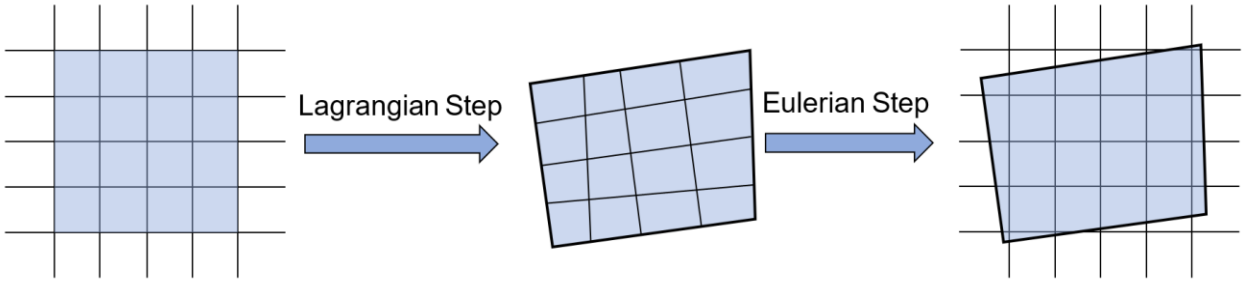

Figure 3.1 The operator splitting for Eulerian-based finite-element method

3.4 Nonlocal strain regularization

Several studies showed that, of the available regularization techniques, the nonlocal methods provide a viable solution, including post-localization in the shear band for different

applications and strain levels considered (e.g., Sluys 1992; de Borst et al. 1993; Summersgill et al. 2017a; Mallikarachchi and Soga 2020). Various nonlocal methods have been proposed and implemented, such as the original nonlocal method (Eringen 1981; Bažant et al. 1984), the G&S nonlocal method (Galavi and Schweiger 2010), and the over-nonlocal method (Brinkgreve 1994). These three nonlocal methods have been implemented in the Imperial College finite-element program (ICFEP) (Summersgill 2014; Summersgill et al. 2017a; b). Summersgill (2014) also stated that a conventional Lagrangian-based FE has inherent difficulty in handling large displacement slope failure due to 'severe distortion of elements within a continuum mesh.' For example, a nonlocal Lagrangian-based FE analysis of a biaxial test was terminated at a relatively small vertical displacement (4.6 mm) due to the convergence issue (Mánica et al. 2018). In other words, many applications of nonlocal methods, as they were implemented with a conventional Lagrangian-based FE, are not suitable for significantly large deformation problems. In the present study, the original nonlocal, G&S nonlocal, and over-nonlocal methods are applied to Eulerian-based FE code, which is free from mesh distortion and convergence issues.

3.4.1 The original nonlocal method

The nonlocal strain increment of the original nonlocal method (Bažant et al. 1984; Eringen 1981) is calculated from Eqs. (3.7–3.9).

$$d\varepsilon^{\mathrm{p}}_{\mathrm{q(NL)}}(\mathbf{x}_{\mathrm{n}}) = \frac{1}{V_{\mathrm{w}}}\iiint \left[\omega_{\mathrm{o}}(\mathbf{x}'_{\mathrm{n}})\, d\varepsilon^{\mathrm{p}}_{\mathrm{q}}(\mathbf{x}'_{\mathrm{n}})\right] dx' dy' dz' \tag{3.7}$$

$$\omega_{\mathrm{o}}(\mathbf{x}'_{\mathrm{n}}) = \frac{1}{l\sqrt{\pi}} \exp\left[-\frac{|\mathbf{x}'_{\mathrm{n}} - \mathbf{x}_{\mathrm{n}}|^2}{l^2}\right] \tag{3.8}$$

$$V_{\mathrm{w}} = \iiint \omega_{\mathrm{o}}(\mathbf{x}'_{\mathrm{n}})dx'dy'dz' \tag{3.9}$$

where $d\varepsilon^{\mathrm{p}}_{\mathrm{q(NL)}}(\mathbf{x}_{\mathrm{n}})$ is the nonlocal equivalent plastic shear strain increment at the integration point at location $\mathbf{x}_{\mathrm{n}}$ where the subscript n denotes the dimension of the model; $d\varepsilon^{\mathrm{p}}_{\mathrm{q}}(\mathbf{x}'_{\mathrm{n}})$ is the equivalent plastic shear strain increment at location $\mathbf{x}'_{\mathrm{n}}$ which refers to all the reference integration points for location $\mathbf{x}_{\mathrm{n}}$; $\omega_{\mathrm{o}}(\mathbf{x}'_{\mathrm{n}})$ is a Gaussian-type weight function that is centered at the point $\mathbf{x}_{\mathrm{n}}$, defining the weight of all the reference points $\mathbf{x}'_{\mathrm{n}}$ in the calculation of $d\varepsilon^{\mathrm{p}}_{\mathrm{q(NL)}}(\mathbf{x}_{\mathrm{n}})$; l is an internal length parameter that is related to the shear band width; V_{w} is the reference volume, where x', y' and z' are the three dimensions. Figure 3.2(a) shows the included reference integration points for the nonlocal strain calculation for one Eulerian element. The radius of influence (r_{inf}) specifies the range of the reference integration points. The nonlocal equivalent plastic shear strain value remains constant when $r_{\mathrm{inf}} > 3l$ (Summersgill et al. 2017a).

The variation of weighting function with distance from the calculation point for the original nonlocal method ($l = a$) with different mesh sizes (t_{FE}) is shown in Fig. 3.2(b). The gap between the distribution function and FE discretized segments is smaller for a finer mesh. In other words, an adequately fine mesh is required to capture the shape of the weighting function of the nonlocal methods.

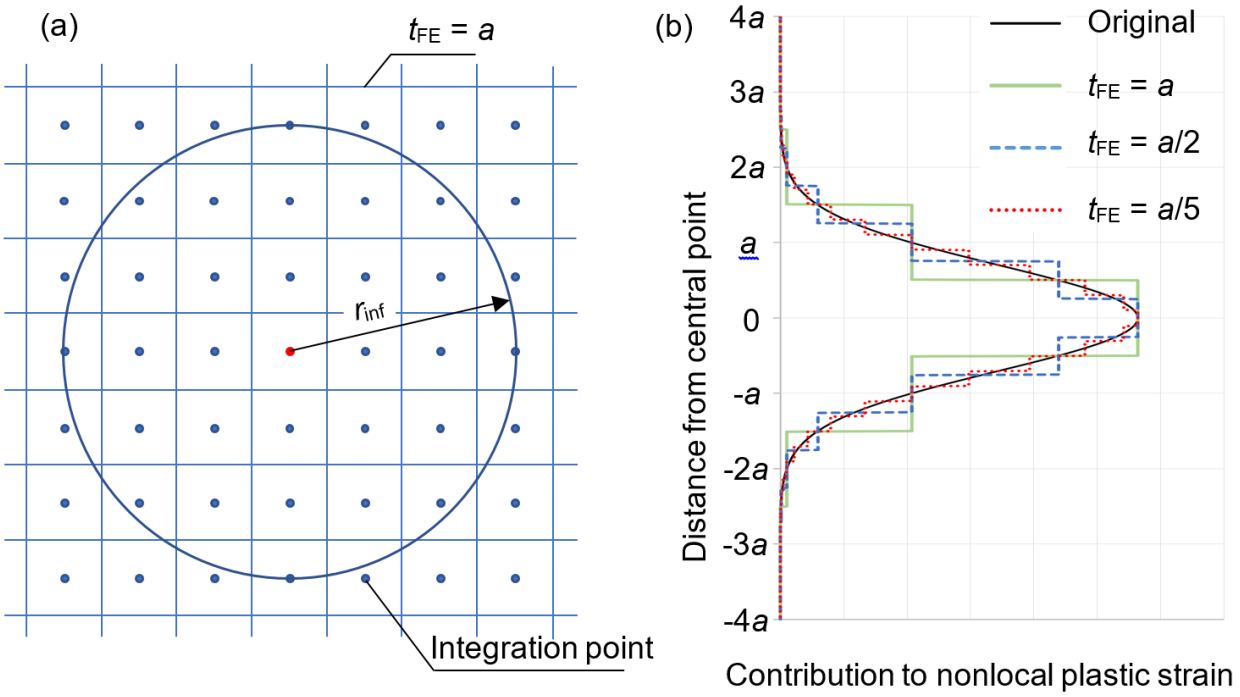

Figure 3.2 (a) Reference integration points for nonlocal calculation; (b) the variation of weighting function

3.4.2 The G&S nonlocal method

The G&S nonlocal method is proposed by Galavi and Schweiger (2010). A different weighting function, $\omega_g(\mathbf{x}'_n)$ (Eq. (3.10)), substitutes the original nonlocal weight function, $\omega_o(\mathbf{x}'_n)$, in Eqs. (3.7) and (3.9) to calculate the nonlocal equivalent plastic shear strains.

$$\omega_g(\mathbf{x}'_n) = \frac{|\mathbf{x}'_n - \mathbf{x}_n|}{l^2} \exp\left[-\frac{|\mathbf{x}'_n - \mathbf{x}_n|^2}{l^2}\right] \tag{3.10}$$

3.4.3 The over-nonlocal method

The over-nonlocal method adopted a new formulation (Eq. (3.11)) to calculate the nonlocal equivalent plastic shear strain increment, $d\varepsilon^{p}_{q(NL)}$ (Brinkgreve 1994).

$$d\varepsilon^{p}_{q(NL)}(\mathbf{x}_n) = (1-\alpha)d\varepsilon^{p}_{q}(\mathbf{x}_n) + \frac{\alpha}{V_w}\iiint [\omega_o(\mathbf{x}'_n)d\varepsilon^{p}_{q}(\mathbf{x}'_n)]dx'dy'dz' \tag{3.11}$$

where α is the amplification factor, which was introduced to reduce the contribution of the local strain to the nonlocal strain; $\omega_o(\mathbf{x}'_n)$ can be calculated from a Gaussian-type formulation (e.g., Eq. (3.8)); V_w is calculated using Eq. (3.9). α should be larger than 1.0 when using the over-nonlocal method (Brinkgreve 1994). However, the value for α has to be determined based on a 'trial-and-error' process (Summersgill et al. 2017a). Note that when $\alpha = 0$, it turns to the local method where no regularization is applied; when $\alpha = 1.0$, Eq. (3.11) changes into Eq. (3.7), the original nonlocal formulation.

The weighting function of the over-nonlocal method, $\omega_{ov}(\mathbf{x}'_n)$, can be deduced from Eq. (3.11), by combining a concentrated weight function, $\omega_{loc}(\mathbf{x}'_n)$, and the original nonlocal weight function, $\omega_o(\mathbf{x}'_n)$, as shown in Eqs. (3.12) and (3.13).

$$\omega_{ov}(\mathbf{x}'_n) = (1-\alpha)\cdot\omega_{loc}(\mathbf{x}'_n)\cdot V_w + \alpha\cdot\omega_o(\mathbf{x}'_n) \tag{3.12}$$

$$\omega_{loc}(\mathbf{x}'_n) = \begin{cases} t_{FE}^{-dim}, & \text{for the centre element} \\ 0, & \text{for other elements} \end{cases} \tag{3.13}$$

where t_{FE} is the element size; dim is the dimension of the problem (e.g., dim = 1 for one-dimensional problem). The main advantage of this over-nonlocal weight function (Eq. (3.12)) is to enable a direct comparison with original and G&S nonlocal weight functions (Fig. (3.3)). Figure

3.3 shows the three weight functions for a one-dimensional condition, where V_w equals 1. Note that the $\omega_o(\mathbf{x}'_n)$ here for the over-nonlocal method is computed from Eq. (3.8). Figure 3.3 shows that the original nonlocal weight function has its peak at the center, which means that the nonlocal strain of one integration point is still largely dependent on its local strain and thus could possibly lead to an undesirable effect on strain regularization. However, both over-nonlocal and G&S nonlocal weight functions present a low weight at the center, which facilitates more plastic energy diffusion outside the shear localization zone. Further discussions on the three nonlocal methods are provided in later sections with evidence from numerical tests.

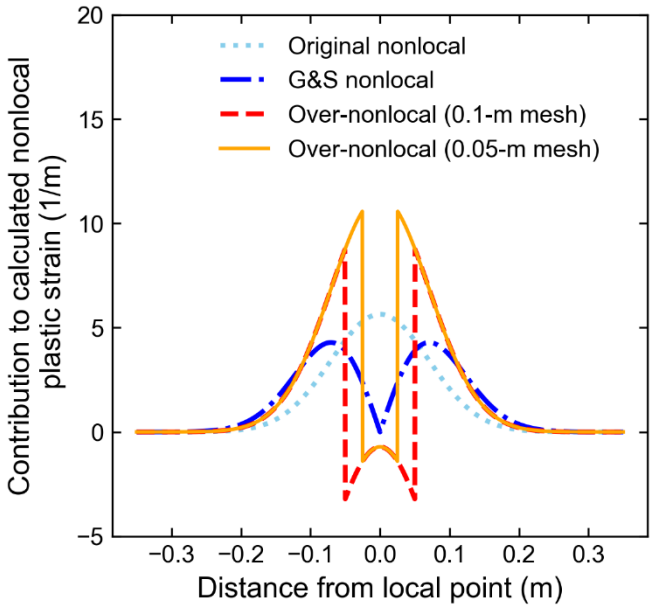

Figure 3.3 Comparison of the three nonlocal weight functions

(l = 0.1 m; α = 2.0 for over-nonlocal method)

3.5 Implementation of nonlocal methods in Eulerian FE code

The mathematical formulations used to implement the nonlocal method are presented in this section. The von Mises yield criterion with undrained strain softening is adopted. Note, however, that a similar algorithm can be used for other constitutive models of soil with necessary changes in appropriate locations.

3.5.1 The von Mises failure criterion with strain-softening

The radial return algorithm (Wilkins 1964) is adopted to compute the equivalent plastic strain increment $d\varepsilon_q^p$ for each time increment (Fig. 3.4). As shown in Eq. (3.14), the difference between the yield strength at the end of each time increment, $\sigma_y^{(2)}$, and the yield strength at the beginning of each time increment, $\sigma_y^{(1)}$, are the product of hardening modulus, H, and the equivalent plastic strain increment, $d\varepsilon_q^p$. In a strain-softening scenario, H is negative, and $\sigma_y^{(2)}$is less than $\sigma_y^{(1)}$ (as shown in Fig. 3.4).

$$\sigma_y^{(2)} = \sigma_y^{(1)} + Hd\varepsilon_q^p \tag{3.14}$$

$\sigma_y^{(2)}$ and $d\varepsilon_q^p$ remain unknown at the beginning of each time increment; thus, as seen in Eqs. (3.15–3.17), a trial stress, $\boldsymbol{\sigma}^t$, is introduced to build another equation that contains $\sigma_y^{(2)}$ and $d\varepsilon_q^p$ so that their values can be calculated from a system of linear equations with two unknowns.

$$\boldsymbol{\sigma}^t = \boldsymbol{\sigma}^{(1)} + \mathbf{C}d\boldsymbol{\varepsilon} = \boldsymbol{\sigma}^{(1)} + \mathbf{C}(d\boldsymbol{\varepsilon}^e + d\boldsymbol{\varepsilon}^p) = \boldsymbol{\sigma}^{(2)} + \mathbf{C}d\boldsymbol{\varepsilon}^p \tag{3.15}$$

where $\boldsymbol{\sigma}^{(1)}$ is the stress tensor at the beginning of each time increment.

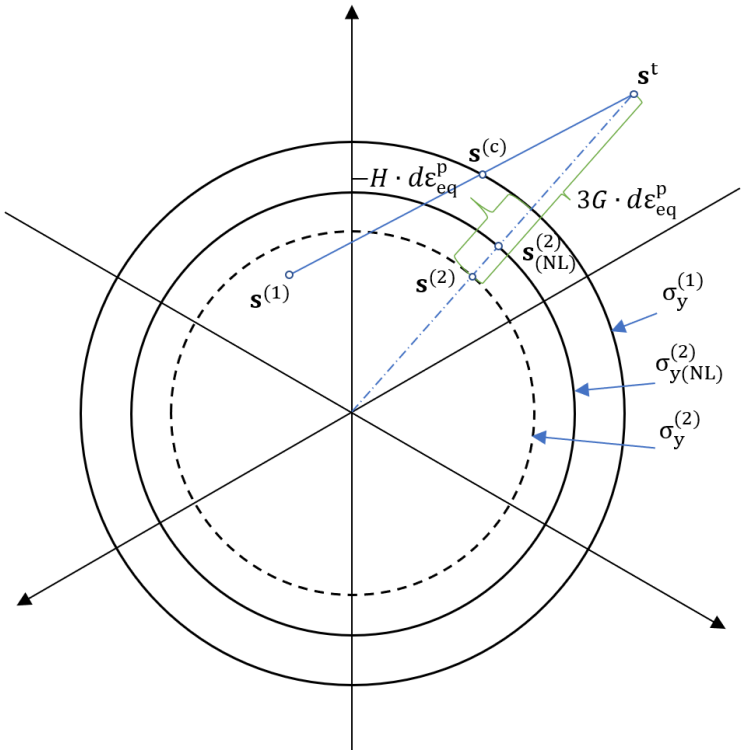

Figure 3.4 The return method for the von Mises softening model

From Eq. (3.15), we can derive that:

$$\sigma_{v}^{t} = \sigma_{y}^{(2)} + 3Gd\varepsilon_{q}^{p} \tag{3.16}$$

where σ_{v}^{t}, the von Mises stress at the trial state, is calculated from Eq. (3.17). In this equation, $\mathbf{s}^{t}$ is the deviatoric stress tensor of the trial stress.

$$\sigma_{v}^{t} = \sqrt{\frac{3}{2}\mathbf{s}^{t}:\mathbf{s}^{t}} \tag{3.17}$$

Based on Eqs. (3.14) and (3.16), $d\varepsilon_{q}^{p}$ can be calculated from Eq. (3.18).

$$d\varepsilon_{\mathrm{q}}^{\mathrm{p}} = \frac{\sigma_{\mathrm{v}}^{\mathrm{t}} - \sigma_{\mathrm{y}}^{(1)}}{H + 3G} \tag{3.18}$$

where G is the shear modulus.

$\sigma_{\mathrm{y}}^{(2)}$ can be computed from Eq. (3.16), after $d\varepsilon_{\mathrm{q}}^{\mathrm{p}}$ is calculated. Equation (3.19) is then established to calculate the deviatoric stress tensor at the end of the time increment, $\mathbf{s}^{(2)}$. Further details of the calculation of $\mathbf{s}^{(2)}$, are shown in Eq. (3.20) and Fig. 3.4. Note that $\mathbf{s}^{(2)}$ here is the deviatoric stress tensor without any implementation of strain regularization, as only the local strains are used at this point.

$$\frac{\mathbf{s}^{(2)}}{\sigma_{\mathrm{y}}^{(2)}} = \frac{\mathbf{s}^{\mathrm{t}}}{\sigma_{\mathrm{v}}^{\mathrm{t}}} \tag{3.19}$$

$$\begin{aligned} \mathbf{s}^{(2)} = \frac{\mathbf{s}^{\mathrm{t}}}{\sigma_{\mathrm{v}}^{\mathrm{t}}} \cdot \sigma_{\mathrm{y}}^{(2)} = \frac{\mathbf{s}^{\mathrm{t}}}{\sigma_{\mathrm{v}}^{\mathrm{t}}} \cdot \left(\sigma_{\mathrm{v}}^{\mathrm{t}} - 3G \cdot d\varepsilon_{\mathrm{q}}^{\mathrm{p}}\right) = \mathbf{s}^{\mathrm{t}} \cdot \frac{\sigma_{\mathrm{y}}^{(2)}}{\sigma_{\mathrm{y}}^{(2)} + 3G \cdot d\varepsilon_{\mathrm{q}}^{\mathrm{p}}} \\ = \mathbf{s}^{\mathrm{t}} \cdot \frac{\sigma_{\mathrm{y}}^{(1)} + Hd\varepsilon_{\mathrm{q}}^{\mathrm{p}}}{\sigma_{\mathrm{y}}^{(1)} + Hd\varepsilon_{\mathrm{q}}^{\mathrm{p}} + 3G \cdot d\varepsilon_{\mathrm{q}}^{\mathrm{p}}} \end{aligned} \tag{3.20}$$

3.5.2 Nonlocal implementation for the von Mises criterion

The nonlocal equivalent plastic strain ($d\varepsilon_{\mathrm{q(NL)}}^{\mathrm{p}}$) is calculated from Eqs. (3.7–3.11) based on the local equivalent plastic strain increment ($d\varepsilon_{\mathrm{q}}^{\mathrm{p}}$). The yield strength at the end of the time increment with the nonlocal strain ($\sigma_{\mathrm{y(NL)}}^{(2)}$) is then computed using Eq. (3.21). Thereafter, substituting $\sigma_{\mathrm{y}}^{(2)}$ with $\sigma_{\mathrm{y(NL)}}^{(2)}$ in Eq. (3.20), Eq. (3.22) can be obtained, which is used to calculate the deviatoric stress tensor at the end of the time increment with the nonlocal strain regularization, $\mathbf{s}_{\mathrm{(NL)}}^{(2)}$.

$$\sigma_{y(NL)}^{(2)} = \sigma_y^{(1)} + H d\varepsilon_{q(NL)}^p \tag{3.21}$$

$$\mathbf{s}_{(NL)}^{(2)} = \frac{\mathbf{s}^t}{\sigma_v^t} \cdot \sigma_{y(NL)}^{(2)} = \mathbf{s}^t \cdot \frac{\sigma_y^{(1)} + H d\varepsilon_{q(NL)}^p}{\sigma_y^{(1)} + (H + 3G) \cdot d\varepsilon_q^p} \tag{3.22}$$

Considering the high computational cost in large-deformation analyses, the local strains of the previous time increment are used to calculate the current nonlocal equivalent plastic strain, $d\varepsilon_{q(NL)}^p$, without an iteration for each time increment. Note that previous studies also avoided such iterative processes (Tvergaard and Needleman 1995; Galavi and Schweiger 2010; Summersgill 2014). The time increment should be small enough to have a reliable solution (Tvergaard and Needleman 1995). As an explicit approach is used in this study, the time increments are naturally minimal; therefore, a non-iterative nonlocal calculation is acceptable. Further validation of the developed numerical technique is presented in later sections. The computational procedure is shown in Algorithm 3.1.

In the present study, the nonlocal regularization together with the von Mises model is implemented in the Eulerian FE code available in Abaqus/Explicit. Fortran codes are developed using user subroutines VUMAT, VEXTERNALDB, and VUSDFLD. Note that nonlocal methods have also been implemented previously in this software; for example, in Abaqus/Standard for drained and undrained behaviour of dense sand adopting the NorSand critical state model (Mallikarachchi and Soga 2020) and in Arbitrary Lagrangian Eulerian (ALE) code in Abaqus/Explicit for metal softening (Zhu 2017). However, the implementation in the Eulerian approach is different, because there are a limited number of options available in the element library,

and the mesh is fixed. An efficient algorithm, with the capability of parallel computing, needs to be developed, as the Eulerian FE can be computationally very expensive for a large-scale problem.

Algorithm 3.1 Implementation of nonlocal methods with von Mises yield criterion

---

do loop for integration points k = 1: NOEL, where NOEL = number of elements

- Compute trial stress, $\boldsymbol{\sigma}^{t}$ [Eq. (3.15)]
- Compute σ_{v}^{t} [Eq. (3.16)]
- Obtain $d\varepsilon_{q(NL)}^{p}$ from the Fortran module
- Update H based on constitutive relationship and $\sigma_{y}^{(1)}$
- Update $\sigma_{y(NL)}^{(2)}$ [Eq. (3.21)]

if $\sigma_{v}^{t} > \sigma_{y}^{(1)}$ **then**

- Compute $d\varepsilon_{q}^{p}$ [Eq. (3.18)] and pass it to the module
- Update stress components [Eq. (3.22)]

else

- Update stress components using $\boldsymbol{\sigma}^{t}$ from Eq. (3.15)

end if

- Calculate $x(k)$ and $y(k)$ [Eqs. (3.23) & (3.24)]
- Store $x(k)$ and $y(k)$ in the module

end do loop

- Compute $d\varepsilon_{q(NL)}^{p}$ [Eq. (3.7) or Eq. (3.11)] using Algorithm 3.2 or Algorithm 3.3
- Update $d\varepsilon_{q(NL)}^{p}$ in the Fortran module

When an integration point is near the material boundary, its nonlocal weight function covers a certain area of the void, in which no soil exists (i.e., EVF = 0). In that case, the void area is not included in the calculation of V_w, reference volume (Eq. (3.9)), and thus $d\varepsilon_{q(NL)}^{p}$, the nonlocal equivalent plastic strain increment (Eq. (3.7) or (3.11)). In the subroutine, EVF is called and stored as a state variable which is then used to identify the zone of void in the reference volume.

Figure 3.5 is a flowchart that explains the main components of the implementation of nonlocal methods. At the beginning of each time increment, the stress and strain tensors of the previous time increment are obtained as inputs from the VUMAT. As shown in Fig. 3.6, the information of the elements in the reference volume around the element of interest (element X) is needed for nonlocal implementation. In other words, element numbers are required, but are available in the VUMAT subroutine. Therefore, following the work of Zhu (2017), a subroutine VUMATXTRARG is developed where all the information from VUMAT is passed, and the element number is called. Essentially, a major part of the program is written in this subroutine. In the software, the coordinates of the integration point (the center of each element) cannot be called directly from the VUMAT subroutine; therefore, they are calculated from the element number in the VUMATXTRARG subroutine.

Efficiently searching the elements in the control volume (within the circle in Fig. 3.6) is very important because it significantly influences the computational cost. In the present study, a structured mesh of uniform cubical elements is used. Instead of element numbers being auto-generated by the software, the element numbers are given in a sequence, as illustrated in Fig. 3.6 with a few elements. This definition helps find the elements in control volume easily instead of searching the whole domain based on coordinates of the integration points. As shown in the left part of Fig. 3.6, the element number increases by one in the vertical direction and then continues in the same way in the next column. Therefore, the coordinates of the integration point of *k*th element (x(k), y(k)) are:

$$x(k) = t_{\mathrm{FE}} \cdot \lfloor (k-1)/N_y \rfloor + t_{\mathrm{FE}}/2 \tag{3.23}$$

$$y(k) = t_{\mathrm{FE}} \cdot \mathrm{mod}\left[(k-1), N_y\right] + t_{\mathrm{FE}}/2 \tag{3.24}$$

where the '⌊ ⌋' are the floor brackets, N_y means the total number of rows of elements, 'mod' is the remainder calculator.

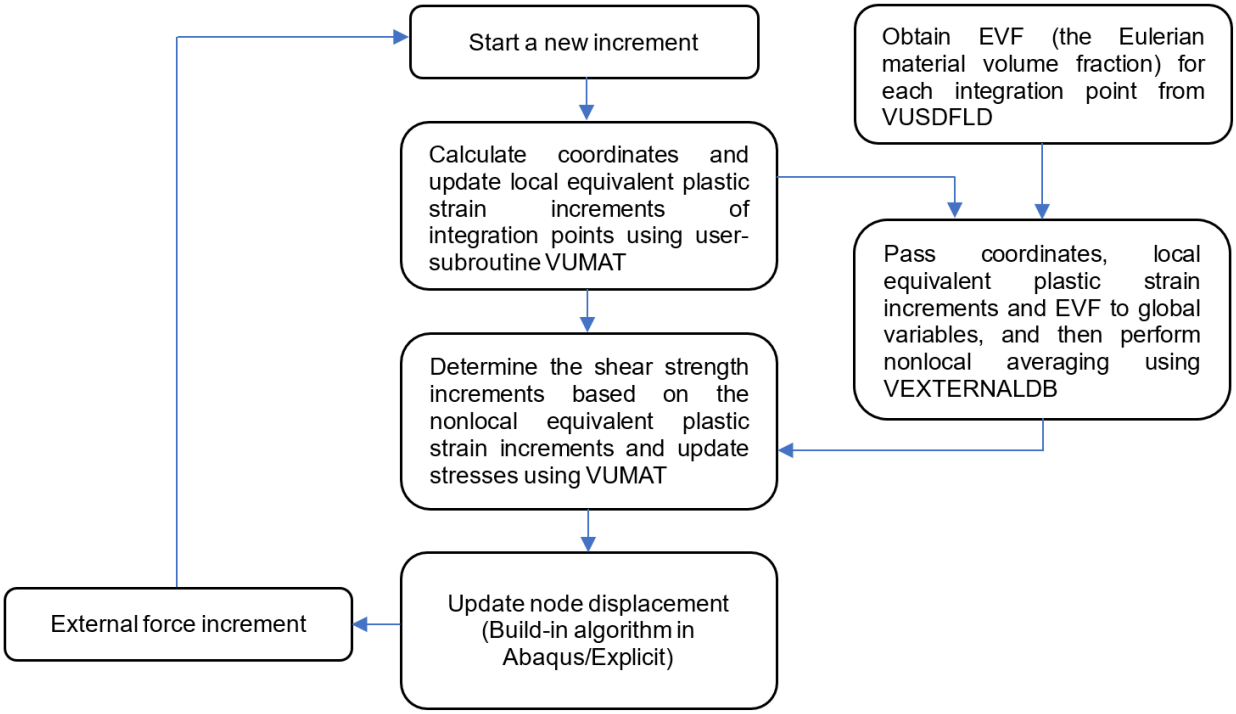

Figure 3.5 Implementation of nonlocal von Mises model in Eulerian-based FE

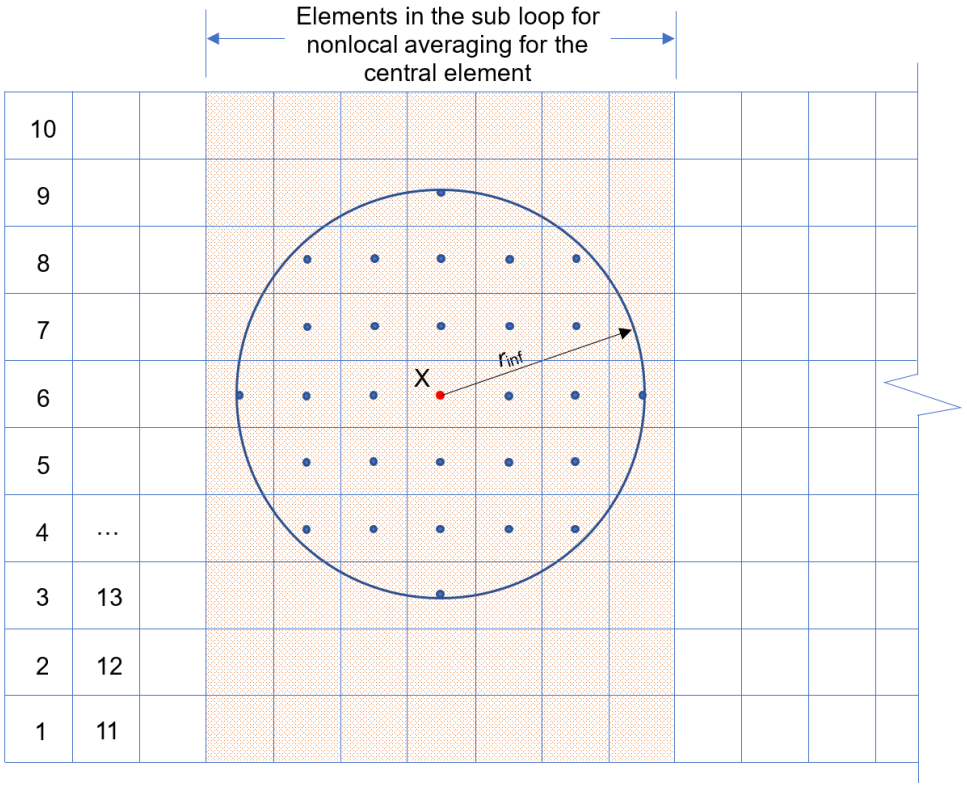

Figure 3.6 The nonlocal searching algorithm for Eulerian-based FE

The variables are called or calculated in a subroutine and then made available in the other subroutines using state variables. For example, the equivalent plastic shear strain ($d\varepsilon_{\mathrm{q}}^{\mathrm{p}}$) that is computed in VUMAT, the *EVF* that is obtained in VUSDFLD, together with the coordinates of integration points, are stored in global variables and passed to VEXTERNALDB for the calculation of the nonlocal equivalent plastic strain increments, $d\varepsilon_{\mathrm{q(NL)}}^{\mathrm{p}}$, to determine the amount of shear strength reduction. The new stress tensors are then updated based on Eq. (3.22).

3.5.3 Attempts to improve computational efficiency

Without any optimization, the computational cost of this nonlocal program can be extremely high, as the nonlocal averaging occurs at every element for every time increment. This

process requires calling the global arrays for NOEL^2 times in each time increment (Algorithm 3.2). Moreover, the existing versions of Abaqus/Explicit support only linear brick elements with reduced integration, which means that there is only one integration point in each element. Therefore, to incorporate a sufficient number of elements around the thin shear band, an adequately small mesh needs to be used. This increases the computational cost further. For example, if 100,000 Eulerian elements are used to model a large-scale landslide, a global array (e.g., the coordinates of an integration point) will be called for 100,000 × "total number of time increments" times. The total number of time increments is generally large (i.e., minimal time increment) in an explicit FE analysis, and calling global arrays is generally expensive. This computational cost can easily be far beyond the capability of conventional computational resources. Therefore, special treatments of the nonlocal algorithm are conducted to reduce the computational time, and especially for large problems such as landslides. In this study, the following steps are taken.

Algorithm 3.2 Calculation of nonlocal strains without optimization

---

do loop for i = one : NOEL
  do loop for k = one : NOEL
    - Compute $|\mathbf{x}'_{\mathrm{n}}(k) - \mathbf{x}_{\mathrm{n}}(i)|$
    if $|\mathbf{x}'_{\mathrm{n}}(k) - \mathbf{x}_{\mathrm{n}}(i)| \leq r_{\mathrm{inf}}$ **then**
      - Compute $\omega_{\mathrm{o}}(\mathbf{x}'_{\mathrm{n}}(k))$ or $\omega_{\mathrm{g}}(\mathbf{x}'_{\mathrm{n}}(k))$ [Eq. (3.8) or (3.10)]
      - Obtain $d\varepsilon^{\mathrm{p}}_{\mathrm{q}}(\mathbf{x}'_{\mathrm{n}}(k))$ in the VUMAT from the module
      - Compute $\omega_{\mathrm{o}}(\mathbf{x}'_{\mathrm{n}}(k))d\varepsilon^{\mathrm{p}}_{\mathrm{q}}(\mathbf{x}'_{\mathrm{n}}(k))$ or $\omega_{\mathrm{g}}(\mathbf{x}'_{\mathrm{n}}(k))d\varepsilon^{\mathrm{p}}_{\mathrm{q}}(\mathbf{x}'_{\mathrm{n}}(k))$
    end if
  end of do loop
  - Calculate $d\varepsilon^{\mathrm{p}}_{\mathrm{q(NL)}}(\mathbf{x}_{\mathrm{n}}(i))$ [Eq. (3.7) or (3.11)]
end do loop

Step 1: Nonlocal strains were calculated only for the elements filled with soil. As shown in Algorithm 3.3 (2nd and 3rd lines), all the void elements (*EVF* = 0) are excluded from the search; instead, a zero nonlocal strain increment is given.

Algorithm 3.3 Calculation of nonlocal strains with optimization

Run the calculations below only when mod (a, m) = 0, otherwise, $d\varepsilon^{\mathrm{p}}_{\mathrm{q(NL)}}(\mathbf{x}_{\mathrm{n}})$ equals its value at the end of the previous time increment, a – 1. (a is the current number of time increments)

do loop for i = one : NOEL
  if EVF(i) = zero, **then**
    - $d\varepsilon^{\mathrm{p}}_{\mathrm{q(NL)}}(\mathbf{x}_{\mathrm{n}}(i)) = 0$
  else
  - lower = max[(i - $N_{\mathrm{y}} \cdot r_{\mathrm{inf}}/l$), one]
  - upper = min[(i + $N_{\mathrm{y}} \cdot r_{\mathrm{inf}}/l$), NOEL]
  do loop for k = lower : upper
    - Compute $|\mathbf{x}'_{\mathrm{n}}(k) - \mathbf{x}_{\mathrm{n}}(i)|$
    if $\left|\mathbf{x}_{\mathrm{n}}^{'}(k) - \mathbf{x}_{\mathrm{n}}(i)\right| \leq r_{\mathrm{inf}}$, **then**
      - Compute $\omega_{\mathrm{o}}(\mathbf{x}'_{\mathrm{n}}(k))$ or $\omega_{\mathrm{g}}(\mathbf{x}'_{\mathrm{n}}(k))$, from Eq. (3.8) or (3.10)
      - Obtain $d\varepsilon^{\mathrm{p}}_{\mathrm{q}}(\mathbf{x}'_{\mathrm{n}}(k))$ from the VUMAT using the module
      - Compute $\omega_{\mathrm{o}}(\mathbf{x}'_{\mathrm{n}}(k))d\varepsilon^{\mathrm{p}}_{\mathrm{q}}(\mathbf{x}'_{\mathrm{n}}(k))$ or $\omega_{\mathrm{g}}(\mathbf{x}'_{\mathrm{n}}(k))d\varepsilon^{\mathrm{p}}_{\mathrm{q}}(\mathbf{x}'_{\mathrm{n}}(k))$
    end if
  end do loop
  - Calculate $d\varepsilon^{\mathrm{p}}_{\mathrm{q(NL)}}(\mathbf{x}_{\mathrm{n}}(i))$, from Eq. (7) or (11)
  end if
end do loop

Step 2: This step is to reduce the time of each sub-loop (4^{th} to 14^{th} lines in Algorithm 3.3) which is used for the nonlocal averaging. Only the distances to a certain range of integration points that are defined with lower and upper bounds in the 5^{th} and 6^{th} lines (shown schematically by the shaded area in Fig. 3.6), rather than to all the integration points, are calculated to decide the included integration points in the nonlocal calculation for each integration point. By identifying the number of each element with the lower and upper bounds, most of the elements are excluded in each sub-loop, which means only the information of these shaded columns of elements that cover the control volume (radius of r_{inf}, in Fig. 3.6) are called. This approach significantly reduces the computational cost.

Step 3: For an explicit FE program, the nonlocal averaging can be performed once for every 10 to 100 time increments rather than doing it for every time increment (e.g., Wisselink and Huetink 2009). As shown in the 1^{st} line in Algorithm 3.3, the same approach is implemented in the nonlocal Eulerian-based FE, where the nonlocal averaging is conducted every m-th time increment. This could also largely reduce the computational cost because the nonlocal averaging accounts for the major portion of total computational time. In the present study, the first benchmarking program (Case I) does not include this technique ($m = 1$ is used). Comparing it with the second benchmark solution (Case II), the accuracy and computational cost are examined for varying m. Further details are provided in the next sections.

In addition, CPU parallel computing is used to boost computational efficiency. However, with the default setting of parallel computing in Abaqus/Explicit, each process cannot access the global arrays that are stored in other processes. This can cause a significant inaccuracy of the results

when the needed information of neighbouring elements needs to be collected from other processes. To solve this problem, a Message Passing Interface (MPI) routine, MPI_Allreduce, is implemented to collect global arrays from all processes and distribute the result back to all processes.

3.6 Numerical simulation

The effectiveness of implemented nonlocal methods in Eulerian-based FE program (NL-EFE) is shown by simulating the following two biaxial loading cases (Figs. 3.7(a) and 3.7(b)). The NL-EFE simulation results are compared with nonlocal methods previously implemented into two numerical techniques: (*a*) Lagrangian-based FE program ICFEP (NL-ICFEP) (Summersgill et al. 2017a), and (*b*) Material Point Method (NL-MPM) (Burghardt et al. 2012). Note that the latter approach can handle large deformation. However, it is not commercially available.

Case I: Biaxial compression tests have been used in previous studies to show the performance of numerical techniques (Brinkgreve 1994; Lu et al. 2012; Summersgill et al. 2017a). In some studies, the simulations were performed without any initial confining pressure (Brinkgreve 1994; Lu et al. 2012), while Summersgill et al. (2017a) simulated softening due to drained and undrained loading after applying 100 kPa and 50 kPa initial pressure on the lateral and vertical directions, respectively. In case I of the present study, the simulation is performed without any initial confining pressure. Note that the confining pressure should not affect the assessment of the performance of NL-EFE simulation for undrained loading because the mobilized undrained shear strength is independent of confining pressure.

Case II: Implementing nonlocal methods in MPM, Burghardt et al. (2012) modelled the failure of a block of gravityless hypothetical material having strain-softening behaviour in plane strain condition (Fig. 3.7(b)). The same problem is modelled using the present NL-EFE. A 4 m × 5 m block, which has a weaker zone (1 m × 1 m) at the bottom left corner, is modelled.

3.6.1 FE model development

The Coupled Eulerian-Lagrangian (CEL) approach available in Abaqus/Explicit FE software is used. In this software, the Eulerian approach has been implemented only for three-dimensional elements. Therefore, the analyses are performed with only one element length in the out-of-plane direction to simulate the plane strain condition. Eulerian domains of 1.2 m × 1.1 m and 5.0 m × 5.1 m in plane are created first for case I and case II, respectively (Figs. 3.7(a) and 3.7(b)). The domains are discretized into 0.1 m, 0.05 m, 0.025 m, and 0.0125 m cubical eight-node linear brick elements (EC3D8R in the software) for Case I and 0.25 m, 0.125 m, and 0.0625 m cubical EC3D8R for Case II. The *EVF* is used to define the material; $EVF = 1$ for the elements filled with material (1.0 m × 1.0 m soil block in case I and 4 m × 5 m in case II), while the rest of the domain is void ($EVF = 0$). The loading caps at the top (Figs. 3.7(a) and 3.7(b)) are first discretized using Lagrangian elements and then transferred to a rigid body.

Zero velocity boundary conditions are applied normal to the bottom and out-of-plane directions. For Case I, $v_x = 0$ is applied at the (symmetrical) left vertical face while no boundary condition is applied to the right vertical face, to ensure that the Eulerian material (soil) can move into the void when loaded. For case II, no boundary condition is applied to the left and right vertical

face, and therefore the Eulerian material can move to the void on both sides. The rigid cap is displaced downward at a uniformly vertical velocity of 0.01 m/s and 7.5 m/s for case I and case II, respectively, maintaining a quasi-static condition. Rough and smooth interface conditions between soil and rigid cap are used for case I and case II, respectively.

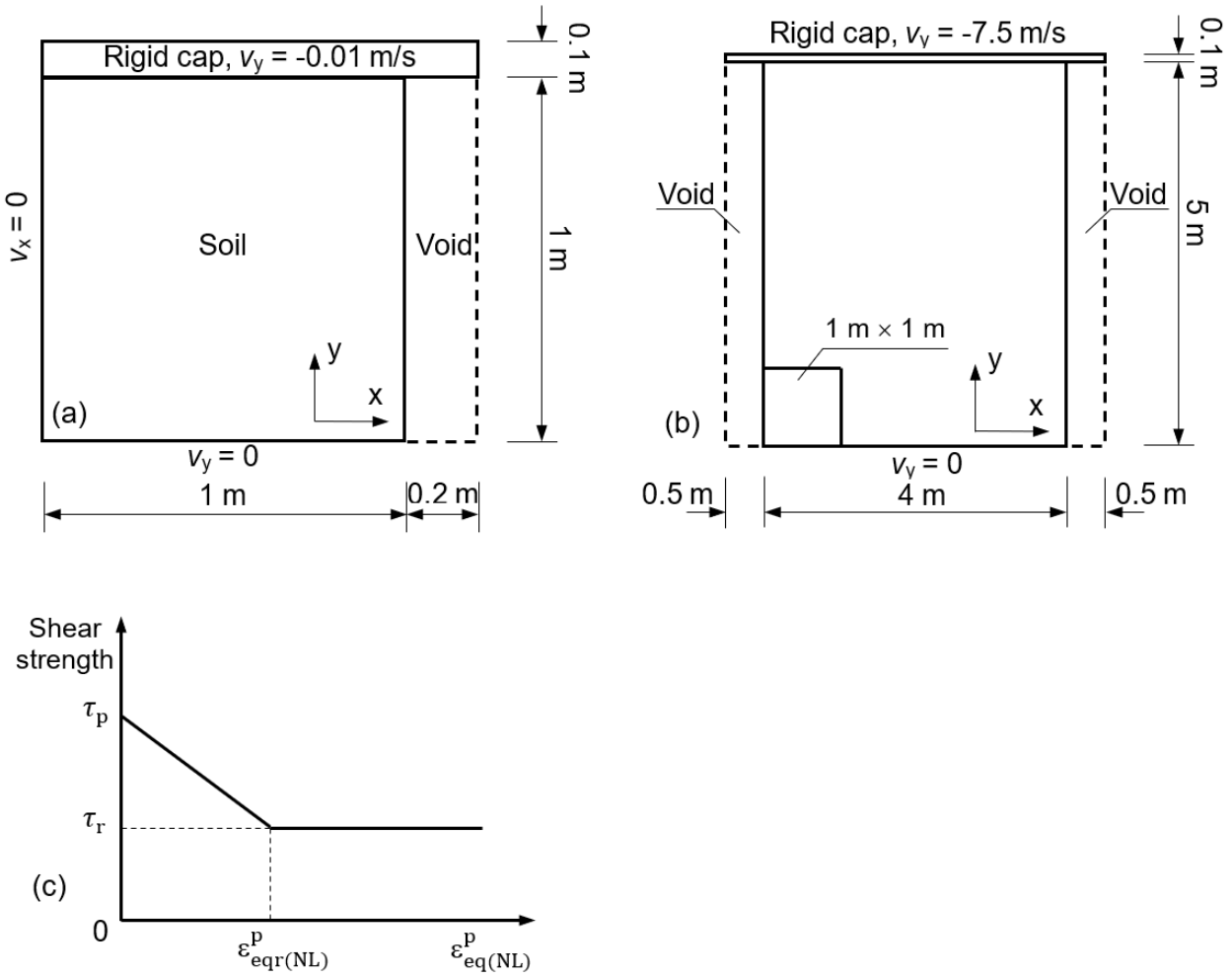

Figure 3.7 (a) Geometry and boundary conditions of Case I; (b) geometry and boundary conditions of Case II; (c) stress-strain curve for the soil

3.6.2 Modeling of soil

A bi-linear post-peak strength degradation relation is used (Fig. 3.7(c)). In this figure, ε_q^p is the equivalent plastic shear strain that represents the integration of the plastic deviatoric strain rate tensor ($\dot{\varepsilon}_{ij}^p$) over the period of analysis (t): $\varepsilon_q^p = \int_0^t \sqrt{\frac{2}{3}\dot{\varepsilon}_{ij}^p : \dot{\varepsilon}_{ij}^p}\, dt$. The shear strength reduces from the peak (τ_p) to the residual (τ_r) at ε_{qr}^p and then remains constant. The linear elastic pre-post behaviour is governed by Young's modulus (E) and Poisson's ratio (ν). Note that Case I represents an undrained loading; therefore, undrained geotechnical properties are used. However, Case II is for a hypothetical material (Burghardt et al. 2012) and the material properties may not represent typical soil properties. Nevertheless, they are used to validate the numerical modelling technique through direct comparison with NL-MPM simulation results. For non-local methods, an internal length parameter l of 0.1 m is used.

The parameters used in these simulations are listed in Table 3.1, which are similar to those used by Summersgill et al. (2017a) and Burghardt et al. (2012). This ensures that the performance of the present Eulerian modelling is directly comparable to their studies. The Tresca failure criterion was used by Summersgill et al. (2017a), while the von Mises criterion is adopted in the present study. Therefore, the strengths shown in the second column of Table 3.1 for Case I are $\sqrt{3}/2$ times of the value they used. Also, Summersgill et al. (2017a) used the deviatoric plastic strain invariant, which is $1/\sqrt{3}$ times of the equivalent plastic shear strain used in this study. The von Mises criterion was used by Burghardt et al. (2012) but with slightly different constitutive equations. The parameters in the column for Case II are converted from the values adopted by Burghardt et al. (2012) to ensure the similarities between the two materials.

Table 3.1 Parameters used in CEL analyses

Parameter	**Case I**	**Case II**
Young's modulus (MPa)	50	70,000
Poisson's ratio	0.49	0.346
Peak shear strength, τ_p (kPa)	86.6	692,800 (649,500)
Residual shear strength τ_r (kPa)	43.3	346,400 (324,750)
Equivalent plastic shear strain requires for strength degradation to residual, $\varepsilon^{p}_{qr(NL)}(\%)$	8.66	10.0
Internal length parameter, l (m)	0.1	0.5
Parameter α for over-nonlocal model	1.5, 2.0	2.0

3.7 Results

3.7.1 Case I simulation results

Figure 3.8 shows the development of the equivalent plastic shear strain (ε^{p}_{q}) for a vertical displacement (δ_v) of 50 mm. For the purpose of discussion, the zone of local $\varepsilon^{p}_{q} \geq \varepsilon^{p}_{qr}$ is considered as the shear band. In the analyses without regularization, strain localization primarily occurs within 3–5 rows of elements in the diagonal direction, and the thickness of the shear band (t_{sb}) decreases with decreasing element size (Fig. 3.8(a)). Note that, although a defined square shape was used in the model, the top right corner (e.g., Fig. 3.8(a)) shows a slightly curved surface because of *EVF* manipulation in the software for contour generation. When nonlocal regularization

methods are used (Figs. 3.8(b)–(e)), the t_{sb} still decreases with the decrease in element size. As shown in the first column, a significantly thick shear band forms for 0.1-m mesh. However, for the smaller mesh (0.0125–0.05 m), the change in t_{sb} with mesh size is not very significant. Further discussions on t_{sb} are presented in Chapter 4.

Figure 3.9 shows the load–displacement curves for different mesh sizes without regularization and with regularization using three nonlocal methods. For comparison, the results presented by Summersgill et al. (2017a) using nonlocal ICFEP are also shown in this figure. In these figures, the vertical stresses of Summersgill et al. (2017a) are shown by subtracting 50 kPa because they used 50 kPa initial confining pressure, while the present simulations are performed without confining pressure. As shown in this figure, the nonlocal CEL models with 0.05-m, 0.025-m, and 0.0125-m mesh are nearly identical with the nonlocal ICFEP using 0.1-m, 0.05-m, and 0.025-m mesh, respectively, which is because each element has four integration points in ICFEP, while only one integration point exists in each Eulerian element in the present CEL modelling. This implies that the nonlocal CEL and nonlocal ICFEP present comparable results when the density of integration points is the same. However, an exception is shown in Fig. 3.9(e) when $\alpha = 2.0$ is adopted for the over-nonlocal method. A large discrepancy was observed between two curves (0.05-m and 0.025-m mesh) from the nonlocal ICFEP, while a mesh-independent solution was found in the nonlocal CEL modeling. A large accumulated plastic shear strain, (> 200%), developed in the shear zone for 0.025-m mesh and $\alpha = 2.0$ (Summersgill et al. 2017a), which can cause a significant mesh distortion in the analysis using ICFEP with Lagrangian elements. However, mesh distortion is not an issue in the present analysis. Therefore, it can be concluded

that present nonlocal CEL analysis can simulate the force–displacement response better, even for a large strain level. The nonlocal CEL shows some fluctuations in load–displacement curve, due to the inherent nature of an explicit FE with contacts between Lagrangian and Eulerian elements.

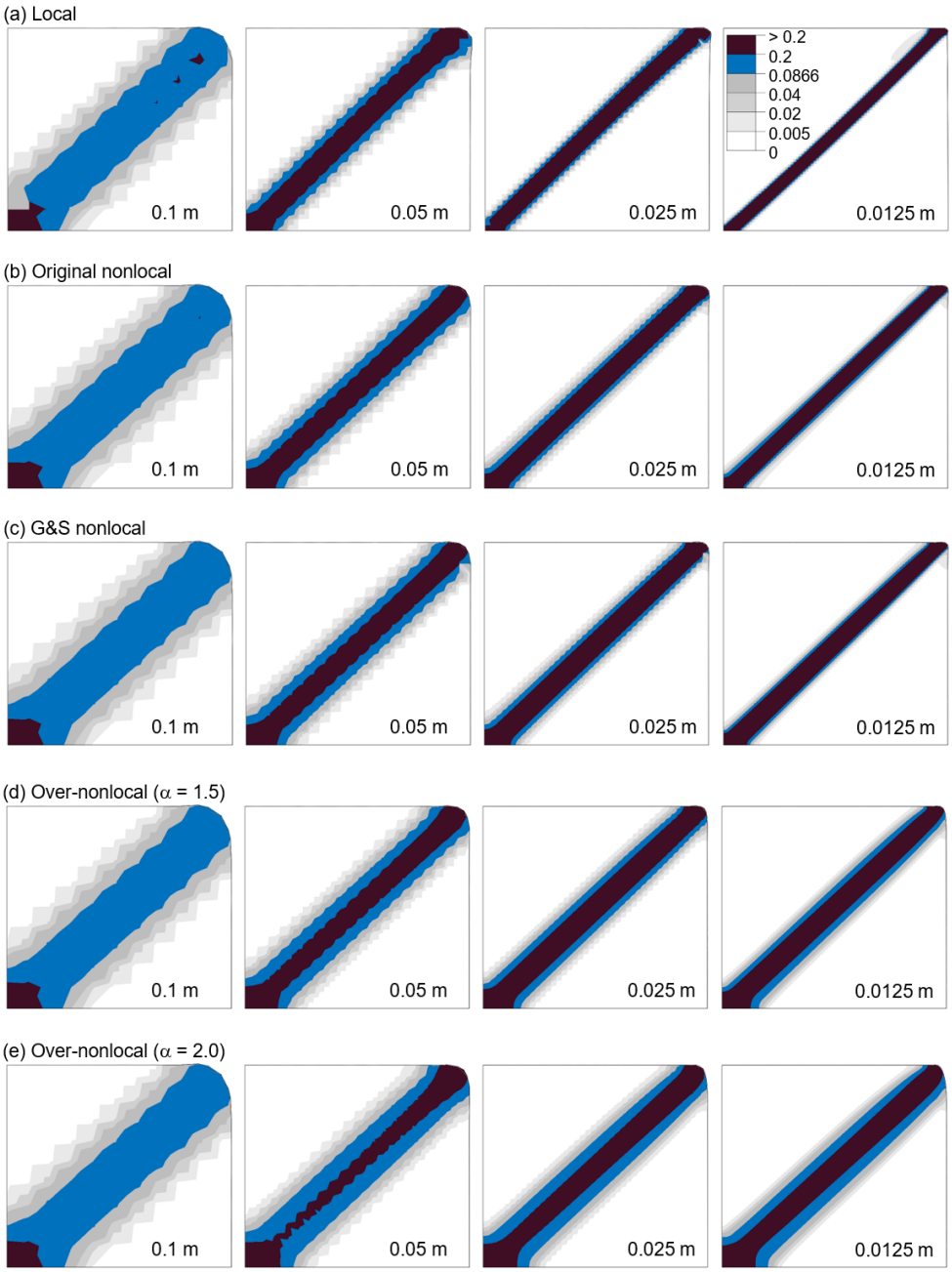

Figure 3.8 Local equivalent plastic shear strain distribution with different mesh sizes after 50 mm vertical displacement

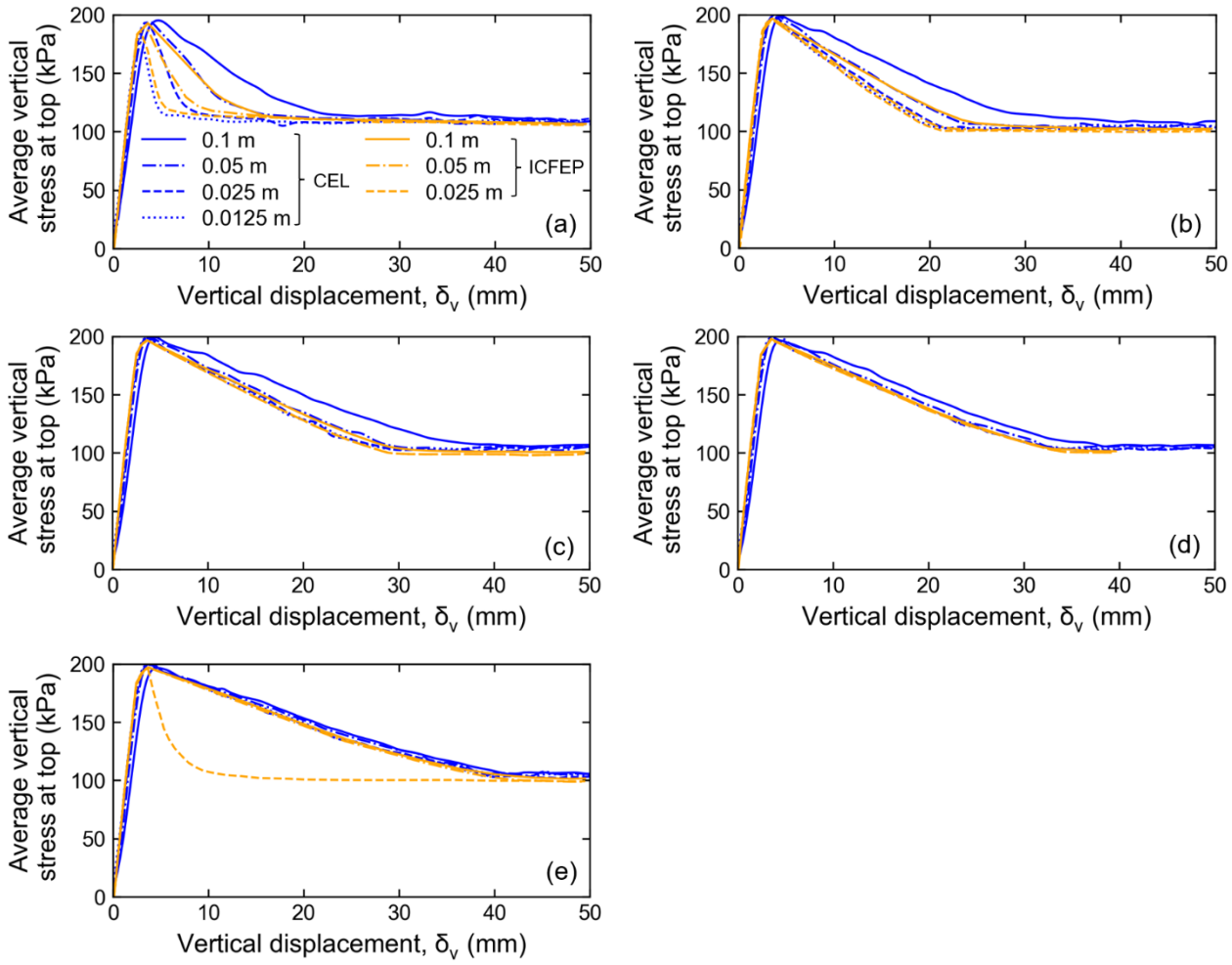

Figure 3.9 Load–displacement curves: (a) local model; (b) original nonlocal; (c) G&S nonlocal; (d) over-nonlocal ($\alpha = 1.5$); (e) over-nonlocal ($\alpha = 2.0$)

3.7.2 Case II simulation results

Figure 3.10 shows the mesh convergence study for Case II. Figure 3.10(a) shows the relationship between applied stress and the apparent axial strain (percent change in height of the block) for both the nonlocal CEL and nonlocal MPM models (Burghardt et al. 2012). The applied stress is computed as the cap reaction force divided by the initial cross-sectional area. In the nonlocal MPM model, Burghardt et al. (2012) used three mesh sizes of 0.25-m, 0.125-m and

0.0625-m, and found that the finer two meshes give almost identical results. For clarity, only the results with the 0.0625-m mesh in the nonlocal MPM simulations are shown in Fig. 3.10(a). Considerable oscillation in stress–strain occurred in the MPM simulation of Burghardt et al. (2012). The nonlocal CEL model predicts mesh-independent stress–strain curves for 0.125-m, 0.0625-m, and 0.06125-m mesh (Fig. 3.10(a)), and they are comparable with the result from the nonlocal MPM of Burghardt et al. (2012). Also, Figs. 3.10(b–d) show the same location of shear bands with three different mesh sizes. Note that, following the work of Burghardt et al. (2012), in the simulations with the over-nonlocal method, $\omega_o(\mathbf{x}'_n) = \exp[-4|\mathbf{x}'_n - \mathbf{x}_n|^2/l^2]$ is used for CEL, rather than Eq. (3.8), to calculate nonlocal strains using Eq. (3.11).

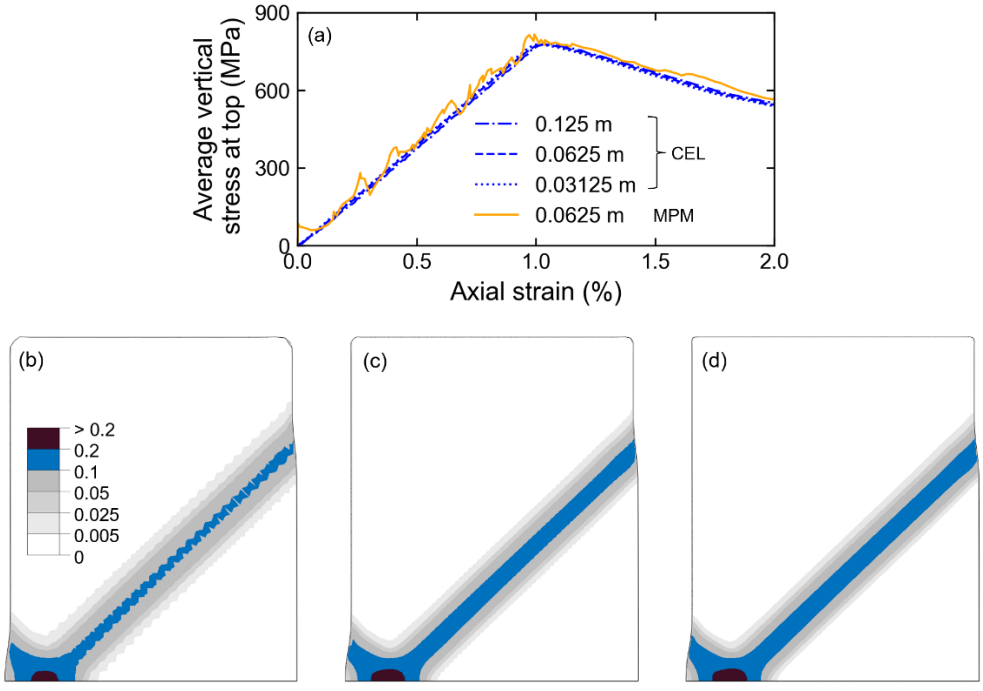

Figure 3.10 Simulation results for case II: (a) comparison of axial stress–strain curves for nonlocal CEL and nonlocal MPM; (b, c, d) plastic shear strains for 0.125-m, 0.0625-m, and 0.03125-m meshes

The nonlocal plasticity algorithm presented by Burghardt et al. (2012) for the MPM requires iterations for each time increment. This involves updating the plastic multiplier ($\Delta\lambda_{\mathrm{p}}^{k}$) in the k-th iteration, by solving a fixed-point equation based on the updated nonlocal state variables, until $\left|\Delta\lambda_{\mathrm{p}}^{k} - \Delta\lambda_{\mathrm{p}}^{k-1}\right|$ is less than the predefined tolerance. The algorithm requires calculating nonlocal strains from the strains of the current time increment, which is a challenging task with Abaqus user-subroutines. This type of algorithm will significantly increase the computational cost because the nonlocal averaging can be conducted several times for every element at every time increment. As aforementioned, the algorithm developed in the present study does not include any iteration within each time increment. Instead, the nonlocal equivalent plastic strain increment ($\Delta\varepsilon_{\mathrm{q(NL)}}^{\mathrm{p}}$) that is equal to the plastic multiplier ($\Delta\lambda_{\mathrm{p}}$) for this algorithm is computed from strains of the previous time increment. As shown in Figs. 3.9 and 3.10, mesh-independent results are displayed in the present nonlocal CEL modelling, which proves that the mesh-independent solution can be correctly obtained without iteration for each time increment.

3.8 Discussions

3.8.1 Comparison of performance of nonlocal methods

Jostad and Grimstad (2011) found that the over-nonlocal method is more robust than the G&S nonlocal method, based on their simulations using the commercial FE program PLAXIS. However, Summersgill et al. (2017a) showed that the G&S nonlocal method provides the best compromise between low mesh dependency and consistency of results, while the solution becomes unstable for the high value of α and fine meshes in the over-nonlocal method. As a result, several

studies selected the G&S nonlocal method for various FE programs (Mallikarachchi and Soga 2020; Mánica et al. 2018; Monforte et al. 2019; Singh et al. 2021). Nevertheless, the present nonlocal CEL model shows no unstable behaviour in the over-nonlocal method, even for the finest mesh (0.0125 m) and high α-value (2.0). Figures 3.9(d) and 3.9(e) show no significant difference in load–displacement curves in the present CEL analysis with the over-nonlocal method for 0.05-m and 0.025-m meshes and $\alpha = 1.5$ and 2.0. For the G&S method, a considerably different load–displacement curve is found for the coarse mesh (0.1 m) than for the finer mesh (Fig. 3.9(c)), which is because of insufficient integration points in the reference volume, as explained below. In summary, the present study shows that the over-nonlocal method produces a better performance in mesh regularization than the G&S nonlocal method.

In addition to the variation of the weight function in different nonlocal methods, capturing its shape by discretized integration points is equally important for a better solution. The shape of the weight function can be better captured with denser mesh (or integration points) but leads to an increased computational cost. The solid lines in Figs. 3.11(a) and 3.11(b) show the distribution of the weight functions (ω) of the G&S nonlocal (Eq. (3.10)) and over-nonlocal (Eq. (3.12)) methods, respectively, while the dashed lines show the FE approximated ω, which has been drawn for an internal length parameter (l) of 0.1 m and 0.1-m mesh. The symbols '+' and '-' in these figures denote an overestimation and an underestimation of the weight functions, respectively, by FE discretization. As shown in Fig. 3.11(a), the FE approximation of the G&S weight function at the center element area (G1) significantly underestimates the weight function, as the weight is equal to zero for the whole element. In the adjacent element area (G2), the FE approximation

overestimates the weight function because the '+' area is larger than the '-' area. Finally, in G3, FE slightly underestimates the weight function. However, the weight of this area is relatively small, and thus only has a minor influence on the result. For a smaller mesh (e.g., 0.05 m and 0.025 m), the FE can approximate the G&S weight function better, while it will always give a zero weight at the center element and thus still underestimates the weight function curve. The inaccuracy induced by this underestimation of the weight at the center (e.g., G1) and the overestimation at its adjacent elements (e.g., G2), can be amplified due to a high concentration of shear strain at the shear band, when calculating the nonlocal plastic shear strain using Eq. (3.10). In comparison, the FE approximation of the over-nonlocal weight function with the same mesh can better represent the weight function (Fig. 3.11(b)). At the O1 area, the weight in the Eulerian element is only marginally higher than the actual weight. The FE approximated weight at O2 is close to the averaged weight at this area, as the highest value of the weight function is always at the edge of the O2 (or the center element), which provides that the areas of '+' and '-' of O2 are nearly equivalent. This feature of the over-nonlocal method enables it to provide a more accurate nonlocal averaging calculation, and a more mesh-independent result is thus expected. Note that, although the over-nonlocal method with $\alpha = 1.5$ and 2.0 shows an effective regularization in the present biaxial compression test simulations, further investigations of the effect of α are discussed in Chapter 4.

Previously, the comparison of the performance of different nonlocal methods was restricted to a relatively small strain problem. With the implementation of nonlocal methods in a large-deformation FE solver, the comparison of various nonlocal methods for a large-strain level becomes possible. The authors are aware that the researchers also used other Gaussian-type

functions, instead of Eq. (3.8), for the over-nonlocal method (e.g., Burghardt et al. 2012). Further research can be conducted to identify the most effective Gaussian function for the over-nonlocal method.

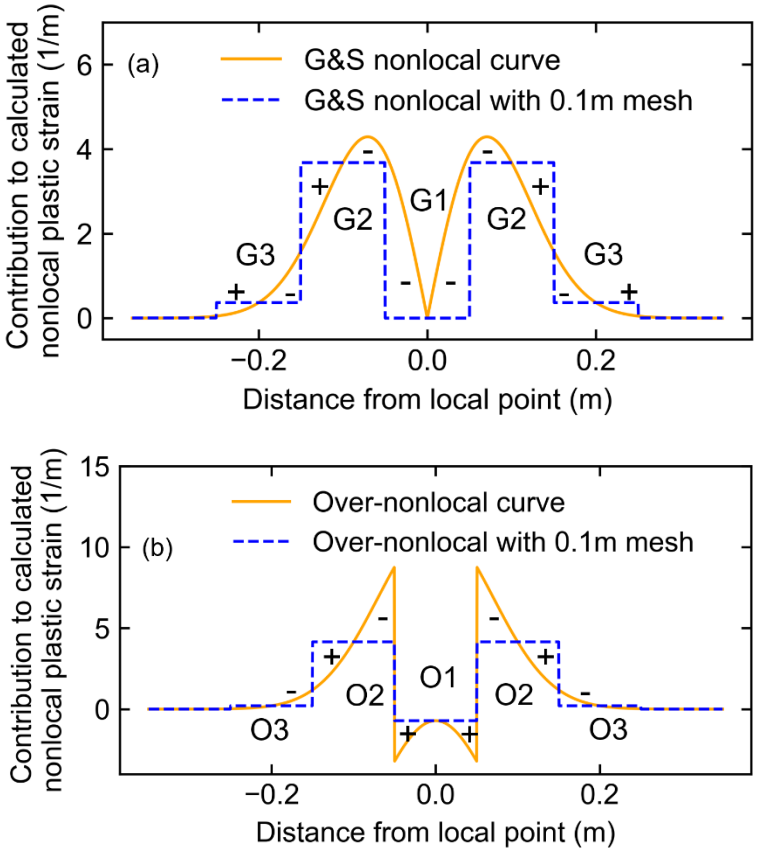

Figure 3.11 Schematic distribution of weight functions and their approximation in Eulerian-based FE

3.8.2 Computational cost

Considering that the ultimate purpose of this nonlocal Eulerian-based FE could be the simulation of large-scale problems (e.g., large-scale landslides), optimizations to the algorithm

have been made to reduce the computational cost (as mentioned in previous sections). The effectiveness of those approaches is presented below.

As shown in Algorithm 3.3, several optimization efforts are made to reduce the computational costs. To show their effectiveness, a set of simulations of the biaxial compression test (Case I) is performed with the over-nonlocal method, with $\alpha = 1.5$ and $l = 0.5$ for different values of m (m = 1, 10, 100, and 1000). m represents the increment interval when the nonlocal calculations are performed, among which $m = 10$ means that the nonlocal calculation is done for every 10 increments. These factors are used for Algorithm 3.3 to investigate their influence on the load–displacement curves and the computational cost.

Figure 3.12 shows the stress–displacement curves for different values of m in the simulations with 0.0125-m mesh. All the five curves in this figure overlap with each other, which means higher values of m, (e.g., 10, 100, and 1000) do not cause any noticeable error. In these analyses, the total number of time increments is ~200,000, which implies that the nonlocal averaging is performed ~200 times (= 200,000/1,000) when $m = 1000$ is used. Note, however, that the effects of m on simulation results are not the same for every scenario, and instead depend on the type of problem analyzed. It is recommended that a sensitivity analysis similar to Fig. 3.12 is performed at the beginning to identify an acceptable value of m.

Figure 3.13 shows the relative computational time, $t_c / t_{c\text{-}L}$, where t_c is the CPU time of each model, and $t_{c\text{-}L}$ represents the CPU times for local modelling. A higher value of m significantly decreases the computational cost. For example, computational costs of nonlocal modeling are 10.27 and 1.33 times that of local modeling for $m = 1$ and $m = 1000$, respectively, for the mesh size of

0.0125 m (8448 elements in total). When no optimization is done (i.e., nonlocal averaging of the whole model is performed for every element at every time increment (m = 1)), t_c is more than 84 times of $t_{c\text{-}L}$, which clearly shows the importance of optimization, as performed in this study.

The inset of Fig. 3.13 shows the comparison of the computational cost ($t_c/t_{c\text{-}L}$) for different mesh sizes. The nonlocal model without optimization (using Algorithm 3.2) is not shown here as its computational cost is too large compared with others, which could make the gap between other rows difficult to identify. As shown, $t_c/t_{c\text{-}L}$ is almost the same in the analyses with 132 elements. However, the solution may not be correct with such a coarse mesh. The nonlocal modelling becomes more expensive with fine mesh. Moreover, a sufficiently large value of m (e.g., m = 10) can reduce the computational costs considerably as compared to that with m = 1.

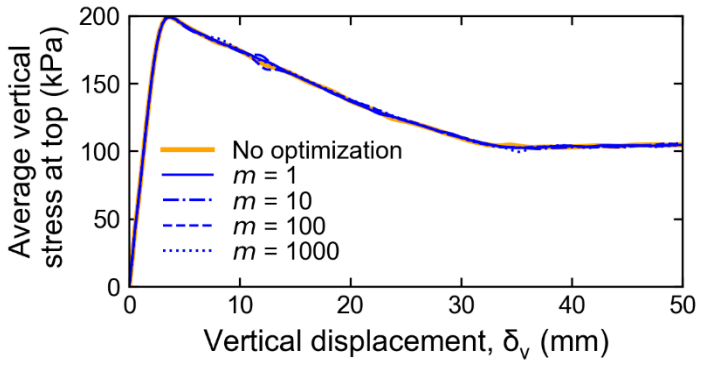

Figure 3.12 Stress–displacement curves of Case I with and without optimization (t_{FE} = 0.0125 m, α = 1.5)

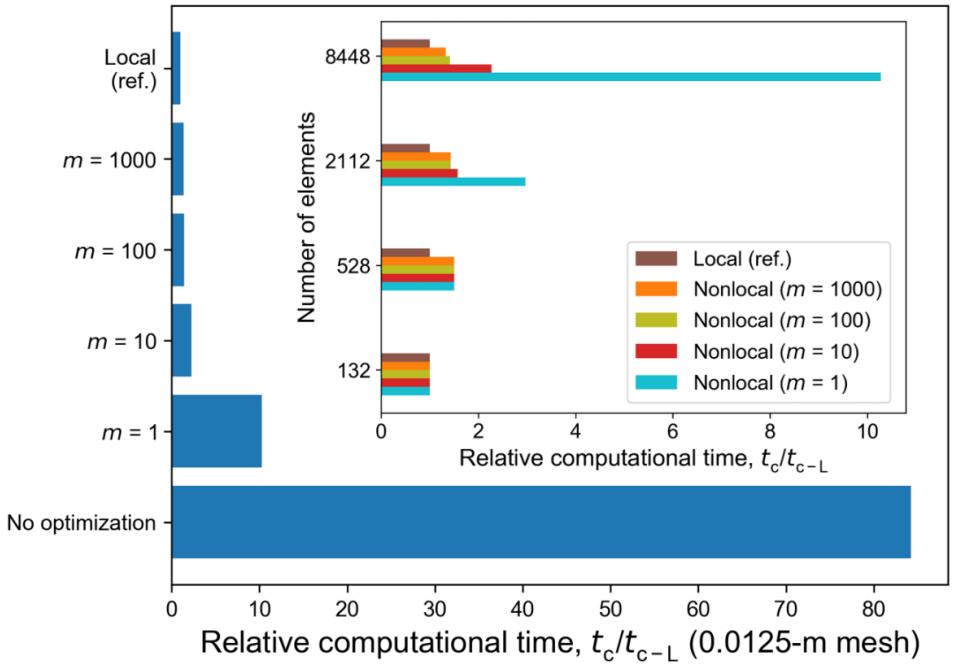

Figure 3.13 Computational cost of Case I with local and over-nonlocal (α = 1.5) methods

Most of the previous studies found that the application of nonlocal averaging is more computationally expensive than the local modelling (e.g., Summersgill 2014). The present simulation with a Eulerian-based FE shows a similar trend. However, in a recent study, Singh et al. (2021) found no significant difference in computational cost between the nonlocal and local modeling. One possible reason behind this might be their Remeshing and Interpolation Technique with Small Strains (RITSS) where the computational cost of the nonlocal calculations is offset by a faster convergence in its implicit algorithm, due to a smoother strain distribution (Singh et al. 2021). Overall, the computational cost is significantly reduced with the optimization approaches presented in this study. Further discussion on computational cost is also presented in Chapter 4.

3.9 Conclusions

The capability of nonlocal methods to minimize mesh sensitivity has been discussed in several previous studies. However, most of these studies implemented nonlocal methods in computer programs that can handle limited deformations. In the present study, nonlocal methods have been implemented in a Eulerian-based FE program, which can be used for large deformation problems. Innovative approaches to develop user subroutines using the existing platforms of the software and the algorithms used for model implementation are presented. The performance of the newly developed computer programs is shown by simulating two biaxial compression tests and comparing the results with similar analyses conducted in previous studies.

Three nonlocal methods are incorporated adopting the von Mises failure criterion, where the post-peak shear strength degradation occurs linearly. The force–displacement relationships in the biaxial compression test simulations using the present Eulerian-based FE are very similar to those reported in the previous FE analysis using an implicit time integration scheme and the Material Point Method (MPM). All three nonlocal methods are found to be effective for mesh-size regularization. However, better performance is shown by the over-nonlocal method, potentially because of better capturing of nonlocal averaged values that are less sensitive to the mesh size, especially when a uniform mesh is used for the whole domain.

Compared to the local method, the nonlocal modeling can be computationally very expensive. In the present study, several techniques are proposed to reduce the computational costs, including performing nonlocal averaging only for elements with $EVF > 0$, narrowing down the searching area for nonlocal averaging, and conducting nonlocal averaging for every m-th time

increment. The proposed optimization efforts show excellent performance in significantly reducing the computational time without sacrificing the accuracy of the solution. In addition, parallel computing is enabled for the nonlocal Eulerian-based FE by using an MPI routine.

Acknowledgments

The works presented in this paper have been supported by the Natural Sciences and Engineering Research Council of Canada (NSERC), InnovateNL, and the former Research and Development Corporation of Newfoundland and Labrador (RDC). Special thanks to Dr. Yazhi Zhu (Tongji University) for his advice on the programming of the nonlocal method.

Notations

α	amplification factor
τ_p	peak shear strength
τ_r	residual shear strength
$\varepsilon^p_{q(NL)}$	nonlocal equivalent plastic shear strain
ε^p_q	equivalent plastic shear strain
$\varepsilon^p_{qr(NL)}$	nonlocal equivalent plastic shear strain requires for residual strength
$\Delta\lambda^k_p$	plastic multiplier
ν	Poisson's ratio
$\boldsymbol{\sigma}^{(1)}$	stress tensor at the beginning of each time increment
$\boldsymbol{\sigma}^t$	trial stress

σ_v^t	von Mises stress at the trial state
$\sigma_y^{(1)}$	yield strength at the beginning of each time increment
$\sigma_y^{(2)}$	yield strength at the end of each time increment
$\sigma_{y(NL)}^{(2)}$	yield strength at the end of the time increment with nonlocal method
ϕ	arbitrary solution variable
$\mathbf{\Phi}$	flux function
$\omega_g()$	G&S weight function
$\omega_{loc}()$	concentrated weight function
$\omega_o()$	Gaussian-type weight function
$\omega_{ov}()$	weighting function of the over-nonlocal method
a	spatial acceleration
dim	dimension of the problem
E	Young's modulus
EVF	Eulerian volume fraction
$\mathbf{F}^{ext}$	external force vector
$\mathbf{F}^{int}$	internal force vector
G	shear modulus
H	hardening modulus
l	internal length parameter
M	diagonal lumped mass matrix
m	number of time increments covered by one calculation of nonlocal strain

NOEL	number of elements
N_y	total number of rows of elements
r_{inf}	radius of influence
$\mathbf{S}$	source term
$\mathbf{s}_{(NL)}^{(2)}$	the deviatoric stress tensor at the end of the time increment with nonlocal method
$\mathbf{s}^{(2)}$	deviatoric stress tensor at the end of the time increment
$\mathbf{s}^{t}$	deviatoric stress tensor of the trial stress
t_c	CPU time of each model
$t_{c\text{-}L}$	CPU times for local modelling
t_{FE}	element size
t_{sb}	thickness of the shear band
V_w	reference volume
$\mathbf{x}$	position vector
x(k), y(k)	horizontal and vertical coordinates of the integration point of kth element

References

Anastasopoulos, I., Gazetas, G., Asce, M., Bransby, M. F., Davies, M. C. R., and El Nahas, A. (2007). "Fault rupture propagation through sand: Finite-element analysis and validation through centrifuge experiments." *Journal of Geotechnical and Geoenvironmental Engineering*, 133(8), 943–958.

Bažant, B. Z. P., and Belytschko, T. B. (1985). "Wave propagation in a strain-softening bar: Exact

solution.” *Journal of Engineering Mechanics*, 111(3), 2–6.

Bažant, Z. P., Belytschko, T. B., and Chang, T. P. (1984). “Continuum theory for strain-softening.” *Journal of Engineering Mechanics*, 110(12), 1666–1692.

Bažant, Z. P., and Lin, F. (1988). “Non-local yield limit degradation.” *International Journal for Numerical Methods in Engineering*, 26, 1805–1823.

Benson, D. J., and Okazawa, S. (2004). “Contact in a multi-material Eulerian finite element formulation.” *Computer Methods in Applied Mechanics and Engineering*, 193(39–41), 4277–4298.

de Borst, R., and Mühlhaus, H. B. (1992). “Gradient-dependent plasticity: Formulation and algorithmic aspects.” *International Journal for Numerical Methods in Engineering*, 35(3), 521–539.

de Borst, R., Sluys, L. J., Mühlhaus, H. B., and Pamin, J. (1993). “Fundamental issues in finite element analyses of localization of deformation.” *Engineering Computations*, 10(2), 99–121.

de Borst, R., and Verhoosel, C. V. (2017). *Damage, Material Instabilities, and Failure*. *Encyclopedia of Computational Mechanics Second Edition*, Wiley.

Brinkgreve, R. (1994). “Geomaterial models and numerical analysis of softening.” Technische Universiteit Delft.

Burghardt, J., Brannon, R., and Guilkey, J. (2012). “A nonlocal plasticity formulation for the material point method.” *Computer Methods in Applied Mechanics and Engineering*, 225–228, 55–64.

Chen, W., and Qiu, T. (2014). “Simulation of earthquake-induced slope deformation using SPH

method." *International Journal for Numerical and Analytical Methods in Geomechanics*, 38(3), 297–330.

Conte, E., Silvestri, F., and Troncone, A. (2010). "Stability analysis of slopes in soils with strain-softening behaviour." *Computers and Geotechnics*, 37(5), 710–722.

Dey, R., Hawlader, B., Phillips, R., and Soga, K. (2015). "Large deformation finite-element modelling of progressive failure leading to spread in sensitive clay slopes." *Géotechnique*, 65(8), 657–668.

Eringen, A. C. (1981). "On nonlocal plasticity." *International Journal of Engineering Science*, 19(12), 1461–1474.

Galavi, V., and Schweiger, H. F. (2010). "Nonlocal multilaminate model for strain softening analysis." *International Journal of Geomechanics*, 10(1), 30–44.

Goodarzi, M., and Rouainia, M. (2017). "Modelling Slope Failure Using a Quasi-static MPM with a Non-local Strain Softening Approach." *Procedia Engineering*, 175, 220–225.

Jostad, H. P., and Grimstad, G. (2011). "Comparison of distribution functions for the nonlocal strain approach." *Computational Geomechanics, COMGEO II - Proceedings of the 2nd International Symposium on Computational Geomechanics*, Cavtat-Dubrovnik, Croatia, 212–223.

Van Leer, B. (1977). "Towards the ultimate conservative difference scheme. IV. A new approach to numerical convection." *Journal of Computational Physics*, 23(3), 276–299.

Loret, B., and Prevost, J. (1990). "Dynamic strain localization in elasto-(visco-)plastic solids, Part 1. General formulation and one-dimensional examples." *Computer Methods in Applied*

Mechanics and Engineering, 83(3), 247–273.

Lu, X., Bardet, J. P., and Huang, M. (2012). "Spectral analysis of nonlocal regularization in two-dimensional finite element models." *International Journal for Numerical and Analytical Methods in Geomechanics*, 36(2), 219–235.

Mallikarachchi, H., and Soga, K. (2020). "Post-localisation analysis of drained and undrained dense sand with a nonlocal critical state model." *Computers and Geotechnics*, 124, 103572.

Mánica, M. A., Gens, A., Vaunat, J., and Ruiz, D. F. (2018). "Nonlocal plasticity modelling of strain localisation in stiff clays." *Computers and Geotechnics*, 103, 138–150.

Monforte, L., Ciantia, M. O., Carbonell, J. M., Arroyo, M., and Gens, A. (2019). "A stable mesh-independent approach for numerical modelling of structured soils at large strains." *Computers and Geotechnics*, 116, 103215.

Qiu, G., Henke, S., and Grabe, J. (2011). "Application of a Coupled Eulerian-Lagrangian approach on geomechanical problems involving large deformations." *Computers and Geotechnics*, 38(1), 30–39.

Singh, V., Stanier, S., Bienen, B., and Randolph, M. F. (2021). "Modelling the behaviour of sensitive clays experiencing large deformations using non-local regularisation techniques." *Computers and Geotechnics*, 133, 104025.

Sluys, L. J. (1992). "Wave Propagation, Localisation and Dispersion in Softening Solids." Delft University of Technology.

Summersgill, F. C. (2014). "Numerical Modelling of Stiff Clay Cut Slopes with Nonlocal Strain Regularisation." Imperial College London.

Summersgill, F. C., Kontoe, S., and Potts, D. M. (2017a). “Critical assessment of nonlocal strain-softening methods in biaxial compression.” *International Journal of Geomechanics*, 17(7), 1–14.

Summersgill, F. C., Kontoe, S., and Potts, D. M. (2017b). “On the use of nonlocal regularisation in slope stability problems.” *Computers and Geotechnics*, 82, 187–200.

Tejchman, J., and Bauer, E. (1996). “Numerical Simulation of Shear Band Formation with a Polar Hypoplastic Constitutive Model.” *Computers and Geotechnics*, 19(3), 221–244.

Thakur, V. (2007). “Strain Localization in sensitive soft clays.” Norwegian University of Science and Technology.

Tvergaard, V., and Needleman, A. (1995). “Effects of nonlocal damage in porous plastic solids.” *International Journal of Solids and Structures*, 32(8–9), 1063–1077.

Vignjevic, R., Djordjevic, N., Gemkow, S., De Vuyst, T., and Campbell, J. (2014). “SPH as a nonlocal regularisation method: Solution for instabilities due to strain-softening.” *Computer Methods in Applied Mechanics and Engineering*, 277, 281–304.

Wilkins, M. L. (1963). “Calculation of elastic-plastic flow.” University of California Lawrence Radiation Lab, Livermore, California.

Wisselink, H. H., and Huetink, J. (2009). “Modelling of ductile failure in metal forming.” *7th European LS-DYNA Conference*, DYNAmore GmbH, Salzburg.

Zhang, X., Sheng, D., Sloan, S. W., and Bleyer, J. (2017). “Lagrangian modelling of large deformation induced by progressive failure of sensitive clays with elastoviscoplasticity.” *International Journal for Numerical Methods in Engineering*, 112(8), 963–989.

Zhu, Y. (2017). “Studies on Strain Localization, Ductile Fracture and Damage in Structural Metal.” The University of Texas at Austin.

CHAPTER 4

Effectiveness of softening-scaling rules of local and nonlocal methods in Eulerian-based large deformation finite element modeling

Co-Authorship: This chapter will be submitted as a technical paper for publication in a journal as: Chen, J., Hawlader, B., Roy, K. and Pike, K., "Effectiveness of softening-scaling rules of local and nonlocal methods in Eulerian-based large deformation finite element modeling."

Most of the research work presented in this chapter was conducted by the first author. He also prepared the draft manuscript. The other authors supervised the research and reviewed the manuscript.

4.1 Abstract

The finite element method can suffer from mesh dependency, especially during the development of shear bands, in the order of a few millimeters to centimeters, in strain-softening soils. An unrealistically fine mesh is required to capture such thin shear bands, which could dramatically increase the computational costs, especially for large-scale problems, such as retrogressive landslides. To address these problems, softening-scaling rules were implemented in local and nonlocal methods. Soil strength decreases with local shear strains in the former, while it varies with nonlocal strains (e.g., weighted average deviatoric plastic strain), in the latter methods. In the present study, the performance of softening-scaling in local and nonlocal approaches is compared, with a specific focus on large deformation. Numerical analyses are performed using a Eulerian-based FE program, which can model large strains in the shear band without any numerical

issues. Implementing strain-softening behaviour and a nonlocal method in this generalized FE program, two idealized cases are simulated: (1) biaxial compression test, (2) slope failure due to surface loading. FE results show that the shear band thickness increases with an increase in deformation after the peak loading conditions. The thickness of the shear band varies with element size in the local method, while it depends on 'internal length' in the nonlocal method. With softening scaling, both local and nonlocal methods give consistent and comparable load–displacement curves. For large deformation, the rate of increases in shear band thickness with loading is explained using energy concepts.

4.2 Introduction

Strain-softening occurs in many types of soils under drained or undrained loading conditions. The strain-softening of soil causes the progressive formation of thin shear bands (slip surfaces) in many engineering problems, e.g., sensitive clay landslides, which cannot be examined using the traditional limit equilibrium methods that are commonly used in geotechnical analysis. Finite element (FE) analysis can simulate the progressive formation of shear bands. However, mesh dependence is one of the main issues in FE modeling of a strain-softening material.

In the dynamic FE analysis, the mesh-dependency issues arise due to the ill-posed boundary value problem that converts the governing differential equations from hyperbolic into elliptical form. However, for static or quasi-static analysis, the mesh-dependency issue is caused by an ill-posed boundary value problem that loses ellipticity. For example, the dynamic equation for a

one-dimensional problem is hyperbolic for no softening conditions (Eq. (4.1)) while it is elliptical in the case of softening (Eq. (4.2)) (Bazant and Belytschko 1985; Chen et al. 1999).

$$\frac{E}{\rho} \cdot \frac{\partial^2 u}{\partial x^2} - \frac{\partial^2 u}{\partial t^2} = 0 \tag{4.1}$$

$$\frac{E'}{\rho} \cdot \frac{\partial^2 u}{\partial x^2} + \frac{\partial^2 u}{\partial t^2} = 0 \tag{4.2}$$

where E is the elastic modulus, ρ is the mass density, u is the displacement, x is the length coordinate, t is time, and E' is the softening modulus. For the static or quasi-static conditions, the governing equations before (Eq. (4.3)) and after (Eq. (4.4)) softening are:

$$E \cdot \frac{\partial^2 u}{\partial x^2} = 0 \tag{4.3}$$

$$E' \cdot \frac{\partial^2 u}{\partial x^2} = 0 \tag{4.4}$$

To minimize mesh-dependency of the FE solutions, several strain regularization techniques were proposed previously, e.g., an element size scaling method (Anastasopoulos et al. 2007; Pietruszczak and Mroz 1981), nonlocal method (Bažant and Lin 1988; Brinkgreve 1994; Conte et al. 2010; Galavi and Schweiger 2010), strain gradient method (de Borst and Mühlhaus 1992), and viscoplastic model (Prevost and Loret 1990). The element size scaling method in a local model considers the softening modulus proportional to the thickness of the finite element. In nonlocal regularization, the shear strength of an element is related to a weighted average value of strains of its surrounding elements. Both of these regularization techniques have been implemented in FE programs in previous studies (e.g., Anastasopoulos et al. 2007; Brinkgreve 1994; Galavi and Schweiger 2010; Pietruszczak and Mroz 1981). However, in-depth comparisons of the

performance of these two methods, especially for large-deformation geotechnical problems, are very limited.

Dey et al. (2015) used the element size scaling method; a Eulerian-based FE code was used to simulate large-scale landslides. A similar approach based on the size of the grid cell was also used in the Material Point Method (MPM) for large-deformation analysis (Tran and Sołowski 2019). In recent years, the trend of using nonlocal methods in different types of numerical codes has increased, such as in MPM (Burghardt et al. 2012), Point Finite Element Method (Monforte et al. 2019), and Eulerian-based FE (Chapter 3).

The shear band is extremely thin in real soil (Guo 2012). The computational costs to model an actual shear band in FE can be unrealistically high (Brinkgreve 1994). Previous studies showed that the shear band thickness is proportional to the element size and an internal length parameter in the local and nonlocal models, respectively (Anastasopoulos et al. 2007; Brinkgreve 1994; Galavi and Schweiger 2010). To obtain the same macroscopic response from modeling of a thicker shear band in FE analysis, a softening-scaling rule needs to be used for both local and nonlocal models. The softening-scaling rule in the nonlocal method defines the softening modulus proportional to the internal length parameter, similar to the element size in the local model (Brinkgreve 1994). Therefore, the element size scaling method can also be viewed as softening-scaling from the local modeling perspective.

Various approaches were used to define the shear band thickness, such as incremental displacement (Galavi and Schweiger 2010), and the distribution of the deviatoric strain rate (Maier 2003). A wide variation in FE calculated shear band thickness (t_{sFE}) was reported in the past; for

example, 1–7 times of the internal length in the nonlocal simulations of biaxial tests (Galavi and Schweiger 2010; Maier 2003). Mallikarachchi and Soga (2020) showed that the shear band thickness increases with loading. However, they did not continue the simulation over large displacements, potentially due to mesh distortion issues in their Lagrangian-based FE program. In addition, multiple shear bands might form in large-deformation problems (e.g., landslides). The interaction between them while calculating the weighted average nonlocal shear strains can also affect the simulation results. In summary, the following are the key questions related to strain regularization and large-deformation modeling:

(a) Does element size scaling in local and softening scaling in nonlocal methods give comparable results, as they are conceptually similar to some extent?

(b) What are the limitations of these methods and challenges in numerical modeling? At least it is known that most of the publicly available computer programs do not have built-in methods for nonlocal modeling. Also, computational costs can be an important factor.

(c) How applicable are these regularization techniques for large-deformation problems?

The present study aims to answer these questions through simulations of two idealized cases. This paper is organized as follows. First, an overview of Eulerian-based FE modeling and nonlocal methods is presented. Second, the softening-scaling rules in local and nonlocal simulations are discussed. Finally, a biaxial compression test and a slope failure are analyzed to compare both local and nonlocal softening-scaling methods.

4.3 Eulerian-based finite-element method

Traditional Lagrangian-based FE programs are not capable of modeling very large deformation in geotechnical problems, due to the significant mesh distortion around the failure planes and its resulting numerical instabilities (e.g., Griffiths and Lane 1999). In the present study, Eulerian-based FE method available in Abaqus/Explicit FE software is used. The soil is modeled as a Eulerian material that can 'flow' through the fixed mesh without causing numerical issues related to mesh distortion. Further details of the mathematical formulations of Eulerian-based FE approach and its applications to large-deformation quasi-static/dynamic problems are available in previous studies (Benson and Okazawa 2004; Dey et al. 2015). However, the software does not have any built-in technique for nonlocal regularization.

4.4 Nonlocal methods

Several studies show that the nonlocal method can better address mesh-dependency problems (de Borst et al. 1993; Sluys 1992), as the well-posedness of the boundary value problems can be restored (Bažant and Jirásek 2002). Various integral-type nonlocal methods have been proposed and implemented in FE programs. Among them, the original nonlocal method (Eringen 1981), the over-nonlocal method (Brinkgreve 1994), and the G&S nonlocal method (Galavi and Schweiger 2010) were widely used and validated (e.g., Conte et al. 2010; Jostad and Grimstad 2011; Mallikarachchi and Soga 2020). These three nonlocal methods have been implemented in conventional Lagrangian-based FE programs to simulate a biaxial compression test by Summersgill et al. (2017). An unstable response was observed when using the over-nonlocal

method with a fine mesh and the amplification factor, $\alpha \geq 2.0$, and the G&S nonlocal method was considered to be the most advantageous among the three. Although it was not explicitly mentioned, the instability could be caused by an excessive distortion of the Lagrangian elements, as large shear strains were generated in the shear band (Summersgill et al. 2017). However, Jostad and Grimstad (2011) showed that the over-nonlocal method is a preferable option for strain regularization.

The author developed algorithms and implemented these three nonlocal methods in Eulerian-based FE program in Abaqus software using user-defined subroutines. The details of the implementation are presented in Chapter 3. Similar to the work of Jostad and Grimstad (2011), the over-nonlocal method shows a better performance. Therefore, in this chapter, all the analyses are performed with the over-nonlocal method for further investigation of the effectiveness of this regularization, which is referred to as the nonlocal method only in this chapter. The governing equations for the over-nonlocal method are:

$$d\varepsilon^{\mathrm{p}}_{\mathrm{d(NL)}}(\mathbf{x}_{\mathrm{n}}) = (1-\alpha)d\varepsilon^{\mathrm{p}}_{\mathrm{d}}(\mathbf{x}_{\mathrm{n}}) + \frac{\alpha}{V_{\mathrm{w}}}\iiint \left[\omega(\mathbf{x}'_{\mathrm{n}})d\varepsilon^{\mathrm{p}}_{\mathrm{d}}(\mathbf{x}'_{\mathrm{n}})\right]dx'dy'dz' \tag{4.5}$$

$$\omega(\mathbf{x}'_{\mathrm{n}}) = \frac{1}{l\sqrt{\pi}}\exp\left[-\frac{|\mathbf{x}'_{\mathrm{n}} - \mathbf{x}_{\mathrm{n}}|^2}{l^2}\right] \tag{4.6}$$

$$V_{\mathrm{w}} = \iiint \omega(\mathbf{x}'_{\mathrm{n}})dx'dy'dz' \tag{4.7}$$

where $d\varepsilon^{\mathrm{p}}_{\mathrm{d(NL)}}(\mathbf{x}_{\mathrm{n}})$ is the nonlocal deviatoric plastic shear strain increment at location $\mathbf{x}_{\mathrm{n}}$, where the subscript *n* denotes the dimension of the model; α is the amplification factor to reduce the contribution of local strain to the nonlocal strain; $d\varepsilon^{\mathrm{p}}_{\mathrm{d}}(\mathbf{x}'_{\mathrm{n}})$ is the deviatoric plastic strain increment at location $\mathbf{x}'_{\mathrm{n}}$ which refers to the integration points in the radius of influence, as discussed later,

for the location $\mathbf{x}_n$, and ε_d^p is the deviatoric plastic strain (invariant), $\varepsilon_d^p = \sqrt{(\varepsilon_{p1} - \varepsilon_{p2})^2 + (\varepsilon_{p2} - \varepsilon_{p3})^2 + (\varepsilon_{p3} - \varepsilon_{p1})^2}$, where ε_{p1}, ε_{p2} and ε_{p3} are the principal components of plastic strains; $\omega(\mathbf{x}'_n)$ is a Gaussian-type weight function that is centered at the point $\mathbf{x}_n$ that defines the weight of all the reference points $\mathbf{x}'_n$ in the calculation of $d\varepsilon^p_{d(NL)}(\mathbf{x}_n)$; l is an internal length parameter that is related to the shear band thickness; V_w is the reference volume, where x', y' and z' are the three dimensions. The shape of an over-nonlocal weight function is shown in Fig. 4.1(a). The radius of influence (r_{inf}) is introduced to define the area of neighbour integration points to be considered for the nonlocal averaging of each element, as shown in Fig. 4.1(b).

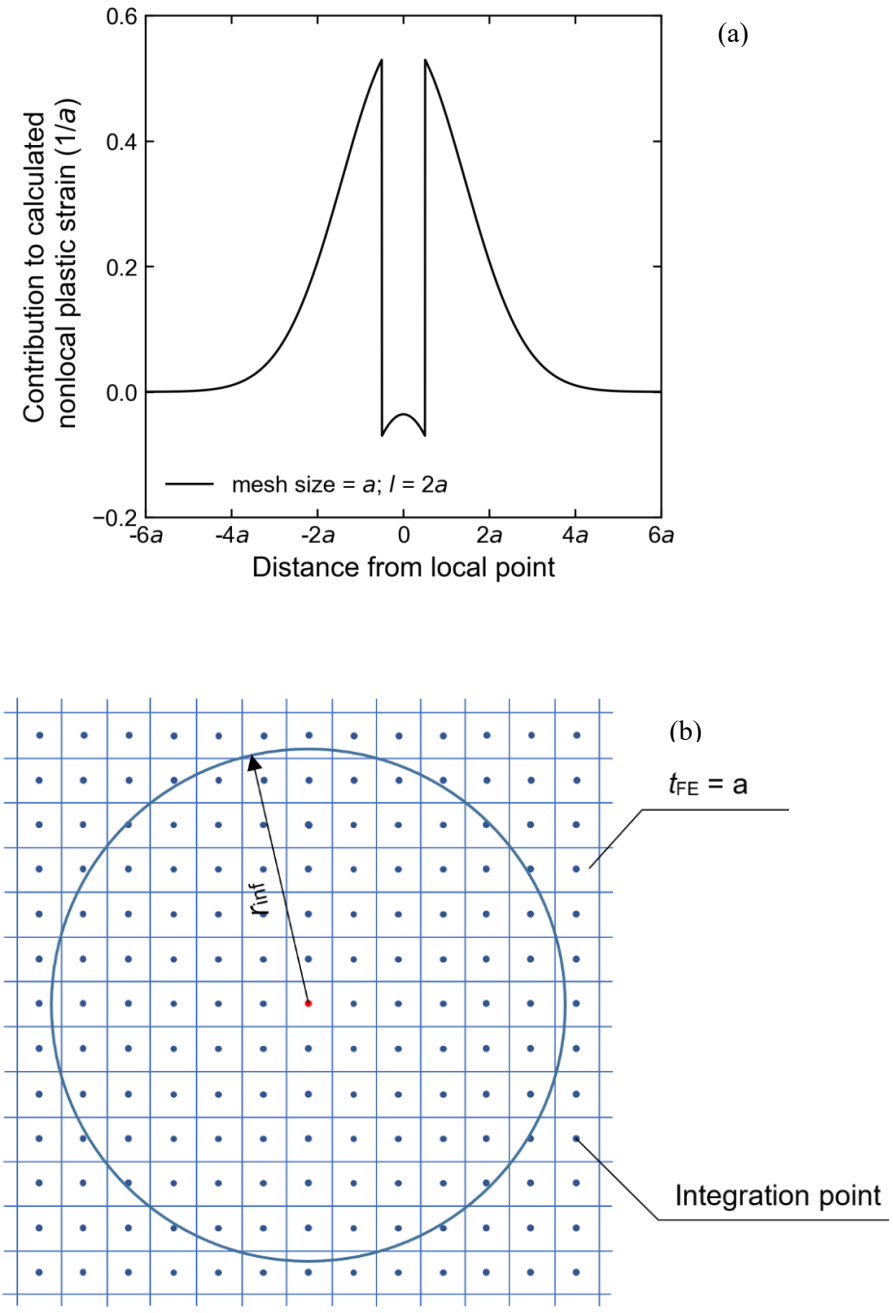

Figure 4.1 The over-nonlocal method in Eulerian-based FE: (a) schematic plot of the weight function; (b) the influencing area

4.5 Softening-scaling rule

Shear band thickness in an FE model (t_{sFE}), irrespective of local or nonlocal simulation, is usually larger than the real conditions. Therefore, the softening-scaling rule was introduced to FE programs to model the same macroscopic behaviour when the shear band thickness is significantly greater than the real condition (Anastasopoulos et al. 2007; Brinkgreve 1994; Pietruszczak and Mroz 1981). The main objective of the softening-scaling rule is to determine the post-peak shear strength reduction based on a scaled shear strain increment for the FE model, because a higher strain develops in a thinner shear band under the same shear displacement. Therefore, the scaled deviatoric plastic shear strain increment ($\Delta\varepsilon^{p}_{dFE}$) can be calculated as:

$$\Delta\varepsilon^{p}_{dFE} = \Delta\varepsilon^{p}_{ds} \cdot \frac{t_s}{t_{sFE}} \tag{4.8}$$

where $\Delta\varepsilon^{p}_{ds}$ is the deviatoric plastic shear strain increment in the shear band in real conditions; t_s is the shear band thickness in real conditions; t_{sFE} is the shear band thickness in the FE model.

In a local model, the strength reduction is determined by the local deviatoric plastic shear strain increment, $\Delta\varepsilon^{p}_{d(L)}$ (i.e., $\Delta\varepsilon^{p}_{dFE} = \Delta\varepsilon^{p}_{d(L)}$). Also, t_{sFE} is equal to the finite element size (t_{FE}), assuming a simple shear condition (Anastasopoulos et al. 2007; Dey et al. 2015). Therefore, Eq. (4.8) can be written as Eq. (4.9), which is also called "element size scaling" in local models.

$$\Delta\varepsilon^{p}_{d(L)} = \Delta\varepsilon^{p}_{ds} \cdot \frac{t_s}{t_{FE}} \tag{4.9}$$

Eulerian-based FE model is well-suited for the use of the element size scaling method. The mesh is fixed in a Eulerian-based FE model, which means that the t_{FE} remains the same at any

time point for each element. Therefore, any inaccuracy in the calculation of t_{FE}, and therefore $\Delta\varepsilon^{\mathrm{p}}_{\mathrm{d(L)}}$, can be avoided. If a uniform element size is used for the whole model (e.g., Dey et al. 2015), t_{FE} is a constant for every element. This makes the calculation of the $\Delta\varepsilon^{\mathrm{p}}_{\mathrm{d(L)}}$ more consistent using Eq. (4.9). In contrast, for a traditional Lagrangian-based FE model, the element size and the shape change when the soil deforms, leading to difficulties in computing t_{FE} and thus causing inaccuracy of $\Delta\varepsilon^{\mathrm{p}}_{\mathrm{d(L)}}$.

In a nonlocal model, the degradation of shear strength is proportional to the nonlocal deviatoric plastic shear strain increment ($\Delta\varepsilon^{\mathrm{p}}_{\mathrm{d(NL)}}$). However, the softening-scaling rule is based on the internal length parameter, instead of the element size, for the nonlocal methods (Brinkgreve 1994; Galavi and Schweiger 2010; Marcher 2003). Similar to Eq. (4.8), the softening-scaling rule for a nonlocal method can be written as:

$$\Delta\varepsilon^{\mathrm{p}}_{\mathrm{d(NL)}} = \Delta\varepsilon^{\mathrm{p}}_{\mathrm{ds}} \cdot \frac{l_{\mathrm{s}}}{l} \tag{4.10}$$

where l_{s} and l are the internal length parameters of the soil and nonlocal FE model, respectively (Maier 2003; Galavi and Schweiger 2010). A detailed methodology on how the internal length parameter in the nonlocal methods contributes to the softening-scaling can be found in Chapter 3.

4.6 Numerical simulations

The implementation of nonlocal methods in Eulerian-based FE and the comparison of its performance with other local methods have been presented in Chapter 3. Note that, in Chapter 3, the von Mises criterion is adopted while the analyses in the current chapter are performed by

adopting the Tresca failure criterion. The implementation techniques, including the algorithms, are very similar for both failure criteria; therefore, the details of numerical implementation are not repeated here. The following two cases are considered to show the effectiveness of the local and nonlocal models, with the use of softening scaling, for strain regularization and the modeling of macroscopic behaviour.

Case 1: Several studies simulated biaxial compression tests to show the effectiveness of strain localization, because the shear band formation occurs in a similar pattern, independent of the mesh size (Brinkgreve 1994; Lu et al. 2012; Summersgill et al. 2017). In some studies, a small zone or an element of weaker material is incorporated to induce shear band formation and propagation (e.g., Burghardt et al. 2012; Mánica et al. 2018). In case 1 of the present study, a weightless soil block of 4 m × 5 m in-plane is modelled, where a weaker zone of 1 m × 1 m at the bottom left corner is considered, from which shear band formation is triggered (Fig. 4.2(a)). The dimension of the block is similar to that used by Burghardt et al. (2012) who implemented nonlocal MPM to simulate the failure.

Case 2: In this case, the failure of the sensitive clay slope (2H:1V) due to upslope loading is modeled (Fig. 4.2(b)). The main purpose of this case is to examine the effects of a stress state along a curved shear band, such as in the direction of principal stresses.

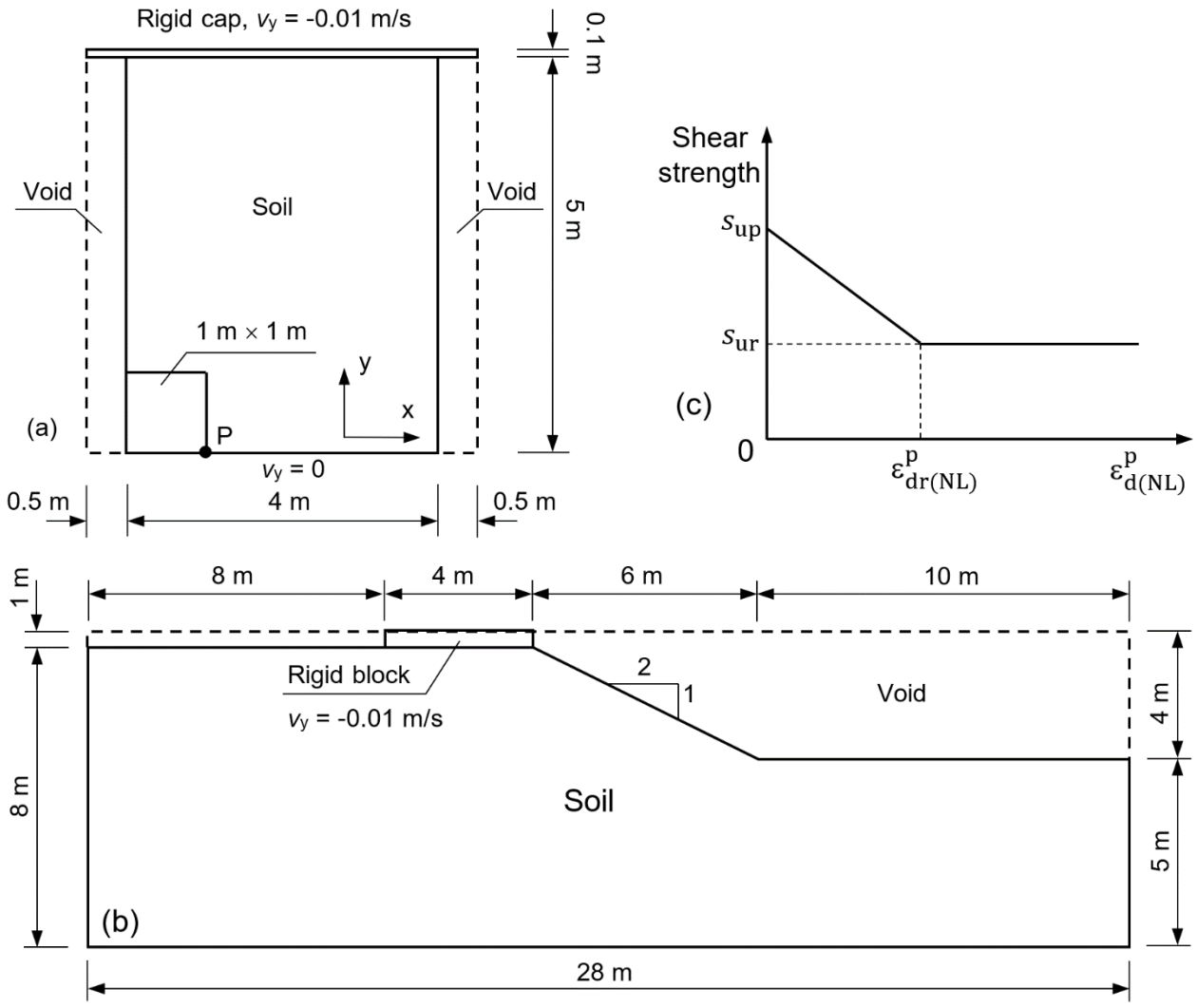

Figure 4.2 (a) Geometry and boundary conditions of case 1; (b) geometry and boundary conditions of case 2; (c) stress–strain curve of soil

4.6.1 FE model development

The numerical analysis is performed using the Coupled Eulerian–Lagrangian (CEL) approach available in Abaqus/Explicit FE software. In this software, the Eulerian approach has been implemented only for three-dimensional elements. Therefore, the analyses are performed with only one element length in the out-of-plane direction to simulate the plane strain condition.

Eulerian domains of 5.0 m × 5.1 m and 8.0 m × 28.0 m in-plane are created for case 1 and case 2, respectively (Fig. 4.2). The domains of both cases are discretized into 0.25 m, 0.125 m, and 0.0625 m cubical eight-node linear brick elements (EC3D8R in the software). The Eulerian volume fraction (*EVF*) is used to define the material; $EVF = 1$ and $0 \leq EVF \leq 1$ mean the elements are fully and partially filled with soil, respectively, while the rest of the domain is void ($EVF = 0$). The loading caps at the top (Figs. 4.2(a) and 4.2(b)) are first discretized using Lagrangian elements and then transferred to a rigid body.

4.6.2 Modeling of soils

Analyses are performed for both case 1 and case 2 for three scenarios: (i) without mesh regularization, (ii) with element size scaling, and (iii) with the nonlocal method of regularization. A linear post-peak degradation of undrained shear strength (s_u) with deviatoric plastic strain (ε_d^p) is used (Fig. 4.2(c)). The pre-peak stress–strain behaviour is modeled as linear elastic materials using the undrained Young's modulus (E_u) and Poisson's ratio (ν_u). In case 1, s_u decreases linearly from the peak value (s_{up}) of 100 kPa to the residual value (s_{ur}) of 50 kPa at $\varepsilon_d^p = \varepsilon_{dr}^p$. For nonlocal modeling, $\varepsilon_d^p = \varepsilon_{d(NL)}^p$, (Eq. (4.5)) is used for s_u degradation, as shown in Fig. 4.2(c), while for local modeling, it is calculated based on the local ε_d^p ($\varepsilon_{dr(L)}^p$). This implies that strength degradation occurs slowly in the shear bands for the nonlocal method, as compared to the local method, because $\varepsilon_{d(NL)}^p$ includes the effects of lower strains in the surrounding soil elements of the element in the shear band. In the nonlocal method, the internal length parameter (l) primarily controls the thickness of the shear band (t_{sFE}). In the first set of analyses, $l = 0.25$ m is used (Table

4.1). A set of nonlocal analyses with l = 0.25 m and local analyses with 0.25-m mesh are found to result in a similar post-peak load–displacement curve for the biaxial test (case 1) when $\varepsilon^{p}_{dr(L)}$ for local analysis is approximately $2\varepsilon^{p}_{dr(NL)}$. The shear band thickness is almost independent of mesh size in the nonlocal analysis for a given l. However, it is almost proportional to mesh size in the local method. Therefore, ε^{p}_{dr} for local (element size scaling) analysis for varying mesh sizes can be estimated as:

$$\varepsilon^{p}_{dr(L)} = 2\varepsilon^{p}_{dr(NL)}\left(\frac{l}{t_{FE}}\right) \tag{4.11}$$

Analyses are also performed without element size scaling, where $\varepsilon^{p}_{dr(L)} = 2\varepsilon^{p}_{dr(NL)}$ is used. The peak and residual shear strength of the soil in the weaker corner are 50 kPa and 25 kPa, respectively. However, it follows the similar strain-softening behaviour of the soil in the other part. For case 2, the peak and residual shear strengths increase with depth (z, in meter, measured from the ground surface) as 15 + 1.8z and 6 + 0.72z, respectively. For case 1, $\varepsilon^{p}_{dr(NL)}$= 15% is used, following Summersgill et al. (2017). A slightly more brittle soil is used for case 2 (i.e., $\varepsilon^{p}_{dr(NL)}$= 10%). Table 4.1 shows the mesh size and the soil parameters used in FE simulations. The internal length parameter in a nonlocal analysis should not be less than the element size (Summersgill et al. 2017) and therefore, l = 0.25 m is used in the first set of analyses, which equals the largest element size in this study. Analyses are performed for amplification factors (α) of 1.2, 1.5, 2.0, 2.5, and 3.0, for case 1, to show its effects on the simulation results. For case 2, α = 2.0 is used, as it shows better performance in case 1 simulation and was also suggested by previous authors (Jostad and Grimstad 2011; Vermeer and Brinkgreve 1994).

Table 4.1 Parameters used in FE simulations

	case 1	case 2
Element size, t_{FE} (m)	0.25, 0.125, 0.0625	0.25, 0.125, 0.0625
Young's modulus, E_u (GPa)	50	7.5
Poisson's ratio, ν_u	0.495	0.495
Peak undrained shear strength, s_{up} (kPa)	100 (50*)	15 + 1.8z
Residual undrained shear strength, s_{ur} (kPa)	50 (25*)	6 + 0.72z
Residual deviatoric plastic strain for nonlocal analysis, $\varepsilon^p_{dr(NL)}$ (%)	15	10
Internal length parameter, l (m)	0.25	0.25
Amplification factor, α	1.2, 1.5, 2.0, 2.5, 3.0	2.0

Note: *values in () are for the weak zone in case 1

Table 4.2 shows the soil parameters used to examine the efficacy of softening scaling in the nonlocal method. The analysis with l = 0.25 m and $\varepsilon^p_{dr(NL)}$ = 15% is considered for the base case. To reproduce the same macroscopic behaviour, different values of $\varepsilon^p_{dr(NL)}$ are selected for each internal length parameter based on the softening-scaling rule, as listed in Table 4.2. For comparison, internal length parameters l = 0.125 m and 0.0625 m are implemented without softening scaling for case 1. This is to adopt the same $\varepsilon^p_{dr(NL)}$ while different internal length parameters are implemented, as shown in Table 4.2. As previously discussed, the value of α is chosen to be 2.0. The element size 0.0625 m is used for all the nonlocal models. The other parameters remain the same as in Table 4.1.

Table 4.2 Input data for the study of softening scaling for the over-nonlocal method

	Case 1		Case 2
	No softening scaling	Softening scaling	Softening scaling
Residual plastic deviatoric strain, $\varepsilon^{p}_{dr(NL)}$ (%)	15	3.75/l	2.5/l
Internal length parameter, l (m)	0.0625, 0.125	0.0625, 0.125, 0.25, 0.5, 1.0	0.0625, 0.125, 0.25

4.6.3 Results

4.6.3.1 Mesh convergence in case 1 simulations

The advantages and limitations of the three methods (no regularization, element size scaling, and nonlocal) are discussed based on failure patterns (Fig. 4.3) and load–displacement curves (Fig. 4.4). Figure 4.3 shows the local deviatoric plastic strains ($\varepsilon^{p}_{d(L)}$) in the soil block for 0.2-m vertical displacement of the loading cap (δ_v). The failure initiates through strain concentration at the bottom right corner of the weaker soil (point P in Fig. 4.2(a)). Two shear bands form in all cases, a shorter one at the lower-left corner in the weaker soil and a longer one through the other soil. The locations of the shear bands are mesh-dependent when no regularization is applied (Fig. 4.3(a)). The left shear band becomes longer, and the length of the right shear band decreases with a decrease in the mesh size. A possible reason could be that the shear strength drops at a faster rate under the same shear displacement with a finer mesh. This could induce a smaller energy dissipation (Mánica et al. 2018) and a different stress redistribution. Note that the dissipated energy equals the external work in this quasi-static problem (i.e., the area under the load–displacement curve). Previous studies also showed that the location and thickness of the shear

band can be mesh-dependent in a local model without strain regularization (e.g., Summersgill et al. 2017; Liu and Li 2019). A more brittle load–displacement curve is found with a finer mesh (Fig. 4.4(a)). This is also a piece of evidence for less energy dissipation (Mánica et al. 2018).

The element size scaling and nonlocal methods give mesh independent shear band locations (Figs. 4.3(b)–4.3(g)). Note that the shear band thickness is still dependent on the mesh size when using element size scaling (Fig. 4.3(b)). This is in line with the observation of many other studies (e.g., Anastasopoulos et al. 2007; Dey et al. 2015). As mentioned in Section 4.5, the shear band thickness is dependent on the internal length parameter in a nonlocal model. The mesh dependence of shear band thickness becomes marginal in nonlocal methods (Figs. 4.3(c)–4.3(g)). However, the shear band thickness in the nonlocal model is too large compared to real situations. Figures 4.3(c)–4.3(g) also show that the shear band thickness is larger for higher values of α because of increasing nonlocal strains outside of the central area of the shear band, while its value decreases in the central part (Summersgill et al. 2017).

The mesh dependency and the effect of α are further explored with the load–displacement curves. Figure 4.4(b) displays the load–displacement curves with element size scaling, and Figs. 4.4(c)–4.4(g) show the load–displacement curves of different mesh sizes with α = 1.2, 1.5, 2.0, 2.5 and 3.0. The load–displacement curves are mostly mesh independent for both the element size scaling and nonlocal methods (Figs. 4.4(b)–4.4(g)). Note that the load–displacement curves and energy dissipation become mesh independent by adjusting the softening modulus for each mesh size in the element size scaling method, and by implementing the internal length parameter in the nonlocal method. The load–displacement behaviour becomes more ductile with a larger value of

α, due to a smaller increase rate of nonlocal strain (Eq. (4.5)) and thus causes a slower strength reduction at the central part of the shear band. Figure 4.4(h) presents the load–displacement curves of the nonlocal models with different values of α and the local models of 0.25-m mesh with $\varepsilon^{p}_{dr(L)}$ = 15% and 30%. The load–displacement curve of $\varepsilon^{p}_{dr(L)}$ = 30% of the local model is close to the curves of α = 2.0, 2.5, and 3.0 of the nonlocal models with $\varepsilon^{p}_{dr(NL)}$ = 15% (Fig. 4.4(h)). This is in line with Eq. (4.11) which is used for the comparison between the local and nonlocal methods.

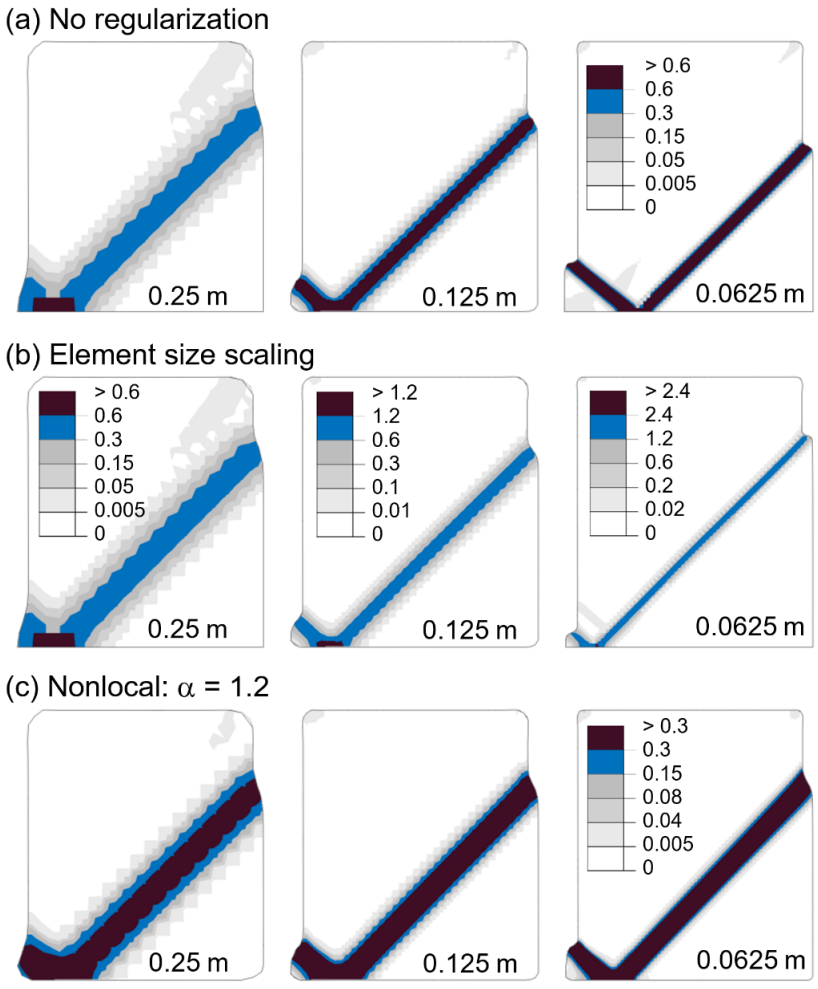

Figure 4.3 Local deviatoric plastic strain contours from three methods with different mesh sizes (case 1): (a) local model; (b) element size scaling; (c–g) nonlocal (α = 1.2–3.0)

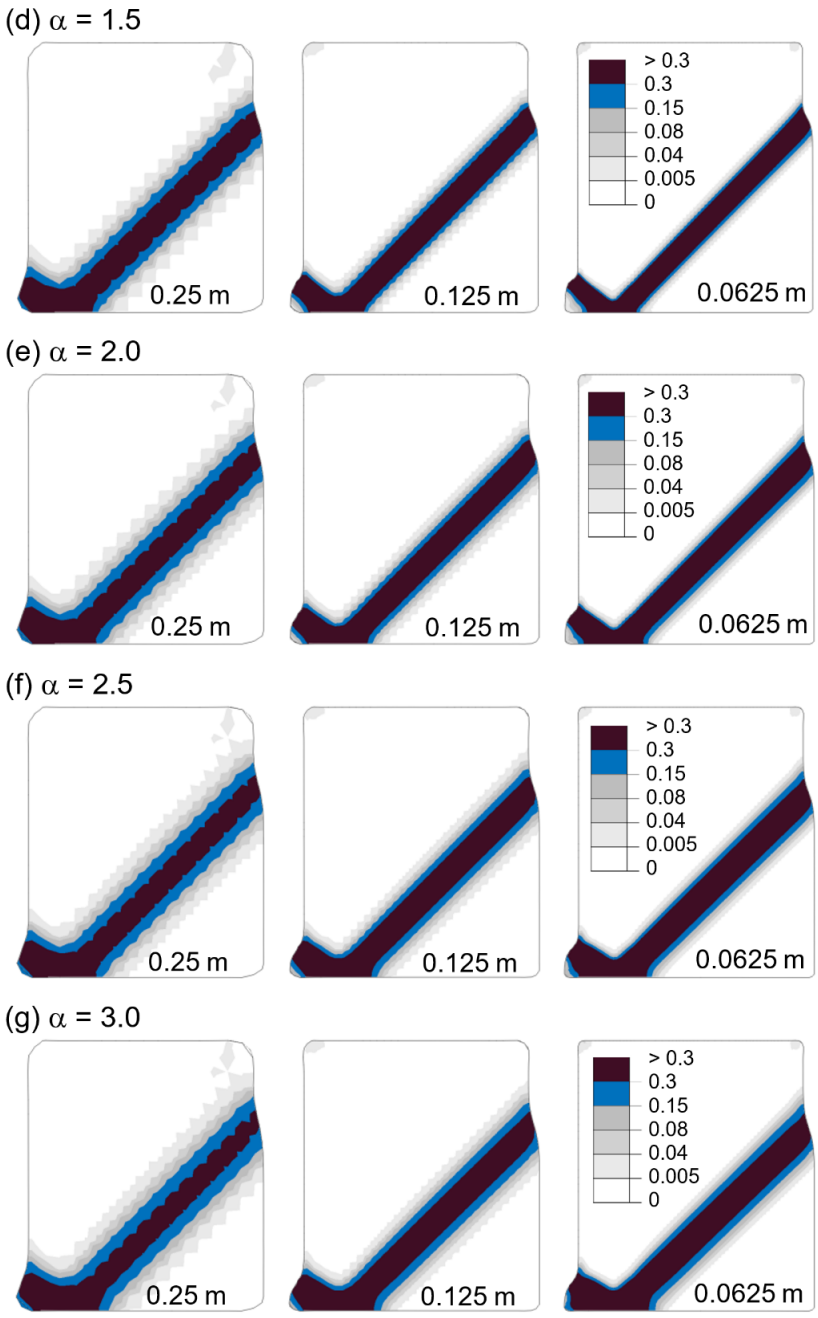

Figure 4.3 continued

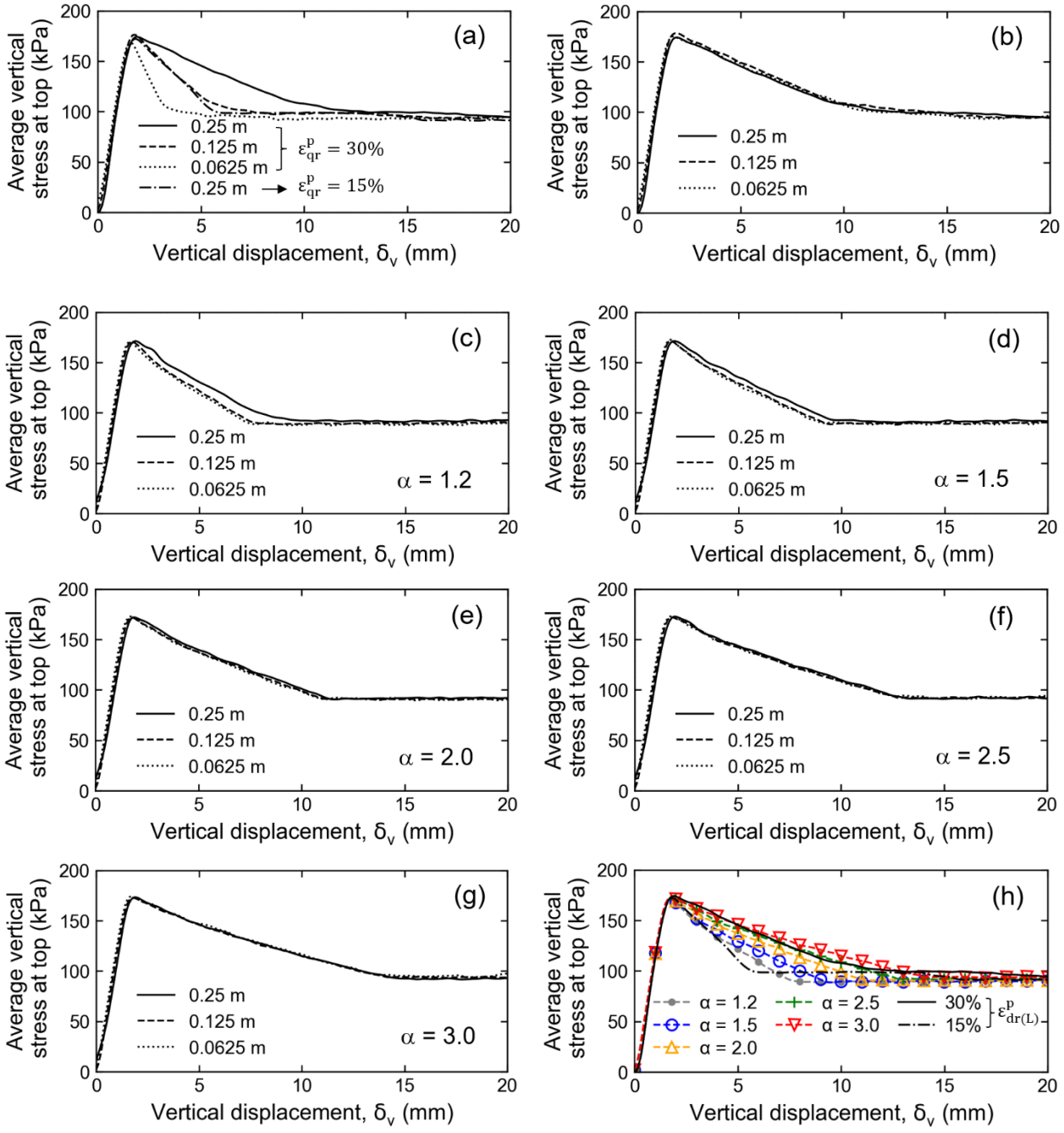

Figure 4.4 Load–displacement curves with three mesh sizes (case 1): (a) local model; (b) element size scaling; (c–g) nonlocal (α = 1.2–3.0); (h) comparison between nonlocal and local analyses

4.6.3.2 Effects of softening scaling for case 1

The softening-scaling rule allows modeling of macroscopic behaviour while using larger mesh and also internal length parameters in a nonlocal model. The deviatoric plastic strain contours (Figs. 4.3(b) and 4.5) and the load–displacement curves (Figs. 4.4(b) and 4.6) are used to validate the efficacy of the softening-scaling rule for the local and nonlocal methods.

For local models, Figs. 4.3(b) and 4.4(b) show that the shear band location and the load–displacement curves do not change with the element size. However, they are different for different mesh sizes when the softening-scaling rule is not used (Figs. 4.3(a) and 4.4(a)). Also, for nonlocal models, analyses are performed with and without the softening rule for varying internal lengths (Table 4.2). Figure 4.5 shows the local deviatoric plastic strain contours of these models at the vertical displacement of 0.2 m. The location of the shear band remains nearly unchanged for all the models (with or without softening scaling), and the shear band thickness is dependent on the internal length parameter. In addition, Fig. 4.6 presents the load–displacement curves of the nonlocal models with softening scaling. This figure shows that similar macroscopic behaviour can be simulated when the softening scaling rule is used in a nonlocal model. Therefore, the softening-scaling rule is effective for the nonlocal method in Eulerian-based FE. However, it is worth noting that the shear band thickness in Fig. 4.5(g) is slightly larger than Fig. 4.5(e). Both figures show nonlocal models with an internal length parameter of 0.0625 m, while no softening scaling is implemented for the model of Fig. 4.5(g), which means the $\varepsilon^{p}_{dr(NL)}$ for Fig. 4.5(g) is only a quarter of the value for Fig. 4.5(e). Further discussion on shear band thickness is provided in Section 4.7.1.

In the local model, t_{FE} does not exceed 0.25 m, to maintain a sufficient number of elements in the strain concentrated zones. In the nonlocal models, a large value of l (e.g., 0.5 m, 1.0 m) is also unacceptable due to an extremely thick shear band (Figs. 4.5(a) and 4.5(b)). Furthermore, in a nonlocal model with multiple shear bands, such thick shear bands may influence each other profoundly, leading to a questionable failure pattern. More details of this influence are discussed in Section 4.6.3.4.

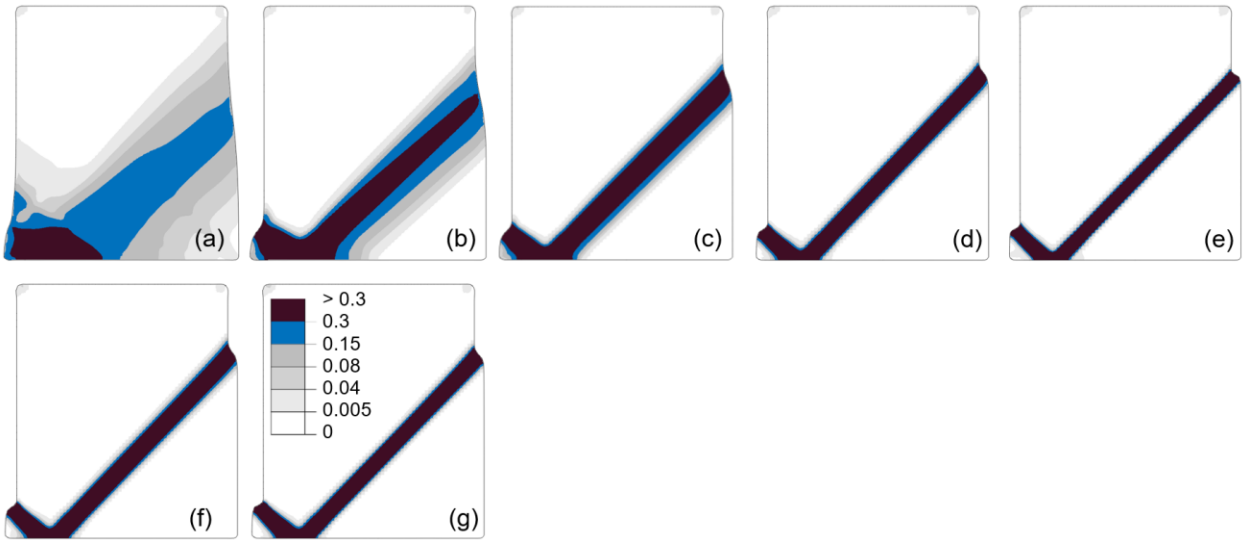

Figure 4.5 Local deviatoric plastic strain contours for nonlocal models (t_{FE} = 0.0625 m): (a) l = 1.0 m; (b) l = 0.5 m (softening scaling); (c) l = 0.25 m (base); (d) l = 0.125 m (softening scaling); (e) l = 0.0625 m (softening scaling); (f) l = 0.125 m (no softening scaling); (g) l = 0.0625 m (no softening scaling)

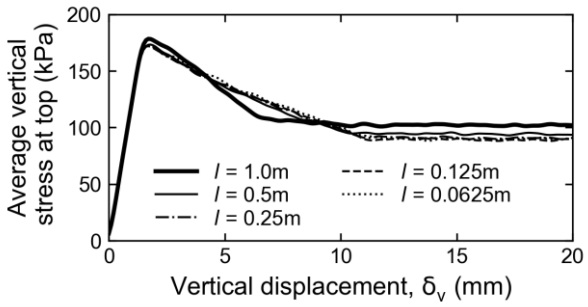

Figure 4.6 Load–displacement for nonlocal models with softening scaling (t_{FE} = 0.0625 m)

Figure 4.7 shows the load–displacement curves with various element sizes (t_{FE}) for the local models and various internal length parameters (l) for nonlocal models when softening scaling is not adopted. That means, $\varepsilon^{p}_{dr(NL)} = 15\%$ and $\varepsilon^{p}_{dr(L)} = 30\%$ for the nonlocal and local models, respectively, are used for all the mesh sizes. This figure aims to further validate Eq. (4.11) and show an analogy between local and nonlocal methods. This figure shows that the load–displacement curves from local and nonlocal models are comparable when satisfying Eq. (4.11). The post-peak curves have a similar slope before the reaction loads reach the residual state. However, Fig. 4.7 also shows a gap between the residual reaction loads of the local and nonlocal models, which might be attributed to the different nature of local and nonlocal models. In a local model, the t_{FE} is used for both strain regularization and macroscopic behaviour modeling; nevertheless, l is only used for macroscopic modeling for the nonlocal method. Therefore, the influence of t_{FE} can be excluded in a nonlocal model.

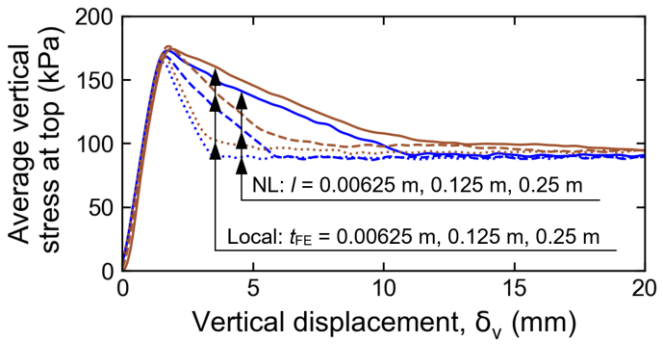

Figure 4.7 Load–displacement curves of local and over-nonlocal models without scaling

4.6.3.3 Mesh convergence in case 2

In the biaxial tests (case 1), primarily only one linear shear band forms. However, in real life, multiple shear bands might form, and the shear band can be a curved shape. Therefore, strain accumulation around one shear band might affect another one. In addition, the stress state varies along the curved shear band. For example, a segment of the shear band might be in plane strain compression conditions while some segments can be in direct simple shear or other conditions. These factors are examined from the simulation results of case 2.

Figure 4.8 shows the failure pattern when the loading block moves 0.2 m vertically. The major shear band propagates from the lower-left corner of the rigid block and ends at the toe of the slope. Another shear band starts from the lower right corner of the rigid block and finally reaches the major shear band during the failure process. The size and shape of the sliding blocks are similar with or without strain regularization. The deviatoric plastic strain, and thereby the strength reduction, are higher for finer mesh in the simulations without regularization (Figs. 4.8(a)–4.8(c)), which is due to a rapid increase in shear strain in finer mesh for the same shear displacement.

Similar to biaxial test simulations, as discussed in Section 4.6.3.1, the shear band thickness (t_{sFE}) increases with mesh size (t_{FE}) in these local models (Figs. 4.8(a)–4.8(f)). In addition, t_{sFE} varies with an inclination of the failure plane, and t_{sFE} is minimal at the bottom of the sliding surface, where the failure occurs along a horizontal plane under direct simple shear conditions (e.g., point Q in Fig. 4.8(d)). At this segment of the failure plane, the convection of material in the Eulerian step mainly occurs in a single row of elements with a limited amount of strain remapping to surrounding rows of elements. However, in the other inclined segments of the shear band, larger convection of the Eulerian material (soil) widens the shear band (e.g., points P and R in Fig. 4.8(d)).

The failure pattern with element size scaling (Figs. 4.8(d)–4.8(f)) is similar to that simulated without regularizations (Figs. 4.8(a)–4.8(c)). However, the generated strains are different (e.g., in Figs. 4.8(b) and 4.8(e)). The effects of strain variation within the shear band affect the load–displacement curves, as discussed later (Fig. 4.9). In comparison, the shear band thickness in the nonlocal model barely changes with different mesh sizes and shear modes for given values of α (= 2.0) and l (=0.25 m) (Figs. 4.8(g)–4.8(i)). The influence of the shear mode on strain accumulation and shear band thickness is further discussed in Section 4.7.1.4.

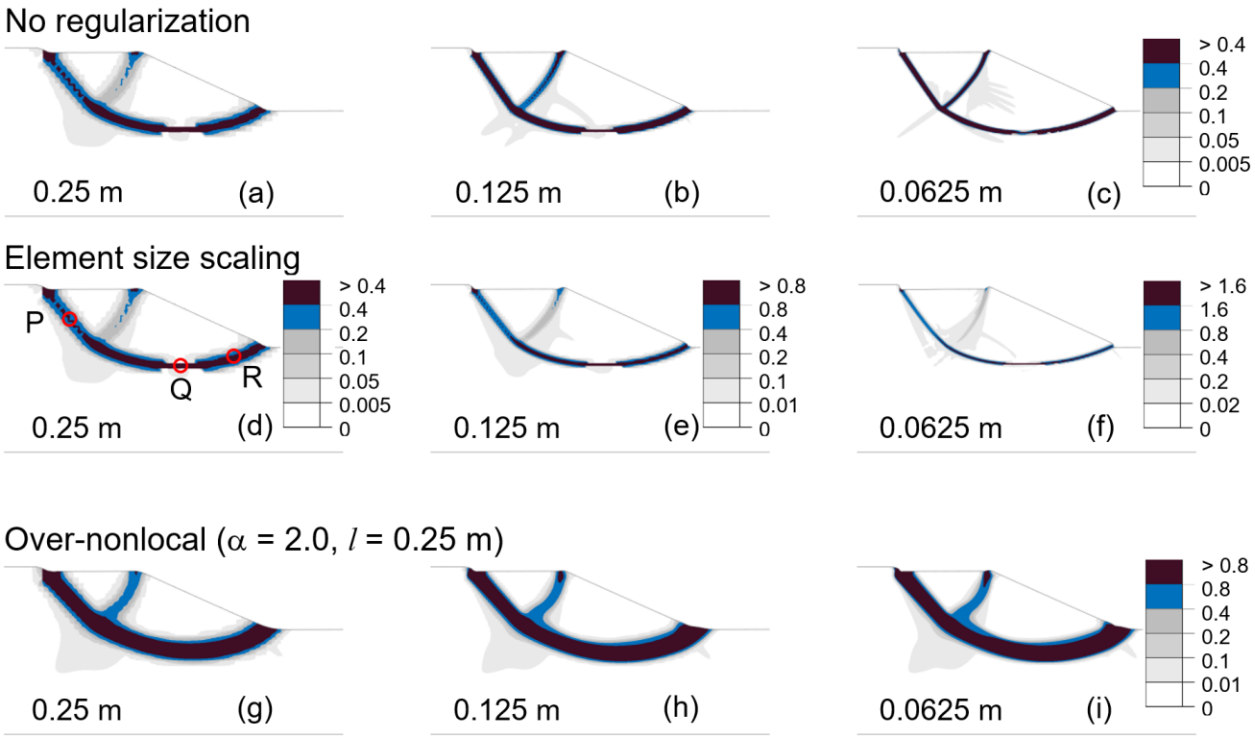

Figure 4.8 Local deviatoric plastic strain contours of three methods with different mesh sizes

Figure 4.9 shows the variation of average vertical pressure on the soil from the rigid block with its displacement. The load–displacement curve shows a significant mesh dependency near the peak and post-peak degradation when no regularization is used (Fig. 4.9(a)). For a finer mesh, the reaction load reaches a lower peak and drops more rapidly after the peak. Again, it is due to a quick decrease in strength with increasing plastic shear strain for a finer mesh. This could even lead to a temporary zero reaction load before reaching the residual state for the finest mesh (Fig. 4.9(a)), which is due to a slower movement of the loading cap than the sliding soil block. However, if strain regularization is used, the load–displacement curves become independent of mesh size (Figs. 4.9(b) and 4.9(c)). Both element size scaling and nonlocal methods can reduce mesh sensitive issues

significantly. Moreover, the load–displacement curves are comparable for the analyses using both regularization methods, with a minor difference between their residual resistance (Fig. 4.9(d)). A possible reason for this gap at large displacement can be the slight difference in the shape of the sliding block. A horizontal segment forms at the bottom of the major shear band in the local models (Figs. 4.8(a), 4.8(b) and 4.8(d)–4.8(f)). This can produce a higher resistance than the curved slip surface shown in the nonlocal model (Figs. 4.8(g)–4.8(i)). In the model with 0.0625-m mesh in the local model without regularization ((Fig. 4.8(c)), the horizontal segment is neglectable. The residual reaction load of this model is nearly identical to the nonlocal model (Fig. 4.9(d)). This can be evidence of the influence of the horizontal segment on the reaction load.

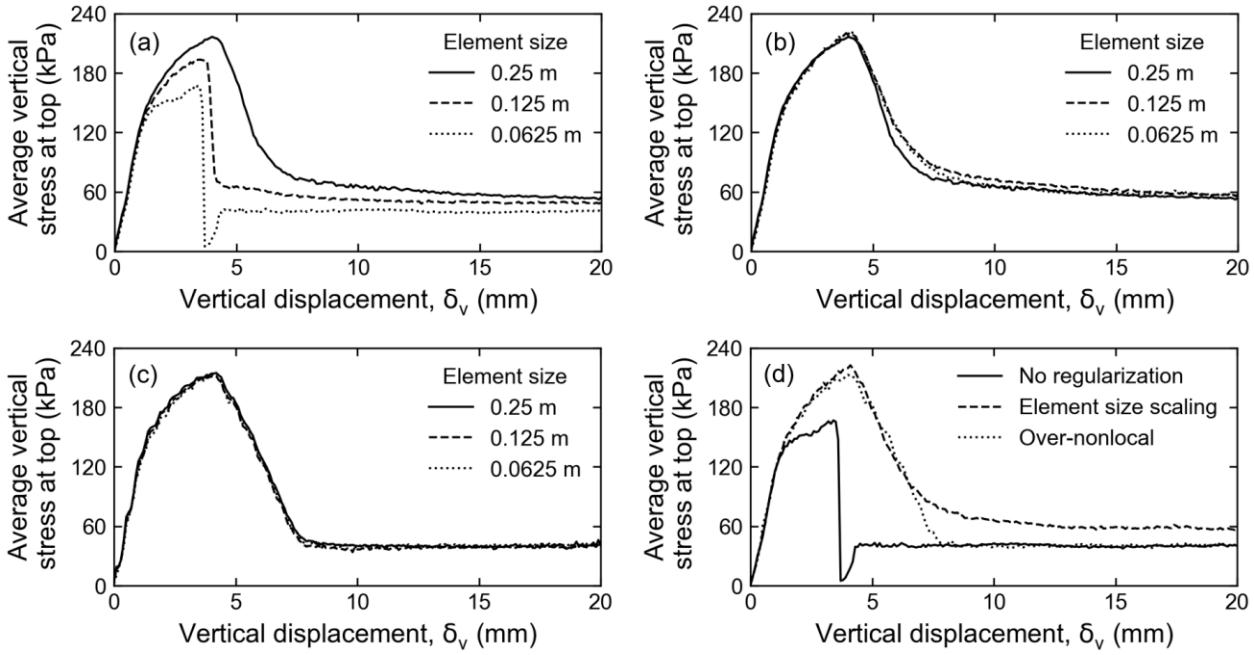

Figure 4.9 Load–displacement curves: (a) local model; (b) element size scaling; (c) over-nonlocal; (d) comparison of three methods with t_{FE} = 0.0625 m

4.6.3.4 Effect of softening scaling for case 2

The softening scaling in a local model (i.e., element size scaling) is proven to be effective in strain regularization, as shown in Figs. 4.8(d)–4.8(f) and 4.9(b). In other words, the macroscopic load–displacement behaviour can be modeled by using a coarse mesh (e.g., 0.25-m mesh for case 2). This can reduce the computational cost significantly.

As shown in Figs. 4.8(g)–4.8(i), the shear band of the nonlocal models is very thick, which is significantly larger than the real condition. The effectiveness of the nonlocal model becomes in doubt as the shear band is too thick (e.g., Figs. 4.5(a) and 4.5(b)). Therefore, only three internal lengths, 0.25 m, 0.125 m, and 0.0625 m are chosen for three over-nonlocal models with the $\varepsilon^{p}_{dr(NL)}$ = 10%, 20%, and 40%, respectively, based on the softening scaling so that different thicknesses of the shear band can be modeled. A uniform mesh size of 0.0625 m is adopted in all three models. Figure 4.10 shows that the shear band thickness decreases almost proportionally to the decrease of the internal length parameter, while the locations of the shear bands and the shape of the sliding blocks remain unchanged. In addition, the load–displacement curves are nearly identical for the three cases (Fig. 4.11). Therefore, the softening scaling is also effective for modeling the macroscopic behaviour with the nonlocal method for case 2.

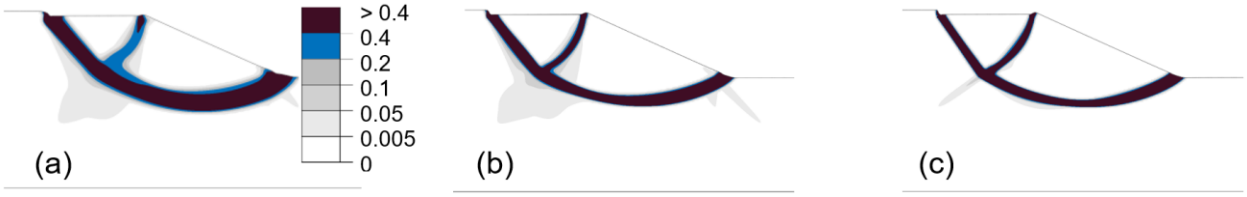

Figure 4.10 Local deviatoric plastic strain contours of over-nonlocal models with softening scaling: (a) l = 0.25 m; (b) l = 0.125 m; (c) l = 0.0625 m

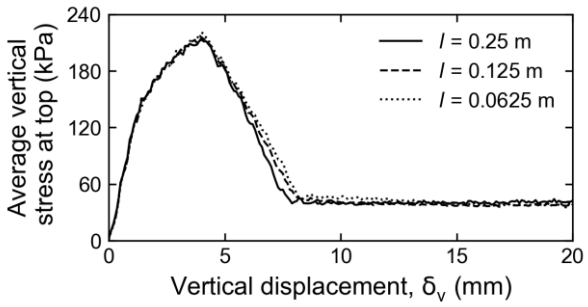

Figure 4.11 Load–displacement curves of over-nonlocal models with softening scaling

Multiple shear bands might form in a landslide—for example, progressive failure of several soil blocks occurs in a spread in a sensitive clay slope (Dey et al. 2015). The direction of shear band propagation can affect failure patterns due to the progressive nature of the failure. Therefore, the effects of local and nonlocal models on the propagation of multiple shear bands need to be examined. The scenario of two shear bands existing in case 2 is discussed in this study.

For a nonlocal model, the shear strength of soil near a shear band is reduced by the nonlocal averaging, and the energy can be distributed outside of the shear band. In other words, two shear bands can affect each other when they are close enough. Figure 4.12(a) shows the local deviatoric plastic shear strain of the local model and Figs. 4.12(b) and 4.12(c) present the nonlocal deviatoric plastic shear strains of the nonlocal models with internal length parameters of 0.25 m and 0.125 m. The strength reduction can be reflected from these figures because the local strain and nonlocal strain control the shear strengths in the local and nonlocal models, respectively. With the increase of vertical displacement of the loading cap, an excessive reduction of strength can be eventually seen at the lower end of the minor shear band (which is adjacent to the intersection between the

minor and major shear bands) in the nonlocal models (Figs. 4.12(b) and 4.12(c)). This is not observed in the local model (Fig. 4.12(a)). As a result, a more significant deformation occurs at the intersection area in the nonlocal models, and the larger the internal length parameter is, the higher local deviatoric plastic shear strain can be observed at this area (Fig. 4.13). Further research needs to be conducted to understand this effect for larger-scale problems, such as a spread-type sensitive clay landslide, where many shear band formations at different inclinations are expected.

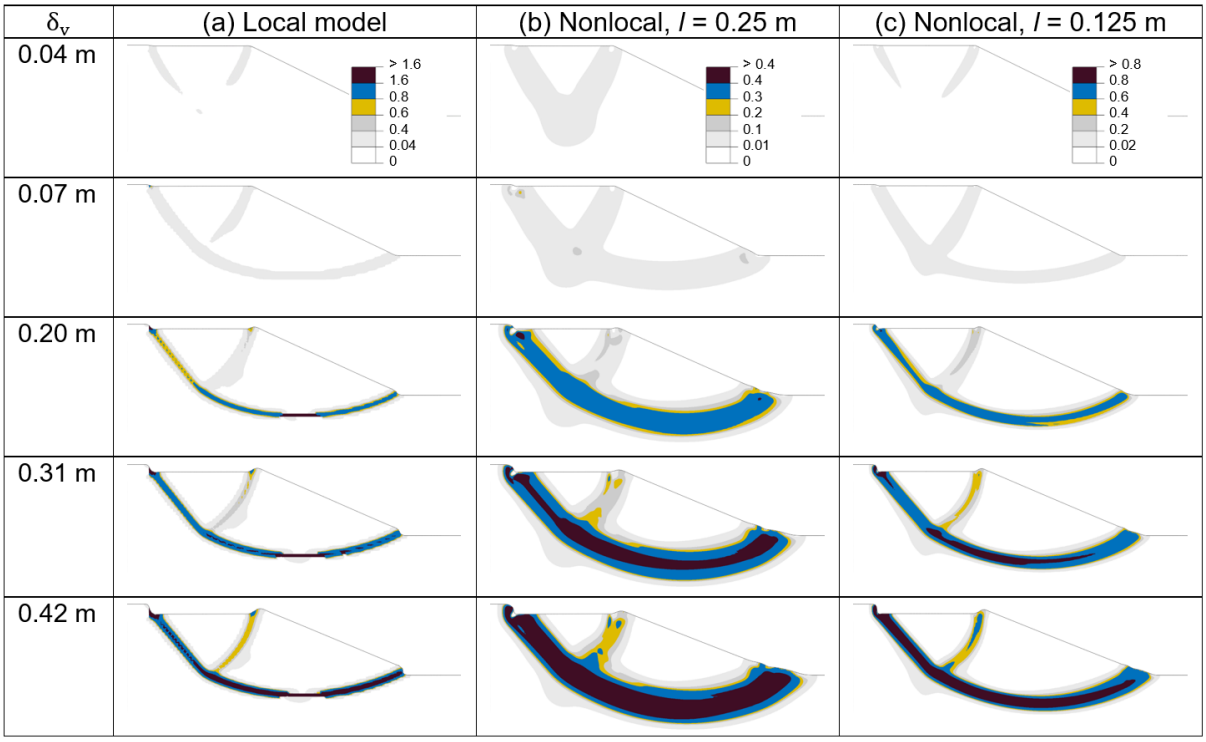

Figure 4.12 Shear band formation and propagation in local and nonlocal models (Note: local deviatoric plastic shear strain contour is presented for (a), and nonlocal deviatoric plastic shear strain contour is shown for (b) and (c))

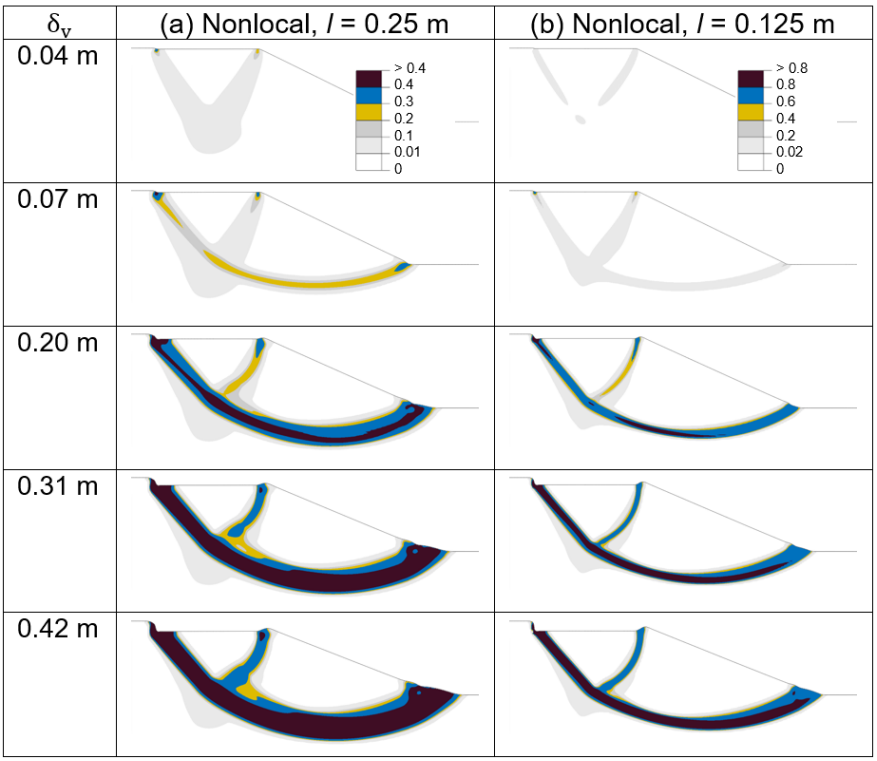

Figure 4.13 Shear band formation and propagation (local deviatoric plastic shear strain contour)

4.7 Discussions

4.7.1 Discussion on the shear band thickness

4.7.1.1 Shear band thickness with the over-nonlocal method

Comparable shear band thickness (t_{sFE}), independent of the mesh size, is reported to be one of the main advantages of nonlocal regularization (Mallikarachchi and Soga 2020; Mánica et al. 2018; Singh et al. 2021; Summersgill et al. 2017). However, these studies showed that t_{sFE} depends on the selection of the internal length parameter (l) and also on α in the over-nonlocal method. Summersgill et al. (2017) reported that while t_{sFE} is comparable for different mesh sizes, a thinner shear band is formed in a fine mesh for the over-nonlocal method with $\alpha = 2$, resulting in

excessively high plastic shear strain up to 200%. Mánica et al. (2018) compared t_{sFE} in a 60-mm × 100-mm block under biaxial loading. However, their numerical analyses were stopped after 4.6-mm vertical displacement due to the convergence problem. Similarly, 300–400% plastic shear strain in the shear band was calculated by Mallikarachchi and Soga (2020). In summary, the Lagrangian-based analyses could not be continued to a large-strain level, or encountered significant mesh distortion that might give misleading results. As the mesh distortion is not an issue in the present Eulerian-based FE model, the shear band thickness is examined even for a large strain. Note that in the field, for example, in a landslide, large deformation behaviour is required.

Figure 4.14 shows the shear band thickness normalized by the internal length parameter (t_{sFE}/l) for different values of α at δ_v = 0.2 m. Note that t_{sFE} also depends on δ_v, as discussed in the later sections. All the simulations shown in this figure were conducted using 0.0625-m mesh and with nonlocal regularization. All the analyses of case 1 with parameters listed in Table 4.1 and Table 4.2, except for l = 1.0 m, are also shown in Fig. 4.14. In addition, the analysis of l = 0.5 m without softening scaling is performed to provide more data. The parameter α is also varied in these analyses. For α = 2, the thickness of the shear band is 1.8 m, 0.9 m, 0.5 m, and 0.2 m for the internal lengths of 0.5 m, 0.25 m, 0.125 m, and 0.0625 m, respectively, with softening scaling. Such a trend of decreasing t_{sFE} with decreasing internal length parameter has also been reported in previous studies (e.g., Galavi and Schweiger 2010).

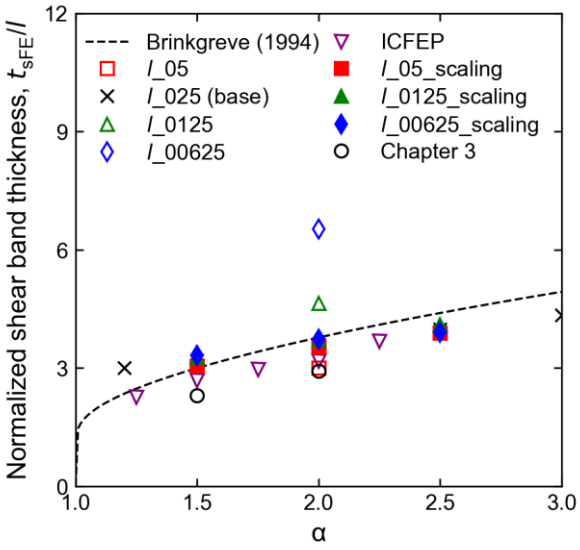

Figure 4.14 Normalized shear band thickness (t_{sFE}/l) vs. α

Figure 4.14 shows that when softening scaling is used, for a given α, the normalized shear band thickness (t_{sFE}/l) is almost independent of internal length parameters (l). However, t_{sFE}/l increases with α. Brinkgreve (1994) proposed an analytical solution (Eq. (4.12)) for a one-dimensional necking problem to calculate its localization zone length. This analytical solution has also been used for estimating the shear band thickness for two-dimensional applications (Brinkgreve 1994; D'Ignazio et al. 2017).

$$t_{\mathrm{sFE}} = \frac{\pi l}{\sqrt{\ln(\alpha) - \ln(\alpha - 1)}} \tag{4.12}$$

The FE calculated t_{sFE}/l for case 1 is comparable to the analytical solution, Eq. (4.12) (Fig. 4.14). For further comparison, t_{sFE}/l of a soil block (without a weaker zone at the bottom left corner) under biaxial undrained loading in Chapter 3, and the nonlocal ICFEP (Summersgill et al. 2017), are shown in Fig. 4.14, which also shows a similar trend.

Based on computational cost and accuracy, previous studies recommended $\alpha = 2$ for the problem they considered (Jostad and Grimstad 2011; Vermeer and Brinkgreve 1994), which leads to $t_{sFE} = 3.77l$ from Eq. (4.12). Note that, even with the finer mesh, the FE calculated t_{sFE} is much larger than an actual shear band typically observed in a laboratory and field (Guo 2012; Islam et al. 2019). An extremely small value of l and t_{FE} might capture such a shear band. However, it will be computationally impractical. Further discussion on the computational cost can be seen in Section 4.7.2.

A wide variation of t_{sFE}/l exists when the softening scaling is not used in case 1, as shown for $\alpha = 2.0$ (Fig. 4.14). The softening scaling brings the data points closer and approximately follows a similar pattern with the results from Eq. (4.12). However, as will be discussed in later sections, the shear band thickness is also dependent on the vertical displacement, which was not explicitly discussed by Brinkgreve (1994). That means Eq. (4.12) may not be the right solution for every scenario. This is explained in the next sections.

4.7.1.2 Variation of shear band thickness based on energy theory

In addition to the internal length and α, an increase in shear strain/deformation increases the thickness of the shear band. For example, Mallikarachchi and Soga (2020) found $t_{sFE} \approx 2.0l$ and $t_{sFE} \approx 2.2l$ during softening and the critical state, respectively, for an undrained shearing of dense sand. Note that the type of element (shape, size, number of nodes and integration points) and material model can also have some effects on t_{sFE} (Galavi and Schweiger 2010; Mallikarachchi and Soga 2020; Summersgill et al. 2017; Vermeer and Brinkgreve 1994), which is not investigated

in the present study, primarily because the existing Eulerian formulation of the software does not have sufficient flexibility in using different types of elements. In these studies, the simulations were limited to a certain level of deformation. In the present study, the simulations can continue even when significant strains develop in the shear band. Therefore, the mechanisms of enlarging shear band thickness at large strains are explored using an energy balance approach. Note that the enlargement of shear band thickness can have a significant practical implication, especially in the problems where multiple shear bands form, and the reduction of strength in such an enlarged zone can interfere with other shear band formations (e.g., retrogressive landslides). This has been explained using a simplified example in Section 4.6.3.4.

In a quasi-static analysis, the kinetic energy is negligible, which means the internal energy of the whole model is approximately equal to the external work (W_e). At large strains, the major portion of the internal energy is the dissipated plastic energy (E_d). Therefore, the energy balance in incremental form can be written as:

$$\Delta W_e \approx \Delta E_d \tag{4.13}$$

As mentioned earlier, the shear band is defined as the zone where the shear strength reduces to the residual state. In other words, there will be at least a thin band of residual strength from where expansion occurs. At this stage, the mobilized shear strength in the shear band equals the residual shear strength, which implies that the force F is almost constant at the residual state (F_r) (Fig. 4.15(a)). Therefore,

$$\Delta W_{\mathrm{e}} = F_{\mathrm{r}} \Delta \delta_{\mathrm{v}} \tag{4.14}$$

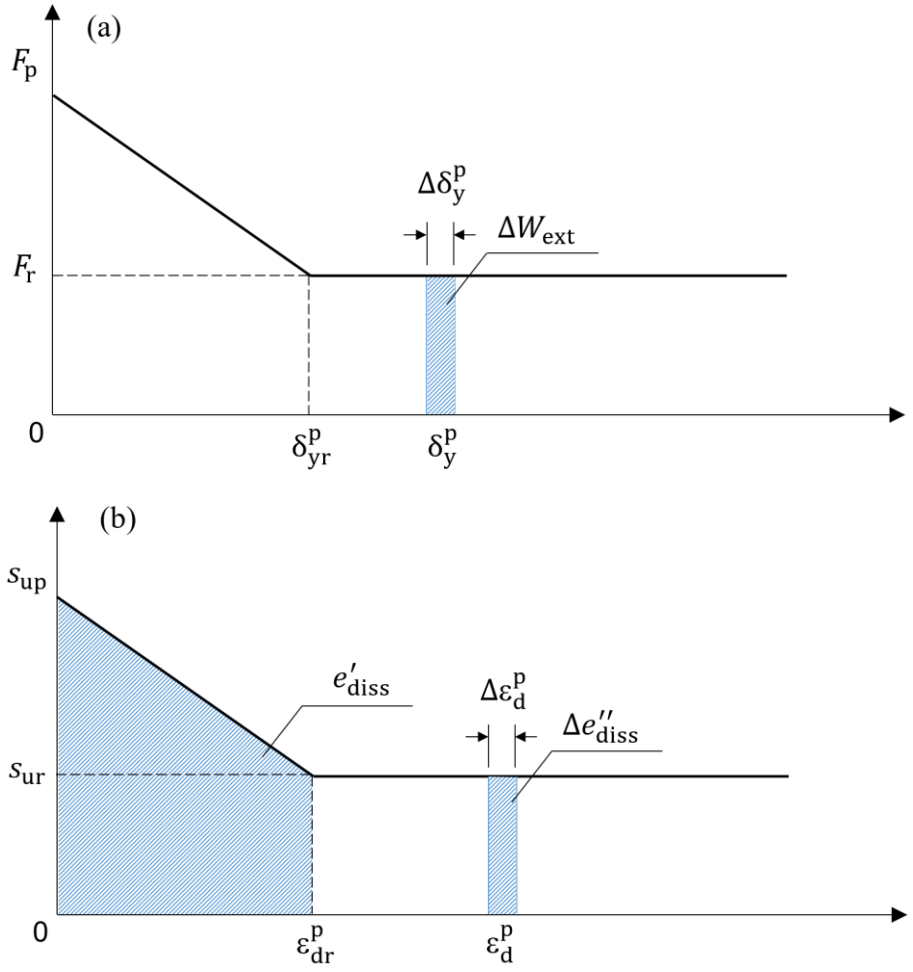

Figure 4.15 Schematic view of (a) external work increment; (b) dissipated plastic energy per cubic meter

ΔE_{d} has two components: (*a*) energy dissipation due to expansion of the shear band ($\Delta E'_{\mathrm{d}}$), and (*b*) energy dissipation due to an increase of shear strain in the shear band with loading ($\Delta E''_{\mathrm{d}}$).

$$\Delta E_{\mathrm{d}} = \Delta E'_{\mathrm{d}} + \Delta E''_{\mathrm{d}} \tag{4.15}$$

The energy dissipation per unit volume due to shear band expansion (e'_{d}) and shear strain increase ($\Delta e''_{\mathrm{d}}$) are the area of the trapezoid and rectangle, respectively, of the strength degradation curve (Fig. 4.15(b)). Now, multiplying $\Delta e''_{\mathrm{d}}$ and e'_{d} by the volume of the shear band and its increment, respectively, $\Delta E''_{\mathrm{d}}$ and $\Delta E'_{\mathrm{d}}$ can be calculated as:

$$\Delta E'_{\mathrm{d}} = \left[0.5(s_{\mathrm{up}} + s_{\mathrm{ur}})\varepsilon^{\mathrm{p}}_{\mathrm{dr}}\right] \times (\Delta t_{\mathrm{sFE}} L_{\mathrm{sFE}}) \tag{4.16}$$

$$\Delta E''_{\mathrm{d}} = \left[s_{\mathrm{ur}} \Delta\varepsilon^{\mathrm{p}}_{\mathrm{d}}\right] \times (t_{\mathrm{sFE}} L_{\mathrm{sFE}}) \tag{4.17}$$

The terms in parentheses (.) in Eqs. (4.17) and (4.16) represent the volume of the elements in the shear band and its change of unit thickness in the out-of-plane direction, where L_{sFE} is the length of the shear band and Δt_{sFE} is the increase in thickness of the shear band with loading.

Assume that for a given $\Delta\delta_{\mathrm{v}}$, the percentage of external work that dissipates for the increase in shear band thickness is

$$\Delta E'_{\mathrm{d}} = c_1 \cdot \Delta W_{\mathrm{e}} \tag{4.18}$$

where the value of c_1 could vary between 0 and 1.0. At this stage, c_1 is not known, which will be examined through FE results. Now, inserting $\Delta E'_{\mathrm{d}}$ from Eq. (4.18) into Eq. (4.16) and replacing ΔW_{e} by Eq. (4.14) and then rearranging, the increase in shear band thickness for a given $\Delta\delta_{\mathrm{v}}$ can be calculated.

$$\frac{\Delta t_{\mathrm{sFE}}}{\Delta\delta_{\mathrm{v}}} = \left[\frac{2F_{\mathrm{r}}}{(s_{\mathrm{up}} + s_{\mathrm{ur}})L_{\mathrm{sFE}}}\right]\frac{c_1}{\varepsilon^{\mathrm{p}}_{\mathrm{dr}}} \tag{4.19}$$

For the cases analyzed in this study, the length of the shear band (L_{sFE}) and residual reaction force do not change significantly once a complete shear band is formed. Therefore, the term in the square bracket is almost constant. The left side of Eq. (4.19) shows the slope of the t_{sFE}–δ_v curve. Now, obtaining t_{sFE} for varying δ_v from FE results, the variation of c_1 and the shear band thickness increases pattern can be examined.

4.7.1.3 Shear band thickness in case 1

Figure 4.16 shows the variation of t_{sFE} with δ_v for different mesh sizes (t_{sFE} = 0.0625 m, 0.125 m and 0.25 m) and internal length parameters (l = 0.0625 m, 0.125 m and 0.25 m) for the local and nonlocal models, respectively. The residual shear strength in these simulations is half of the peak shear strength, as shown in Table 4.1. The higher the internal length is, the larger the shear band thickness. Moreover, t_{sFE} increases with vertical loading and is more than 1.0 m for a higher value of l (= 0.25 m) at δ_v > 0.3 m (Fig. 4.16(a)). For the local analyses, the shear band thickness is almost proportional to the element size (t_{FE}). For example, t_{sFE} is 1 m and 0.5 m for t_{FE} of 0.125 m and 0.25 m, respectively, at δ_v = 0.8 m (Fig. 4.16(a)). The shear band thickness is defined as the width of the zone that reached the residual strength in this study. The shear band thicknesses of the "×" and "+" points are also calculated based on local strain for a calibration purpose. Both methods of calculation show a comparable result. However, the former one is selected for further discussion. This can facilitate a direct comparison with Eq. (4.19) where the definition of the shear band thickness is identical. Furthermore, the upward trend of shear band thickness observed with the increase of δ_v, is contrary to the analytical solution, Eq. (4.12) (Brinkgreve 1994), where the shear

band thickness is a constant for each analysis. This analytical solution was derived for a one-dimensional tension bar, and the nonlocal strain rate was assumed to be constant within the localization zone, which is not valid in the current biaxial test model.

Figure 4.16(a) shows a wide variation in t_{sFE}. Therefore, some normalizations are performed in this section for a better presentation of the results. Except for ε_{dr}^{p} and c_1, the right-hand side of Eq. (4.19) is identical for all the analyses in case 1. Figure 4.16(b) shows the variation of t_{sFE} with $\delta_v/\varepsilon_{dr}^{p}$, which brings the slopes of data points closer compared to that shown in Fig. 4.16(a). This implies that the c_1 could be nearly the same for all analyses of this biaxial test. As discussed before, the thickness of the shear band depends on t_{FE} and l for the local and nonlocal models, respectively. Therefore, the parameters in the vertical and horizontal axes in Fig. 4.16(b) are further normalized by t_{FE} and l for the local and nonlocal models, respectively, and then t_{sFE}/l vs. $\delta_v/(\varepsilon_{dr}^{p} l)$ and t_{sFE}/t_{FE} vs. $\delta_v/(\varepsilon_{dr}^{p} t_{FE})$ are plotted in Fig. 4.16(c). The data points are closer in this figure than those in Figs. 4.16(a) and 4.16(b) and spread over the same normalized vertical displacement. From Fig. 4.16(c), the increase rate of the normalized shear band thickness of local and nonlocal models is comparable. This further proved that the values of c_1 for both models are close, indicating that a similar percentage of external work dissipates for the increase of shear band thickness. This is contrary to the general understanding that energy cannot be dissipated outside of the shear band in a local model. A possible reason can be that energy is dissipated in the convection process in the

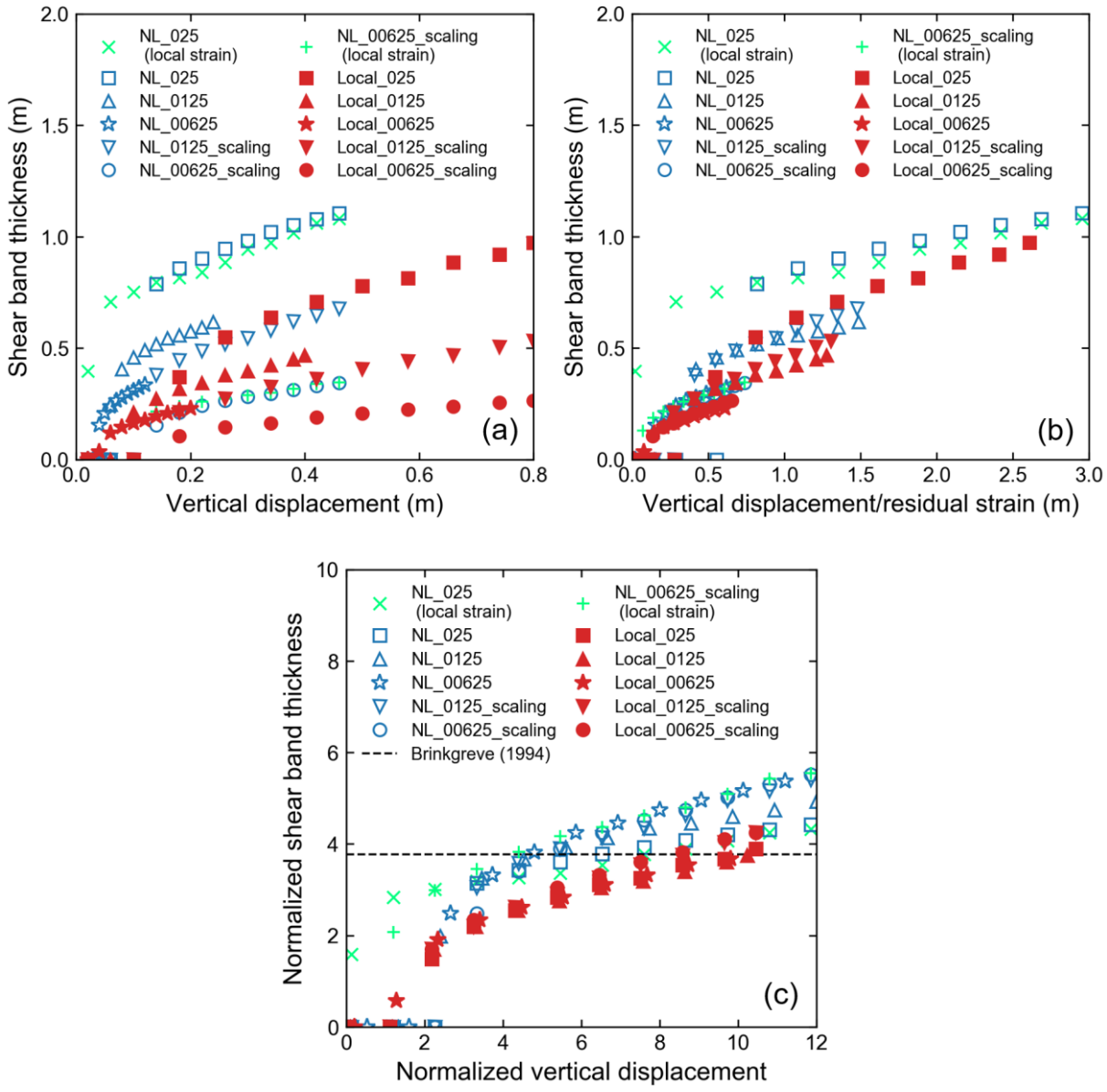

Figure 4.16 Variation of shear band thickness: (a) t_{sFE} vs. δ_{v}; (b) t_{sFE} vs. $\delta_{\mathrm{v}}^{\mathrm{p}}/\varepsilon_{\mathrm{qr}}^{\mathrm{p}}$; (c) Normalized shear band thickness vs. normalized vertical displacement ($t_{\mathrm{sFE}}/t_{\mathrm{FE}}$ vs. $\delta_{\mathrm{v}}^{\mathrm{p}}/(\varepsilon_{\mathrm{qr}}^{\mathrm{p}} \cdot t_{\mathrm{FE}})$ for local model, and t_{sFE}/l vs. $\delta_{\mathrm{v}}^{\mathrm{p}}/(\varepsilon_{\mathrm{qr}}^{\mathrm{p}} \cdot l)$ for nonlocal model)

(Note: 1% local deviatoric plastic shear strain is used for the NL_025 (local strain) case, and 25% local deviatoric plastic shear strain is used for the NL_00625_scaling (local strain) case, to calculate the shear band thickness.)

Eulerian step. The energy dissipation in a nonlocal model is mainly controlled by the internal length parameter. To further understand the energy dissipation in both models, the shear bands with different stress states are analyzed in the next section.

4.7.1.4 Shear band thickness in case 2

Unlike case 1, the direction of the principal stresses varies along the slip surface in case 2. Therefore, the normalized shear band thicknesses at three locations in the slip surface, representing plane strain compression (PSC), direct simple shear (DSS), and plane strain extension (PSE), are investigated (Fig. 4.17). A similar trend of increasing normalized shear band thickness is found for all three loading conditions. While the rate of increase in normalized shear band thickness in PSC is comparable for the local and nonlocal models (Fig. 4.17(a)), a larger difference is found in the other two modes (DSS and PSE) (Figs. 4.17(a)–4.17(c)). In other words, the shear band thicknesses in local models are more dependent on the direction of the principal stresses. A possible reason can be the convection process of the Eulerian materials, as discussed before. When the shear band is parallel to the mesh orientation, the plastic strain of the local element is not significantly distributed to the neighbouring rows of elements that are not in the shear band, which gives a narrower shear band in the local model. This also explains why the shear band is only one element thick in the DSS model, even at large displacements, (Fig. 4.17(b)). However, when the shear band forms at an oblique angle to the mesh orientation, the remapping of solution variables can transfer the plastic strains to the neighbouring elements more easily. Therefore, a thicker shear band is observed under

the plane strain compression and extension conditions in the local models (Figs. 4.17(a) and 4.17(c)).

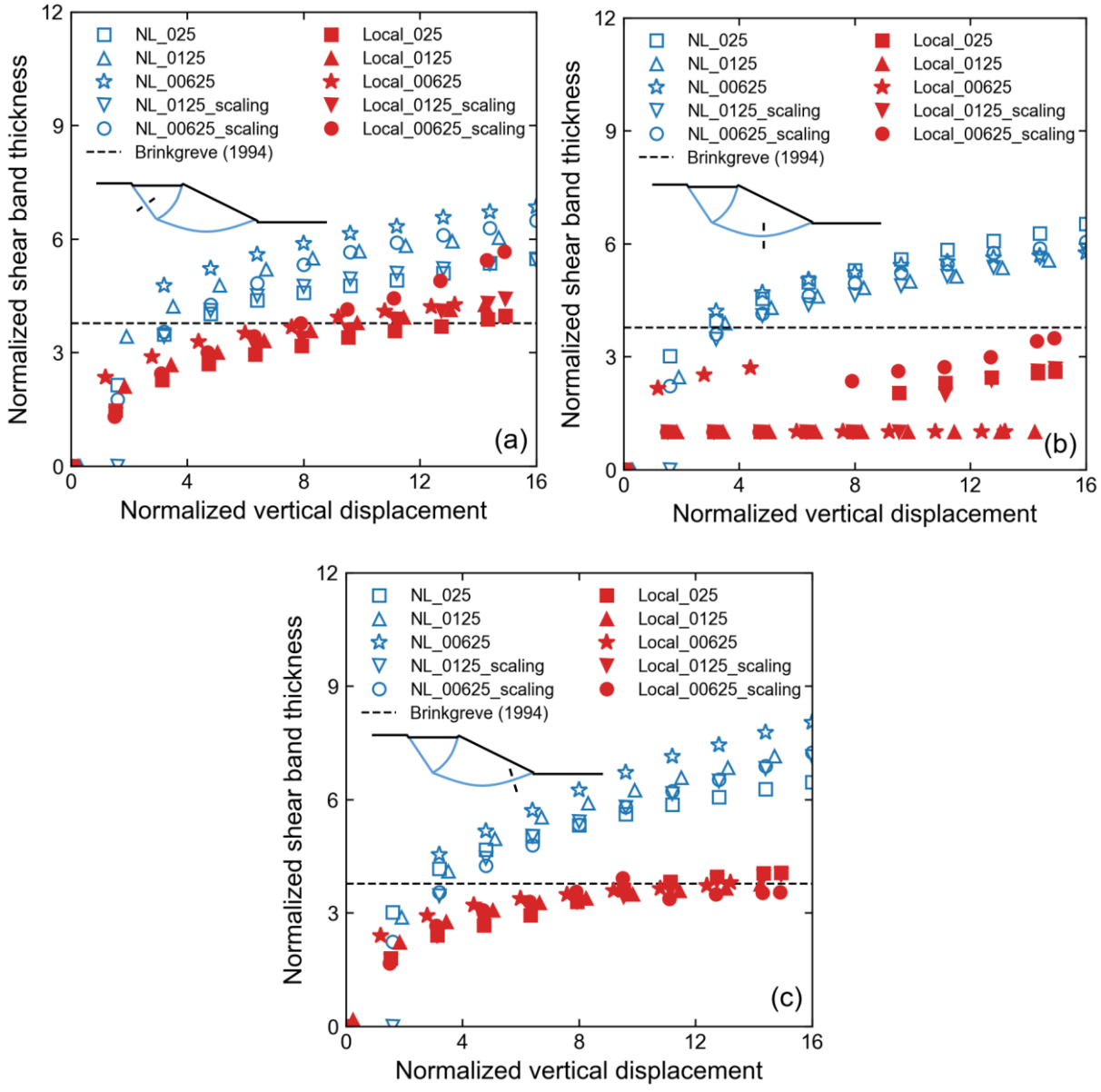

Figure 4.17 Normalized shear band thickness vs normalized vertical displacement (a) plane strain compression; (b) direct simple shear; (c) plane strain extension

4.7.2 Computational costs

The computational costs of FE analysis with nonlocal regularizations are generally higher than those of local methods (Summersgill 2014), although Singh et al. (2021) reported that the nonlocal method does not increase the computational costs significantly, even with very fine mesh, using their RITSS. Such inconsistent conclusions can be attributed to the algorithms of numerical modeling techniques. The nonlocal method reduces the gradient of shear strain in the localized zone, which can lead to a faster rate of convergence in an implicit FE analysis, as used by Singh et al. (2021). However, an explicit method is adopted by Eulerian-based FE method, and therefore, convergence is not a concern as in the implicit method.

4.7.2.1 Computational costs of case 1

Figure 4.18 shows the CPU time required to simulate the biaxial test using the local (element size scaling) and nonlocal methods. The element sizes are 0.25 m, 0.125 m, and 0.0625 m for both methods. In addition, $l = 0.25$ m and $\alpha = 2.0$ are used for the nonlocal method. The other parameters are the same as in Table 4.1. Chapter 3 introduced a technique to reduce the computational cost by calculating the nonlocal strains once in every m time increment. The CPU time for different m (m = 1, 10, 100) are shown in Fig. 4.18, which clearly shows that the nonlocal method costs more CPU time than the local method, and this gap increases when a finer mesh is used. A larger value of m (e.g., m = 100) can reduce the CPU time of the nonlocal method significantly.

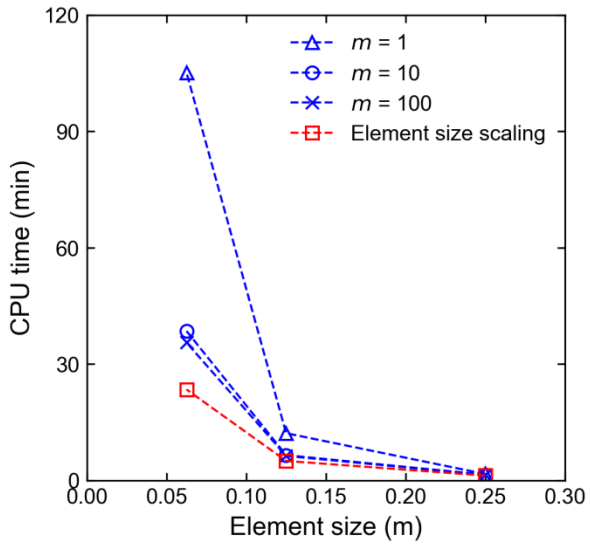

Figure 4.18 Computational costs of the biaxial test with local (element size scaling) and over-nonlocal methods

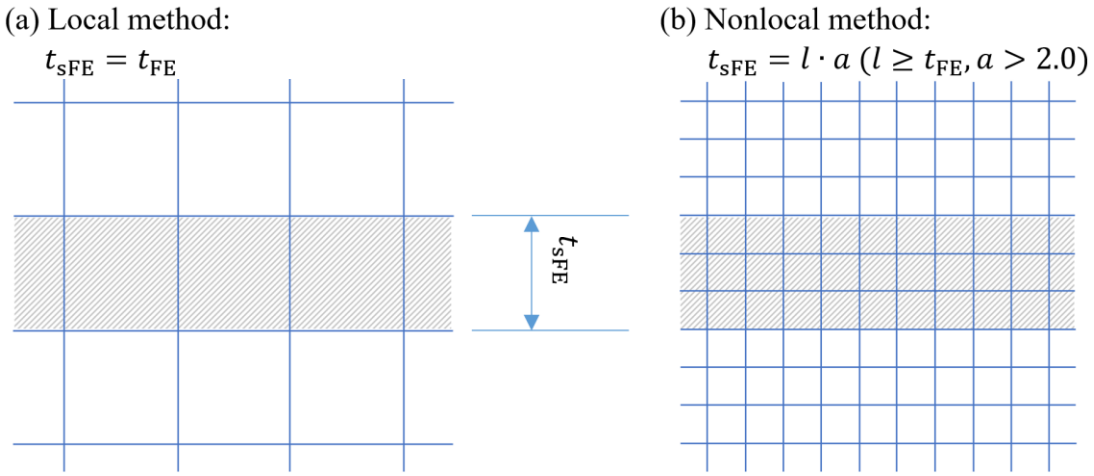

Figure 4.19 Modeling of comparable shear band thickness in local and nonlocal models (schematic)

Although a higher value of m can help the nonlocal method reach a closer computational cost to the local method, the shear band is still much thicker in the nonlocal model. To model a comparable shear band thickness in both methods, a smaller mesh size is required for the nonlocal

method, as schematically shown in Fig. 4.19. The computational costs increase rapidly in the nonlocal method for the finest mesh (0.0625 m).

4.7.2.2 Computational costs of case 2

In engineering practice, a larger model than a biaxial test is usually simulated. Similar to the biaxial test in case 1, the nonlocal method is computationally more expensive than the local (element size scaling) method in FE modeling of slope failure (case 2). As an example, with a 0.0625-m mesh, the analysis took ~3 hours CPU time for nonlocal (with an internal length, l = 0.0625 m, and m = 10) while it took only 40 minutes with element size scaling using a 3.4 GHz Intel Core i7-6700 CPU (8 processors) and 16 GB RAM. Compared to case 1, the difference between the computational costs for local and nonlocal regularizations is significantly higher in case 2, although the calculation of $\Delta\varepsilon^{p}_{d(NL)}$ only occurs once for every 10-time increment (m = 10). This is mainly caused by a larger number of elements than for the biaxial test, which is in line with the trend shown in Fig. 4.18. Similar to the biaxial test, the shear band of this slope is thicker in the nonlocal model when the same element size is used, as explained in the last section. To model the identical shear band thickness with the nonlocal method, even higher computational costs are expected, as a finer mesh has to be used.

When modeling a large-scale landslide, the size of the model can be many times larger than that of the present slope analysis; e.g., the failed soil can travel more than 100 km after a submarine landslide (Hampton et al. 1996). The nonlocal algorithm can be extremely expensive for that

scenario. The failed soil moves fast through the fixed mesh to create a remarkable difference between two neighbouring time increments. The calculation of nonlocal strains can be required more frequently (a smaller m) due to the highly dynamic nature of a landslide, thus leading to a significantly higher computational cost. Moreover, as discussed in Chapter 3, to model a large-scale problem, the number of elements increases dramatically, which will further increase the computational costs of the nonlocal averaging.

4.8 Practical implications

Both the local and the nonlocal Eulerian-based FE models can be implemented for large-deformation problems. The softening-scaling rule is an effective way to control the shear band thickness and thus reduces the computational cost for both local and nonlocal models. The shear band thickness is influenced by the mesh orientation in the local mode. Nonlocal models are generally computationally expensive. Further advancement of numerical techniques might provide better results. Potential issues and possible solutions are listed below.

1. In the present study, all the analyses are performed under a pseudo-static condition. Further research is required to understand the efficacy of the local method and the nonlocal method, coupled with softening scaling, on strain regularization and macroscopic modeling for a dynamic problem. Also, the expansion of the shear band should be addressed for a dynamic problem, as it may not be in line with Eq. (4.19), where a quasi-static condition is assumed.
2. The scenario of multiple shear bands for nonlocal models should be further explored (e.g., modeling of a spread failure in sensitive clays). As aforementioned, a large internal length

parameter can affect the shear band propagation when two shear bands interact, while a smaller internal length parameter requires a finer mesh and thus has a high computational cost. Therefore, a proper internal length parameter needs to be determined with caution so that the interactions between shear bands are reasonable, while the computational expense is still acceptable.

3. The Tresca failure criterion is used for this study. Advanced soil constitutive models can be implemented with the current framework to handle more complex soil behaviours.
4. The shear band thickness of real soil depends on soil properties; for example, size, shape and orientation of particles for granular materials, and also on pore pressure generation and dissipation. Therefore, further studies are needed to identify the association between internal length and soil properties, such that the macroscopic behaviour can be correctly modeled when softening scaling is used.

4.9 Conclusions

Both local and nonlocal models, coupled with the softening-scaling rule, can be used for a large-deformation FE analysis. An evaluation of both models is needed so that the best practice can be proposed. In this study, a comparison between the two models was performed, in terms of their mesh dependency, macroscopic modeling, shear band thickness, and computational cost, by modeling two idealized cases, namely a biaxial test and a slope failure analysis. User subroutines were developed to implement the Tresca failure criteria with the over-nonlocal method in Eulerian-

based FE. In addition, the expansion of shear band thickness was investigated by using the energy theory and further studied with numerical modeling results for both local and nonlocal models.

1. Both the local (element size scaling) and the nonlocal methods present a mesh independent solution of the two cases with a slightly different variation of post-peak reaction, and the shear band thickness of the element size scaling method is still mesh dependent.
2. The shear band thickness in the FE program is usually too large compared to the real condition. The softening-scaling rule is proven effective to model the macroscopic strain-softening behaviour with both local and nonlocal methods.
3. The interactions between two shear bands can become unrealistic in a nonlocal model, as their nonlocal averaging can affect each other. An appropriate internal length parameter needs to be determined to avoid this undesirable interaction.
4. The shear band thickness increases proportionally with the loading displacement, which is contrary to the analytical solution proposed by Brinkgreve (1994), where the shear band thickness is a constant. This finding is demonstrated by the energy theory and modeling results for both local and nonlocal models. Note that the shear band thickness is influenced by the mesh orientation and the direction of principal stress in a local model.
5. The computational cost of the nonlocal method is significantly higher than the local method in Eulerian-based FE. This can be disadvantageous for the nonlocal method to model a large-scale problem, e.g., retrogressive landslides.

Acknowledgements

The works presented in this paper have been supported by the Natural Sciences and Engineering Research Council of Canada (NSERC), InnovateNL, and the former Research and Development Corporation of Newfoundland and Labrador (RDC).

Notations

α amplification factor

ρ mass density

ν_u Poisson's ratio

δ_v vertical displacement of the loading cap

$\varepsilon^p_{d(L)}$ local deviatoric plastic shear strain

$\varepsilon^p_{d(NL)}$ nonlocal deviatoric plastic shear strain

ε^p_{dFE} scaled deviatoric plastic shear strain

ε^p_d deviatoric plastic strain

$\varepsilon^p_{dr(NL)}$ nonlocal deviatoric plastic strain requires for residual strength

ε^p_{ds} deviatoric plastic shear strain of the shear band in real conditions

ε_{p1}, ε_{p2}, ε_{p3} principal plastic strains

$\omega()$ Gaussian-type weight function

E' softening modulus

E'_d energy dissipation due to expansion of the shear band

E_{d}'' energy dissipation due to increase of shear strain in the shear band

e_{d}' energy dissipation per unit volume due to shear band expansion

e_{d}'' energy dissipation per unit volume due to shear strain increase

l_{s} internal length parameter of soil

t_{s} shear band thickness in a real condition

E elastic modulus

E_{d} the dissipated plastic energy

E_{u} undrained Young's modulus

EVF Eulerian volume fraction

F loading force from the cap

F_{r} the residual value of F

l internal length parameter of the nonlocal model

L_{sFE} length of the shear band

m number of time increments covered by one calculation of nonlocal strain

r_{inf} radius of influence

s_{u} undrained shear strength

s_{up} peak undrained shear strength

s_{ur} residual undrained shear strength

t time

t_{FE} element size

$t_{\mathrm{FE\_R}}$ reference FE element size

t_{sFE} shear band thickness in a FE model

u displacement

V_w reference volume

W_e external work

x length coordinate

z depth measured from the crest of the slope (m)

References

Anastasopoulos, I., Gazetas, G., Asce, M., Bransby, M. F., Davies, M. C. R., and El Nahas, A. (2007). "Fault rupture propagation through sand: Finite-element analysis and validation through centrifuge experiments." *Journal of Geotechnical and Geoenvironmental Engineering*, 133(8), 943–958.

Bažant, Z. P., and Jirásek, M. (2002). "Nonlocal Integral Formulations of Plasticity and Damage: Survey of Progress." *Journal of Engineering Mechanics*, 128(11), 21–51.

Benson, D. J., and Okazawa, S. (2004). "Contact in a multi-material Eulerian finite element formulation." *Computer Methods in Applied Mechanics and Engineering*, 193(39–41), 4277–4298.

de Borst, R., and Mühlhaus, H. B. (1992). "Gradient-dependent plasticity: Formulation and algorithmic aspects." *International Journal for Numerical Methods in Engineering*, 35(3), 521–539.

de Borst, R., Sluys, L. J., Mühlhaus, H. B., and Pamin, J. (1993). "Fundamental issues in finite

element analyses of localization of deformation." *Engineering Computations*, 10(2), 99–121.

Brinkgreve, R. (1994). "Geomaterial models and numerical analysis of softening." Technische Universiteit Delft.

Burghardt, J., Brannon, R., and Guilkey, J. (2012). "A nonlocal plasticity formulation for the material point method." *Computer Methods in Applied Mechanics and Engineering*, 225–228(2012), 55–64.

Chen, Z., Qian, D., and Xin, X. (1999). "Study of localization problems based on the transition between governing equations." *Advances in Structural Engineering*, 2(4), 289–303.

Conte, E., Silvestri, F., and Troncone, A. (2010). "Stability analysis of slopes in soils with strain-softening behaviour." *Computers and Geotechnics*, 37(5), 710–722.

D'Ignazio, M., Länsivaara, T. T., and Jostad, H. P. (2017). "Failure in anisotropic sensitive clays: Finite element study of Perniö failure test." *Canadian Geotechnical Journal*, 54(7), 1013–1033.

Dey, R., Hawlader, B., Phillips, R., and Soga, K. (2015). "Large deformation finite-element modelling of progressive failure leading to spread in sensitive clay slopes." *Géotechnique*, 65(8), 657–668.

Eringen, A. C. (1981). "On nonlocal plasticity." *International Journal of Engineering Science*, 19(12), 1461–1474.

Galavi, V., and Schweiger, H. F. (2010). "Nonlocal multilaminate model for strain softening analysis." *International Journal of Geomechanics*, 10(1), 30–44.

Griffiths, D. V., and Lane, P. A. (1999). "Slope stability analysis by finite elements." *Géotechnique*,

49(3), 387–403.

Guo, P. (2012). “Critical length of force chains and shear band thickness in dense granular materials.” *Acta Geotechnica*, 7(1), 41–55.

Hampton, M. A., Lee, H. J., and Locat, J. (1996). “Submarine landslides.” *Reviews of Geophysics*, 34(1), 33–59.

Islam, N., Hawlader, B., Wang, C., and Soga, K. (2019). “Large-deformation finite-element modelling of earthquake-induced landslides considering strain-softening behaviour of sensitive clay.” *Canadian Geotechnical Journal*, 56(7), 1003–1018.

Jostad, H. P., and Grimstad, G. (2011). “Comparison of distribution functions for the nonlocal strain approach.” *Computational Geomechanics, COMGEO II - Proceedings of the 2nd International Symposium on Computational Geomechanics*, Cavtat-Dubrovnik, Croatia, 212–223.

Liu, P. F., and Li, X. K. (2019). “Dynamic Void Growth and Localization Behaviours of Glassy Polymer Using Nonlocal Explicit Finite Element Analysis.” *Journal of Peridynamics and Nonlocal Modeling*, 1(1), 3–13.

Lu, X., Bardet, J. P., and Huang, M. (2012). “Spectral analysis of nonlocal regularization in two-dimensional finite element models.” *International Journal for Numerical and Analytical Methods in Geomechanics*, 36(2), 219–235.

Maier, T. (2003). “Nonlocal modeling of softening in hypoplasticity.” *Computers and Geotechnics*, 30(7), 599–610.

Mallikarachchi, H., and Soga, K. (2020). “Post-localisation analysis of drained and undrained

dense sand with a nonlocal critical state model." *Computers and Geotechnics*, 124, 103572.

Mánica, M. A., Gens, A., Vaunat, J., and Ruiz, D. F. (2018). "Nonlocal plasticity modelling of strain localisation in stiff clays." *Computers and Geotechnics*, 103, 138–150.

Marcher, T. (2003). "Nichtlokale Modellierung der Entfestigung dichter Sande und steifer Tone." University of Stuttgart.

Monforte, L., Ciantia, M. O., Carbonell, J. M., Arroyo, M., and Gens, A. (2019). "A stable mesh-independent approach for numerical modelling of structured soils at large strains." *Computers and Geotechnics*, 116, 103215.

Pietruszczak, S., and Mroz, Z. (1981). "Finite element analysis of deformation of strain-softening materials." *International Journal for Numerical Methods in Engineering*, 17, 327–334.

Prevost, J. H., and Loret, B. (1990). "Dynamic strain localization in elasto-(visco-)plastic solids, part 2. plane strain examples." *Computer Methods in Applied Mechanics and Engineering*, 83(3), 275–294.

Singh, V., Stanier, S., Bienen, B., and Randolph, M. F. (2021). "Modelling the behaviour of sensitive clays experiencing large deformations using non-local regularisation techniques." *Computers and Geotechnics*, 133, 104025.

Sluys, L. J. (1992). "Wave Propagation, Localisation and Dispersion in Softening Solids." Delft University of Technology.

Summersgill, F. C. (2014). "Numerical Modelling of Stiff Clay Cut Slopes with Nonlocal Strain Regularisation." Imperial College London.

Summersgill, F. C., Kontoe, S., and Potts, D. M. (2017). "Critical assessment of nonlocal strain-

softening methods in biaxial compression." *International Journal of Geomechanics*, 17(7), 1–14.

Tran, Q. A., and Sołowski, W. (2019). "Generalized Interpolation Material Point Method modelling of large deformation problems including strain-rate effects – Application to penetration and progressive failure problems." *Computers and Geotechnics*, 106, 249–265.

Vermeer, P. A., and Brinkgreve, R. B. J. (1994). "A new effective non-local strain measure for softening plasticity." *Proceedings of 3rd International Workshop on Localization and Bifurcation Theory for Soils and Rocks*, A.A. Belkema, Rotterdam, Netherlands, Grenoble, France, 89–100.

CHAPTER 5

Large Deformation Finite-Element Modeling of the Lower San Fernando Dam Failure in 1971

Co-Authorship: This chapter will be submitted as a technical paper for publication in a journal as: Chen, J., Hawlader, B., Roy, K. and Pike, K. "Large deformation finite-element modeling of the Lower San Fernando Dam failure in 1971."

Most of the research work presented in this chapter was conducted by the first author. He also prepared the draft manuscript. The other authors supervised the research and reviewed the manuscript.

5.1 Abstract

The Lower San Fernando dam failure in 1971 is one of the major earthquake-triggered slope failures where the failed soil in the upstream slope displaced several meters. In addition to post-slide investigations, conceptual, analytical, and numerical studies were conducted to understand the potential failure mechanisms. However, most of the numerical studies focused on the triggering mechanism of the failure, and analyses were limited to relatively small deformations. This paper presents a large deformation finite-element (FE) modeling of failed soil that occurred in the post-quake stage. The simulations are performed using a Eulerian FE modeling technique, avoiding any mesh distortion issues. A new technique is developed in the Eulerian FE program to establish an initial steady-state seepage condition in the dam. The calculated seepage forces, together with gravity and buoyancy, are used to define the in-situ stresses. The failure is triggered by a pseudostatic loading over a period, which causes the progressive formation of the failure planes in the post-quake stage. The failure initiates first in the lower part of the hydraulic fill and then

propagates through the upper soil layers. This mechanism causes the upstream slope failure in the form of several soil blocks, which is similar to the post-failure configuration reported in the literature. The roles of strain-softening and apparent cohesion during partially drained shearing in the failure process are also discussed.

5.2 Introduction

The Lower San Fernando Dam was constructed on an approximately 11-m thick natural alluvium soil layer of primarily stiff clay with layers or lenses of sand and gravel (Castro et al. 1992). The maximum height of the dam was about 43 m. The major part of the dam was constructed between 1912–1915, primarily by the hydraulic filling of soil, ranging from coarse silty sand at the edge to clay core at the center of the dam (Lee et al. 1975). On February 9, 1971, a flowslide was triggered in the upstream side of the dam approximately 30 s after an earthquake of 6.6 magnitude. Comprehensive post-failure investigations were carried out to understand the failure mechanisms. Figures 5.1(a) and 5.1(b) show the reconstructed cross-sections of the failed dam (Seed et al. 1973). The following are the key observations. First, several large longitudinal cracks were formed near the crest. Second, the failure occurred by the formation of a number of curved slip surfaces. However, the failure was different from typical flowslides, where the rotational failure of a soil block occurs after sufficient downslope displacement of previously failed soil blocks. In this case, a large soil block was pushed upward near the toe of the slope (block #7 in Fig. 5.1), which is an indication of providing thrust provided by the soil blocks in the upslope area (blocks #1 to #5). Such a thrust could generate if the downslope movement of the #7 block was slower than that of #1 to #5 blocks. In that case, the failure might have been triggered by the formation of an approximately horizontal sliding plane that extended up to the bottom of the #1 to #5 blocks, with curved sliding surfaces then being formed (Fig. 5.1). Cyclic loading during the earthquake could

have generated excess pore water pressure that reduced the shear strength of the soil, especially the loose sand, referred to as the liquefied zone (Fig. 5.1(b)). The horizontal failure plane might have formed through this zone, and then progressive failure of the slope would have occurred.

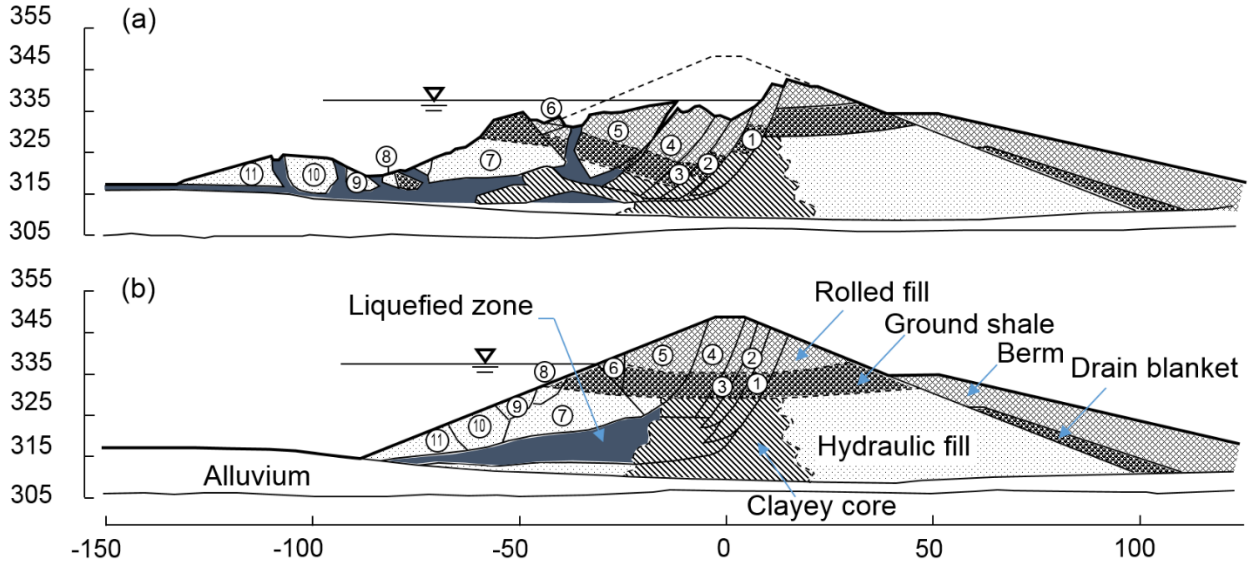

Figure 5.1 Cross-Section through the Lower San Fernando Dam: (a) after 1971 earthquake; (b) reconstruction of failed cross-section (Seed et al. 1973)

Figures 5.1(a) and 5.1(b) show that the maximum displacement of the debris from the toe was about 45.7 m (Castro et al. 1989). The freeboard dropped from 10.7 m to 1.5 m after the failure (Seed et al. 1973), which implies 9.2 m of settlement near the crest. Such a large deformation cannot be modeled using a typical Lagrangian-based finite element (FE) program because of numerical issues due to mesh distortion. Also, the typical limit equilibrium methods are not suitable for modeling progressive failure of the slope.

Post-slide studies include field and laboratory investigations, which include excavation of trenches through the slide area, borehole drilling, in-situ testing, and laboratory testing for monotonic and cyclic behaviour of soil (Seed et al. 1973; Lee et al. 1975; Castro et al. 1989). Olson

(2001) attempted to develop the yield strength ratio ($s_{u(yield)}/\sigma'_{v0}$) and liquefied strength ratio ($s_{u(liq)}/\sigma'_{v0}$), where $s_{u(yield)}$ and $s_{u(liq)}$ are the shear strength at the peak that mobilized at large deformation after flow liquefaction, and σ'_{v0} is a pre-failure vertical effective stress. These strength ratios were used to examine liquefaction triggering and subsequent flow failure of the Lower San Fernando Dam (Olson 2001). To identify the failure pattern using $s_{u(liq)}/\sigma'_{v0}$, simplified kinetics analyses were performed for the soil above the failure plane, assuming that the strength of all the soil elements along the failure surface was mobilized to $s_{u(liq)}$. However, recognizing the inaccuracies in then estimated unique value of $s_{u(liq)}$, due to the involvement of different soil layers (e.g., rolled fill and ground shale), the strength was adjusted simply based on possible length of the predefined slip surface in different materials, which gives a reasonable displacement of the center of gravity of the failed soil mass (5.2 m vertically and 25.9 m horizontally).

Table 5.1 shows a summary of several representative modeling efforts of the Lower San Fernando Dam failure, which can be primarily categorized into two groups: (a) the initiation of the failure, and (b) both the initiation and post-quake deformation analysis. The first group analyzed the stability of the dam based on the limit equilibrium (LE) analysis (e.g., Seed et al. 1973; Seed 1979; Castro et al. 1989; Olson 2001; Olson and Stark 2001, 2002). A pseudostatic load, instead of a seismic load, has been applied to the dam to determine the location of the slip surface and the factor of safety (e.g., Seed et al. 1973; Seed 1979; Castro et al. 1989). Some of them conducted dynamic FE analyses to identify the liquefaction zone before the calculation of the factor of safety (Seed et al. 1973; Seed 1979). However, this type of progressive failure cannot be modeled using the LE method alone, even with the steady-state strength for the initial liquefied zone (Gu et al. 1993), because the liquefied zone will be significantly enlarged, due to stress redistribution after

the initial liquefaction in an earthquake. Furthermore, the displacement of the failed soil mass cannot be simulated using the LE method. The second group extended their work from initiation to a limited post-quake failure stage (e.g., Gu et al. 1993; Jitno 1995; Huang and Zienkiewicz 1998; Beaty and Byrne 2000; Ming and Li 2003; Khoei et al. 2004; Blázquez and López-Querol 2007; Khoei and Haghighat 2011; Huang et al. 2020). The failure was primarily triggered in two different ways: (a) without modeling the earthquake (e.g., Gu et al. 1993; Jitno 1995), and (b) dynamic analysis with post-seismic deformation modeling (e.g., Beaty and Byrne 2000). In group (a), Gu et al. (1993) reduced the shear strength of two elements at the bottom of the upstream hydraulic fill to initiate the failure. Jitno (1995) adopted a pseudo-dynamic FE approach, where the slide is triggered by reducing the shear modulus of the liquefied soil, clay core and shell, to model the post-earthquake displacement. However, the two methods could not consider any shear band that was generated during the earthquake. In group (b), the formation of shear bands during the seismic loading process has been addressed by some studies (e.g., Chowdhury et al. 2019; Huang et al. 2020). Nevertheless, none of them reproduced the whole process of post-earthquake deformation. A possible reason could be that the constitutive models or the numerical modeling technique were not capable of modeling large strains.

Table 5.1 Numerical modeling techniques for the Lower San Fernando Dam

References	Numerical technique	Stage(s) analyzed	Remarks
Seed et al. (1973)	Limit equilibrium (LE) & finite-element (FE)	Initiation of failure	Pseudostatic and dynamic analysis
Castro et al. (1989)	LE	Initiation of failure	Newmark method to estimate the strain and strain-induced strength reduction
Olson (2001); Olson and Stark (2001, 2002)	LE	Initiation of failure	A flow failure susceptibility analysis, a liquefaction triggering analysis, and a flow failure stability analysis
Seed (1979)	LE and FE	Initiation of failure	Pseudostatic and dynamic analysis
Gu et al. (1993)	FE	Initiation and post-quake deformation	Reduce the s_u of two elements to liquefaction state to trigger the failure
Jitno (1995)	FE	Initiation and (limited) post-quake deformation	Extended Newmark method; zero inertia force; the predicted displacement is too small
Huang and Zienkiewicz (1998)	FE	Initiation and (limited) post-quake deformation	Dynamic analysis
Ming and Li (2003)	FE	Initiation and (limited) post-quake deformation	Dynamic analysis
Khoei et al. (2004)	FE	Initiation and (limited) post-quake deformation	Dynamic analysis

References	Numerical technique	Stage(s) analyzed	Remarks
Blázquez and López-Querol (2007)	FE	Initiation and (limited) post-quake deformation	Dynamic analysis
Khoei and Haghighat (2011)	Extended FE	Initiation and (limited) post-quake deformation	Dynamic analysis
Beaty and Byrne (2000)	Finite-difference (FD)	Initiation and (limited) post-quake deformation	Dynamic analysis
Chowdhury et al. (2019)	FD	Initiation and (limited) post-quake deformation	Dynamic analysis
Huang et al. (2020); Feng et al. (2021)	Material Point Method	Initiation and (limited) post-quake deformation	Dynamic analysis, large-deformation analysis
Tjung and Soga (2021)	Material Point Method	Post-quake deformation	No seismic loading, large-deformation analysis

FE modeling of post-quake sliding over a large distance, as observed in the field, is very limited. Some decoupled analyses were performed without modeling the formation of additional slip surfaces within the failed soil block during downslope displacement. Olson (2001) calculated the displacement from simplified kinetics analysis, as mentioned above. Two important aspects need to be considered in the post-quake analysis:

First, the constitutive model of the soil should be carefully selected to ensure that it can capture the behaviour at large deformation as observed in the field (e.g., the liquefied zone where the failure plane is generated). The majority of FE studies focused on the cyclic behaviour during the seismic event rather than the strain-softening behaviour during the event and the post-failure stages (e.g., Blázquez and López-Querol 2007). Gu et al. (1993)used a hyperbolic stress-softening model for loose sand to examine the progressive failure during the post-quake stage. However, their FE analyses were limited to a small displacement level.

Second, a large shear strain generates around the failure planes. Most FE programs that can be used for coupled hydraulic–mechanical analysis cannot handle a large deformation, as occurred in the San Fernando Dam failure (Fig. 5.1(a)), due to mesh distortion. Several studies used the material point method (MPM) which can theoretically model large deformation (Huang et al. 2020; Feng et al. 2021; Tjung and Soga 2021). However, they conducted preliminary analyses in which the failure patterns were still remarkably different from the field observation.

In summary, although several studies were dedicated to modeling the failure of this dam, complete modeling of the delayed slide incorporating large deformation, which has been done in this study, is very limited. This paper is organized in the following way: First, a brief description

of a large-deformation FE modeling technique in a Eulerian-based framework is presented. Second, new techniques for modeling seepage and in-situ stresses are presented. These two factors could significantly affect the failure. Third, simplified constitutive models for liquefiable and non-liquefiable soils are introduced. The estimation of geotechnical parameters is also presented in these sections. Fourth, the simulation results of the Lower San Fernando Dam failure, including the formation of failed soil blocks, their displacements, and comparison with the field observation, are shown. Finally, a parametric study is performed to explore the effect of several factors on the failure.

5.3 FE Modeling

Numerical analysis is conducted using Eulerian-based approach in Abaqus/Explicit FE software. Unlike a Lagrangian-based FE analysis, the mesh remains fixed, and the Eulerian material (soil) flows through the mesh. Therefore, the simulation can be continued over a large distance without any numerical issues due to mesh distortion, as commonly occurred in the Lagrangian-based FE analyses. Eulerian-based FE methods have already been adopted to analyze various geotechnical engineering problems (Qiu et al. 2011; Dutta et al. 2014; Hamann et al. 2015; Dey et al. 2015). The performance of the Eulerian-based FE modeling technique in geotechnical applications has been examined previously by comparing the results with other numerical modeling techniques, e.g., Remeshing and Interpolation Technique with Small Strain (RITSS) (Wang et al. 2013), Computational Fluid Dynamics (Saha et al. 2018), and also calibrated against field and centrifuge test data (Qiu et al. 2011; Zheng et al. 2017).

5.3.1 Model geometry and boundary conditions

Figure 5.2 shows the model geometry of the dam before the earthquake. Eulerian-based FE in Abaqus only supports three-dimensional modeling; therefore, the plane strain condition is modeled with one element length in the out-of-plane direction. The whole domain is discretized with 8-node linear brick (EC3D8RT) elements of uniform 0.5 m cubes. The FE model consists of 10 parts: rolled fill, ground shale, loose and medium to dense zones of upstream hydraulic fill, loose and medium to dense zones of downstream hydraulic fill, clayey core, berm, alluvium, and void (Fig. 5.2). The void and different parts of the soil are defined by the volume fraction tool in the software. $EVF = 0$, $0 < EVF < 1.0$ and $EVF = 1.0$ represent the elements without soil (void), partially and completely filled with soil, respectively.

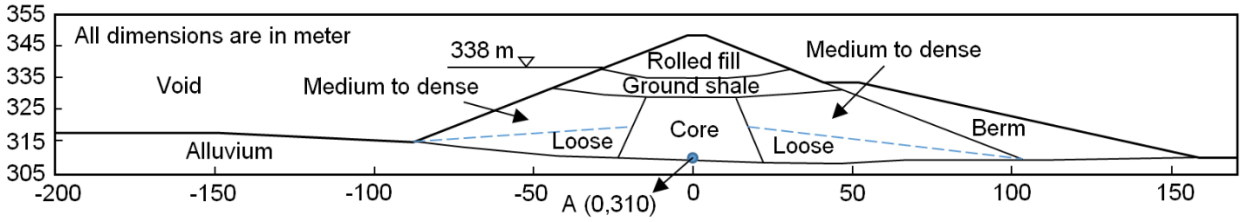

Figure 5.2 Eulerian-based FE model of the Lower San Fernando Dam

5.3.2 Triggering the slide

A pseudostatic analysis is commonly performed for the seismic stability of slopes using the limit equilibrium methods in which the earthquake load is given in the form of acceleration of the sliding soil mass ($K_h g$), where K_h is the seismic coefficient, and g is the gravitational acceleration. Note that $K_h g$ is generally well below the peak accelerations (Kramer 1996). For the Lower San

Fernando Dam, Seed (1979) calculated the factor of safety of 1.3 with his best possible approximation of K_h of 0.15, which means the failure should not have occurred unless there were some other factors in the post-slide stage (e.g., stress redistribution and strain-softening). The original pseudostatic method does not provide the displacement of the soil block, which can be obtained from the rigid sliding block analysis (Newmark 1965). Sarma (1975) extended the Newmark sliding block theory for seismic stability of an earth dam and soil displacement due to an earthquake. Rectangular, triangular, and half-sine pulses with the maximum earthquake acceleration of $K_m g$ were applied for half of the predominant period of the earthquake (T_0) to initiate displacement of the soil. For the cases they studied, the triangular pulse better modeled the strong earthquake scenarios. A simplified pseudo-dynamic FE approach, which is essentially an extension of Newmark's method, was developed in a Lagrangian-based framework to calculate the displacements of the Lower and Upper San Fernando Dams (e.g., Byrne et al. 1992; Jitno 1995). However, their method cannot simulate the formation of failure planes during downslope movement, as discussed above. Tan and Sarma (2008) also used a pseudostatic approach in FE modeling to determine the critical acceleration that causes the failure of a slope; however, they did not study post-slide displacement of the failed soil.

The major slide of the Lower San Fernando Dam started approximately 30 seconds after the earthquake ceased (Seed 1979). That means the flowslide occurred at the post-seismic stage due to gravitational loading and strain softening, rather than from the inertial force during the earthquake. However, strain-softening might have also occurred in some zones during the earthquake. Therefore, in this study, sliding is triggered by pseudostatic loading with a triangular

pulse of horizontal acceleration, as suggested by Sarma (1975), which allows the simulation of weakening of the soil even during the earthquake.

5.3.3 Modeling seepage

The seepage plays a major role in slope failure. Prior to the earthquake, the slope was in a steady-state seepage condition. Therefore, steady-state seepage modeling is performed first to establish in-situ stresses in the soil. The Eulerian-approach of the software can handle only single-phase material and does not have any built-in technique for modeling seepage. The following technique has been developed for seepage analysis.

The governing differential equation for two-dimensional seepage in saturated soil is

$$\frac{\partial}{\partial x}\left(k_{\mathrm{x}}\frac{\partial H}{\partial x}\right)+\frac{\partial}{\partial y}\left(k_{\mathrm{y}}\frac{\partial H}{\partial y}\right)+Q=m_{\mathrm{v}}\gamma_{\mathrm{w}}\frac{\partial H}{\partial t} \tag{5.1}$$

where H = total head; k_{x} and k_{y} = hydraulic conductivity in the x and y directions, respectively; Q = applied boundary flux (usually equal to 0 in an earth dam); m_{v} = coefficient of volume compressibility; γ_{w} = the unit weight of water; and t = time.

The pore water flow through Eulerian material is modeled using the thermal–hydraulic analogy, as used by Hamann et al. (2015) for pile installation. The governing equations for the seepage (Darcy's law) and heat conduction are

$$\mathbf{q}=\frac{\mathbf{k}}{\gamma_{\mathrm{w}}}(-\nabla p_{\mathrm{w}}) \tag{5.2}$$

$$\mathbf{f}=\boldsymbol{\kappa}(-\nabla T) \tag{5.3}$$

where $\mathbf{q}$ = Darcy velocity in porous media; $\mathbf{k}$ = hydraulic conductivity (a diagonal matrix of which k_x and k_y lie on the main diagonal, where k_x and k_y are the hydraulic conductivity in the *x* and *y* direction, respectively); p_w = pore water pressure; ρ_w = density of water; $\mathbf{f}$ = heat flux; $\boldsymbol{\kappa}$ = thermal conductivity; and T = temperature. Equations (5.2) and (5.3) show that p_w, $\mathbf{q}$ and $\mathbf{k}/\gamma_w$ in seepage analysis are analogous to T, $\mathbf{f}$ and $\boldsymbol{\kappa}$ in heat transfer analysis, respectively.

The coefficient of volume compressibility (Eq. (5.4)) is similar to $c\rho$ in heat transfer analysis (Eq. (5.5)).

$$m_v = \frac{\Delta\theta_v}{\Delta p_w} \tag{5.4}$$

$$c\rho = \frac{\Delta E}{\Delta T} \tag{5.5}$$

where c = specific heat capacity; ρ = density of the soil; $\theta_v = V_w/V_{wet}$ is the volumetric water content (where V_w is the volume of water, and V_{wet} is the total volume of the wet soil); E = thermal energy. In saturated soil, $\Delta\theta_v = \Delta V_w/V_{wet}$ is the increment of the water volume in a unit volume of soil, caused by a small increment of pore water pressure (Δp_w). In a seepage problem, the energy redistribution progresses with the water flow and leads to the change of θ_v. Therefore, $\Delta\theta_v$ in Eq. (5.4) is analogous to ΔE in Eq. (5.5). Here, ΔE is the increment of thermal energy (heat) due to a small increment in temperature (ΔT). In other words, $c\rho$ is analogous to m_v. Now, using the analogous parameters, heat transfer analysis is performed. In the present study, EC3D8RT elements are used, which are 8-noded thermally coupled linear brick, multi-material, and include reduced integration with hourglass control elements that allow heat transfer (conduction) analysis using thermal conductivity and specific heat capacity. In other words, seepage is modeled by heat

transfer analysis, where the initial hydraulic conditions (e.g., water pressure at the upstream surface of the dam) is defined by temperature, hydraulic conductivity by thermal conductivity, and the coefficient of volume compressibility by the product of specific heat capacity and soil density. Further discussion on seepage modeling parameters is provided in Section 5.4.6.

5.3.4 In-situ stress under steady-state seepage

In-situ stress, and especially the deviatoric stress, plays a major role in triggering slope failure. Therefore, the in-situ stresses need to be established properly, incorporating the effects of seepage, before slope stability analysis.

Based on the results of the steady-state seepage, the seepage forces can be calculated as

$$\boldsymbol{F} = \gamma_w \boldsymbol{i} V \tag{5.6}$$

where $\boldsymbol{F}$ is the seepage force on a cubical element; $\boldsymbol{i}$ is the hydraulic gradient; V is the volume of a cubical element. A computer program is written in Matlab to calculate the seepage force in the horizontal and vertical directions for the elements under the phreatic line. In the Matlab program, $\boldsymbol{i}$ is calculated from the temperature distribution and coordinates of the element ($i_x = \Delta T/\Delta x$ and $i_y = \Delta T/\Delta y$). The in-situ effective stresses are established by two-step loadings. In the first step, the initial stress fields (before filling the reservoir) are established by increasing gravitational acceleration to 9.81 m/s^2. In the second step, the seepage forces (Eq. (5.6)) and buoyancy forces are added to the elements under the phreatic line.

5.4 Modeling of soil

Earthquake-induced slope failure can be divided into three stages (Ambraseys and Srbulov 1995). Castro et al. (1989) proposed a similar concept for the failure of the Lower San Fernando Dam (Fig. 5.3), where the duration of co-seismic, post-seismic (before the major slide), and sliding phases are shown. The main purpose of the present study is to simulate the large-deformation behaviour of the slide; therefore, the sliding stage (Phase-III in Fig. 5.3) is the main focus in this study.

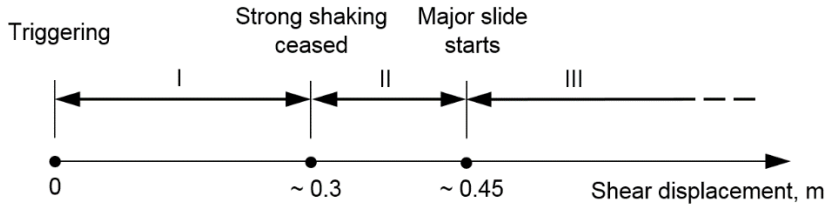

Figure 5.3 Schematic diagram of the phases of the failure of the Lower San Fernando Dam (adapted from Castro et al. 1989)

The geotechnical properties used in FE analysis are listed in Table 5.2. Further details on the selection of these model parameters are discussed below.

5.4.1 Hydraulic fill

Each of the upstream and downstream hydraulic fills is divided into a loose zone and a medium to dense zone in the model. As shown in Fig. 5.2, the loose zones are located at the bottom of the hydraulic fill (below the dashed lines). This assumption is based on the SPT tests conducted by Castro et al. (1989), where smaller blow counts occurred at the bottom of the hydraulic fill. The rest of the sandy hydraulic fill (above dashed lines) is assumed to be medium to dense, as larger

blow counts were reported (Seed et al. 1973; Castro et al. 1989). The following approaches are used to model hydaulic fills.

Table 5.2 Soil parameters used in FE analysis

Parameter	Rolled fill	Berm	Ground shale	Clayey Core	Hydraulic fill (loose)	Hydraulic fill (medium to dense)	Alluvium
ρ (kg/m^3)	2146	2146	1954	1954	2017	2017	2082
E (kPa)	2.0×10^4	2.0×10^4	2.0×10^4	2.0×10^4	2.0×10^4	2.0×10^4	1.0×10^6
ν	0.35	0.4	0.35	0.48	0.48	0.48	0.48
ϕ_p (°)	45	50	45	-	-	37	-
ϕ_c (°)	35	40	35	-	-	30	-
ψ_p (°)	12.5	12.5	12.5	-	-	8.75	-
ψ_c (°)	0	0	0	-	-	0	-
c_p (kPa)	2	2	20 (2, 50)	-	-	60 (2, 20, 100)	-
c_r (kPa)	2	2	2	-	-	2	-
$s_{u(yield)}$ (kPa)	-	-	-	$0.3\sigma'_{vo}$	$0.281\sigma'_{vo}$	-	-
$s_{u(liq)}$ (kPa)	-	-	-	$0.1\sigma'_{vo}$	$0.056\sigma'_{vo}$ ($0.112\sigma'_{vo}$)	-	-
ε_r^p	30%	30%	30% (60%)	30% (60%)	8%	30% (60%)	-

Note: Parameters in parenthesis are used for parametric study.

(a) Loose hydraulic fill

The generated excess pore water pressure due to the earthquake (Fig. 2.13(a)) could liquefy the loose soil, which was considered the potential cause of triggering the failure (Seed et al. 1973). In a simplified way, Gu et al. (1993) reduced the shear strength of two elements in this zone to trigger the failure. Note, however, that a zone of soil might have been weakened due to the earthquake, although a global failure of the slope did not occur. Such an incomplete failure (i.e., formation of shear bands) is modeled in this study by applying a pseudostatic load.

In the present study, an undrained strength analysis (USA) approach (Ladd 1991) is adopted to model the loose part of the hydraulic fill. The USA was originally proposed for modeling undrained behaviour of clay (Ladd 1991). However, the failure of the loose hydraulic fill in this case occurred in a short period; and therefore, the dissipation of pore water pressure was limited. In addition, the failed soil block continuously displaced over the failure plane formed through this soil (Fig. 5.1), which implies that rapid shearing occurred along the failure planes through the loose hydraulic fill during the whole period of failure. Therefore, an undrained condition is used for this soil. The peak undrained shear strength ($s_{u(yield)}$ in Table 5.2) is defined as a function of initial effective vertical pressure (σ'_{v0}) that has been calculated considering the seepage-induced pore water pressure, as discussed above. Note that although the undrained shear strength is defined in terms of effective stresses, the total stress analysis is performed without calculating the excess pore pressure and effective stress. In this study, the total stress represents the stress without initial pore water pressure, which is equal to the initial effective stress plus the shear-induced excess pore water

pressure. Following the work of Olson and Stark (2001), $s_{u(yield)} = 0.281\sigma'_{v0}$ is used for the representative case analysis (Table 5.2).

The undrained behaviour of the loose hydraulic fill in triaxial compression condition is shown schematically in Figs. 5.4(a) and 5.4(b). These figures are used only to explain the mechanisms, including stress–strain behaviour, excess pore water pressure (Δu), total stress path (TSP) and effective stress path (ESP). However, the numerical simulations are performed using the undrained shear strength. Figure 5.4(b) shows that the deviatoric stress (q) increases to point B′ and then gradually decreases to the minimum value (point C′) as the effective stress decreases due to the generation of excess pore water pressure. This minimum strength is called the undrained steady-state shear strength or the liquefied shear strength ($s_{u(liq)}$). In the present study $s_{u(liq)} = 0.056\sigma'_{v0}$ is used, which is in the range between the lower bound and upper bound values reported by Olson and Stark (2002). A larger $s_{u(liq)}$ of $0.112\sigma'_{v0}$, suggested by Olson and Stark (2002) to consider kinetics of failure, is used in the parametric study.

During the earthquake, excess pore water pressure might have developed due to cyclic loading, which could have brought the stress state of a soil element to any point on AB′C′ in Fig. 5.4(a). Also, a considerable shear displacement occurred before the major slide (Fig. 5.3). As mentioned above, Phase-I and Phase-II are not simulated, as the focus of the present study is to model the large displacements in Phase-III. For simplicity, the calculation starts from the initial state of the soil element (point A) and then deforms elastically (path AB) until it reaches the yield envelope during pseudo-static loading and subsequent failure. After that, the undrained shear strength decreases with shear strain, which is modeled using a tri-linear line (Fig. 5.4(b)). The shear

stress reaches the peak undrained shear strength elastically, from where the plastic shear strain (ε^p) starts to develop. Subsequently, s_u decreases linearly to $s_{u(liq)}$ at ε_r^p and then remains constant.

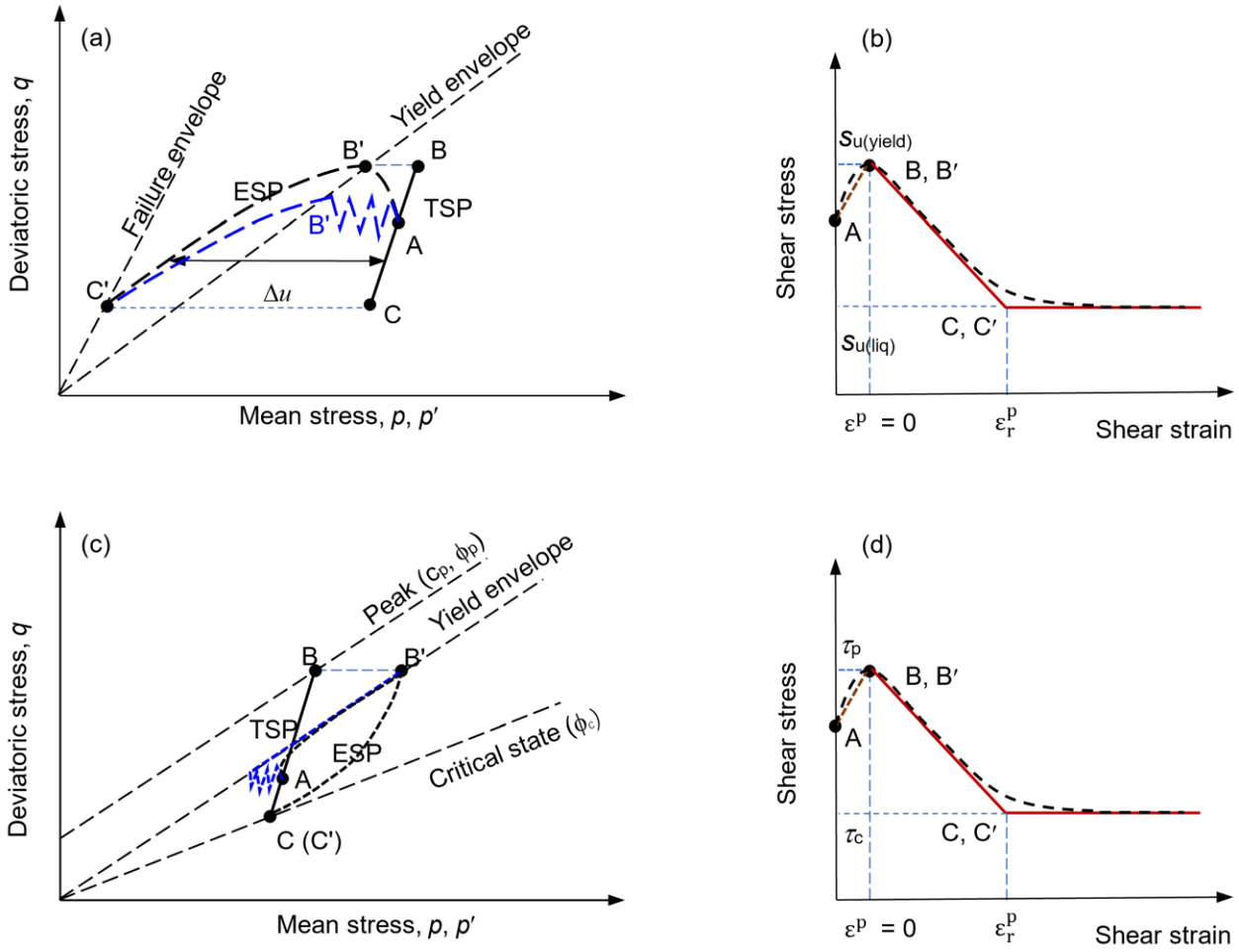

Figure 5.4 Schematic behaviour of the sandy hydraulic fill: (a) undrained stress path of loose sand; (b) stress–strain behaviour; (c) stress paths of medium to dense sands; (d) stress–strain behaviour

(b) Medium and dense hydraulic fills

The medium to dense hydraulic fills over the loose hydraulic fill are not expected to liquefy due to cyclic loading during an earthquake; instead, the soil will have the tendency to expand, which will generate negative excess pore water pressure (Fig. 2.13(b)). Castro et al. (1989) also recognized the effects of this dilative tendency in the toe dike of the San Fernando dam.

Figures 5.4(c) and 5.4(d) show schematically the total and effective stress path and stress–strain curve that might be followed by a soil element in the medium and dense fill under triaxial loading conditions. Positive pore pressure might be generated during the earthquake (Phase-I) and then soil might follow the yield line in both Phase-I and Phase-II loading stages, and finally reach point B′ in Fig. 5.4(c) at the end of Phase-II. The stress state of some soil elements might move to point B′, also due to monotonic shearing in Phase-II. At this stage, the total stress in the soil element is at point B, which is above the effective stress yield envelope. In other words, the soil gained some strength because of negative excess pore pressure generation. As mentioned before, the objective of this study is to simulate large deformation behaviour in Phase-III, without simulating Phases-I and II. Therefore, the shear strength at the start of the calculation should be defined considering the strength gain due to negative pore pressure generation during Phases-I and II.

Phase-III failure is relatively slower, at least compared to that in the earthquake loading stage. Therefore, partial drainage is expected along the shear plane, at least locally. Note that, unlike the loose fill over which the failed soil displaces, the overlying medium and dense sands might get more time for partial local drainage as they move as an intact block unless there is a shear

band formation, as described in later sections. Therefore, modeling of these medium to dense fills is more complicated because the shear strength reduces due to two interrelated processes:

(i) time-dependent reduction of suction that develops during Phases-I and II, which is related to local drainage, and

(ii) the reduction of angles of internal friction and dilation due to accumulated plastic shear strains (Castro et al. 1989; Han and Vardoulakis 1991).

In addition, the software used in this study allows the simulation only for single-phase material. This means excess pore pressure and effective stress cannot be calculated as in a coupled analysis. Therefore, the Mohr–Coulomb model of total stress is used to define the soil behaviour, using an apparent cohesion (c) and friction angle (ϕ). The apparent cohesion in total stress analysis was used in previous studies (Bishop and Eldin 1950; Idinger and Wu 2019). Seed et al. (1973) conducted undrained triaxial compression tests on the hydraulic fill used for this dam and showed the peak apparent cohesion (c_p) of 60 kPa in some cases; however, it is negligible (~ 2 kPa) at large strains. In the present study, c_p = 60 kPa is used for the base case analysis, while it varies between 2 kPa and 100 kPa in the parametric study. Similarly, ϕ at the peak (ϕ_p) and critical state (ϕ_c) are assumed to be 37° and 30°, respectively, based on laboratory test data presented by Seed et al. (1973) and Castro et al. (1989). The maximum dilation angle (ψ_p) is 8.75°, which reduces linearly to zero at ε_r^p. The friction and dilation angles are decreased linearly, as shown in Fig. 5.4(d).

Similar to the loose hydraulic fill modeling, the Phase-I and Phase-II are not simulated in this medium to dense hydraulic fill; instead, the effects of those two phases are incorporated by defining a higher strength above the yield envelope using c_p and ϕ_p. The soil elements reach the

peak strength envelope due to undrained elastic deformation. With further shear deformation, the shear strength parameters diminish gradually from ϕ_p to ϕ_c and ψ_p to zero (Fig. 5.4(d)).

In finite element program, a user-subroutine VUSDFLD is used to define the material properties. The peak shear strength ($s_{u(yield)}$)/parameters (ϕ_p and ψ_p) are calculated using the initial stresses. The plastic shear strain is called in each time increment, which is then used to calculate the mobilized s_u for loose fill (Fig. 5.4(b)) and c and ϕ for medium and dense fill (Fig. 5.4(d)).

5.4.2 Clayey core

Castro et al. (1989) showed that the core was mainly composed of a silty clay with about 20% of sandy layers ranging from about 25.4 to 762 mm thick. About 70% sandy layers and 30% clayey layers were seen in the transition zone between the clayey core and the sandy hydraulic fill. Dafalla et al. (2020) indicated that the hydraulic conductivity of sand-clay mixtures is governed by the clayey fraction, which leads to an undrained condition during the dam failure. The clayey core is expected to have a strain-softening behaviour under undrained conditions. In the present study, a bilinear stress−strain behaviour is adopted again. The $s_{u(yield)}/\sigma'_{v0}$ is chosen to be 0.3, which is in line with $s_{u(yield)}/\sigma'_{v0}$ = 0.2–0.3 that was presented for the clayey core by Castro et al. (1989). Liquefied sand filled the failure cracks in the clayey layers (Seed et al. 1973); therefore, the residual strength of the clayey core is highly dependent on the liquefied sand, and the $s_{u(liq)}/\sigma'_{v0}$ is assumed to be 0.1 for the representative case, based on the stress−strain curve proposed by Castro et al. (1989). ε_r^p is assumed to be 30% in the representative analysis. Considering the uncertainty of ε_r^p, 60% is used for the parametric study.

5.4.3 Rolled fill and ground shale

The ground shale layer was mainly composed of widely graded sand and silty sand (Castro et al. 1989). The rolled fill was a mixture of shale and gravelly material (Castro et al. 1989). Both the rolled fill and ground shale layer were in a dense condition, based on SPT results (Castro et al. 1989). The critical state friction angle of 35° is used for both layers, following the work of Castro et al. (1989). The peak friction angle is assumed to be 45° for these two dense layers. Based on Bolton (1986), the dilation angles at the peak and critical state are 12.5° and 0°, respectively. The peak cohesion (c_p) and residual cohesion (c_r) are assumed to be 20 kPa and 2 kPa, respectively, for the ground shale, to consider the effects of induced suction. The drained condition with a constant cohesion of 2 kPa (to avoid numerical issues) is adopted for the rolled fill, as it is well above the phreatic line. Different values of apparent cohesion are also used in the parametric study to investigate its effects on failure. The same bilinear stress–strain curve is adopted for both soils and ε_r^p is assumed to be 30%. Considering the uncertainty of ε_r^p, analyses are also performed with ε_r^p = 60% in the parametric study. The reduction of the friction angle and dilation angle are modeled using a modified Mohr–Coulomb model, by developing a user-subroutine VUSDFLD.

5.4.4 Berm

The berm was essentially rolled fill, and most of it was above the phreatic line before the slide. Based on Castro et al. (1989), the critical state friction angle of 40° is used. The peak friction angle is assumed to be 50° for this dense soil. Based on Bolton (1986), the peak dilation angle and the residual dilation angle are 12.5° and 0°, respectively. ε_r^p is assumed to be 30%.

5.4.5 Alluvium

The alluvium consisted of stiff clay with lenses of dense sandy material (Castro et al. 1989). As no failure occurred through this soil layer, an elastic model is used to model the alluvium.

5.4.6 Seepage parameters

Isotropic hydraulic conductivity ($k = k_x = k_y$) is assumed in the simulation of the steady-state seepage of the Lower San Fernando Dam (Table 5.3). The seepage parameters are selected following Ming and Li (2003). Those seepage parameters listed in Table 5.3 are transferred to thermal parameters in Eulerian-based FE, based on the theory introduced in Section 5.3.4. The total heads of upstream and downstream are 338.0 m and 309.5 m, respectively, and they are transferred to a temperature boundary in this model.

Table 5.3 Soil parameters used in seepage analysis

Parameters	Rolled fill	Berm	Ground shale	Clayey Core	Hydraulic fill	Alluvium
Density, ρ (kg/m^3)	2146	2146	1954	1954	2017	2082
Hydraulic conductivity, k (m/s)	5.0×10^{-6}	1.0×10^{-4}	1.0×10^{-4}	5.0×10^{-6}	1.0×10^{-4}	1.0×10^{-5}
Coefficient of volume compressibility, m_v (MPa^{-1})	0.3	0.02	0.02	0.3	0.02	0.3

5.4.7 Pseudostatic load

In the 1971 earthquake, the predominant period (T_0) was 0.5 s, and the peak acceleration ($K_m g$) was 0.6g (Chang 1976). Now, following the recommendations of Sarma (1975), a triangular impulse of 0.25 s duration (i.e., $T_0/2$) and a horizontal maximum acceleration ($K_m g$) of 0.6g are applied to the upstream side. The effects of T_0 and K_m on failure are discussed in the parametric study. Analyses are also performed for the rectangular pulse for earthquake loading (Sharma 1975) and pseudostatic loading in the downstream direction.

5.5 Results

5.5.1 Steady-state seepage

The seepage analyses are conducted in Eulerian-based FE, as discussed above, and the results are compared with SEEP/W (GEOSLOPE International Ltd 2012) analysis. Figures 5.5 and 5.6 show the total head distributions at t = 1 day and at the steady state, respectively. Eulerian-based FE simulation (banded contours) produced similar results as the SEEP/W analysis (the equipotential lines). At the initial stage of the analysis (t = 1 day), the total head at the central and the downstream part is significantly lower than the steady state, indicating a transient state at that time. The change of the total head with time at point A (as shown in Fig. 5.2) is shown in Fig. 5.7. The total head increases rapidly in the first 4 days and reaches a plateau at around 6 days, and a very small difference is found for the two numerical techniques. In summary, the developed numerical techniques of the Eulerian-based FE method can simulate the seepage properly.

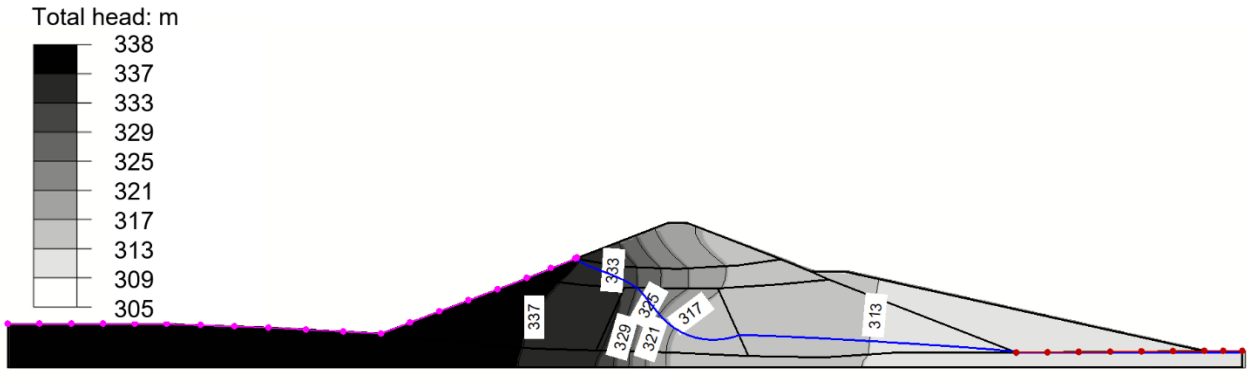

Figure 5.5 Total head distribution 1 day after reservoir filling

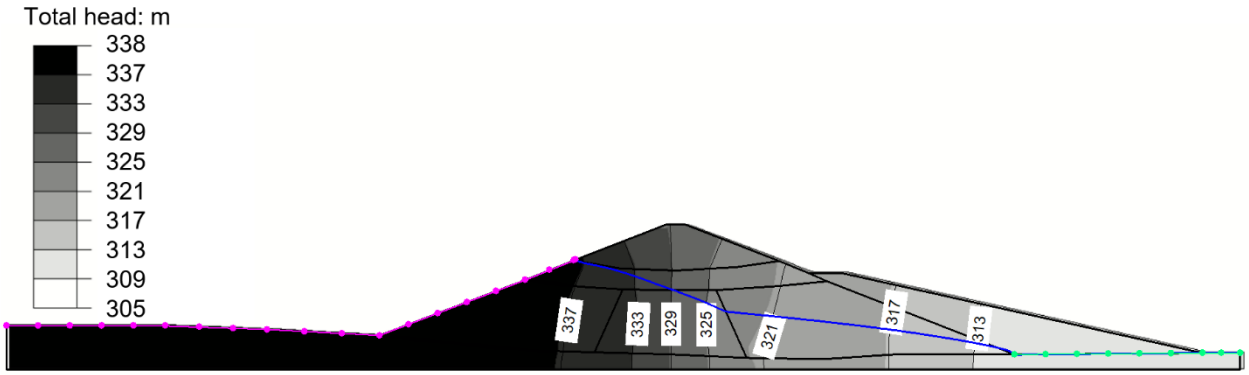

Figure 5.6 Total head distribution at the steady state

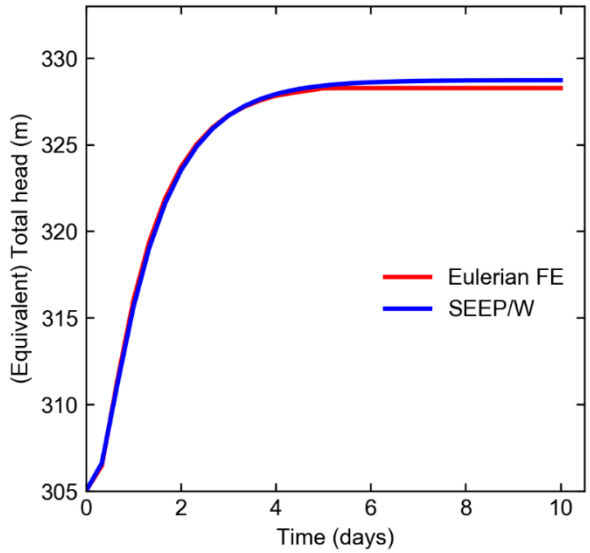

Figure 5.7 Total head variation with time at point A in Fig. 5.2

5.5.2 Initial stress

Based on the steady-state seepage, the seepage forces and buoyancy for each element are calculated and applied to the submerged Eulerian elements. At this stage only, the materials are assumed to be elastic to establish the in-situ stresses. A highly elastic modulus is used to ensure a minimal deformation.

To validate the proposed in-situ stress modeling technique in Eulerian-based FE, simulation is also performed using SIGMA/W (GEOSLOPE International Ltd 2013). Figure 5.8 presents the deviatoric stresses from Eulerian-based FE and SIGMA/W. Minimal difference is seen in the two models, proving the effectiveness of the proposed technique in modeling the in-situ stress of the Lower San Fernando Dam.

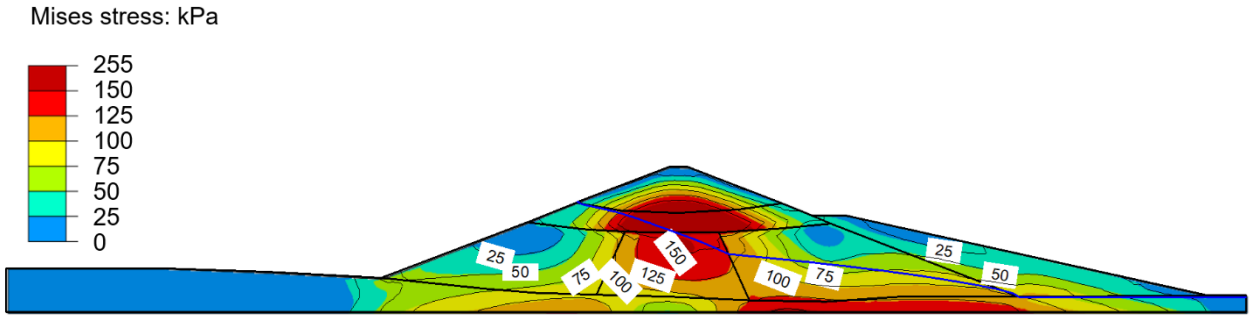

Figure 5.8 Deviatoric stress in Eulerian-based FE and SIGMA/W

5.5.3 Progressive failure of the Dam

A representative analysis with the soil parameters in Table 5.2 is conducted to show the failure mechanisms and the failure pattern. To validate the proposed modeling technique, the FE

simulated failure pattern is compared to the field observation reported in previous studies. The deviatoric plastic strain contours are used to show the failure surfaces (Fig. 5.9).

As mentioned above, the failure is triggered by pseudostatic analysis, instead of simulating the earthquake shaking. At the end of the pseudostatic loading, a shear band (f_1) is initiated from the upstream toe and propagates towards the clayey core along the interface between the upstream hydraulic fill and the alluvium (Fig. 5.9(a). The location of the shear band (f_1) is similar to the liquefaction zone observed in the field (Fig. 5.1). This indicates that a comparable triggering effect is simulated from this numerical model. Also, the slide does not occur during this loading process, which is consistent with the field condition; the slide occurred after the earthquake (Seed et al. 1973).

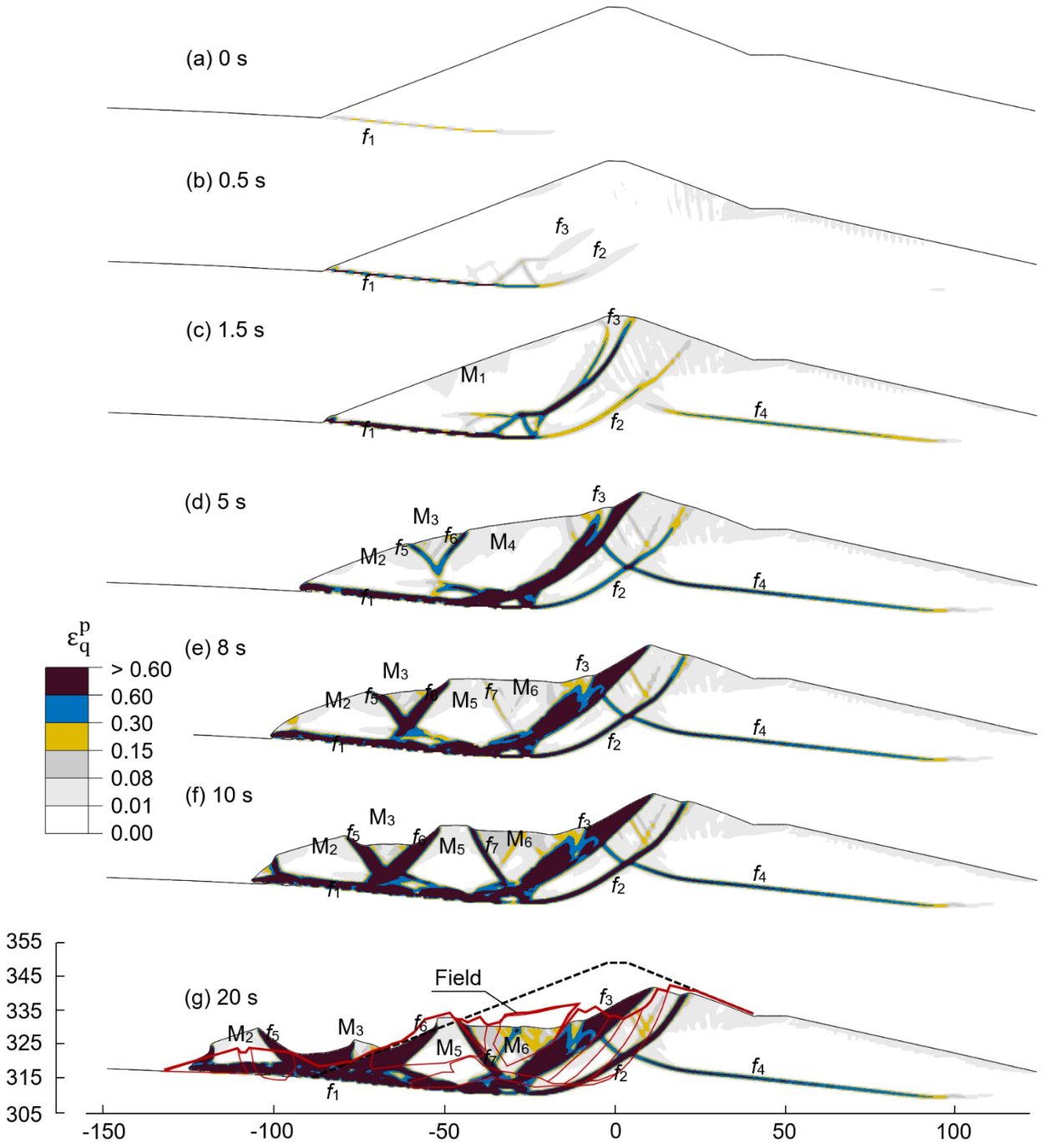

Figure 5.9 Deviatoric plastic strain contours of the representative case

As the shear band f_1 reaches the core area, two curved shear bands f_2 and f_3 start to form from the right end of f_1 as the lateral resistance decreases (Fig. 5.9(b)). With the strain-softening process and its induced stress redistribution, the shear band f_2 propagates up towards the downstream surface of the dam, and f_3 diverges into two shear bands approaching the crest of the dam (Fig. 5.9(c)). Close to the f_2 and f_3, a couple of almost parallel minor shear bands are generated almost parallelly. These shear bands, together with f_2 and f_3, present a similar pattern to the multiple parallel shear bands observed in the field (Fig. 5.1).

With further development of the shear band f_3, a rotational slide of a soil block (M_1) starts to move towards the upstream direction along the failure plane formed by shear bands f_1 and f_3 (Fig. 5.9(c)). A failure plane is not fully developed through the shear band f_2; however, the length and shear strain of this shear band increase with the movement of this major slide. This is in line with the explanation by Seed (1979), who showed that the factor of safety of the backscarp was 1.03 following the major slide. Nevertheless, this retrogressive nature was not successfully captured in any numerical analysis.

Furthermore, a shear band (f_4) forms in the downstream hydraulic fill and propagates towards dam crest; however, a downstream slope failure does not fully develop (Fig. 5.9(c)). The occurrence of the f_4 was validated by field investigations (Castro et al. 1989; Seed et al. 1973). The absence of a downstream slide can be explained with a higher shear resistance added by the berm (Ming and Li 2003), or the unloading effect caused by the upstream slide (Castro et al. 1989).

As the failure block M_1 displaces further towards the upstream direction, new shear bands (f_5 and f_6) occur to divide M_1 into three failure blocks, M_2, M_3 and M_4, at around 5 s (Fig. 5.9(d)).

Among them, M_2 is a "Δ-shape" block, and M_3 is a "∇-shape" block. With further displacement of the slide, the failure block M_2 moves further than other blocks, leaving a shallower zone between them (Figs. 5.9(e)–5.9(g)). This can explain the occurrence of block 9 and the separation of blocks 7 and 10 in the field (Fig. 5.1(b)).

Another shear band (f_7) forms with further settlement of the failure mass. This divides the M_4 into a trapezoid block, M_5, and a "∇-shape", M_6. M_5, which is nearly a "Δ-shape" block, can be identified as block 7 in the field, while M_6 is similar to block 5, observed by comparing Fig. 5.9(g) and Fig. 5.1. Note that these blocks are similar to horsts and grabens, which were commonly observed in a spread type of sensitive clay landslide (Dey et al. 2015). Though a spread failure was not present in the failure of the Lower San Fernando Dam, the occurrence of horsts and grabens can still be generated in a rotational slide (Zhang et al. 2020).

5.6 Parametric studies

The results of a parametric study are presented in this section. However, the purpose is not to provide a comprehensive set of results; instead, the focus is to examine the effects of the following parameters: (i) apparent cohesion, (ii) rate of strength degradation, (iii) residual strength of liquefiable soil, and (iv) pseudostatic load. The relative influence of these parameters on the failure patterns and the displacement of soil are investigated.

5.6.1 Effects of the apparent cohesion

The value of apparent cohesion of the ground shale and the medium to dense hydraulic fill depends on dissipation of pore water pressure. In the field, their drainage condition is expected to be somewhere between drained and undrained conditions, and it is difficult to estimate from available data. Therefore, a parametric study is performed with different values of cohesion to understand its influence on failure. First, the drained condition is modeled in Case A, where the cohesion is a constant, 2 kPa, for both the ground shale and the medium to dense hydraulic fill. In Case B, c_p = 50 kPa and c_r = 2 kPa are used for the ground shale, while the parameters of the rest of the soil remain identical in the representative study. Furthermore, c_p = 20 kPa and c_r = 2 kPa are adopted for both the ground shale and the medium to dense hydraulic fill in Case C. In Case D, larger peak cohesions (c_p = 100 kPa) are used for the medium to dense hydraulic fill, assuming a higher suction in this soil, while the peak cohesion remains 20 kPa for the ground shale in this case. Figure 5.10 shows the deviatoric plastic strain distributions at the end of the failure for different sets of apparent cohesions, from Case A to Case D. The failure patterns of Cases A–D (Figs. 5.10(a)–5.10(d)) are not remarkably divergent from the representative case (Fig. 5.9(g)), as all of them show a similar location of main shear bands (e.g., f_1, f_2, f_3, f_4, f_6 and f_7) and failure blocks (e.g., M_3, M_5 and M_6). Nevertheless, the size of these failure blocks varies from case to case. This could be attributed to the selection of apparent cohesions. A smaller apparent cohesion generally leads to a lower shear strength and thus larger area of plastic zone, which reduces the size of blocks. For example, the upstream toe area is mostly in the residual state in Case A (Fig. 5.10(a)) due to a low value of apparent cohesion ($c_p = c_r$ = 2 kPa) for the medium to dense hydraulic fill. Even when

c_p = 20 kPa and c_r = 2 kPa are adopted for this soil in Case C, the toe block, M_2, in the representative case (Fig. 5.9(g)) and Case D (Fig. 5.10(d)) cannot be observed (Fig. 5.10(c)); instead, two small blocks and a larger residual zone are shown at the same area. This is consistent with the field observation; two blocks (10 and 11) existed at the toe (Fig. 5.1), indicating that the value of the peak apparent cohesion in the field might not be as high as we assumed in the representative study (c_p = 60 kPa). The apparent cohesion also affects the size of M_5 and M_6, due to different locations of f_7 (Figs. 5.10(a)–5.10(d)). Note that other factors which can also affect the formation of the failure blocks, e.g., the influence of the viscosity and inertia of the reservoir water on the flowslide motion (Stoecklin et al. 2020), are not considered in this study.

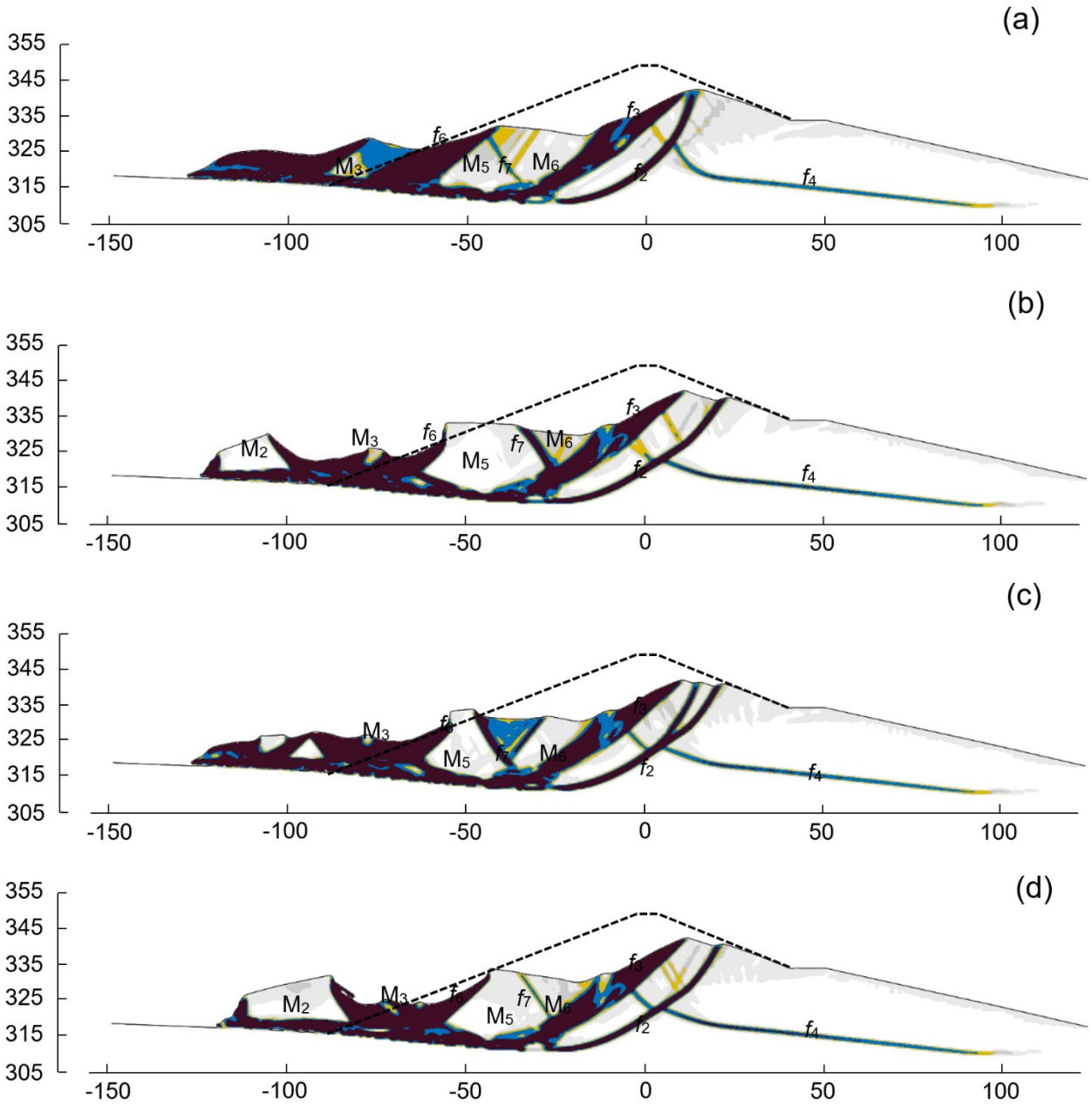

Figure 5.10 Deviatoric plastic strain contours for different apparent cohesions: (a) Case A: both ground shale and medium to dense hydraulic fill: $c_p = c_r = 2$ kPa; (b) Case B: ground shale: $c_p = 50$ kPa and $c_r = 2$ kPa; medium to dense hydraulic fill: $c_p = 60$ kPa and $c_r = 2$ kPa; (c) Case C: both ground shale and medium to dense hydraulic fill: $c_p = 20$ kPa and $c_r = 2$ kPa; (d) Case D: ground shale: $c_p = 20$ kPa and $c_r = 2$ kPa, medium to dense hydraulic fill: $c_p = 100$ kPa and $c_r = 2$ kPa

5.6.2 Effects of the residual shear strength of the liquefiable soil

Figure 5.11 shows the failure patterns of Case E where $s_{u(liq)} = 0.112\sigma'_{vo}$ is used for the loose hydraulic fill. In comparison with the representative case (Fig. 5.9), where $s_{u(liq)} = 0.056\sigma'_{vo}$, a higher value of $s_{u(liq)}$ influences the failure pattern in several ways. In Case E, a significantly smaller runout distance (15.5 m) than the representative case (40 m) is observed, and the failure mass movement ceases at around 14 s, which is 8.5 s earlier than the representative case. This gap can be explained with their difference in the shear resistance. For the same reason, the failure blocks are more intact, as a smaller plastic zone is shown in Case E. The failure still causes formation of horsts and grabens, similar to the representative case. A similar effect was reported by Olson (2001), and therefore $s_{u(liq)}$ was adjusted to match the field results. However, his simplified approach cannot simulate the formation of soil blocks.

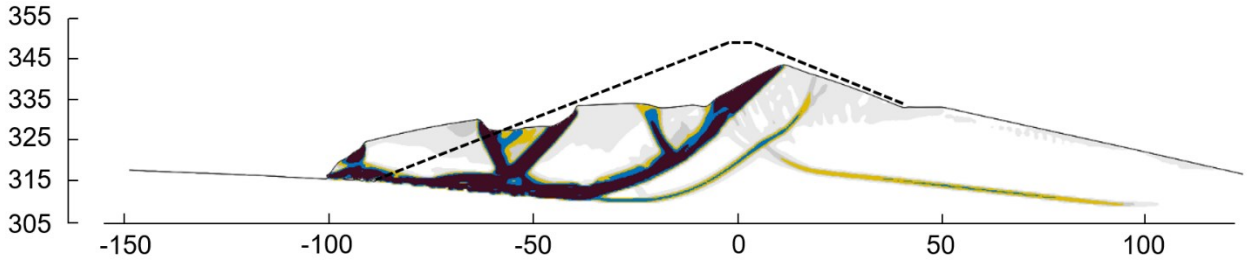

Figure 5.11 Deviatoric plastic strain of Case E: $s_{u(liq)} = 0.112\sigma'_{vo}$ for loose hydraulic fill

5.6.3 Effects of shear strength degradation rate

The effects of the rate of degradation are investigated by using different ε_r^p. The toe movement (38 m) only decreases 2 m, compared to the representative case, while the strength degradation rate decreases by 50% for the ground shale alone in Case F (Fig. 5.12(a)). In contrast,

as shown in Case G and F (Figs. 5.12(b) and 5.12(c)), the decrease of the strength degradation rate of the clayey core and medium to dense hydraulic fill, respectively, poses a more noticeable effect on the mass movement, because their run-out distances are 5.5-m and 10.5-m less than the representative case, respectively. However, the failure patterns of the representative case, Case-F, Case-G, and Case-H are still similar. That is to say, the effect of the strength degradation rate on the failure pattern is not significant.

5.6.4 Effects of the pseudostatic load

As mentioned in Section 5.4.7, various sets of pseudostatic loads (Case I to Case N as presented in Table 5.4) are implemented in Eulerian-based FE model. Figure 5.13 shows the failures that are triggered by different pseudostatic loads. The toe displacement increases when using a larger acceleration or (and) there is a longer loading duration towards the upstream direction (Figs. 5.13(a)–5.13(e)), while the failure patterns remain similar. Therefore, different intensities of the pseudostatic loads do not influence the sliding process significantly. This gives more confidence when determining the pseudostatic load, as its uncertainty can be accommodated to some extent. Nevertheless, an upstream progressive failure is triggered with a remarkably different failure pattern by applying a pseudostatic load towards the downstream direction, as shown in Fig. 5.13(f). A possible reason is that this reversed pseudostatic load led to a different location of the initial slip surface and size of the initial sliding block. Therefore, the following sliding process is altered as the driving force is directly linked to the size and shape of the failure block, especially the initial block.

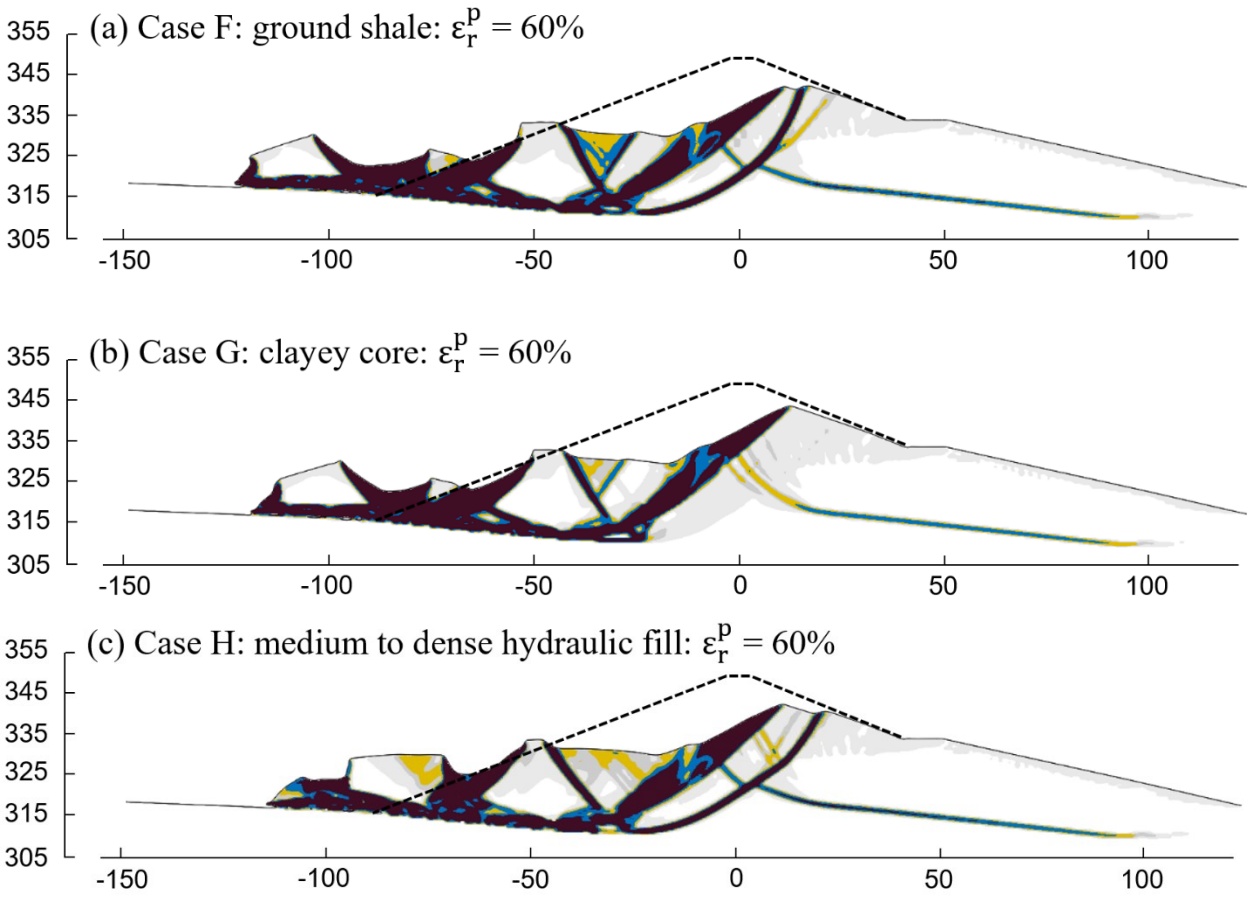

Figure 5.12 Deviatoric plastic strain contours for different strength degradation rates: (a) Case F: ground shale: ε_r^p = 60%; (b) Case G: clayey core: ε_r^p = 60%; (c) Case H: medium to dense hydraulic fill: ε_r^p = 60%

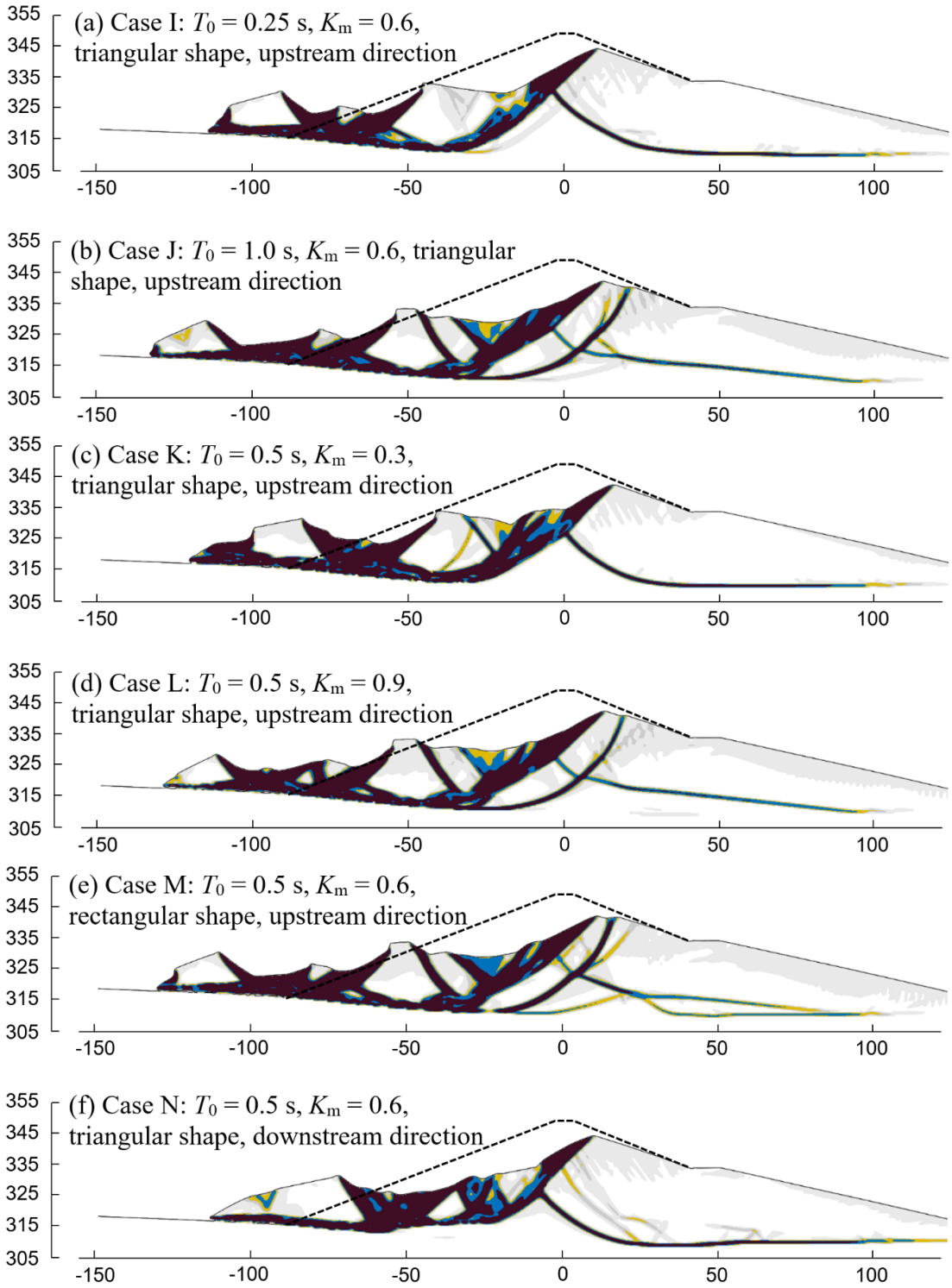

Figure 5.13 Deviatoric plastic strain contours for different pseudostatic loads: (a) Case I; (b) Case J; (c) Case K; (d) Case L; (e) Case M; (f) Case N

5.7 Conclusions

A flow slide occurred at the Lower San Fernando Dam about 30 seconds after a major earthquake (M = 6.6) in 1971. Numerous studies were conducted to investigate this famous failure. However, the post-earthquake sliding process was not adequately addressed, due to the limitations of the analysis tools. A traditional Lagrangian-based FE cannot be used for large-deformation modeling due to mesh distortion. Eulerian-based FE, which is free of mesh distortion, is adopted in this study to simulate the entire process of the flowside of the Lower San Fernando Dam.

A technique is proposed to model transient and steady-state seepage based on the thermal–fluid analogy theory by using thermally coupled Eulerian elements. Based on the seepage analysis, the in-situ stress of the Lower San Fernando Dam is established in Eulerian-based FE analysis. In addition, simplified constitutive soil models are implemented to account for the large-deformation behaviour of the soil layers. A pseudo-static load is chosen to produce a similar liquefaction zone as the field observation and thus trigger the flow slide.

A representative study is conducted first to show the failure mechanism of the slide during the post-earthquake stage. The final failure pattern, e.g., the location of shear bands and failure blocks, is close to the field observation. Moreover, the development of shear bands and failure blocks is successfully explained, based on the complete post-failure process modeled in Eulerian-based FE model, which cannot be explained from the field investigations and previous studies.

A parametric study is performed to investigate the influence of several parameters on the failure pattern. The overall post-failure mechanism is not significantly affected by the value of apparent cohesion, while the intactness of the upstream toe area increases with a higher apparent

cohesion. The run-out distance can decrease when the residual shear strength of the loose hydraulic fill increases. In addition, the change of degradation rate of shear strength of ground shale, clayey core, and medium to dense hydraulic fill poses a marginal difference on the run-out distance and the failure pattern. Furthermore, the overall failure pattern is not greatly influenced by the value and duration of the pseudo-static load. However, the direction of this load can produce a significant effect on the location of the shear bands and failure blocks.

In this study, the reservoir water is not modeled. Instead, its effect is applied on the dam via the seepage forces and buoyancy. Future development is needed to model the soil–reservoir water interaction behaviour. Furthermore, advanced soil constitutive models that can address the co-seismic stage of the failure can be used to better simulate the triggering process. However, this would require a significant effort to calibrate the soil parameters, as these constitutive models usually consist of a larger number of equations and parameters. Due to the limited data from the previous geotechnical investigations, this calibration process can become considerably challenging.

Notations

ε_r^p residual deviatoric plastic strain

θ_v volumetric water content

$\boldsymbol{\kappa}$ thermal conductivity

v Poisson's ratio

ρ density of the soil

ρ_w	density of water
σ'_{v0}	pre-failure vertical effective stress
ϕ_c	critical state friction angle
ϕ_p	peak friction angle
ψ_p	peak dilation angle
ψ_c	critical state dilation angle
c	specific heat capacity
c_p	peak apparent cohesion
c_r	residual apparent cohesion
E	thermal energy
E	Young's modulus
$\mathbf{f}$	heat flux
$\boldsymbol{F}$	seepage force
g	gravitational acceleration
H	total head
$\boldsymbol{i}$	hydraulic gradient
$\mathbf{k}$	hydraulic conductivity
K_h	seismic coefficient
K_m	maximum acceleration/g at the record
m_v	coefficient of volume compressibility
p_w	pore water pressure

$\mathbf{q}$ Darcy velocity in porous media

Q applied boundary flux

$s_{\mathrm{u(liq)}}$ liquefied shear strength

$s_{\mathrm{u(yield)}}$ peak shear strength

T temperature

T_0 predominant period of the earthquake

t time

V volume of an element

V_{w} volume of water

V_{wet} total volume of the wet soil

Acknowledgements

The works presented in this paper have been supported by the Research and Development Corporation of Newfoundland and Labrador and the Natural Sciences and Engineering Research Council of Canada (NSERC).

References

Ambraseys, N., and Srbulov, M. (1995). "Earthquake induced displacements of slopes." *Soil Dynamics and Earthquake Engineering*, 14(1), 59–71.

Beaty, M. H., and Byrne, P. M. (2000). "A Synthesized Approach for Predicting Liquefaction and Resulting Displacements." *Proc. 12th World Conference on Earthquake Engineering*, New

Zealand Society for Earthquake Engineering, Wellington, New Zealand, 2–9.

Bishop, A. W., and Eldin, G. (1950). "Undrained triaxial tests on saturated sands and their significance in the general theory of shear strength." *Géotechnique*, 2(1), 13–32.

Blázquez, R., and López-Querol, S. (2007). "Endochronic-Based Approach to the Failure of the Lower San Fernando Dam in 1971." *Journal of Geotechnical and Geoenvironmental Engineering*, 133(9), 1144–1153.

Bolton, M. D. (1986). "The strength and dilatancy of sands." *Géotechnique*, 36(1), 65–78.

Byrne, P. M., Jitno, H., and Salgado, F. (1992). "Earthquake induced displacements of soil-structures systems" *Earthquake Engineering, Tenth World Conference*, Balkema, Rotterdam, 1407–1412.

Castro, G., Keller, T., and Boynton, S. S. (1989). "Re-Evaluation of the Lower San Fernando Dam, Report 1: An Investigation of the February 9, 1971 Slide." Winchester, Massachusetts.

Chang, F. K. (1976). "An Empirical Interpretation of the Effects of Topography on Ground Motion of the San Fernando, California, Earthquake, 9 February 1971." Vicksburg, Mississippi.

Chowdhury, K., Seed, R. B., Perlea, V., Beaty, M., Ma, F., and Hu, G. (2019). "Lessons Learned from Re-Evaluation of the Upper and Lower San Fernando Dams Using Current State of Practice in Numerical Modeling." *Proceedings of the 39th Annual Conference and Exhibition*, Chicago, IL, 1–34.

Dafalla, M., Shaker, A., Elkady, T., Almajed, A., and Al-Shamrani, M. (2020). "Shear strength characteristics of a sand clay liner." *Scientific Reports*, Nature Publishing Group UK, 10(1), 1–11.

Dey, R., Hawlader, B., Phillips, R., and Soga, K. (2015). “Large deformation finite-element modelling of progressive failure leading to spread in sensitive clay slopes.” *Géotechnique*, 65(8), 657–668.

Dutta, S., Hawlader, B., and Phillips, R. (2014). “Finite element modeling of partially embedded pipelines in clay seabed using Coupled Eulerian–Lagrangian method.” *Canadian Geotechnical Journal*, 52(1), 58–72.

Feng, K., Wang, G., Huang, D., and Jin, F. (2021). “Material point method for large-deformation modeling of coseismic landslide and liquefaction-induced dam failure.” *Soil Dynamics and Earthquake Engineering*, 150, 106907.

GEOSLOPE International Ltd. (2012). “Seepage Modeling with SEEP/W.” GEOSLOPE International Ltd, Calgary, Alberta.

GEOSLOPE International Ltd. (2013). “Stress-Deformation Modeling with SIGMA/W.” GEOSLOPE International Ltd, Calgary, Alberta.

Gu, W. H., Morgenstern, N. R., and Robertson, P. K. (1993). “Progressive Failure of Lower San Fernando Dam.” *ASCE Journal of Geotechnieal Engineering*, 119(2), 333–349.

Hamann, T., Qiu, G., and Grabe, J. (2015). “Application of a Coupled Eulerian-Lagrangian approach on pile installation problems under partially drained conditions.” *Computers and Geotechnics*, 63, 279–290.

Han, C., and Vardoulakis, I. G. (1991). “Plane-strain compression experiments on water-saturated fine-grained sand.” *Géotechnique*, 41(1), 49–78.

Huang, D., B, F. J., Wang, G., and Feng, K. (2020). “Towards Physics-Based Large-Deformation

Analyses of Earthquake-Induced Dam Failure." *Dam Breach Modelling and Risk Disposal. ICED 2020. Springer Series in Geomechanics and Geoengineering.*, Springer, Cham., 117–124.

Huang, M., and Zienkiewicz, O. C. (1998). "New unconditionally stable staggered solution procedures for coupled soil-pore fluid dynamic problems." *International Journal for Numerical Methods in Engineering*, 43(6), 1029–1052.

Idinger, G., and Wu, W. (2019). "Shear Strength of Granular Soil Under Saturated and Unsaturated Conditions." *Recent Advances in Geotechnical Research*, Springer International Publishing, Cham, 79–89.

Jitno, H. (1995). "Liquefaction Induced Deformations of Earth Structures." University of British Columbia.

Khoei, A. R., Azami, A. R., and Haeri, S. M. (2004). "Implementation of plasticity based models in dynamic analysis of earth and rockfill dams: A comparison of Pastor-Zienkiewicz and cap models." *Computers and Geotechnics*, 31(5), 384–409.

Khoei, A. R., and Haghighat, E. (2011). "Extended finite element modeling of deformable porous media with arbitrary interfaces." *Applied Mathematical Modelling*, 35(11), 5426–5441.

Kramer, S. L. (1996). *Geotechnica Earthquake Engineering*. Pearsons.

Ladd, C. C. (1991). "Stability evaluation during staged construction." *Journal of Geotechnical Engineering*, 117(4), 540–615.

Lee, K. L., Seed, H. B., Idriss, I. M., and Makdisi, F. I. (1975). "Properties of soil in the san fernando hydraulic fill dams." *ASCE J Geotech Eng Div*, American Society of Civil Engineers,

101(8), 801–821.

Ming, H. Y., and Li, X. S. (2003). “Fully coupled analysis of failure and remediation of Lower San Fernando Dam.” *Journal of Geotechnical and Geoenvironmental Engineering*, 129(4), 336–349.

Newmark, N. M. (1965). “Effects of earthquakes on dams and embankments.” *Géotechnique*, 15(2), 139–160.

Olson, S. (2001). “Liquefaction analysis of level and sloping ground using field case histories and penetration resistance.” Univ. of Illinois at Urbana–Champaign, Urbana, Ill.

Olson, S. M., and Stark, D. (2001). “Analysis of lower san fernando strength ratios.” *Proceedings of the 4th International Conference on Recent Advances in Geotechnical Earthquake Engineering and Soil Dynamics*, San Diego, California, 26-31 March.

Olson, S. M., and Stark, T. D. (2002). “Liquefied strength ratio from liquefaction flow failure case histories.” *Canadian Geotechnical Journal*, 39(3), 629–647.

Qiu, G., Henke, S., and Grabe, J. (2011). “Application of a Coupled Eulerian-Lagrangian approach on geomechanical problems involving large deformations.” *Computers and Geotechnics*, 38(1), 30–39.

Saha, D., Hawlader, B., Dutta, S., and Dhar, A. (2018). “A comparison using two numerical approaches for modelling the impact of submarine landslides on suspended pipelines.” *71st Canadian Geotechnical Conference, GeoEdmonton 2018*, Edmonton, Alberta, Canada.

Sarma, S. K. (1975). “Seismic Stability of Earth Dams and Embankments.” *Géotechnique*, 25(4), 743–761.

Seed, H. B. (1979). “Considerations in the Earthquake-Resistant Design of Earth and Rockfill Dams.” *Géotechnique*, 29(3), 215–263.

Seed, H. B., Lee, K. L., Idriss, I. M., and Makdisi, F. I. (1973). *Analysis of the slides on the San Fernando Dam during the earthquake of Feb. 1971, EERC report No. EERC73-2*. Berkeley, California.

Stoecklin, A., Trapper, P., and Puzrin, A. M. (2020). “Controlling factors for post-failure evolution of subaqueous landslides.” *Géotechnique*, 71(10), 879–892.

Tan, D., and Sarma, S. K. (2008). “Finite element verification of an enhanced limit equilibrium method for slope analysis.” *Géotechnique*, 58(6), 481–487.

Tjung, E. Y. S., and Soga, K. (2021). “Liquefaction-Induced Dam Failure Simulation -- A Case for the Material Point Method.” *arXiv preprint arXiv:2111.13584.*

Wang, D., Randolph, M. F., and White, D. J. (2013). “A dynamic large deformation finite element method based on mesh regeneration.” *Computers and Geotechnics*, 54, 192–201.

Zhang, X., Wang, L., Krabbenhoft, K., and Tinti, S. (2020). “A case study and implication: particle finite element modelling of the 2010 Saint-Jude sensitive clay landslide.” *Landslides*, 17(5), 1117–1127.

Zheng, J., Hossain, M. S., and Wang, D. (2017). “Numerical investigation of spudcan penetration in multi-layer deposits with an interbedded sand layer.” *Géotechnique*, 67(12), 1050–1066.

CHAPTER 6

Conclusions and Recommendations for Future Research

6.1 Conclusions

The failure of strain-softening materials (e.g., loose sand under undrained loading) during the formation and propagation of shear bands or slip surfaces is essentially strain localization. The present study addressed several challenges in modeling strain localization of a large-deformation failure. The conclusions below are the general overview of the entire thesis. Problem specific conclusions and appendices were shown at the end of each chapter (Chapters 3–5).

In the present study, a framework and multiple algorithms are developed to implement three nonlocal methods in Eulerian-based FE program, which is free from mesh distortion and convergence issues. Several techniques are developed to reduce the computational costs of the nonlocal Eulerian-based FE analyses. The results of a biaxial test simulation are benchmarked with the nonlocal version of ICFEP (Imperial College Finite Element Program). Almost identical results have been obtained from both programs; however, the numerical issues encountered in the over-nonlocal method in the ICFEP are avoided in the present Eulerian-based FE analyses. Furthermore, the over-nonlocal method is proved to be more advantageous than the G&S nonlocal method when an appropriate value of α is selected. Thereafter, another biaxial test simulation is conducted using the present Eulerian-based FE technique with the over-nonlocal method. The results are compared with the same test simulation that is performed in nonlocal MPM, and an identical response is obtained.

The effectiveness of softening scaling on local and nonlocal models is investigated. An algorithm is developed to implement the over-nonlocal method with the Tresca failure criteria in Eulerian-based FE program. Thereafter, a biaxial test and a slope failure are simulated using the developed local and nonlocal Eulerian-based FE with softening scaling. Softening scaling was

effective in controlling the shear band thickness and modeling the macroscopic behaviour. Both the local scaling (element size scaling) and nonlocal methods provided a mesh-independent result. However, the latter was more computationally expensive, being disadvantageous to model a large-scale problem, e.g., retrogressive landslides, using conventional computational resources. In addition, an in-depth investigation was performed on the shear band thickness for both local and nonlocal methods. The shear band thickness increases, rather than remaining constant, with the increase of shear displacement. The mechanisms involved in this process are explained based on an energy-based approach.

A modeling technique for seepage is developed in Eulerian-based FE program by adopting the thermal–fluid analogy. The transient and steady-state seepage are successfully simulated and calibrated against commonly used SEEP/W software. In addition, the in-situ stresses under the steady-state seepage are modeled by applying the seepage forces and buoyancy forces.

The failure of the Lower San Fernando Dam in 1971 has been extensively investigated in the past. However, the post-failure deformation was underexplored. Eulerian-based FE is implemented to model this failure with the focus on the post-failure large deformation behaviour. The proposed seepage modeling technique is used to establish the in-situ effective stress of the dam. Simplified constitutive models are developed and implemented for the different strain-softening soil layers, and the soil properties are determined based on previous site investigations and laboratory test results. A pseudostatic load is applied to trigger the failure. The formation of clear shear bands, and detachment and downslope displacements of several soil blocks in FE simulation, are similar to the post-slide field observation. Furthermore, a parametric study is conducted to show the effects of several parameters on the modeling results.

6.2 Recommendations for future research

Although many advances are presented in the numerical modeling of strain localization with Eulerian-based FE program, this study has some limitations. Some of the limitations were discussed in Chapters 3–5. In addition, some of the following issues could be addressed in the future:

(1) With the development of computational power in the future, the simulation of a large-scale soil failure problem, e.g., a landslide might become efficient by using a nonlocal method in Eulerian-based FE program. Also, further comparison between the local and nonlocal methods for softening-scaling materials can be performed for large-scale landslide modeling.

(2) More research is required to understand the effectiveness of the nonlocal Eulerian-based FE analysis on progressive slope failures where multiple shear bands are present, e.g., how the value of internal length will affect the failure patterns. Also, the use of nonlocal methods in the large deformation of multiple soil layers needs more investigation. Due to the aforementioned computational cost issue, the nonlocal method is not used for the modeling of Lower San Fernando Dam failure in this study.

(3) A framework is proposed to implement three nonlocal methods in Eulerian-based FE program. The nonlocal methods are successfully applied to the von Mises and Tresca failure criteria. In the future, more advanced constitutive models can be implemented with nonlocal methods by using the presented framework for modeling a wide range of geotechnical problems involved strain-softening behaviour.

(4) In the future, the co-seismic stage of the Lower San Fernando Dam failure should be analyzed along with the post-failure large-deformation analysis so that the effects of the triggering process can be more realistically reflected. Advanced constitutive models need

to be incorporated in Eulerian-based FE program to handle both the seismic and large-deformation behaviour of the soils. In addition, uncertainties in determining soil parameters for these models need to be further discussed.

Finally, although the analyses (both local and nonlocal) are performed for some idealized problems with simplified soil constitutive models, the techniques developed in the present study could be extended further for other geotechnical problems with different geometries, loading conditions, and soil behaviours.

REFERENCES

Bažant, Z. P., Belytschko, T. B., and Chang, T. P. (1984). "Continuum theory for strain-softening." *Journal of Engineering Mechanics*, 110(12), 1666–1692.

Bažant, Z. P., and Jirásek, M. (2002). "Nonlocal Integral Formulations of Plasticity and Damage: Survey of Progress." *Journal of Engineering Mechanics*, 128(11), 21–51.

Bažant, Z. P., and Lin, F. (1988). "Non-local yield limit degradation." *International Journal for Numerical Methods in Engineering*, 26, 1805–1823.

Benson, D. J. (1992). "Computational methods in Lagrangian and Eulerian hydrocodes." *Computer Methods in Applied Mechanics and Engineering*, 99(2–3), 235–394.

Blázquez, R., and López-Querol, S. (2007). "Endochronic-Based Approach to the Failure of the Lower San Fernando Dam in 1971." *Journal of Geotechnical and Geoenvironmental Engineering*, 133(9), 1144–1153.

de Borst, R. (2001). "Some recent issues in computational failure mechanics." *International Journal for Numerical Methods in Engineering*, 52(1–2), 63–95.

de Borst, R., and Mühlhaus, H. B. (1992). "Gradient-dependent plasticity: Formulation and algorithmic aspects." *International Journal for Numerical Methods in Engineering*, 35(3), 521–539.

de Borst, R., Sluys, L. J., Mühlhaus, H. B., and Pamin, J. (1993). "Fundamental issues in finite element analyses of localization of deformation." *Engineering Computations*, 10(2), 99–121.

de Borst, R., and Verhoosel, C. V. (2017). *Damage, Material Instabilities, and Failure*. *Encyclopedia of Computational Mechanics Second Edition*, Wiley.

Brabb, E. E. (1991). "The world landslide problem." *Episodes Journal of International Geoscience*, International Union of Geological Sciences, 14(1), 52–61.

Brinkgreve, R. (1994). "Geomaterial models and numerical analysis of softening." Technische

Universiteit Delft.

Bui, H. H., and Nguyen, G. D. (2017). “A coupled fluid-solid SPH approach to modelling flow through deformable porous media.” *International Journal of Solids and Structures*, 125, 244–264.

Burghardt, J., Brannon, R., and Guilkey, J. (2012). “A nonlocal plasticity formulation for the material point method.” *Computer Methods in Applied Mechanics and Engineering*, 225–228, 55–64.

Castro, B. G., Seed, R. B., Keller, T. O., and Seed, H. B. (1992). “Steady-state strength analysis of Lower San Fernando Dam slide.” 118(3), 406–427.

Castro, G., Keller, T., and Boynton, S. S. (1989). *Re-Evaluation of the Lower San Fernando Dam, Report 1: An Investigation of the February 9, 1971 Slide*. Winchester, Massachusetts.

Chowdhury, K., Seed, R. B., Perlea, V., Beaty, M., Ma, F., and Hu, G. (2019). “Lessons Learned from Re-Evaluation of the Upper and Lower San Fernando Dams Using Current State of Practice in Numerical Modeling.” *Proceedings of the 39th Annual Conference and Exhibition*, Chicago, IL, 1–34.

Chu, J., and Wanatowski, D. (2009). “Effect of Loading Mode on Strain Softening and Instability Behaviour of Sand in Plane-Strain Tests.” *Journal of Geotechnical and Geoenvironmental Engineering*, 135(1), 108–120.

Conte, E., Silvestri, F., and Troncone, A. (2010). “Stability analysis of slopes in soils with strain-softening behaviour.” *Computers and Geotechnics*, 37(5), 710–722.

Cosserat, E., and Cosserat, F. (1909). *Theorie des corps deformables*. Herman et Flis, Paris.

Cuomo, S., Prime, N., Iannone, A., Dufour, F., Cascini, L., and Darve, F. (2013). “Large deformation FEMLIP drained analysis of a vertical cut.” *Acta Geotechnica*, 8(2), 125–136.

D’Ignazio, M., Länsivaara, T. T., and Jostad, H. P. (2017). “Failure in anisotropic sensitive clays:

Finite element study of Perniö failure test." *Canadian Geotechnical Journal*, 54(7), 1013–1033.

Dafalla, M., Shaker, A., Elkady, T., Almajed, A., and Al-Shamrani, M. (2020). "Shear strength characteristics of a sand clay liner." *Scientific Reports*, Nature Publishing Group UK, 10(1), 1–11.

Dey, R., Hawlader, B., Phillips, R., and Soga, K. (2015). "Large deformation finite-element modelling of progressive failure leading to spread in sensitive clay slopes." *Géotechnique*, 65(8), 657–668.

Eringen, A. C. (1981). "On nonlocal plasticity." *International Journal of Engineering Science*, 19(12), 1461–1474.

Feng, K., Wang, G., Huang, D., and Jin, F. (2021). "Material point method for large-deformation modeling of coseismic landslide and liquefaction-induced dam failure." *Soil Dynamics and Earthquake Engineering*, 150, 106907.

Finno, R. J., Harris, W. W., Mooney, M. A., and Viggiani, G. (1997). "Shear bands in plane strain compression of loose sand." *Géotechnique*, 47(1), 149–165.

Galavi, V., and Schweiger, H. F. (2010). "Nonlocal multilaminate model for strain softening analysis." *International Journal of Geomechanics*, 10(1), 30–44.

Goodarzi, M., and Rouainia, M. (2017). "Modelling Slope Failure Using a Quasi-static MPM with a Non-local Strain Softening Approach." *Procedia Engineering*, 175, 220–225.

Griffiths, D. V., and Lane, P. A. (1999). "Slope stability analysis by finite elements." *Géotechnique*, 49(3), 387–403.

Gu, W. H., Morgenstern, N. R., and Robertson, P. K. (1993). "Progressive Failure of Lower San Fernando Dam." *ASCE Journal of Geotechnieal Engineering*, 119(2), 333–349.

Guo, P. (2012). "Critical length of force chains and shear band thickness in dense granular

materials." *Acta Geotechnica*, 7(1), 41–55.

Gylland, A. S., Jostad, H. P., and Nordal, S. (2014). "Experimental study of strain localization in sensitive clays." *Acta Geotechnica*, 9(2), 227–240.

Hamann, T., Qiu, G., and Grabe, J. (2015). "Application of a Coupled Eulerian-Lagrangian approach on pile installation problems under partially drained conditions." *Computers and Geotechnics*, 63, 279–290.

Heeres, O. M., Suiker, A. S. J., and de Borst, R. (2002). "A comparison between the Perzyna viscoplastic model and the consistency viscoplastic model." *European Journal of Mechanics, A/Solids*, 21(1), 1–12.

Hsu, S. T., and Liao, H. J. (1988). "Uplift behaviour of cylindrical anchors in sand." *Canadian Geotechnical Journal*, NRC Research Press Ottawa, Canada, 35(1), 70–80.

Huang, D., Jin, F., Wang, G., and Feng, K. (2020). "Towards Physics-Based Large-Deformation Analyses of Earthquake-Induced Dam Failure." *Springer Series in Geomechanics and Geoengineering*, Springer, 117–124.

Huang, M., and Zienkiewicz, O. C. (1998). "New unconditionally stable staggered solution procedures for coupled soil-pore fluid dynamic problems." *International Journal for Numerical Methods in Engineering*, 43(6), 1029–1052.

Islam, N., Hawlader, B., Wang, C., and Soga, K. (2019). "Large-deformation finite-element modelling of earthquake-induced landslides considering strain-softening behaviour of sensitive clay." *Canadian Geotechnical Journal*, 56(7), 1003–1018.

Jirásek, M., and Bauer, M. (2012). "Numerical aspects of the crack band approach." *Computers and Structures*, 110–111, 60–78.

Jirásek, M., and Rolshoven, S. (2009). "Localization properties of strain-softening gradient plasticity models. Part I: Strain-gradient theories." *International Journal of Solids and*

Structures, Pergamon, 46(11–12), 2225–2238.

Jitno, H. (1995). "Liquefaction Induced Deformations of Earth Structures." University of British Columbia.

Khoei, A. R., Azami, A. R., and Haeri, S. M. (2004). "Implementation of plasticity based models in dynamic analysis of earth and rockfill dams: A comparison of Pastor-Zienkiewicz and cap models." *Computers and Geotechnics*, 31(5), 384–409.

Kumar, R., and Dodagoudar, G. (2009). "Element free Galerkin method for two dimensional contaminant transport modelling through saturated porous media." *International Journal of Geotechnical Engineering*, Taylor & Francis, 3(1), 11–20.

Lee, K. L., Seed, H. B., Idriss, I. M., and Makdisi, F. I. (1975). "Properties of soil in the san fernando hydraulic fill dams." *ASCE J Geotech Eng Div*, American Society of Civil Engineers, 101(8), 801–821.

Li, X. S., and Ming, H. (2004). "Seepage driving effect on deformations of San Fernando dams." *Soil Dynamics and Earthquake Engineering*, 24(12), 979–992.

Loret, B., and Prevost, J. (1990). "Dynamic strain localization in elasto-(visco-)plastic solids, Part 1. General formulation and one-dimensional examples." *Computer Methods in Applied Mechanics and Engineering*, 83(3), 247–273.

Lu, X., Bardet, J. P., and Huang, M. (2012). "Spectral analysis of nonlocal regularization in two-dimensional finite element models." *International Journal for Numerical and Analytical Methods in Geomechanics*, 36(2), 219–235.

Maier, T. (2003). "Nonlocal modeling of softening in hypoplasticity." *Computers and Geotechnics*, 30(7), 599–610.

Mallikarachchi, H., and Soga, K. (2020). "Post-localisation analysis of drained and undrained dense sand with a nonlocal critical state model." *Computers and Geotechnics*, 124, 103572.

Mánica, M. A., Gens, A., Vaunat, J., and Ruiz, D. F. (2018). "Nonlocal plasticity modelling of strain localisation in stiff clays." *Computers and Geotechnics*, 103, 138–150.

Marcher, T. (2003). "Nichtlokale Modellierung der Entfestigung dichter Sande und steifer Tone." University of Stuttgart.

Marello, S. (2004). "Studio del comportamento meccanico di argille consistenti e marne." Université J. Fourier de Grenoble (France).

Mesri, G., Wang, C., and Kane, T. (2021). "Meaning, Measurement, and Field Application of Fully Softened Shear Strength of Stiff Clays and Clay Shales." *Canadian Geotechnical Journal*.

Ming, H. Y., and Li, X. S. (2003). "Fully coupled analysis of failure and remediation of Lower San Fernando Dam." *Journal of Geotechnical and Geoenvironmental Engineering*, 129(4), 336–349.

Monforte, L., Ciantia, M. O., Carbonell, J. M., Arroyo, M., and Gens, A. (2019). "A stable mesh-independent approach for numerical modelling of structured soils at large strains." *Computers and Geotechnics*, 116, 103215.

Moore, I. D., and Rowe, R. K. (1988). "Numerical models for evaluating progressive failure in earth structures-A review." *Computers and Geotechnics*, 6(3), 217–239.

Muhihaus, H.-B., and Vardoulakis, I. (1987). "The thickness of shear hands in granular materials." *Géotechnique*, 37(3), 271–283.

Needleman, A. (1988). "Material rate dependence and mesh sensitivity in localization problems." *Computer Methods in Applied Mechanics and Engineering*, 67(1), 69–85.

Olson, S. (2001). "Liquefaction analysis of level and sloping ground using field case histories and penetration resistance." Univ. of Illinois at Urbana–Champaign, Urbana, Ill.

Olson, S. M., and Stark, D. (2001). "Analysis of lower san fernando strength ratios." *Proceedings of the 4th International Conference on Recent Advances in Geotechnical Earthquake*

Engineering and Soil Dynamics, San Diego, California, 26-31 March.

Pamin, J., Askes, H., and de Borst, R. (2003). "Two gradient plasticity theories discretized with the element-free Galerkin method." *Computer Methods in Applied Mechani*, 192(20–21), 2377–2403.

Perzyna, P. (1963). "The constitutive equations for rate sensitive plastic materials." *Quarterly of Applied Mathematics*, 20(4), 321–332.

Pietruszczak, S., and Mroz, Z. (1981). "Finite element analysis of deformation of strain-softening materials." *International Journal for Numerical Methods in Engineering*, 17, 327–334.

Prevost, J. H., and Loret, B. (1990). "Dynamic strain localization in elasto-(visco-)plastic solids, part 2. plane strain examples." *Computer Methods in Applied Mechanics and Engineering*, 83(3), 275–294.

Qiu, G., Henke, S., and Grabe, J. (2011). "Application of a Coupled Eulerian-Lagrangian approach on geomechanical problems involving large deformations." *Computers and Geotechnics*, 38(1), 30–39.

Sadrekarimi, A., and Olson, S. M. (2010). "Shear Band Formation Observed in Ring Shear Tests on Sandy Soils." *Journal of Geotechnical and Geoenvironmental Engineering*, American Society of Civil Engineers, 136(2), 366–375.

Seed, H. B. (1979). "Considerations in the Earthquake-Resistant Design of Earth and Rockfill Dams." *Géotechnique*, 29(3), 215–263.

Seed, H. B., Lee, K. L., Idriss, I. M., and Makdisi, F. I. (1973). *Analysis of the slides on the San Fernando Dam during the earthquake of Feb. 1971, EERC report No. EERC73-2*. Berkeley, California.

Singh, V., Stanier, S., Bienen, B., and Randolph, M. F. (2021). "Modelling the behaviour of sensitive clays experiencing large deformations using non-local regularisation techniques."

Computers and Geotechnics, 133, 104025.

Sluys, L. J. (1992). "Wave Propagation, Localisation and Dispersion in Softening Solids." Delft University of Technology.

Soga, K., Alonso, E., Yerro, A., Kumar, K., Bandara, S., Kwan, J. S. H., Koo, R. C. H., Law, R. P. H., Yiu, J., Sze, E. H. Y., and Ho, K. K. S. (2016). "Trends in large-deformation analysis of landslide mass movements with particular emphasis on the material point method." *Géotechnique*, 66(3), 248–273.

Summersgill, F. C. (2014). "Numerical Modelling of Stiff Clay Cut Slopes with Nonlocal Strain Regularisation.", Imperial College of London.

Summersgill, F. C., Kontoe, S., and Potts, D. M. (2017a). "Critical assessment of nonlocal strain-softening methods in biaxial compression." *International Journal of Geomechanics*, 17(7), 1–14.

Summersgill, F. C., Kontoe, S., and Potts, D. M. (2017b). "On the use of nonlocal regularisation in slope stability problems." *Computers and Geotechnics*, 82, 187–200.

Thakur, V. (2007). "Strain Localization in sensitive soft clays." Norwegian University of Science and Technology.

Toupin, R. (1962). *Archive for Rational Mechanics and Analysis*. Springer Verlag.

Tran, Q. A., and Sołowski, W. (2019). "Generalized Interpolation Material Point Method modelling of large deformation problems including strain-rate effects – Application to penetration and progressive failure problems." *Computers and Geotechnics*, 106, 249–265.

Troncone, A. (2005). "Numerical analysis of a landslide in soils with strain-softening behaviour." *Géotechnique*, 55(8), 585–596.

Wang, C., Hawlader, B., Perret, D., and Soga, K. (2020). "Effects of geometry and soil properties on type and retrogression of landslides in sensitive clays." *Géotechnique*, 1–15.

Wang, C., Hawlader, B., Perret, D., Soga, K., and Chen, J. (2021). “Modeling of initial stresses and seepage for large deformation finite element simulation of sensitive clay landslides.” *ASCE Journal of Geotechnical and Geoenvironmental Engineering*.

Wang, D., Randolph, M. F., and White, D. J. (2013). “A dynamic large deformation finite element method based on mesh regeneration.” *Computers and Geotechnics*, 54, 192–201.

Zhang, W., Randolph, M. F., Puzrin, A. M., and Wang, D. (2019). “Transition from shear band propagation to global slab failure in submarine landslides.” *Canadian Geotechnical Journal*, 56(4), 554–569.

Zhang, X., Sheng, D., Sloan, S. W., and Bleyer, J. (2017). “Lagrangian modelling of large deformation induced by progressive failure of sensitive clays with elastoviscoplasticity.” *International Journal for Numerical Methods in Engineering*, 112(8), 963–989.

APPENDIX-I

Comparison of Two Mesh Regularization Approaches for Large Deformation Finite Element Analysis

This paper has been published in the 4th International Symposium on Frontiers in Offshore Geotechnics (ISFOG), Austin, Texas, 2020 (postponed to 2022).

Most of the research work presented in this paper was conducted by the first author. He also prepared the draft manuscript. The other authors supervised the research and reviewed the manuscript.

COMPARISON OF TWO MESH REGULARIZATION APPROACHES FOR LARGE DEFORMATION FINITE ELEMENT ANALYSIS

Jin Chen, Memorial University of Newfoundland, St. John's, NL, Canada, 709-770-5889, jinc@mun.ca
Bipul Hawlader, Memorial University of Newfoundland, St. John's, NL, Canada, 709-864-8945, bipul@mun.ca

ABSTRACT

Strain-softening behaviour of soil poses a significant challenge in finite element (FE) modeling of many offshore and onshore geotechnical problems. The FE results are mesh size dependent; therefore, several mesh regularization techniques have been proposed. FE modeling becomes more difficult for large deformation problems, such as submarine landslides and penetration of surface laid pipelines in deepwater. In the present study, FE analyses are performed for two idealized problems to show the performance of two regularization techniques: (i) element size scaling, and (ii) nonlocal method. Both approaches are implemented in a Eulerian-based FE modeling technique that can handle large deformation without causing numerical issues related to mesh distortion. Conducting analyses for the undrained loading condition, advantages and limitations of these approaches are presented.

Keywords: Strain-softening, large deformation, Eulerian-based finite-element, strain localization

INTRODUCTION

Many geotechnical problems in offshore and onshore environments involve large deformation. For example, large-scale submarine landslides generally initiate through a weak soil layer and the failed soil mass displaces a large distance over the failure planes. In some cases, the failed soil mass moves over the continental slope and then displaces downslope several hundred kilometers and might cause a tsunami. Similarly, the installation of offshore piles, suction caissons, and penetration and lateral displacement of surface-laid pipelines in deepwater offshore environments also involve large deformation. The large displacement of soil also creates extremely large shear strain, especially around the failure planes. Post-peak degradation of shear strength occurs with accumulated plastic shear strain (strain-softening), which is observed both in clay and sand for undrained and drained loadings, although the causes of the strength reduction are different. In the present study, numerical modeling is performed for undrained loading condition.

Finite element (FE) modeling is widely used for numerical modeling of many geotechnical problems. Most of the FE programs have been developed in a Lagrangian framework that cannot handle a very large deformation because of mesh distortion. In recent years, several numerical techniques have been developed to simulate very large deformations, such as Remeshing and Interpolation Technique using Small Strain (Hu and Randolph, 1998) and Material Point Method (Burghardt et al., 2012) and Eulerian-based FE modeling.

Mesh convergence analyses are essential for any FE analysis to ensure that the results are not dependent on the mesh size. Various regularization techniques have been developed to overcome this issue, such as element size scaling (Anastasopoulos et al., 2007), nonlocal

methods (Eringen, 1981; Bažant et al., 1984; Brinkgreve, 1994; Galavi and Schweiger, 2010), viscoplastic models (Loret and Prevost, 1990), strain gradient models (de Borst and Muhlhaus, 1992), polar models or Cosserat continuum models (de Borst, 1993). Most of these studies show the success and limitations of these approaches for small strain finite-element analysis. Some of these techniques are mathematically complex and computationally expensive, which are primarily applicable to simple problems and might be used for academic exercise.

This study aims to present the comparison of the performance of two mesh regularization techniques by conducting Eulerian FE analysis of two simplified cases: (i) axial compression of a block (Case 1), and (ii) failure of a sensitive clay slope due to upslope loading (Case 2). Analysis is performed using a Eulerian-based FE modeling technique. The long-term objective of this research is to identify a relatively simple, yet can capture strain localization reasonably, for FE modeling of large-deformation problems, such as large-scale landslides, using currently available computational facilities.

NUMERICAL MODELING TECHNIQUE

Eulerian-based finite-element method

Typical Lagrangian-based finite-element programs cannot simulate very large deformation that occurs in many geotechnical problems, such as landslides, due to the significant mesh distortion around the failure plane and resulting numerical instabilities (Griffiths and Lane, 1999). Eulerian-based finite-element method available in Abaqus/Explicit FE software is used in this study for numerical modeling. In this approach, the Eulerian material flows through the fixed mesh without causing numerical issues related to mesh distortion. Further details of the mathematical formulations of Eulerian-based FE approach and its applications to large-deformation problems (e.g., landslides) are available in previous studies (Benson and Okazawa, 2004; Dey et al., 2015). The general purpose Abaqus software does not have a direct option for modeling strain localization. In this study, the following two mesh-size regularization techniques are implemented in Abaqus using user subroutines.

Shear strain regularization

The following two mesh regularization techniques are used in this study: (i) element size scaling, and (ii) the nonlocal method.

1) Element size scaling

A simple approach for reducing mesh sensitive issues is to use the element size scaling rule (Pietruszczak and Mróz, 1981; Anastasopoulos et al., 2007). For a given shear displacement (δ), the shear strain of a soil element (γ) is inversely proportional to the thickness of the finite element (t_{FE}) as $\gamma = \delta / t_{\mathrm{FE}}$ if the element deforms as simple shear condition. Therefore, in FE modeling, the rate of reduction of shear strength with γ is given as a function of $1/t_{\mathrm{FE}}$. In other words, the smaller the size of the mesh the larger the shear strain requires to reduce the strength. This approach has been used in many studies, including in the simulation of large-scale landslides (Dey et al. 2015).

2) Nonlocal method

This approach has been developed aiming to calculate the reduction of shear strength of the soil elements in the shear band by distributing the highly localized shear strain to the surrounding

elements using some mathematical functions. Different types of nonlocal methods have been proposed, such as original nonlocal method (Eringen, 1981; Bažant et al., 1984), over-nonlocal method (Brinkgreve, 1994) and G&S nonlocal method (Galavi and Schweiger, 2010). The main difference between these approaches is the use of the weight function to calculate the nonlocal shear strain. These approaches have been implemented in Lagrangian-based FE programs (Summersgill, 2014) and proved to be able to reduce the mesh sensitivity and maintain the shear band thickness independent of mesh size when the mesh size is sufficiently small. Attempts have also been taken to implement a nonlocal method in the Material Point Method (MPM) (Burghardt et al., 2012; Goodarzi and Rouainia, 2017), while Smoothed-Particle Hydrodynamics (SPH) is demonstrated to be inherently nonlocal (Vignjevic et al., 2014).

In the present study, the original nonlocal method (Eqs. (1–3)) is implemented in Eulerian-based approach available in Abaqus/Explicit FE software. A user-subroutine is developed to implement the nonlocal method.

$$\varepsilon^{\mathrm{p}}_{\mathrm{q(eq)}}(x_{\mathrm{n}}) = \frac{1}{V_{\omega}} \iiint \left[\omega(x'_{\mathrm{n}})\varepsilon^{\mathrm{p}}_{\mathrm{q}}(x'_{\mathrm{n}})\right] dx'_1 dx'_2 dx'_3 \tag{1}$$

$$\omega(x'_{\mathrm{n}}) = \frac{1}{DL\sqrt{\pi}} \exp\left[-\frac{(x'_{\mathrm{n}}-x_{\mathrm{n}})^T(x'_{\mathrm{n}}-x_{\mathrm{n}})}{DL^2}\right] \tag{2}$$

$$V_{\omega} = \iiint \omega(x'_{\mathrm{n}}) dx'_1 dx'_2 dx'_3 \tag{3}$$

where $\varepsilon^{\mathrm{p}}_{\mathrm{q}}$ is accumulated equivalent plastic shear strain; $\varepsilon^{\mathrm{p}}_{\mathrm{q(eq)}}$is the nonlocal equivalent plastic shear strain to calculate the shear strength after strain softening; and x_{n} is the point at which the calculation of the $\varepsilon^{\mathrm{p}}_{\mathrm{q(eq)}}$is required; x'_{n} refers to the reference integration points; $\varepsilon^{\mathrm{p}}_{\mathrm{q}}(x'_{\mathrm{n}})$ means the reference strain at the reference points; $\omega(x'_{\mathrm{n}})$, the weight function that is centered at the location x_{n} to define the weight of all the reference points x'_{n} in the calculation of $\varepsilon^{\mathrm{p}}_{\mathrm{q(eq)}}$. Finally, *DL* is the internal length which decides the range of weighting distribution; V_{ω} is the reference volume, where x'_1, x'_2 and x'_3 are the three dimensions.

CASE 1: AXIAL COMPRESSION

Problem definition

The failure of a rectangular block of a weightless hypothetical material having strain-softening behaviour in plane strain condition is simulated first (Fig. 1). The model geometry is similar to that used by Burghardt et al. (2012) to show the performance of simulations using Material Point Method.

To initiate the failure, the yield strength of the material of a 1 m x 1 m weak block is assumed to be very small (1.0 kPa). In addition, a rigid cap is placed at the top surface and displaced downward at a constant velocity (v_y = 0.01 m/s). In the simulation v_y is sufficiently small that maintains a quasi-static loading condition, which has been verified from low kinetic energy during analysis. A rigid cap is used to obtain axial load on the top. Meanwhile, zero velocity in the vertical direction (v_y = 0) is used for the bottom boundary, while no boundary condition is given in the lateral direction, which allows it to deform laterally. A smooth interface condition is used between the rigid body and rectangular block.

The Coupled Eulerian-Lagrangian (CEL) approach in the software is used. The loading cap is discretized using Lagrangian elements and then transferred to a rigid body. The loaded block is

modeled as a Eulerian material by discretizing it using cubical EC3D8R, which are 8-noded linear brick elements with reduced integration and hourglass control. Only 3D elements can be used in the present Eulerian-based finite-element software; therefore, to model the plane strain condition (i.e., the block is one element thick).

A bi-linear post-peak strength degradation relation (softening) is used, as shown in the inset of Fig. 1. The peak yield strength (σ_{yp}) of the material is 40 kPa, which reduces linearly to a residual value (σ_{yr}) of 10 kPa at an accumulated plastic shear strain at residual ($\varepsilon^{p}_{q(r)}$) of 10% (i.e., $\varepsilon^{p}_{q(r)}$= 0.1) for the 0.5-m mesh size. In the simulations with element size scaling, $\varepsilon^{p}_{q(r)}$ is 0.2, 0.4 and 0.5 and 0.8 for mesh size (t_{FE}) of 0.25 m, 0.125 m, 0.1 m and 0.0625 m, respectively. In other words, the post-peak plastic shear strain required to mobilize a shear strength is inversely proportional to the thickness of the finite element. The von Mises criterion is adopted. Prior to the plastic deformation, the material behaviour is modeled as elastic using Young's modulus of 7.5 MPa and Poisson's ratio of 0.495. In the simulations with nonlocal method, the internal length *DL* of 0.5 m is used.

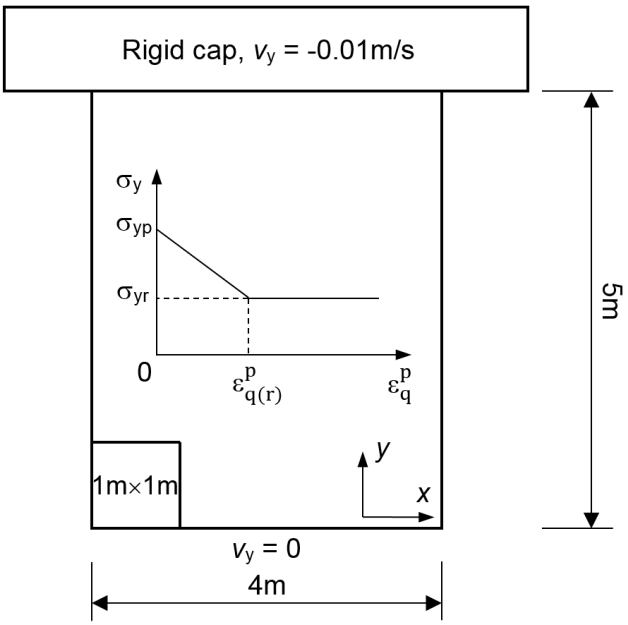

Figure 1 Geometry and boundary conditions for Case 1 simulations

Results

Figure 2 shows the development of failure planes at 0.5 m vertical displacement of the rigid block. The top row (Figs. 2(a)–(d)) the shows results for four mesh sizes without any mesh regularization (i.e., $\varepsilon^{p}_{q(r)}$= 0.1 for all four analyses). The following key observations are noted: (i) the failure pattern changes with mesh size; (ii) higher plastic shear strains generate in the shear band for a smaller mesh; and (iii) the width of the shear band decreases with decrease in element size. When element size scaling rule is used, only one failure plane is generated, emanating from the corner of the weak block, irrespective of the mesh size. However, the shear band is wider for larger element size (e.g., compare Figs. 2(e) & 2(h)).

Figures 2(i–l) show the failure planes in the simulations with the nonlocal method for regularization. As the width of the shear band is somehow controlled using the parameter *DL*, unlike Figs. 2(e–h), the shear band width does not change significantly with mesh size when it is smaller than 0.125 m. However, the shear band width is considerably large for 0.25 m mesh (Fig. 2(i)). Note however that, although the mesh size effect is significantly reduced in the simulations with regularization technique, overall strains in the shear band is generally higher in the simulation with smaller mesh.

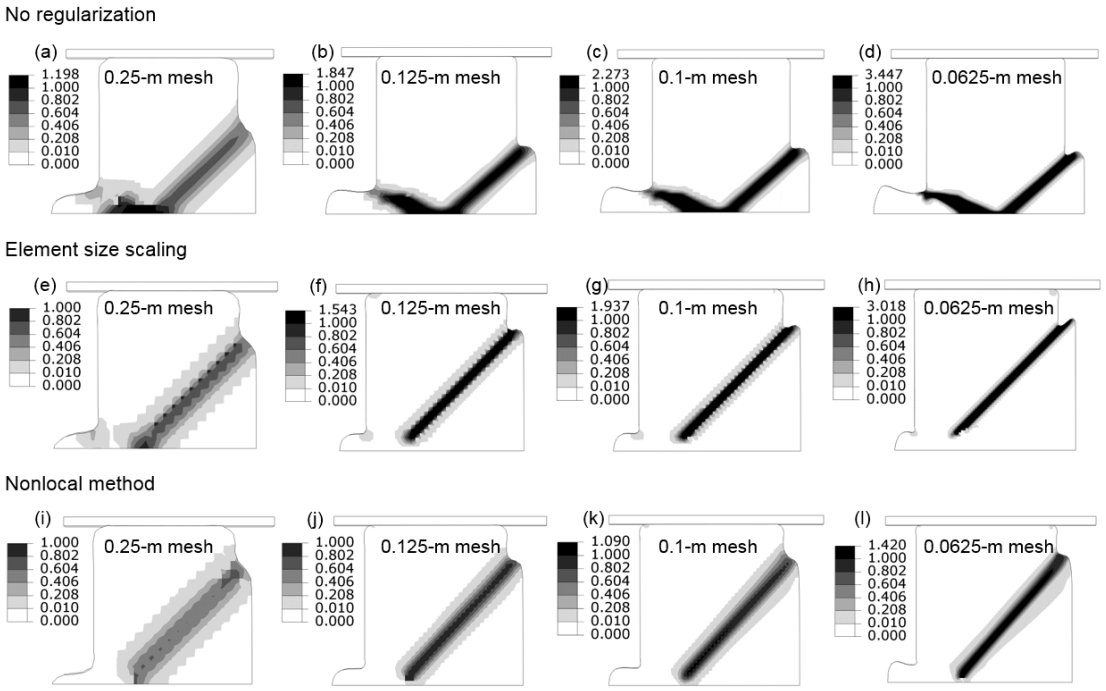

Figure 2 Plastic shear strain at 0.5 m displacement of the loading cap
(strains in 1 m × 1 m weak block are not shown)

Mesh size effects can be better explained using the force–displacement behaviour (Fig. 3). The displacement of the loading cap is directly related to the strain in the shear band and thus the mobilized shear strength and axial force. Therefore, the closeness of the force–displacement curves represents that similar strain is generated in the shear band for a given load.

A very different load–displacement response is found for different mesh sizes if the regularization is not used (Fig. 3(a)). The post-peak reduction of the force is slower for a larger mesh. However, if the element size scaling is used, the force–displacement curves are almost similar.

Figure 3(c) shows that force–displacement curve is almost identical for nonlocal method except for the simulation with largest mesh size (0.25 m). This implies that nonlocal method can significantly reduce the mesh sensitive issue if sufficiently small mesh is used.

Figure 3(d) shows the comparison between force–displacement curves with nonlocal and element size scaling regularization for 0.0625 m mesh. Both curves are very similar when regularization is used. However, a very different force–displacement curve is obtained when regularization is not used.

In summary, both mesh size scaling and nonlocal methods reasonably reduce the mesh sensitive issues for the presented quasi-static axial compression of a block.

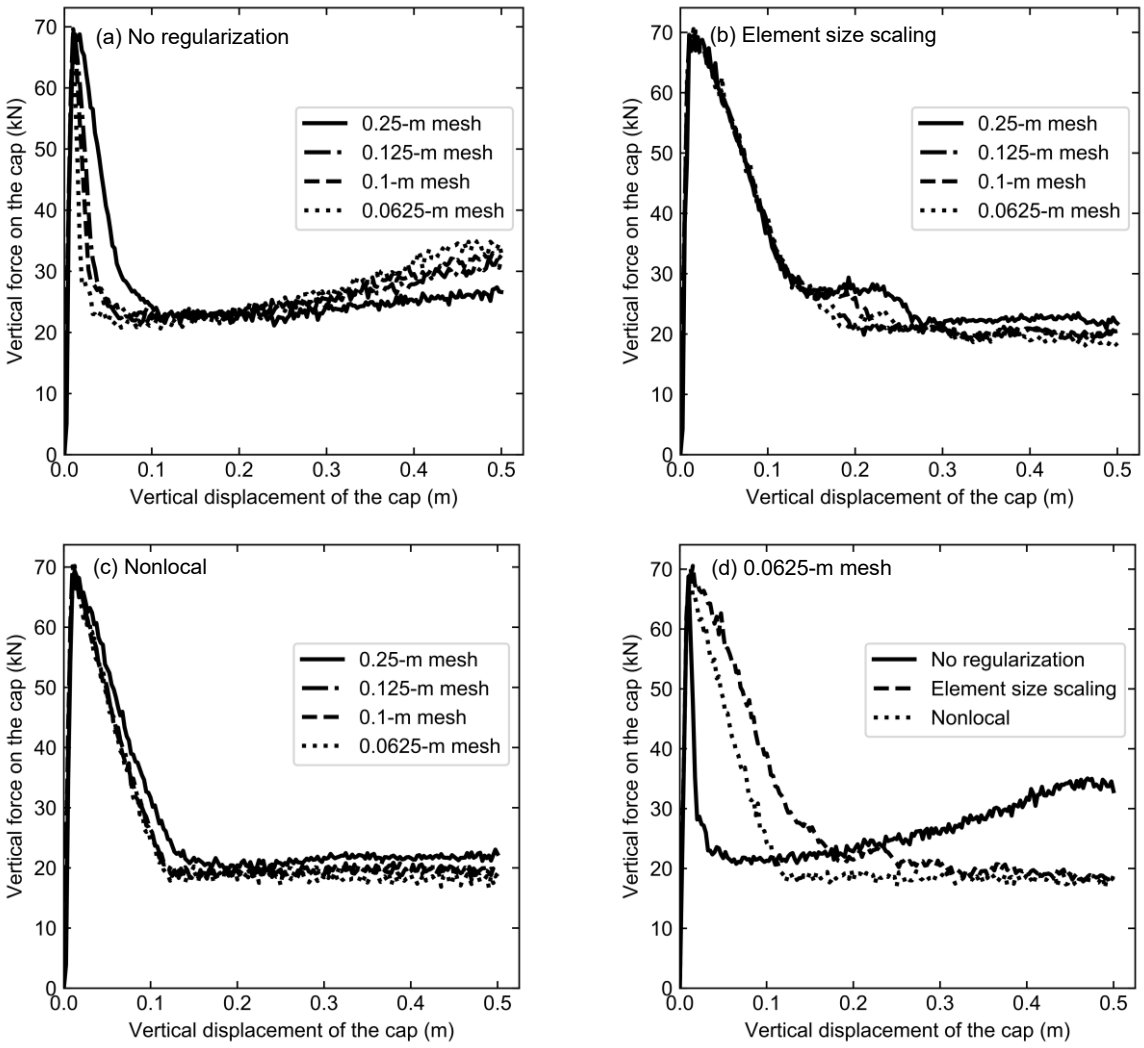

Figure 3 Load–displacement behaviour for Case 1

CASE 2: SLOPE FAILURE BY UPSLOPE LOADING

Problem definition

Figure 4 shows the geometry of a sensitive clay slope analyzed to show the performance of the above-mentioned mesh regularization techniques. A similar model was examined by D'Ignazio and Länsivaara (2015). The failure is triggered by a surcharge on the upslope area. A 4-m wide rigid block is pushed downward at constant velocity of 0.01 m/s maintaining quasi-static condition. Similar to Case 1, the CEL approach in Abaqus is used for the numerical analysis. The domain is discretized into 0.0625-m to 0.25-m mesh.

Zero velocity boundary condition is applied normal to the bottom and all vertical faces. The strain-softening behaviour is modeled using linearly decreasing undrained shear strength as shown in the inset of Fig. 4. The initial (peak) undrained shear strength (s_u^p) increases linearly with depth. The other soil parameters used in the analysis are shown in Table 1.

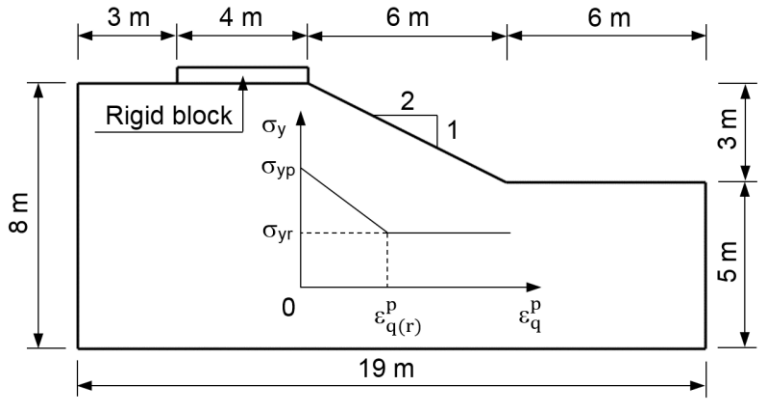

Figure 4 Geometry of the slope (Case 2)

Table 1 Soil parameters used for slope stability analysis

Soil parameters	No regularization	Element size scaling	Nonlocal
Undrained Young's modulus *E* (MPa)	7.5	7.5	7.5
Undrained Poisson's ratio ν	0.495	0.495	0.495
Peak undrained shear strength s_u^p (kPa)	25+3*z*	25+3*z*	25+3*z*
Residual undrained shear strength s_u^r (kPa)	10+1.2*z*	10+1.2*z*	10+1.2*z*
Sensitivity S_t	2.5	2.5	2.5
Equivalent plastic shear strain at residual strength ε_q^r	10%	20% for 0.25-m mesh 40% for 0.125-m mesh 80% for 0.0625-m mesh	10%
Internal length *DL* (m)	-	-	0.5

Note: *z* is the depth from the ground surface

Results

Figure 5 shows the failure plane when the rigid block is displaced vertically to 0.1 m. The failure plane develops progressively starting from the left side of the rigid block and ends at the toe. The size of the sliding blocks is similar when mesh regularization is used. When mesh regularization is not used, additional failure planes generate in the failed soil mass for the finer mesh. This is primarily due to rapid reduction of shear strength with plastic shear strain.

Figure 6 shows the variation of force applied to the soil from the rigid block with its displacement. The force–displacement curve significantly depends on mesh size if mesh regularization is not used (Fig. 6(a)). For the smaller mesh, the force dropped rapidly immediately after the peak, which occurs when the failure plane is fully formed. Again, it is because of quick decrease in strength with plastic shear strain for finer mesh. However, if mesh regularization is used, the force–displacement curves are very similar. Moreover, the force–displacement curves are comparable for the analyses with element size scaling and nonlocal methods (Figs. 6(b)–6(d)). In other words, both regularization techniques could reduce mesh sensitive issues significantly.

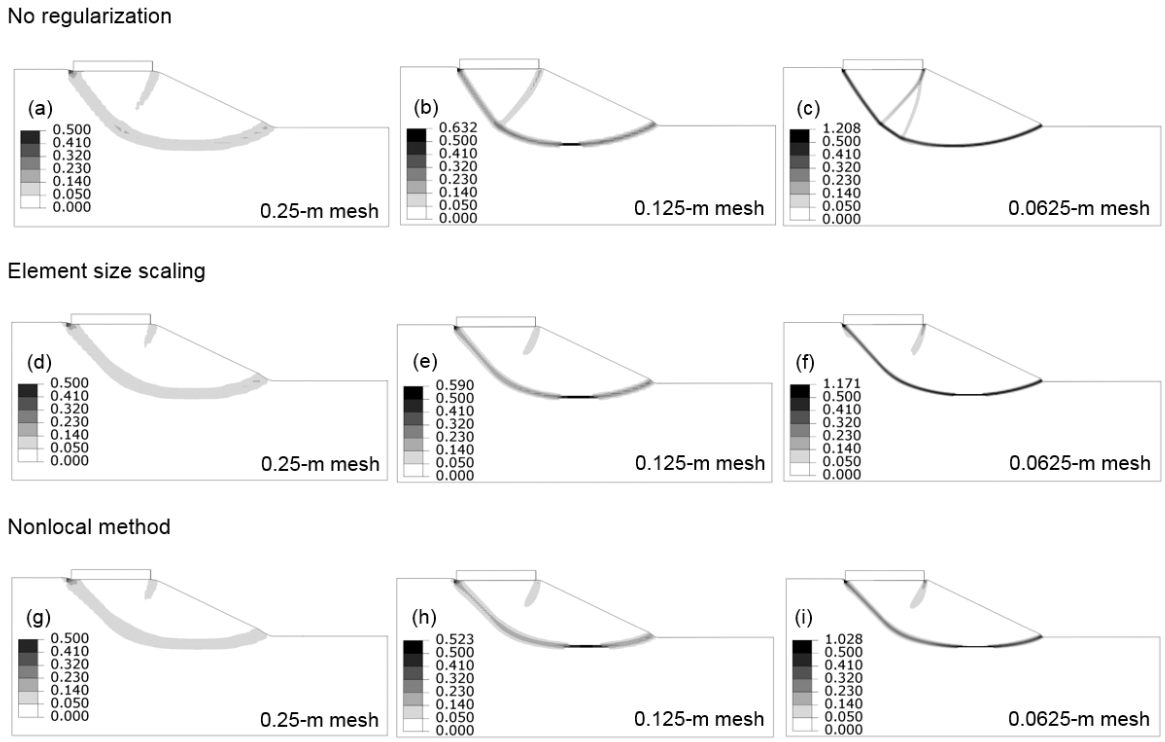

Figure 5 Failure pattern at 0.1 m vertical displacement of rigid block

It is worth to mention that the nonlocal method is computationally very expensive. As an example, for 0.0625-m mesh, the analysis took ~11 hours for nonlocal while it took only 20 minutes with element size scaling using a 3.4 GHz Intel Core i7-6700 CPU (8 processors) and 16 GB RAM. Significantly higher computational cost in the nonlocal method results from the calculation of $\varepsilon^{p}_{q(eq)}$ which requires searching of variables in neighbouring elements.

CONCLUSIONS

The performance of two mesh regularization techniques is presented in this study with an aim to use a large deformation finite element modeling technique to simulate extremely large deformation problems, such as large-scale landslides. Two idealized problems are modeled which has been modeled in previous studies to show the effectiveness of mesh regularization techniques using different numerical techniques, such as MPM and Lagrangian FE modeling. The present study shows that the element size scaling could reduce the mesh sensitivity issues, while the nonlocal method shows a better performance including mesh size independent shear band thickness. However, the nonlocal method is computationally very expensive. In terms of practical applications, the modeling of large-scale problems using a Eulerian-based FE approach is inherently computationally expensive. Therefore, with nonlocal method, the computational cost of a Eulerian-based FE model might increase to a much higher level, depending upon the size of the problem and availability of computing facility.

In recent years, Eulerian-based FE approaches (e.g., Abaqus Coupled Eulerian-Lagrangian (CEL) approach) have been used for modeling many offshore geotechnical problems, such as penetration and lateral displacement of surface-laid pipelines, jacking of pile and spudcan

foundations, and large-scale landslides. Most of these cases, the soil has strain-softening behaviour and therefore mesh sensitivity in FE analyses is expected. While CEL approach can handle large deformation, the present study will provide a better understanding in FE modeling to reduce mesh sensitivity.

One of the limitations of this study is that the simulations are performed only for idealized cases. Comparisons with other numerical approaches for modeling large deformation problems are required.

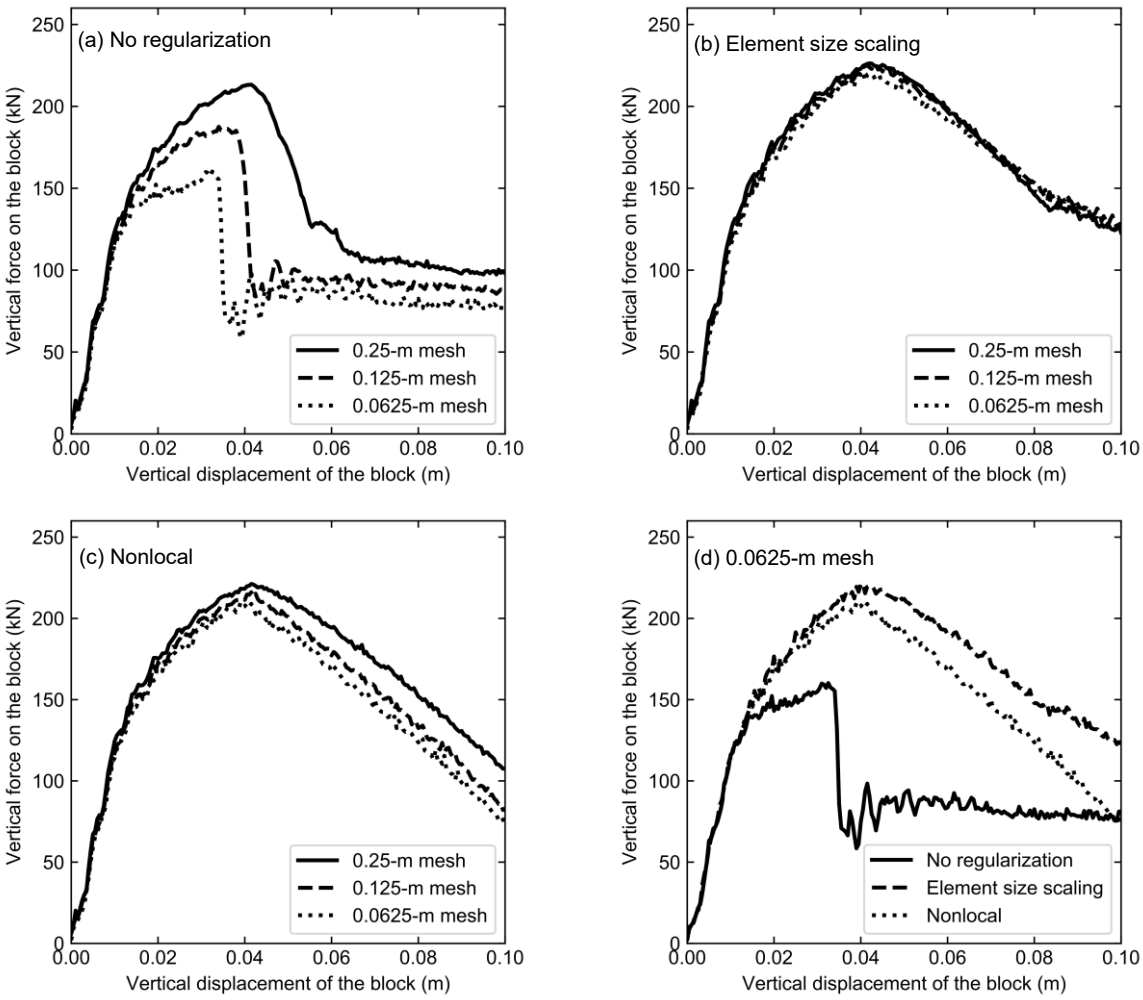

Figure 6 Variation of force with displacement of the rigid block in the upslope area

ACKNOWLEDGMENTS

The works presented in this paper have been supported by the Natural Sciences and Engineering Research Council of Canada (NSERC), InnovateNL and former Research and Development Corporation of Newfoundland and Labrador (RDC).

REFERENCES

Anastasopoulos, I., Gazetas, G., Bransby, M.F., Davies, M.C.R. and El Nahas, A., 2007. Fault rupture propagation through sand: finite-element analysis and validation through centrifuge experiments. Journal of Geotechnical and Geoenvironmental Engineering, 133(8), 943–958.

Bažant, Z.P., Belytschko, T.B. and Chang, T.P., 1984. Continuum theory for strain-softening. Journal of Engineering Mechanics, 110(12), 1666–1692.

Benson, D.J. and Okazawa, S., 2004. Contact in a multi-material Eulerian finite element formulation. Computer methods in applied mechanics and engineering, 193(39–41), 4277–4298.

Brinkgreve, R.B.J., 1994. Geomaterial models and numerical analysis of softening. Ph.D. thesis, Technische Universiteit Delft.

Burghardt, J., Brannon, R. and Guilkey, J., 2012. A nonlocal plasticity formulation for the material point method. Computer Methods in Applied Mechanics and Engineering, 225, 55–64.

D'Ignazio, M. and Länsivaara, T., 2015. Shear bands in soft clays: strain-softening behaviour in finite element method. Rakenteiden Mekaniikka J. Struct. Mech., 48(1), 83–98.

De Borst, R. and Mühlhaus, H.B., 1992. Gradient-dependent plasticity: formulation and algorithmic aspects. International Journal for Numerical Methods in Engineering, 35(3), 521–539.

de Borst, R., 1993. A generalisation of J2-flow theory for polar continua. Computer Methods in Applied Mechanics and Engineering, 103(3), 347–362.

Dey, R., Hawlader, B., Phillips, R. and Soga, K., 2015. Large deformation finite-element modeling of progressive failure leading to spread in sensitive clay slopes. Géotechnique, 65(8), 657–668.

Eringen, A.C., 1981. On nonlocal plasticity. International Journal of Engineering Science, 19(12), 1461–1474.

Galavi, V. and Schweiger, H.F., 2010. Nonlocal multilaminate model for strain softening analysis. International Journal of Geomechanics, 10(1), 30–44.

Goodarzi, M. and Rouainia, M., 2017. Modelling slope failure using a quasi-static MPM with a non-local strain softening approach. Procedia Engineering, 175, 220–225.

Griffiths, D.V. and Lane, P.A., 1999. Slope stability analysis by finite elements. Géotechnique, 49(3), 387–403.

Hu, Y. and Randolph, M. F., 1998. A practical numerical approach for large deformation problems in soil. International Journal for Numerical and Analytical Methods in Geomechanics, 22(5), 327–350.

Jostad, H. P., and Andresen, L. 2004. Modelling of shear band propagation in clays using interface. In Numerical Models in Geomechanics: In Proceedings of the Ninth International Symposium on Numerical Models in Geomechanics-NUMOG IX, 25–27 August 2004, Ottawa, Canada.121–128.

Loret, B. and Prevost, J.H., 1990. Dynamic strain localization in elasto-(visco-) plastic solids, Part 1. General formulation and one-dimensional examples. Computer Methods in Applied Mechanics and Engineering, 83(3), 247–273.

Pietruszczak, S.T. and Mroz, Z., 1981. Finite element analysis of deformation of strain-softening materials. International Journal for Numerical Methods in Engineering, 17(3), 327–334.
Summersgill, F., 2014. Numerical modelling of stiff clay cut slopes with nonlocal strain regularization. Ph.D. thesis, Imperial College London.
Vignjevic, R., Djordjevic, N., Gemkow, S., De Vuyst, T. and Campbell, J., 2014. SPH as a nonlocal regularisation method: Solution for instabilities due to strain-softening. Computer Methods in Applied Mechanics and Engineering, 277, 281–304.

APPENDIX-II

Modeling of Seepage Using a Eulerian-based Finite Element Method

This paper has been published in the 72nd Canadian Geotechnical Conference, GeoSt. John's, St. John's, NL, 2019.

Most of the research work presented in this paper was conducted by the first author. He also prepared the draft manuscript. The other authors reviewed and edited the manuscript.

Modeling of seepage using a Eulerian-based finite element method

Jin Chen, Bipul Hawlader, Chen Wang
Memorial University of Newfoundland, St. John's, Canada
Kshama Roy
Northern Crescent Inc., Calgary, Canada
Kenton Pike
TechnipFMC, St. John's, Canada

ABSTRACT
Seepage plays a significant role in many geotechnical problems such as the stability of earth dams and riverbanks. In addition, the large-deformation behaviour of soil is equally important in many cases, including progressive failure of slopes, and landslides in sensitive clays. The large-deformation can be successfully simulated using Eulerian-based finite-element (FE) modeling techniques. In the present study, a technique is developed for a Eulerian-based FE analysis using Abaqus FE software to simulate both transient and steady-state seepage through an earth dam. The FE simulation results, including the seepage, in-situ stresses and slip surface in slope stability analysis, are compared with the analyses using the GeoStudio software package. In terms of practical implication, the developed seepage model could be coupled with the large-deformation FE technique in Abaqus to simulate the progressive failure of a riverbank.

RÉSUMÉ
Les infiltrations jouent un rôle important dans de nombreux problèmes géotechniques tels que la stabilité des barrages en terre et des berges des rivières. De plus, le comportement du sol en grandes déformations est tout aussi important, y compris la rupture progressive des pentes et les glissements de terrain dans les argiles sensibles. Les grandes déformations peuvent être simulées avec succès à l'aide de techniques de modélisation par éléments finis (FE) basées sur Eulerian. Dans la présente étude, une technique est développée pour une analyse FE basée sur Eulerian utilisant le logiciel Abaqus FE pour simuler des infiltrations transitoires et stables à travers un barrage en terre. Les résultats de la simulation FE, y compris l'infiltration, les contraintes in situ et la surface de glissement dans l'analyse de la stabilité des pentes, sont comparés aux analyses effectuées à l'aide du logiciel GeoStudio. En termes d'implication pratique, le modèle de suintement développé pourrait être associé à la technique d'évaluation à grande déformation d'Abaqus pour simuler la défaillance progressive d'une rive.

1 INTRODUCTION

Seepage of water through soil could be a potential cause of slope failure. Seepage could alter both effective and total stresses in soil elements and thereby, the shear resistance. In addition, seepage force increases the driving force that could fail a slope which might be stable without seepage. For example, a high artesian groundwater condition along the Savail River in Quebec was recognized as one of the main causes of the 2010 St. Jude Landslide (Locat et al., 2011). The artesian groundwater condition and resulting seepage increased the pore water pressure, and thus reduced the effective stress and the shear strength of soils to nearly zero near the bottom of the river. This might have caused a small slide near the toe of the riverbank. Because of the stress redistribution, the failure then propagates further through the sensitive clays resulting in the large-scale St. Jude landslide on May 10, 2010. Note that seepage is not the only cause of a large-scale landslide. Many other factors are also involved in this process, e.g., in-situ stress condition, shear strength reduction, natural and human activities. In the present study, the role of seepage is primarily discussed.

Several methods have been developed in the past to conduct the slope stability analyses with seepage effects, e.g., limit equilibrium (LE), finite-element (FE). Among these methods, the LE method is widely used in the industry to assess the factor of safety (FOS) of the slope. By applying the precalculated seepage forces to the LE model, the FOS under steady-state seepage can be calculated. Locat et al. (2011) used the SLOPE/W software (GeoStudio, 2007), which is based on the LE theory, to conduct the slope stability analysis of the 2010 St. Jude Landslide. Prior to the LE analysis for stability, the groundwater condition was evaluated through a steady-state seepage modeling using SEEP/W software (GeoStudio, 2007). The LE analysis shows a similar first slip surface as observed in the field. However, the LE method failed to explain the formation of the horizontal shear plane, the horsts, and grabens.

The FE method has also been used for analyzing slope stability under seepage effects (Lane and Griffiths, 2000). The traditional Lagrangian-based FE method can capture the post-peak softening behaviour of sensitive clay and strain localization in a slope stability analysis. However, a significant mesh distortion occurs during the large deformation and therefore, the traditional Lagrangian-based FE analysis cannot handle the large-deformation behaviour of the slope failure, e.g., the progressive failure in a spread type of landslide.

Eulerian-based FE approach has been used in the past for the large-deformation analysis of sensitive clay slope

failures (Dey et al., 2015; 2016). The progressive failure of sensitive clay landslides was successfully modeled by using Eulerian-based FE method. Comparison between FE and LE analysis of the failure of the first soil block for an undrained loading condition has been performed in Saha et al. (2014). However, in these studies, the effects of seepage were not considered. Hamann et al. (2015) showed that the partially drained condition (transient seepage), for pile jacking into a fully saturated soil, can be simulated in a Eulerian-based FE approach where the pore water pressure was simulated with the thermal–hydraulic analogy theory. However, the seepage condition in a slope has not been modeled to establish the in-situ stresses for a Eulerian-based FE code.

In the present study, a methodology based on the thermal–hydraulic analogy theory is proposed for the seepage modeling in a slope with a Eulerian-based FE code. The results are benchmarked with SEEP/W analysis. Furthermore, the in-situ stresses under the influence of the steady-state seepage are simulated by SIGMA/W and Eulerian-based FE code, respectively. Finally, the strength reduction method is implemented to trigger the slope failure in Eulerian-based FE code to compare with the LE results from SLOPE/W.

2 NUMERICAL MODELING TECHNIQUE

For numerical analyses, GeoStudio software package (SEEP/W, SIGMA/W, and SLOPE/W) and Eulerian-based FE code available in Abaqus FE software are adopted for the seepage, in-situ stress and slope failure modeling.

2.1 GeoStudio

SEEP/W is a finite element software product, available in GeoStudio package, for modeling groundwater flow in porous media (soils). SEEP/W is capable of modeling both steady-state and transient seepage problems. Therefore, it has been widely applied in the analysis and design process of geotechnical engineering (Ng and Pang, 2000; Oh and Vanapalli, 2010).

SIGMA/W is also based on the finite element method. This software product can model stress and deformation in geotechnical problems with different constitutive models to represent a wide range of soils or structural materials (Oh and Vanapalli, 2011; Qi and Vanapalli, 2015).

SLOPE/W, which is based on limit equilibrium (LE) theories, is also one component in a complete suite of GeoStudio. It can model a variety of stability problems with different slip surface shapes, pore water pressure conditions, soil properties and loading conditions (Ng and Pang, 2000; Oh and Vanapalli, 2010).

2.2 Eulerian-based FE Method

Eulerian-based FE method available in Abaqus/Explicit FE software is used in the present study for numerical analysis. Note that typical FE programs developed in a Lagrangian framework cannot simulate very large deformation in a large-scale landslide because the significant mesh distortion around the failure plane causes numerical instabilities and non-convergences of the solutions (Griffiths and Lane, 1999). In the numerical technique used in the present study, the soil is modeled as a Eulerian material which can 'flow' through the fixed mesh without causing numerical issues related to mesh distortion. Further details of the mathematical formulations of Eulerian-based FE approach and its applications to large-deformation quasi-static/dynamic problems (e.g., onshore and offshore landslides) are available in previous studies (Benson, 1992; Benson and Okazawa, 2004; Dey et al., 2015, 2016; Islam et al., 2018).

In the present study, Eulerian-based FE code is used to simulate both the transient and steady-state seepage. Currently, built-in coupled pore pressure-stress elements are not available in Eulerian-based FE code in Abaqus to model the seepage. Therefore, thermal–hydraulic analogy theory is implemented in this study, to model the seepage with thermally coupled Eulerian elements (EC3D8RT, eight-node thermally coupled linear brick elements with reduced integration and hourglass control) available in Abaqus. Based on the analogy theory (Section 2.3), the total water pressure and pore pressure can be successfully calculated from the temperature.

2.3 Thermal–hydraulic Analogy

Hamann et al. (2015) simulated pile jacking into a fully saturated soil under partially drained conditions using Abaqus CEL. They modelled the soil as a two-phase medium with the thermally coupled Eulerian elements by considering the fluid flow analogous to heat transfer. In other words, an analogy exists between the Darcy's law for fluid flow (Eq. (1)) and heat conduction in a medium (Eq. (2)), which are the governing equations for the Darcy's law and heat conduction, respectively.

$$\mathbf{q} = \frac{\kappa}{\mu_w}(-\nabla p_w) \tag{1}$$

$$\mathbf{f} = k(-\nabla\theta) \tag{2}$$

where $\mathbf{q}$ = Darcy flux or Darcy velocity in porous media; κ = intrinsic permeability; μ_w = dynamic viscosity; p_w = pore water pressure or total head pressure; $\mathbf{f}$ = heat flux; k = thermal conductivity; and θ = temperature. From Eqs. (1) and (2), it can be concluded that $p_w :: \theta$, $\mathbf{q} :: \mathbf{f}$, $\kappa/\mu_w :: k$ ("::" is a symbol of analogy). Therefore, the relationship between the thermal parameters and the seepage parameters can be developed as Eqs. (3–5) (Hamann et al., 2015).

$$k :: \frac{\kappa}{\mu_w} = \frac{K\mu_w/\gamma_w}{\mu_w} = \frac{K}{\gamma_w} \tag{3}$$

$$c\rho :: \frac{1}{Q} \tag{4}$$

$$\rho = (1-n)\rho_s + n\rho_w \tag{5}$$

where K = hydraulic conductivity; γ_w = specific weight (unit weight) of water; c = specific heat; Q = bulk modulus of the mixture of fluid and soil particles; ρ = density of the soil; n = porosity of the soil; ρ_s = density of the solid grains; ρ_w = density of water.

To describe the behaviour of the fluid phase in a porous media, a continuity equation (Eq. (6)) is applied by Lewis and Schrefler (1998):

$$div\left\{\frac{\kappa}{\mu_w}[-\nabla p_w - \rho_w(\mathbf{a}_{ws} + \mathbf{a}_s) + \rho_w \mathbf{b}]\right\} + \alpha_{biot}\mathbf{m}\dot{\boldsymbol{\varepsilon}}_s + \frac{\dot{p}_w}{Q} = 0 \quad (6)$$

where $\mathbf{a}_{ws}$ = relative acceleration of the fluid phase with respect to the soil skeleton; $\mathbf{a}_s$ = acceleration of the soil skeleton; $\mathbf{b}$ = body force per unit mass; $\mathbf{m}$ = second order unit tensor; $\dot{\boldsymbol{\varepsilon}}_s$ = strain rate of the solid skeleton. The first term of Eq. (6), meaning the diffusion of pore water, is solved by heat conduction within the temperature–displacement analysis procedure of Abaqus ($\mathbf{a}_{ws}$ is small and thus being neglected (Zienkiewicz et al., 1999); $\mathbf{a}_s$ remains zero when simulating the steady-state seepage); and the second term, meaning the change of pore pressure due to volumetric straining of the solid skeleton $\alpha_{biot}\mathbf{m}\dot{\boldsymbol{\varepsilon}}_s$, is not necessary to be calculated for the purpose of simulating initial steady-state seepage.

SEEP/W also neglected the change of pore pressure due to the volumetric strain of the solid skeleton. The governing differential equation used in SEEP/W finite element formulation is:

$$\frac{\partial}{\partial x}\left(K_x\frac{\partial H}{\partial x}\right) + \frac{\partial}{\partial y}\left(K_y\frac{\partial H}{\partial y}\right) + F = m_w\gamma_w\frac{\partial H}{\partial t} \quad (7)$$

where H = total head; K_x and K_y: hydraulic conductivity in the x and y directions, respectively; F = applied boundary flux (usually equals to 0); m_w = slope of the storage curve ($\partial\theta_v = m_w\partial p_w$, θ_v = volumetric water content, and p_w = pore water pressure or total head pressure); γ_w = the unit weight of water; and t = time. In the saturated region, m_w becomes equivalent to m_v, the coefficient of volume compressibility (Krahn, 2004). Equation (7) is the same equation of Eq. (6) ignoring the term $\alpha_{biot}\mathbf{m}\dot{\boldsymbol{\varepsilon}}_s$, and m_w is equivalent to $1/Q$. Therefore, the same results should be obtained when simulating the same seepage problem by using Eulerian-based finite element model (with thermal-fluid analogy) and SEEP/W. Note that *K* and m_v in SEEP/W, and *k* and *c* in Abaqus influence only the transient state of analysis.

3 PROBLEM DEFINITION

An embankment consisted of sandy soil is studied. The geometry of the embankment is shown in Fig. 1. The embankment is 12 m high, 52 m base width, and an 8-m drainage is located at the toe of the downstream of the embankment. A rapid fill in the reservoir is considered. The water level of the reservoir is assumed to raise from 0 m to 11 m instantaneously (Fig. 1). Note that this assumption may not be able to reflect a realistic scenario. The transient seepage inside the embankment within 8 hours is studied using both Eulerian-based FE method and SEEP/W. The results of the two methods are compared including the variation of the total water head distribution with time, the effective stresses distribution and factor of safety of the embankment. Furthermore, the progressive failure with strength reduction method is simulated using the Eulerian analysis.

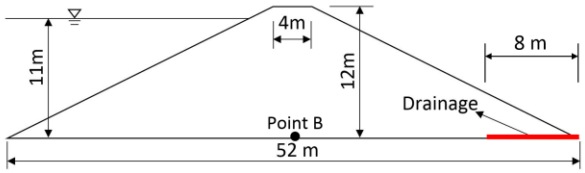

Figure 1. Geometry of rapid reservoir fill

4 FINITE ELEMENT MODELING

4.1 Load and Boundary Conditions

To simulate the rapid fill of the reservoir in SEEP/W analysis, a total head of 11 m is applied to the upstream surface of the embankment in an infinitely small time interval (blue line in Fig. 2(a)), and a total head of 0 m is applied to the drainage at the bottom of the embankment at downstream area (red line in Fig. 2(a)). On the other hand, adopting the fluid-thermal analogy, temperature boundary conditions are applied to the Eulerian model. A temperature boundary condition of 107910 °C (ρgh = 1000×9.81×11) is applied to the upstream of the embankment representing an 11 m total head (blue line in Fig. 2(b)), and a 0 °C boundary condition is applied to the area of the drainage (red line in Fig. 2(b)). The transient seepage analysis and transient thermal analysis for an 8-h time period are performed in SEEP/W and Abaqus CEL, respectively.

Based on the steady-state seepage results, the in-situ stresses are established in SIGMA/W and Eulerian-based FE code, respectively. The gravity load is applied to the soils for both models. Zero displacement and zero velocity are implemented on the bottom of both SIGMA/W and Eulerian-based FE code, respectively.

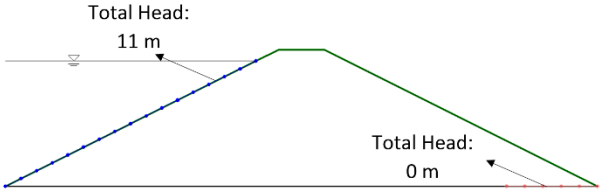

(a) SEEP/W model

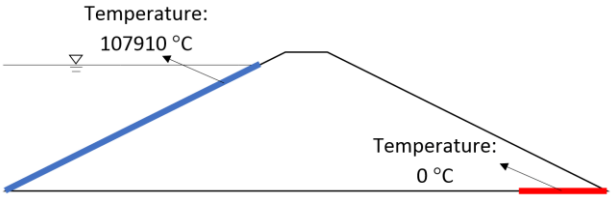

(b) Abaqus CEL model

Figure 2. Load and boundary conditions used for the embankment

Eulerian-based FE code can model only three-dimensional condition. Therefore, the plane strain condition is simulated using the model thickness of one element in the out of plane direction. A uniform mesh size (0.25 m x 0.25 m x 0.25 m) is used for all Eulerian-based FE analyses.

4.2 Soil Parameters

The soil parameters used in the GeoStudio and Eulerian-based FE code are shown in Table 1. Medium dense sand is assumed as the filling material of the embankment. The soil is modeled using the Mohr-Coulomb model and the analyses are performed for the drained condition. The soil density, ρ is calculated from Eq. (5). The thermal parameters for the Eulerian analysis, i.e., thermal conductivity, k and specific heat, c, are calculated using Eqs. (3) and (4), respectively.

Table 1. Soil parameters used in numerical analyses

Young's modulus, E (MPa)	50
Poisson's ratio, ν	0.25
Porosity, n	0.35
$1/Q$ or m_v, (MPa^{-1})	0.02
Density of soil, ρ (kg/m^3)	2076
Hydraulic conductivity, K (m/s)	1×10^{-5}
Cohesion, c' (kPa)	1
Effective friction angle, φ′ (°) (Eulerian model)	40 to 28.5
Dilation angle, ψ (°) (Eulerian model)	15 to 0.625
Effective friction angle, φ′ (°) (SLOPE/W)	40 and 28.5

Note: The dilation angle ψ is calculated from $\varphi' - \varphi_c' = 0.8\psi$ (Bolton, 1986), where the φ_c' (the critical state friction angle) is assumed to be 28°.

5 FINITE ELEMENT RESULTS

5.1 Seepage Analysis

Both SEEP/W and Eulerian-based FE models reached steady-state within 4 h, based on the total head distribution. The total head distributions inside of the embankment at 0.5 h and 4 h in SEEP/W are shown in Figs. 3(a) and 4(a), respectively. The temperature distributions at 0.5 h and 4 h in Eulerian-based FE model are shown in Figs. 3(b) and 4(b), respectively. Note that, the temperature 9810 °C is equivalent to 1 m total head, based on the thermal–hydraulic analogy. To better compare the results of SEEP/W and Eulerian-based FE model, the equivalent total head at point B (midpoint of the bottom of the embankment, as shown in Fig. 1) with time is plotted in Fig. 5. As can be observed in Figs. 3-5, the results from Eulerian-based FE model perfectly matches the SEEP/W results. The comparison strongly supports the effectiveness of the thermal–hydraulic analogy in the present Eulerian-based FE model. Also, the relationships between thermal and seepage parameters (Eqs. (3–5)) are validated.

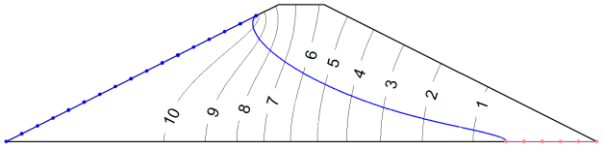

a) Total head at t = 0.5 h in SEEP/W (unit: m)

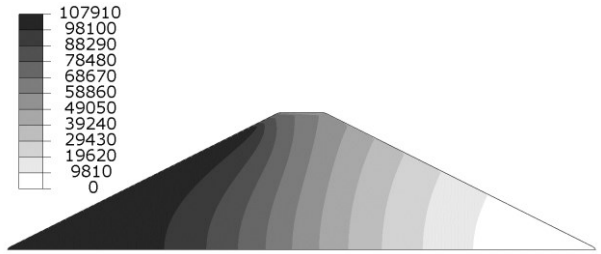

b) Temperature distribution or total head pressure at t = 0.5 h in Eulerian-based FE model (unit: °C or Pa)

Figure 3. (Equivalent) Total head distribution after 0.5 h

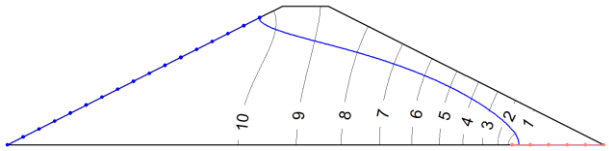

(a) Total head at t = 4 h in SEEP/W (unit: m)

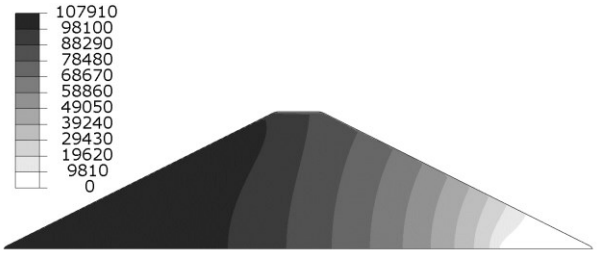

(b) Temperature distribution or total head pressure at t = 4 h in Eulerian-based FE model (unit: °C or Pa)

Figure 4. (Equivalent) Total head distribution in the embankment at 4 h

Fig. 5 shows that the total head becomes a constant after t ~ 4 h. At the same time, not only point B reaches a constant total head, but also other parts of the embankment come to the steady state. For the in-situ situation, the seepage condition usually remains steady-state when the boundary conditions do not change significantly in a short period. Therefore, only the steady-state seepage is considered for in-situ stresses modeling.

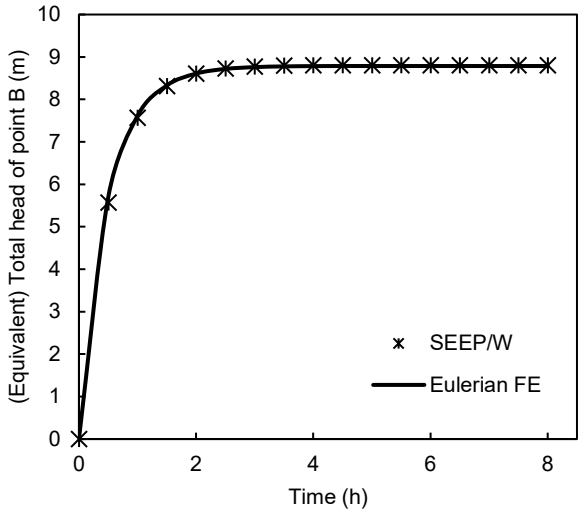

Figure 5. (Equivalent) Total head at point B

5.2 In-situ Stresses

The distribution of in-situ stresses can directly influence the location of the critical slip surface. Therefore, it is important to accurately establish the in-situ stresses, in order to effectively analyze slope stability.

Based on the results of the equivalent total head, the seepage forces can be calculated and then applied to the Eulerian elements under the phreatic line. Coupled with the gravity load, the in-situ stresses under the seepage condition are modeled using Eulerian-based FE code. The vertical, horizontal, and deviatoric (von Mises) stresses obtained from Eulerian-based FE modeling are presented in Figs. 6(a), 7(a) and 8(a), respectively. For comparison, the in-situ stresses calculated from SIGMA/W, together with seepage analysis results from SEEP/W, are shown in Figs. 6(b), 7(b) and 8(b).

From the comparison, the in-situ stress distributions are found to be quite similar between Eulerian-based FE and SIGMA/W analyses. The maximum vertical stresses in SIGMA/W and Eulerian-based FE code are 136.2 kPa and 137.1 kPa, respectively (Fig. 6). Furthermore, SIGMA/W and Eulerian-based FE code calculate the maximum horizontal stress of 48.2 kPa and 44.9 kPa, respectively (Fig. 7). For the maximum deviatoric stress, the values are 97.6 kPa and 100.5 kPa in SIGMA/W and Eulerian-based FE, respectively (Fig. 8). This slight difference is potentially due to the solution algorithms used in these software packages.

5.3 Slope Stability and Deformation Analysis

In the present study, the strength reduction method is used to trigger the failure of the slope and find the slip surface from Eulerian-based FE analysis. To conduct the strength reduction, the effective friction angle (φ') is decreased from 40° to 28.5°. The dilation angle (ψ) is also reduced accordingly as $\psi = (\varphi' - \varphi_c')/0.8$ (Bolton, 1986). Furthermore, the slope stability analysis is conducted with the limit equilibrium method using SLOPE/W, based on the in-situ stresses from SEEP/W (considering seepage result). The Spencer method is selected for the calculation of factor of safety and slip surfaces in SLOPE/W.

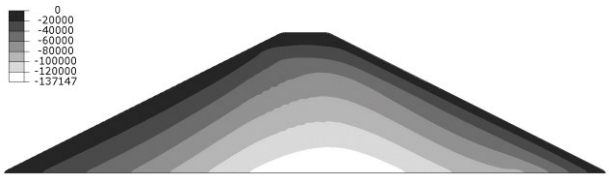

a) Eulerian-based FE (unit: Pa)

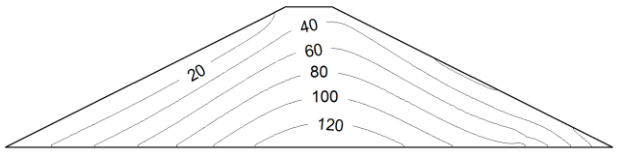

b) SIGMA/W (unit: kPa)

Figure 6. Vertical stress under steady-state seepage

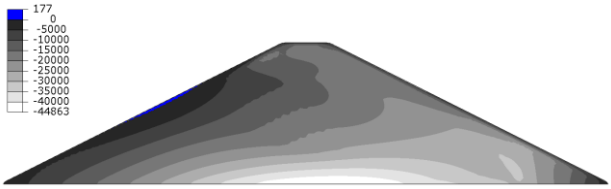

a) Eulerian-based FE (unit: Pa)

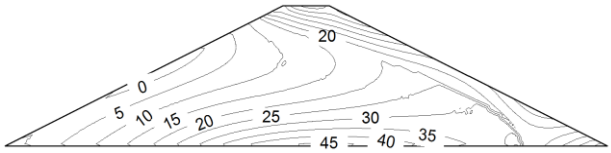

b) SIGMA/W (unit: kPa)

Figure 7. Horizontal stress under steady-state seepage

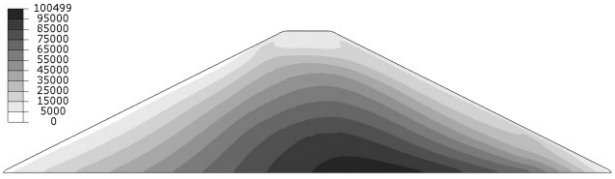

a) Eulerian-based FE code (unit: Pa)

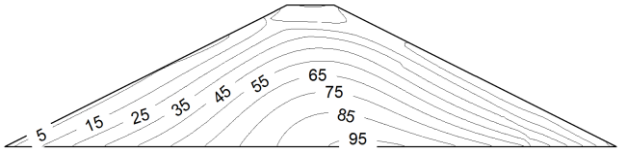

b) SIGMA/W (unit: kPa)

Figure 8. Deviatoric stress under steady-state seepage

The accumulated plastic shear strain in the Eulerian FE analysis for different friction angles (φ' = 40°, 30° and 28.5°) is shown in Figs. 9(a), 9(b) and 9(d), respectively. The slope

is stable, and no plastic shear strain develops in the soil elements for $\varphi' = 40°$ (Fig. 9(a)). The failure plane does not form instantaneously rather the failure starts from the toe of the slope and gradually progresses to the left and up (Fig. 9(b)). As shown in Fig. 9(d), a complete failure plane forms when the shear strength is reduced significantly (e.g., $\varphi' = 28.5°$). Figure 9(c) shows the instantaneous velocity vector of the soil elements above the failure plane.

For comparison, the critical slip circles and factor of safety for these values of φ' obtained from SLOPE/W analysis are also shown in Fig. 9. The slight difference between the location of the critical circle in SLOPE/W and high shear strain zone in FE analysis is potentially due to the progressive formation of the failure plane and displacement of the failed soil mass in the latter one. The FOS ~ 1.0 for $\varphi' = 28.5°$ (Fig. 9(d)).

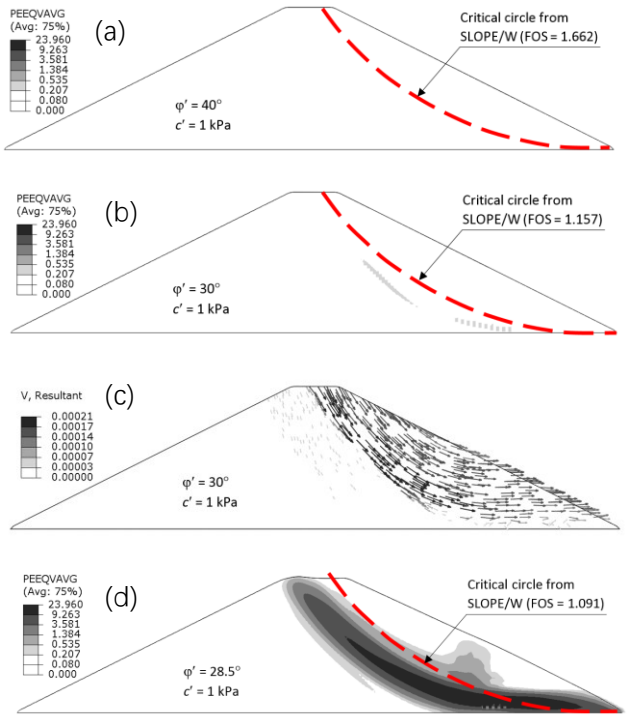

Figure 9. Plastic shear strain and instantaneous velocity vectors in slope stability analysis

5.4 Influence of Seepage Forces on Slope Failure

If the seepage force is not considered in the model, the failure pattern is usually different. To demonstrate it, the same problem as presented in Section 5.3 is analyzed using the Eulerian FE approach. In this case, the seepage force is not added to the soil elements; however, the buoyancy is still applied to the soil elements below the phreatic line. Figure 10 shows that the in-situ deviatoric stress is very different from the values obtained with seepage effects (compare Figs. 8(a) and 10).

Using the same strength reduction approach presented in Section 5.3, the stability of the slope is checked without considering the seepage. The slope remains stable in this case (i.e., without seepage) even for $\varphi' = 28.5°$ while it fails when the seepage force is considered (Fig. 9(d)). In other words, seepage force significantly influences the result of slope stability analysis because of the change in in-situ effective stresses.

In a large-scale landslide modeling, the in-situ seepage conditions might be important, especially in triggering of the landslide by the failure of the first soil block.

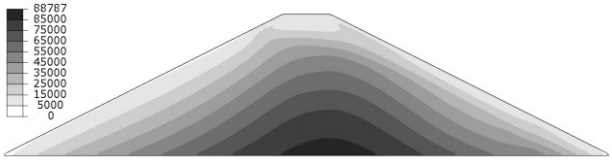

Figure 10. Deviatoric stress in Eulerian-based FE analysis without seepage forces

6 CONCLUSIONS

In this study, a technique is developed to model the seepage for finite element modeling of slope failures using Eulerian-based FE code. Both transient and steady-state seepage conditions are modeled based on the thermal–hydraulic analogy. The FE results are comparable to those obtained from SEEP/W analysis. The in-situ stresses at the steady-state seepage condition are modeled in both Eulerian-based FE model and SIGMA/W. The two methods give nearly identical results. Furthermore, the location of the critical failure plane inferred from Eulerian-based FE analysis and obtained from SLOPE/W is similar. However, the SLOPE/W could not handle the post-failure process while Eulerian-based FE model can simulate the complete failure mechanisms.

In conclusion, the technique developed in the present study is applicable to slope stability analysis considering the seepage effects in Eulerian-based FE code. Coupled with its advantage to handle large deformation analysis, the progressive landslides, e.g., the 2010 St. Jude Landslide, can be modeled with the consideration of both seepage effects and large deformation. Note that the simulation results presented in this study is only for idealized soil properties and boundary conditions; however, the developed technique could be used case specific scenarios.

ACKNOWLEDGEMENTS

The works presented in this paper have been supported by the Natural Sciences and Engineering Research Council of Canada (NSERC), InnovateNL and former Research and Development Corporation of Newfoundland and Labrador (RDC).

REFERENCES

Benson, D. J. 1992. Computational methods in Lagrangian and Eulerian hydrocodes. *Computer methods in Applied Mechanics and Engineering*, 99 (2-3), 235–394.

Benson, D. J., and Okazawa, S. 2004. Contact in a multi-material Eulerian finite element formulation. *Computer methods in applied mechanics and engineering*, 193(39-41), 4277–4298.

Bolton, M. D. 1986. Strength and dilatancy of sands. *Géotechnique*, 36(1), 65–78.

Dey, R., Hawlader, B., Phillips, R. and Soga, K. 2015. Large deformation finite element modeling of progressive failure leading to spread in sensitive clay slopes. *Géotechnique*, 65 (8), 657–668.

Dey, R., Hawlader, B., Phillips, R. and Soga, K. 2016. Numerical modelling of submarine landslides with sensitive clay layers, *Géotechnique*, 66 (6), 454–468.

GeoStudio 2007. GEOSLOPE International Ltd. Calgary, AB, Canada.

Griffiths, D. V., and Lane, P. A. 1999. Slope stability analysis by finite elements. *Géotechnique*, 49 (3), 387–403.

Hamann, T., Qiu, G., and Grabe, J. 2015. Application of a Coupled Eulerian–Lagrangian approach on pile installation problems under partially drained conditions. *Computers and Geotechnics*, 63, 279–290.

Islam, N., Hawlader, B. C., Wang, C., and Soga, K. 2018. Large deformation finite-element modelling of earthquake-induced landslides considering strain-softening behaviour of sensitive clay. *Canadian Geotechnical Journal*, https://doi.org/10.1139/cgj-2018-0250.

Krahn, J. 2004. *Seepage modeling with SEEP/W: An engineering methodology.* GEO-SLOPE International Ltd. Calgary, Alberta, Canada.

Lane, P. A., and Griffiths, D. V. 2000. Assessment of stability of slopes under drawdown conditions. *Journal of Geotechnical and Geoenvironmental Engineering*, 126 (5), 443–450.

Lewis, R. W., and Schrefler, B. A. 1998. *The finite element method in the static and dynamic deformation and consolidation of porous media*. John Wiley, New York.

Locat, P., Fournier, T., Robitaille, D. and Locat, A. 2011. Glissement de terrain du 10 mai 2010, Saint-Jude, Montérégie – Rapport sur les caractéristiques et les causes. Ministère des Transports du Québec, Service Géotechnique et Géologie, Rapport MT11-01.

Ng, C. W., and Pang, Y. W. 2000. Influence of stress state on soil-water characteristics and slope stability. *Journal of Geotechnical and Geoenvironmental Engineering*, 126(2), 157–166.

Oh, W. T., and Vanapalli, S. K. 2010. Influence of rain infiltration on the stability of compacted soil slopes. *Computers and Geotechnics*, 37(5), 649-657.

Oh, W. T., and Vanapalli, S. K. 2011. Modelling the applied vertical stress and settlement relationship of shallow foundations in saturated and unsaturated sands. *Canadian Geotechnical Journal*, 48(3), 425–438.

Qi, S., and Vanapalli, S. K. 2015. Hydro-mechanical coupling effect on surficial layer stability of unsaturated expansive soil slopes. *Computers and Geotechnics*, 70, 68–82.

Saha, B., Hawlader, B., Dey, R., and McAffee, R. 2014. Slope stability analysis using a large deformation finite element modeling technique. In 67th Canadian Geotechnical Conference GeoRegina. Regina, Saskatchewan, Canada.

Zienkiewicz, O. C., Chan, A. H. C., Pastor, M., Schrefler, B. A., and Shiomi, T. 1999. *Computational geomechanics with special reference to earthquake engineering*, Wiley, New York.